An Anatomically-Based Mathematical Model of the Human Pulmonary Circulation

By Kelly Suzanne Burrowes.

Supervised by Dr Merryn Tawhai and Professor Peter Hunter.

A thesis submitted in partial fulfilment of the requirements for the degree of Doctor of Philosophy in Biomedical Engineering at The University of Auckland.

Bioengineering Institute,
The University of Auckland,
April 27, 2005.

Abstract

This research develops a detailed, anatomically-based model of the human pulmonary circulatory system from the large scale arterial and venous vessels, to the microcirculatory alveolar-capillary unit. Flow is modelled through these networks enabling structure-function simulations to be conducted to increase our understanding of this complex system.

Voronoi meshing is applied in a novel technique to represent the three-dimensional structure of the alveoli, and the corresponding capillary plexus intimately wrapped over the alveolar surface. This technique is used to create the alveolar-capillary structure of a single alveolar sac, closely representing the geometry measured in anatomical studies.

A Poiseuille type flow solution technique is implemented within the capillary geometry. The solution procedure incorporates calculations of red and white blood cell transit time frequencies. Novel predictions of regional microcirculatory blood cell transit in the anatomically-realistic alveolar-capillary model compare well with experimental measures.

An anatomically-based finite element model of the arterial and venous vessels, down to the level of their accompanying respiratory bronchioles, is created using a combination of imaging and computational algorithms, which includes generation of supernumerary vessels. Large arterial and venous vessels and lobar geometries are derived from multi-detector row x-ray computed tomography (MDCT) scans. From these MDCT vessel end points a volume-filling branching algorithm is used to generate the remaining blood vessels that accompany the airways into the MDCT-derived host volume. An empirically-based algorithm generates supernumerary blood vessels - unaccompanied by airways that branch to supply the closest parenchymal tissue. This new approach produces a model of pulmonary vascular geometry that is far more anatomically-realistic than previous models in the literature.

A reduced form of the Navier-Stokes equations are solved within the vascular geometries to yield pressure, radius, and velocity distributions. Inclusion of a

gravitational term in the governing equations allows application of the model in investigating the relative effects of gravity, structure, and posture on regional perfusion.

Gravity is shown to have a lesser influence on blood flow distribution than suggested by earlier experimental studies, and by comparison between different model solutions the magnitude of the gravitational flow gradient is predicted. This study clearly demonstrates the significant role that asymmetric vascular branching has in determining the distribution of blood flow. The influence of branching geometry is revealed by solution in symmetric, human, and ovine vascular models.

Preface

This thesis builds on established techniques for accurately modelling the geometry of the bronchial tree, and on previous models of blood flow through simple representations of the pulmonary microcirculation and through coronary blood vessels. It includes the following original developments:

- a novel Voronoi/Delaunay meshing technique developed to generate geometric representations of the 3D alveolar structure, and the accompanying capillary plexus;
- investigation of regional variations in microcirculatory flow and cellular transit phenomena in an anatomically-based geometry;
- the first anatomically-based model of the human pulmonary arterial and venous trees including supernumerary vessels;
- solution of Navier-Stokes flow equations - incorporating a gravitational term - in the large vascular geometries to provide the most detailed model of pulmonary blood flow developed to date;
- application of the blood flow model to investigate the relative influence of structure and gravity on blood distribution.

The research presented in this study has resulted in four papers to date. These papers have either been published or submitted for publication to peer reviewed journals:

1. M H Tawhai, **K S Burrowes**. (2003) Developing integrative computational models of pulmonary structure. *The Anatomical Record (Part B: The New Anatomist)*. 275(1):207-218.

2. **K S Burrowes**, M H Tawhai, and P J Hunter. (2004) Modeling RBC and neutrophil distribution through an anatomically-based pulmonary capillary network. *Annals of Biomedical Engineering*. 32(4):585-595.

3. **K S Burrowes**, M H Tawhai, and P J Hunter. Anatomically-based finite element models of the human pulmonary arterial and venous trees including supernumerary vessels. *Submitted to Journal of Applied Physiology*.

4. **K S Burrowes**, M H Tawhai, and P J Hunter. (2005) Evaluation of arterial blood flow heterogeneity in an image-based computational model. *Physiology, Function, and Structure from Medical Images: Proceedings of SPIE medical imaging conference*. Volume 5746.

The first paper provides an overview of the microcirculatory model, the second paper has been divided into chapters 2 and 3, the third paper forms the basis of chapter 4, and the fourth paper is a small component of the work described in chapter 5.

Chapter 1 Introduction: Contains an introduction to pulmonary physiology and details of the morphology of the pulmonary circulatory system. This chapter also discusses previous modelling work done in this area.

Chapter 2 Geometric modelling of the pulmonary microcirculation: Describes the development of the alveolar and capillary geometric models.

Chapter 3 Microcirculatory blood flow: Details the blood flow solution method used to model flow through the pulmonary capillary network.

Chapter 4 Geometric modelling of the large pulmonary vessels: Describes the techniques used to create an anatomically-based model of the human pulmonary arterial and venous vessels.

Chapter 5 Blood flow in the large vessels: Contains a description of the numerical methods used to solve for blood flow distribution through the larger arterial and venous vessels. This model is used to conduct structure-function investigations.

Chapter 6 Summary: Contains a summary of the work provided in this thesis and future directions for the model.

Acknowledgements

This work would not have been possible without the help and support of so many people. Completing a thesis has turned out to be an endurance test which cannot be faced alone.

First of all I want to thank my supervisors, Dr Merryn Tawhai and Professor Peter Hunter, for all the time and effort they have put into me and this work, and for believing that a Chemical Engineer can come through with the goods. I am indebted to them both and none of this work would have been possible without them. I am glad to have been Merryn's first student, and hopefully have not discouraged her from repeating the process.

The first three years of this work was supported by a doctoral fellowship provided by the Foundation for Research, Science and Technology (FRST) and Auckland Uniservices Limited. The final year was funded by a RSNZ Marsden grant (01-UOA-070). I am very grateful for the support provided by these three agencies.

There have been several other people at the Bioengineering Institute (which has been a wonderful place to work demonstrating why people never seem to leave) who have provided me with a lot of help. This includes Nic Smith and Jack Lee for helping me with the Navier-Stokes flow solution, Maria Fung and Nirosha Herat for everything administrative (and for organising all the parties), Shane Blackett for visualisation techniques, and David Bullivant for assisting with the Voronoi meshing technique. Also to David Nickerson for pretty much knowing everything there is to know and being able to fix any problems I had along the way, and equally as importantly for his coffee making skills.

Thank you to my family for offering me so much love and support, and to my mum for always being able to feed me when I needed it! I also owe a lot to my Chris who has been with me for the majority of this project and has managed to keep my feet on the ground and give me so much support, love, and patience.

Finally I want to thank my friends, in advance, for hopefully helping to relocate me back into the wild.

Contents

List of Figures **xi**

List of Tables **xvii**

Glossary of Acronyms **xix**

List of Symbols **xix**

1 Introduction **1**

1.1 The lungs . . . 1
1.2 Alveolar-capillary network geometry . . . 3
1.2.1 Pulmonary alveoli . . . 3
1.2.2 The blood-gas barrier . . . 6
1.2.3 Pulmonary capillaries . . . 9
1.2.4 Mechanical support . . . 10
1.3 Capillary blood flow . . . 14
1.3.1 Properties of blood in the microvascular network . . . 14
1.3.2 Zones of flow . . . 15
1.3.3 Capillary perfusion: recruitment versus distension . . . 17
1.3.4 Neutrophil Margination . . . 19
1.4 The pulmonary vasculature . . . 20
1.4.1 Supernumerary blood vessels . . . 24
1.4.2 Classification of branches in tree-like systems . . . 25
1.5 Pulmonary blood flow . . . 28
1.5.1 Pressures in and around the pulmonary blood vessels . . . 28
1.5.2 Changing perspectives on blood flow distribution . . . 29
1.5.3 Ventilation-perfusion relationships . . . 30
1.6 Previous work . . . 30

1.6.1 Alveolar-capillary geometric models . . . 30
1.6.2 Capillary flow models . . . 34
1.6.3 Pulmonary vascular models . . . 37
1.6.4 Pulmonary blood flow models . . . 37

2 Geometric modelling of the pulmonary microcirculation 39
2.1 Introduction . . . 39
2.2 Methods . . . 40
2.2.1 Voronoi diagrams and Delaunay triangulation . . . 40
2.2.2 The alveolar geometric model . . . 42
2.2.3 The capillary geometric model . . . 45
2.3 Results . . . 47
2.3.1 Alveolar geometry . . . 47
2.3.2 Capillary geometry . . . 47
2.4 Discussion . . . 50
2.4.1 Alveolar model . . . 50
2.4.2 Capillary model . . . 51
2.5 Conclusions . . . 52

3 Microcirculatory blood flow 53
3.1 Introduction . . . 53
3.2 Methods . . . 54
3.2.1 Dimensional changes of the capillary cross-section . . . 54
3.2.2 Flow in a single vessel . . . 58
3.2.3 The network flow model . . . 61
3.2.4 Hematocrit distribution . . . 61
3.2.5 Cell transit time models . . . 64
3.2.6 Parameters used in the model . . . 68
3.2.7 Normal simulation conditions . . . 68
3.2.8 Cell transit time distributions in the upright lung . . . 69
3.2.9 Variation in blood pressure in the upright lung . . . 69
3.3 Results . . . 70
3.3.1 Blood flow results . . . 70
3.3.2 Analysis of the flow model . . . 73
3.3.3 Corner vessels . . . 78
3.3.4 Breathing cycle . . . 79

3.3.5 Neutrophil traversing . . . 81
3.3.6 Sensitivity analysis . . . 83
3.3.7 Cell transit time distributions in the upright lung . . . 83
3.3.8 Variation in blood pressure in the upright lung . . . 88
3.4 Discussion . . . 92
3.4.1 Cell transit time distributions in the upright lung . . . 92
3.4.2 Variation in blood pressure in the upright lung . . . 94
3.5 Conclusions . . . 99

4 Geometric modelling of the large pulmonary vessels 101
4.1 Introduction . . . 102
4.2 Methods . . . 103
4.2.1 Vessels from MDCT images . . . 103
4.2.2 Accompanying vessels . . . 104
4.2.3 Supernumerary vessel algorithm . . . 108
4.2.4 Analysis of branching geometry . . . 109
4.3 Results . . . 110
4.3.1 Vessels from MDCT . . . 110
4.3.2 Accompanying vessels . . . 111
4.3.3 Supernumerary vessels . . . 113
4.3.4 Geometric analysis . . . 113
4.4 Discussion . . . 117
4.4.1 MDCT vessels . . . 118
4.4.2 Accompanying blood vessels - VFB algorithm . . . 119
4.4.3 Supernumerary vessels . . . 119
4.4.4 Geometric analysis . . . 120
4.5 Conclusions . . . 121

5 Blood Flow in the Large Vessels 123
5.1 Introduction . . . 124
5.2 Methods . . . 125
5.2.1 Navier-Stokes flow equations . . . 125
5.2.2 The Lax-Wendroff numerical scheme . . . 129
5.2.3 Calculating flow through bifurcations . . . 135
5.3 Single vessel results . . . 138
5.4 Full model results . . . 141

5.4.1 Blood flow distribution as a function of vascular branching . . . 142
5.4.2 Blood flow distribution as a function of gravity 146
5.4.3 Solution at different resolutions 163
5.4.4 Pleural pressure versus blood flow distribution 166
5.4.5 Effect of body posture on blood flow distribution 168
5.4.6 Effect of vessel distensibility 174
5.4.7 Network transit times 176
5.4.8 Pulsatile flow solutions 181
5.4.9 Comparison of model results with functional imaging 184
5.4.10 Comparison of flow in the human versus sheep lung 185
5.5 Discussion 192
5.6 Conclusions 201

6 Summary **203**
6.1 Future work 205

A CMISS command files **207**
A.1 Creating the alveolar model 207
A.2 Generating the capillary model over the alveolar surface geometry . . . 208
A.3 Solving for flow through the capillary network 209
A.4 Generating the arterial and venous geometries 209
A.5 Creating the supernumerary vessel geometry 211
A.6 Solving the Navier-Stokes flow equations through the arterial and venous models 212

B Movies **213**

List of Figures

1.1 SEM of alveoli 4
1.2 SEM of an alveolar duct and surrounding alveoli, and the capillary layer between adjacent alveoli 5
1.3 TEM of the alveolar-capillary barrier 7
1.4 SEM of a section of the pulmonary capillary network 9
1.5 Photomicrograph of a section of the rabbit capillary network 9
1.6 Schematic of the fibre continuum weaving throughout the capillary meshwork 11
1.7 Schematic illustration of the balance between alveolar surface tension, fibre tension, and capillary pressure 12
1.8 SEM of rabbit capillaries in zones 2 and 3, illustrating the patency of corner vessels 13
1.9 Schematic illustration of the four different 'zones' of flow in the lung . . 17
1.10 Schematic demonstrating locations of the main pulmonary arterial and venous vessels emerging from the heart 22
1.11 Photograph of a cast of the human pulmonary arteries and airways, illustrating the presence of supernumerary vessels 24
1.12 Illustration of generation, Horsfield, and Strahler ordering schemes on a simple tree network 26
1.13 Oblique section of a human alveolar duct and surrounding alveoli . . . 31

2.1 Illustration of the Voronoi meshing technique 41
2.2 Alveolar mesh generation using 3D Voronoi meshing technique, illustrated in 2D 42
2.3 Full alveolar model in 3D 43
2.4 Generation of the capillary geometric model using a 2D Voronoi meshing method 45

2.5 Finite element computational Voronoi alveolar mesh 49
2.6 Finite element computational Voronoi capillary mesh 49

3.1 Schematic of capillary cross-section, illustrating dimensional model development 55
3.2 Flow solution in the alveolar sac model 71
3.3 Pressure and hematocrit solutions in the alveolar sac model 72
3.4 Flow, diameter, and hematocrit distributions with respect to the percentage of pathways 73
3.5 Plot of alveolar volume and septal elasticity coefficient versus transpulmonary pressure during inspiration and expiration, determined using the alveolar dimensional model 74
3.6 Comparison of constant versus non-linear viscosity models: apparent viscosity and resistance versus hydraulic diameter 75
3.7 Relationship between RBC fluxes and flow rates (Q_i/Q_0) at a bifurcation as defined by the sigmoidal function (G), investigating changes in the flux cut-off parameter (r) and the preferential flux parameter (b) 76
3.8 Cell transit time results with and without the hematocrit model 77
3.9 Cell transit time results with different initial hematocrit values 78
3.10 RBC, flow, and hematocrit distributions at different stages of breathing . 80
3.11 WBC transit time distributions and stoppage at different stages of breathing 81
3.12 WBC transit time distributions and stoppage with varying cell cortex tension 82
3.13 Comparison of WBC stopping frequency in the upper, mid, and lower regions of the lung 83
3.14 Blood flow solutions in the alveolar sac model in the upper, mid and lower regions of a vertical human lung 86
3.15 Model cell transit time frequency distributions with respect to the percentage of pathways 87
3.16 Model cell transit time frequency distributions with respect to the percentage of flow 87
3.17 Model capillary diameters and flow in relation to lung height 89
3.18 Cell transit time results for simulations at 2 cm intervals over the height of a 30 cm lung 90

3.19 Comparison of model results with measured experimental values of RBC transit time and blood flow (relative to mean) with respect to gravitationally-dependent height 91
3.20 Alveolar sac capillary volume and average capillary sheet height in relation to vertical position in the lung 92

4.1 Grayscale bitmap masks of the large arterial and venous vessels segmented from MDCT data of a normal human male 104
4.2 Schematic diagram illustrating the relationship between the three conducting trees in the lung 105
4.3 Definition of lobar volumes via reconstruction of rendered iso-surfaces from MDCT 106
4.4 Illustration of the volume-filling branching (VFB) algorithm used to generate the geometry of the accompanying arterial and venous vessels 107
4.5 Schematic illustration of the supernumerary algorithm 110
4.6 Arterial and venous vessels obtained from MDCT scan data 111
4.7 Resulting arterial and venous models generated using the volume-filling branching (VFB) algorithm, including major vessels from MDCT scan data 112
4.8 Close in view of the model supernumerary arterial blood vessels emerging from the larger accompanying blood vessels 113
4.9 Strahler order number versus number of branches showing the progression of the model towards anatomical data for the arterial and venous networks 115
4.10 Strahler order number versus branch diameter showing the progression of the model towards anatomical data for the arterial and venous networks 116
4.11 Strahler order number versus branch length showing the progression of the model towards anatomical data for the arterial and venous networks 116

5.1 The velocity profile defined across a vessel cross-section 127
5.2 Plot of pressure versus radius demonstrating the form of the pressure-radius relationship incorporated into the Navier-Stokes flow solution . . 128
5.3 Comparison of analytic solution versus numerical Navier-Stokes solution in a single vessel 134
5.4 Schematic diagram of a vessel junction showing nomenclature used for grid point locations, flows, and pressure at a junction 135
5.5 Comparison of pressure, radius, and velocity profiles within a single vessel oriented vertically with and without gravity 139

5.6 Comparison of steady-state pressure, radius, and velocity profiles in a single vessel oriented vertically with and without gravity 140
5.7 Convergence analysis in a single vessel including gravity 141
5.8 Pressure, velocity, and flow solutions in a symmetric arterial model compared with solutions in the anatomically-based arterial model without gravity 143
5.9 Comparison of pressure, radius, velocity and flow solutions with respect to vertical height in the symmetric versus the anatomically-based arterial model without gravity at all terminal nodal locations averaged within 1 and 50 mm slices 145
5.10 Comparison of path lengths and transit time solutions in the symmetric versus anatomically-based arterial model without gravity 146
5.11 Pressure, velocity, and flow solutions in the symmetric and anatomically-based arterial models with gravity 147
5.12 Comparison of pressure, radius, velocity, and flow solutions with respect to gravitationally-dependent height at terminal nodes in the symmetric and anatomically-based models averaged within 1 and 50 mm slices with and without gravity 149
5.13 Comparison of path lengths and transit time solutions in the symmetric versus anatomically-based arterial models with gravity 150
5.14 Comparison of pressure, velocity, and flow solutions in the anatomically-based arterial model with and without gravity 151
5.15 Comparison of pressure, radius, velocity, and flow solutions with respect to gravitationally-dependent height at terminal nodes in the anatomically-based arterial model with and without gravity 153
5.16 Flow (relative to mean) with respect to vertical position in the lung, including least squares regression line of flow as a function of gravitationally-dependent height for the arterial model with and without gravity 154
5.17 Comparison of model flow results (relative to mean) with experimental measurements of blood flow in the supine pig and upright baboon lungs 154
5.18 Comparison of pressure, velocity, and flow solutions in the anatomically-based venous model with and without gravity 156
5.19 Comparison of pressure, radius, velocity, and flow solutions at terminal nodes with respect to gravitationally-dependent height in the anatomically-based venous model with and without gravity 157

5.20 Flow (relative to mean) with respect to vertical position in the lung, including least squares regression line of flow as a function of gravitationally-dependent height in the venous model with and without gravity 158
5.21 Comparison of pressure, radius, velocity and flow solutions with increasing amounts of gravity (0G, 1G, 1.8G) in the arterial model 159
5.22 Comparison of pressure, radius, velocity and flow solutions with increasing amounts of gravity (0G, 1G, 1.8G) in the venous model 161
5.23 Flow (relative to mean) with respect to vertical position in the lung, including least squares regression line, for the arterial and venous trees with increased gravity (1.8G) 162
5.24 Comparison of model flow results (relative to mean) with respect to gravitationally-dependent height with flow measurements from supine pig lungs with increased gravity (1.8G) 162
5.25 Pressure, radius, velocity, and flow solutions at all terminal locations in the arterial model averaged within different slice thicknesses 164
5.26 Pressure, radius, velocity, and flow solutions at all terminal locations in the venous model averaged within different slice thicknesses 165
5.27 Pressure, radius, velocity, and flow solutions at terminal locations in the arterial model averaged within 1 and 50 mm slices with varying amounts of pleural pressure 167
5.28 Comparison of pressure, radius, velocity, and flow solutions at terminal locations averaged within 1 and 50 mm slices in the arterial model in different postures 170
5.29 Comparison of pressure, radius, velocity, and flow solutions at terminal locations averaged within 1 and 30 mm slices in the arterial model in the prone versus supine positions 171
5.30 Comparison of pressure, radius, velocity, and flow solutions at terminal locations averaged within 1 and 50 mm slices in the venous model in different postures 172
5.31 Comparison of pressure, radius, velocity, and flow solutions at terminal locations averaged within 1 and 30 mm slices in the venous model in the prone versus supine positions 173
5.32 Comparison of pressure, radius, velocity, and flow solutions at terminal locations averaged within 1 mm slices in the arterial model with various vessel distensibility values 175

5.33 Transit time results through the arterial model with normal gravity (1G) and pleural pressure (-0.49 kPa) conditions 178
5.34 Transit time results through the venous model with normal gravity (1G) and pleural pressure (-0.49 kPa) conditions 179
5.35 Transit time, path length, and number of vessels per path for all pathways plus averages within 1 and 50 mm slices plotted with respect to gravitationally-dependent height for the arterial and venous models . 180
5.36 Pulsatile pressure boundary conditions applied at the pulmonary trunk inlet 181
5.37 Series of images displaying the pulsatile pressure solution (kPa) over time in the arterial model 182
5.38 Series of images displaying the velocity solution ($\mathrm{mm\ s^{-1}}$) over time in the arterial model with pulsatile pressure boundary conditions prescribed 183
5.39 Example of blood flow data extracted from MDCT functional imaging of sheep and human lungs 184
5.40 Comparison of model results with flow information extracted from MDCT imaging of normal human males in the supine position 186
5.41 Finite element model of the sheep lung, airway branches detected from MDCT, plus additional branches generated using the VFB algorithm, used to obtain an arterial flow solution 187
5.42 Flow results in the sheep arterial model without gravity and with gravity in the prone and supine postures 189
5.43 Comparison of pressure, radius, velocity, and flow solutions at terminal locations averaged within 1 and 30 mm slices plotted with respect to gravitationally-dependent height in the sheep arterial model without gravity and with gravity in the prone and supine postures 190
5.44 Comparison of pressure, radius, velocity, and flow solutions at terminal locations averaged within 1 and 30 mm slices plotted with respect to gravitationally-dependent height in the sheep and human arterial model in the supine posture with gravity 191
5.45 Comparison of flow solutions (relative to mean) in the supine sheep model compared with experimental measurements from the supine pig 192

List of Tables

2.1 Comparison of model alveolar dimensions with published anatomical data 48
2.2 Comparison of model generated dimensional data with published anatomical data 48

3.1 Parameters used in the capillary model 68
3.2 Pressure boundary conditions used in regional variation simulations . . 69
3.3 Pressure boundary conditions applied in flow simulations at 2 cm height intervals 70
3.4 Comparison of model results with and without the hematocrit model . . 77
3.5 Alveolar and pleural pressure conditions at different stages of breathing, for comparisons of WBC stoppage 80
3.6 Average model results at different stages of the respiratory cycle 80
3.7 Sensitivity analysis of model parameters and boundary conditions . . . 84

4.1 Strahler-based branching, diameter, and length ratios for the three stages of model development: MDCT vessels, plus VFB vessels, plus supernumerary vessels, compared with anatomical data 114
4.2 Branching angles of the model generated using a combination of MDCT-derived vessels, VFB algorithm, and supernumerary vessel algorithm, compared with model and anatomical data for the conducting airways . 115

5.1 Average transit times through the arterial and venous networks in various conditions 177

Glossary of Acronyms

1D one-dimensional

2D two-dimensional

3D three-dimensional

CT computed tomography

FEM finite element method

FEV1 forced expiratory volume in 1 second

FRC functional residual capacity

MDCT multi-detector row x-ray computed tomography

Ptm transmural pressure (capillary minus alveolar gas pressure)

Ptp transpulmonary pressure (alveolar minus pleural pressure)

RBC red blood cell

SEM scanning electron micrograph

VFB volume-filling branching (algorithm)

WBC white blood cell

TLC total lung capacity

List of Symbols

The following symbols (listed in order of appearance) are used in this thesis:

Chapter 2

s_A	Alveolar surface area
v_A	Alveolar volume
$\overline{\sigma}_A$	Alveolar surface area to volume ratio

Chapter 3

a	Length of tissue portion of the circumference of a capillary cross-section at zero Ptm
C	Length of the membrane segment of the circumference of the capillary cross-section
R	Radius of a capillary vessel
h	Height of capillary cross-section
a_1	Length of tissue portion of the circumference of a capillary cross section at non-zero Ptp and Ptm
θ	Angle used in the capillary dimensional model
d	The distance between two capillaries
L_a	Alveolar septal length
T_c	Tension around the capillary circumference
V	Alveolar volume
A, B, M	Empirically determined constants for the capillary dimensional model
L_0	Initial alveolar septum length at zero Ptp

a_0	Length of tissue portion of the circumference of a capillary cross-section at zero Ptm and zero Ptp
V_0	The alveolar volume at zero Ptp
T_s	The force per unit length in the septal wall
$E(Ptp)$	The elastic coefficient of the capillary wall as a function of Ptp
C_0	Length of membrane segment of capillary cross-section at zero Ptm
k_c	The stiffness of the capillary wall
P	Perimeter of the elliptical capillary cross-section
a^*	Major axis of an elliptical capillary cross-section
b^*	Minor axis of an elliptical capillary cross-section
l	Length of capillary segment
P	Capillary pressure
$\dot{Q}$	Capillary flow rate
μ_{app}	Apparent viscosity of blood in capillary vessels
A_c	Local cross-sectional area of a capillary segment
s	Distance along a capillary vessel axis
D_h	Hydraulic diameter of a capillary vessel
Re_{D_h}	Reynolds number, based on hydraulic diameter (D_h)
f_d	Darcy friction factor
μ_c	The cytoplasmic viscosity
D^*	Parameter used in the hematocrit model
D_m	The diameter of the smallest vessel that a RBC can pass through
μ_p	Blood plasma viscosity
R_{seg}	The resistance to flow in a capillary segment
R_{cap}	Resistance in capillary, after junction accounted for
R_{junc}	Resistance in junction
S_{seg}	Surface area of capillary segment
S_{junc} or $SA_{junction}$	Surface area of capillary junction

SA_{total}	Total surface area of capillary element
$L_{overlap}$	The overlapping length of each element at a junction
n_j	The total number of overlapping capillary segments at a junction
n	Total number of capillary segments in a network
m	Total number of capillary junctions in a network
$\dot{Q}_{ip}$	The flow rates in each segment connected to junction i
P_{j1}, P_{j2}	Pressures at either end of a capillary segment
H_d	Hematocrit (=RBC fraction of blood)
f	The volumetric flux of RBCs in a vessel segment
r	The RBC flux cut-off parameter
b	The preferential RBC flux parameter
t_i	RBC transit time through vessel i
V_i	Volume of vessel i
C_{tt}	Ratio of RBC transit time to plasma transit time in capillaries
P_{cr}	The critical pressure drop required over a capillary segment for a WBC to pass through it
τ_0	The average cortical tension in a WBC
R_{WBC}	WBC radius
R_p	Tube radius
t_e	WBC entrance time
t_p	WBC passage time
t_{WBC}	Total WBC transit time through a capillary segment
R	Average capillary radius, used in WBC transit calculations
R_{cv},Q_{cv}	Resistance and flow in an alveolar corner vessel

Chapter 4

R_d	The Strahler-based diameter ratio
D	Vessel diameter
x	The Strahler order number

N	The highest Strahler order number in the network
R_b	The Strahler-based branching ratio
R_l	The Strahler-based length ratio
θ_{branch}	The angle between a parent and its child branch
γ	The angle between the plane containing the parent branch and its sibling and the plane containing the two daughter branches
θ_{major},θ_{minor}	Angle between the parent and the major and minor daughter branches, respectively
R^2	Correlation coefficient

Chapter 5

ρ	Density of blood
μ	Viscosity of blood
p	Blood pressure within vessel
R	Vessel radius
V	Mean axial velocity
t	Time
Θ	The vertical angle between the gravitational vector and the vector of the vessel centreline
g	The acceleration due to gravity (1G: g=9.81 $\mathrm{m\ s^{-2}}$)
ν	The kinematic viscosity of blood
α	The vessel cross-section velocity profile parameter
G_0,β	Vessel distensibility coefficients for pressure-radius relationship
R_0	The unstrained vessel radius at p=0
k	A grid point at time step k
i	A grid point at a spatial location i
Δx	The distance between grid points (spatial discretisation)
S	The cross-sectional area of a vessel
F_a, F_b, F_c	Flow rate through the parent and two daughter vessels at a bifurcation
p_0	The pressure at a bifurcation

Chapter 1

Introduction

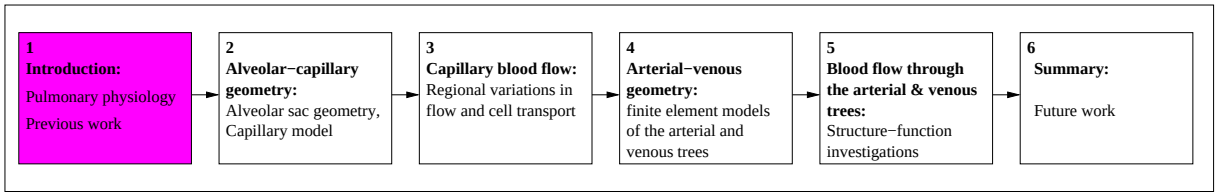

This chapter introduces the pulmonary system and provides information for specific areas of interest contained in this thesis. Firstly, an overview of the lung as a whole is provided (Section 1.1), followed by more specific details corresponding to the modelling work contained in the following four chapters. Section 1.6 outlines previous work conducted in the area of pulmonary blood flow, corresponding to work in each of the four modelling chapters.

1.1 The lungs

The human lung is divided into five functionally independent bronchopulmonary units or lobes. Each lobe is surrounded by connective tissue continuous with the visceral pleura, and is a separate respiratory unit (Hlastala & Berger 2001). The right upper, mid, and lower lobes are separated by the oblique and lateral fissures, and the left upper and lower lobes by the oblique fissure. The lungs fill most of the thoracic cavity and consist largely of the three conducting trees, including the bronchial system, arterial and venous trees. The primary function of the lung is gas exchange: to expel carbon dioxide from the blood and extract oxygen from ambient air for circulation to cells around the body. This function is carried out by intimate interactions between the bronchial (air) and vascular (blood) systems.

During inspiration the volume of the lung is increased by both contraction of the diaphragm, which causes it to descend, and an outward pull from the intercostal muscles, which raise the ribs. This increase in volume causes the pressure in the terminal airways to fall below atmospheric pressure, which, provided the glottis is open, causes air to flow down the pressure gradient into the lungs. During expiration the muscles passively relax and the reverse procedure occurs due to recoil of the lung tissue. The outer surface of the lungs (the visceral pleura) and the inner surface of the chest wall (the parietal pleura) are held together by a negative intrapleural pressure. A thin layer of serosal fluid is contained between these two layers which allows the lungs to easily slide around within the chest cavity.

Air enters the lung via the upper airways (including the nasal cavity, mouth and larynx) followed by the trachea, which bifurcates into the left and right main pulmonary bronchi - one to each lung. Lobar bronchi begin to emerge from this level such that each lobe is supplied by a single airway. Successive bifurcations into tubes with decreasing diameter and length carries the air through the increasing number of conducting airways towards the respiratory surface. Airway branches fall into one of two discrete categories: conducting or respiratory. As their name suggests, conducting airways simply conduct air to and from the respiratory surface, having nothing to do with the gas exchange process. The conducting airways therefore comprise the anatomical dead space, making up around 150 ml of the lung volume. After an average of 17-19 generations of branching (Weibel 1963) the respiratory bronchioles are reached. Alveoli begin to arise at this level becoming more numerous towards the periphery of the bronchial tree. Alveoli are the blind ending sacs of the airway system (described further in Section 1.2.1) where gas exchange takes place. All branches distal to a terminal bronchiole are surrounded by alveoli, participate in gas exchange, and constitute an acinar unit. There are an estimated 30,000 acini in an average human lung (Haefeli-Bleuer & Weibel 1988).

The distance from a terminal bronchiole to the most distal alveolus is only a few mm, but the respiratory zone makes up around 2.5 - 3 L of the lung volume (West 2000). The alveoli contain a dense layer of capillary blood vessels over their surface, the structure of which is elaborated on in Section 1.2.3. There are an estimated 300 million alveoli in an average human lung, each alveolus being enwrapped by approximately 1000 capillary vessels, resulting in an estimated colossal 280 billion pulmonary capillaries in the human lung. The vast number of alveoli result in a very large surface area (of approximately 80-100 m^2 (Weibel 1984)), thereby increasing the efficiency of gas exchange. The partial pressure gradient across the blood-air membrane is the driving

force for gas diffusion.

The pulmonary blood vessels also consist of a series of branching tubes, diverting blood from the right ventricle of the heart through the arteries, to the capillary bed, then back to the left atrium of the heart through a series of converging pulmonary venous vessels (Section 1.4). The pulmonary trunk receives the whole output from the right heart, but due to the relatively small resistance through the pulmonary circuit, a much smaller pressure is required to pump the blood through the pulmonary circuit than the systemic circuit.

Anatomical investigations have shown that each airway has an accompanying artery and vein (Elliot & Reid 1965, Weibel 1963, Maina & van Gils 2001). The arteries are positioned in close proximity to their partner airway, and the veins are found to run half-way between pairs of arteries and airways. These vessels have been termed 'accompanying' blood vessels, as they accompany an airway branch. A characteristic feature of the pulmonary vascular networks is the emergence of many more branches, known as supernumerary vessels (Elliot & Reid 1965), described further in Section 1.4.1. The lung has an additional blood system, the bronchial circulation, which provides oxygenated blood to the lung tissue, more details are given in Section 1.4.0.2.

1.2 Alveolar-capillary network geometry

As stated previously, the key role of the pulmonary system is respiratory gas-exchange: to supply oxygen to and remove carbon dioxide from the blood. The alveolar-capillary network is the site of this gas-exchange. The physiology of this delicate and valuable system is described below.

1.2.1 Pulmonary alveoli

The conducting airways distribute air to around 300 million alveoli, each one approximately 0.3 mm in diameter (at 75% of maximum lung volume) (Hlastala & Berger 2001, West 2000). Ventilation is described as the movement of air from the atmosphere into the body, to the alveoli where gas exchange occurs, and the movement of the gas back out of the body (Hlastala & Berger 2001). During the breathing cycle, the pressure within alveoli fluctuates between about -1 cmH_2O (-0.09806 kPa), during inspiration, to around +1 cmH_2O (0.09806 kPa), during expiration (Guyton & Hall 2000), as a result of an increase in lung and alveolar volume via forces exerted by the diaphragm and intercostal muscles.

Due to the dense packing arrangement of the alveoli, as shown by the scanning electron micrograph (SEM) in Figure 1.1, the shape of each alveolus tends to be described as an irregular polyhedron, typically consisting of fourteen faces, with one face cut off at its entrance to allow ventilation (Hlastala & Berger 2001, Hoppin & Hildebrandt 1977). A 3D Voronoi meshing technique is used to represent the volume-filling structure of the alveoli in Section 2.2.2.

Gravitational forces have an influence on the distribution of sizes of alveoli; the largest alveoli are found in the upper or least gravitationally-dependent regions of the lung. The greater distension of alveoli displayed in the upper regions of the lung is due to the downwards pull of gravitational forces on the lung tissue. This also results in smaller, more compressed alveoli in the lower, dependent regions of the lung. This size distribution varies with posture or changes in lung volume (Hlastala & Berger 2001).

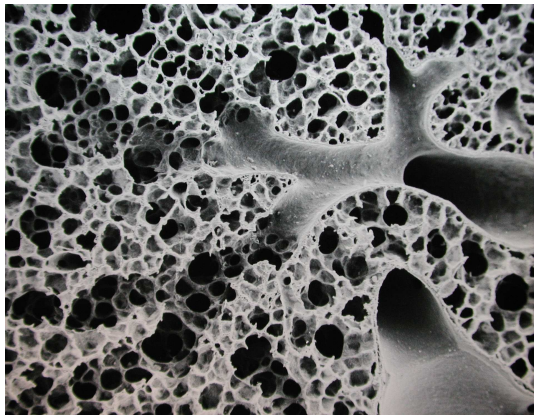

FIGURE 1.1: *SEM of densely packed, volume-filling alveolar structure, showing respiratory bronchioles transitioning into alveolar ducts (therefore becoming surrounded by alveoli). Figure courtesy of E. R. Weibel, Institute of Anatomy, University of Berne.*

The top portion of Figure 1.2 shows a SEM of an alveolar duct (D) and its surrounding alveoli (A), the lower portion displays the capillary layer (C) covering the alveolar septa between adjacent alveoli. The thin tissue layer (T) separating RBCs from air can be seen.

1.2.1.1 Alveolar stability & pulmonary surfactant

The structure of the thin walled, volume-filling alveoli results in a system that is fundamentally unstable. The liquid layer covering the alveolar surfaces induces large surface tension forces which tend to collapse the alveoli, due to the attractive forces between adjacent liquid molecules being greater than that between air and

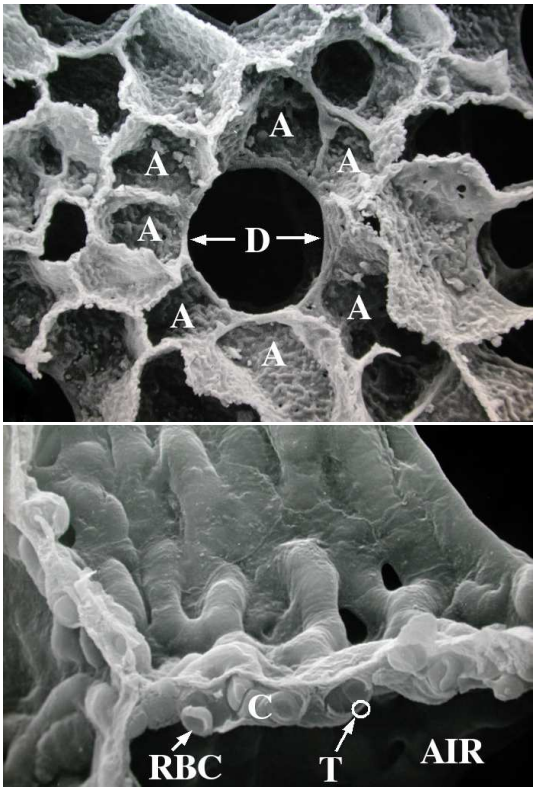

FIGURE 1.2: *SEM of (top) alveolar duct (D) and surrounding alveoli (A), and (bottom) the capillary layer (C), containing red blood cells (RBCs) enclosed from air by a thin tissue layer (T). Figure courtesy of E. R. Weibel, Institute of Anatomy, University of Berne.*

liquid molecules. This surface tension helps to maintain the integrity of the surface. The presence of a lipoprotein lining layer, known as pulmonary surfactant, largely decreases the surface tension forces in the alveoli and helps to prevent collapse. By reducing the surface tension in the alveoli the compliance of the lung is increased (this means the lung is more easily expanded, compliance = Δ volume/Δ pressure) which reduces the work during inspiration. Another role of pulmonary surfactant is in keeping the alveolar surfaces dry. Surface tension forces in the alveoli have the effect of sucking fluid in from the capillary side of the membrane (into the alveolus); surfactant reduces surface tension forces and therefore reduces the transudation of fluid from the capillaries (Weibel 1984).

Surfactant is produced within the type II alveolar epithelium cells (see Section 1.2.2 for a description of these cells) and is secreted into the alveolar lining liquid. Surfactant consists mainly of the lipid dipalmitoyl phosphatidylcholine (DPPC) and a protein that helps stabilise DPPC at the air-liquid interface, among other components. DPPC is manufactured in the lung from fatty acids, which are extracted from the blood or made

in the lung. Surfactant is quick to produce and has a high turnover rate (West 2000). The DPPC molecules are hydrophobic (water repelling) at one end and hydrophilic (water loving) at the other, and they align themselves on the surface of the liquid. The intermolecular repulsive forces then oppose the normal liquid surface attraction forces, thus reducing surface tension.

Infant respiratory distress syndrome (IRDS) is caused by a lack of surfactant at birth in premature infants. Surfactant is not produced until relatively late in fetal development, therefore babies born too early without sufficient surfactant develop IRDS and may die. The lack of surfactant leads to increased surface tension forces in the alveoli (reduced compliance), alveolar collapse (atelectasis), therefore increased work during breathing, and increased fluid in the alveoli. Recent evidence suggests that the incidence of IRDS can be reduced in premature infants by externally delivering surfactant into the lungs (Hlastala & Berger 2001).

1.2.2 The blood-gas barrier

The blood-gas barrier is the thin tissue layer separating alveolar gas and capillary blood with a thickness of only around 0.1-0.3 μm (Hlastala & Berger 2001). Gases are able to freely diffuse across this membrane. The barrier is made up of three distinct layers: the alveolar epithelium lining the air spaces; the interstitium, which accommodates the connective tissue fibres and basement membranes; and the capillary endothelium. Figure 1.3 shows a transmission electron micrograph (TEM) of the extremely thin alveolar-capillary barrier. The alveolar epithelial (EP1), interstitial (IS), and capillary endothelial (EN) layers can be clearly identified separating the alveolar gas region (A) and the capillary region, containing a red blood cell (RBC).

The epithelium and endothelium each make up approximately 25% of the tissue in the alveolar walls, the interstitial cells account for around 35%, and connective tissue fibres constitute only 15% of the tissue. Alveolar macrophages make up about 4% of the volume in the alveolar walls (Weibel 1984).

1.2.2.1 Alveolar epithelium

The alveolar epithelium is composed of three main cell types: type I and type II epithelial cells and alveolar macrophages. Type I, or squamous (small) alveolar epithelial cells rest on the basement membrane and are found mostly in concavities formed by capillaries bulging into the alveolar air spaces. A thin cytoplasmic layer extends out laterally from these cells in broad, thin plates only a few microns thick.

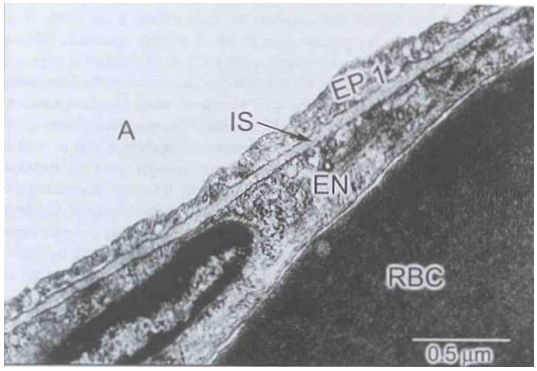

FIGURE 1.3: *Transmission electron micrograph (TEM) of the alveolar-capillary barrier. Constituents of the layer include alveolar type I epithelial cells (EP1) on the alveolar side (A), capillary endothelial cells (EN) separating a red blood cell (RBC) on the capillary side. These layers are separated by interstitial space (IS). Picture from (Hlastala & Berger 2001).*

Adjacent epithelial cells form intercellular junctions creating a continuous layer of cytoplasm covering the surface of each alveolus. The type II, or granular (large) alveolar epithelial cells are roughly spherical in shape, and contain microvilli on their surface. These cells are found throughout the type I cell epithelial lining. Alveolar surfactant is manufactured in the type II alveolar epithelial cells; the lipoprotein is stored in the lamellar bodies of the cell and secreted into the alveolar lining liquid when required (Hlastala & Berger 2001). The third type of alveolar epithelial cells are the free alveolar cells also known as alveolar macrophages. These are not in contact with the basement membrane and are thought to originate from the large alveolar cells (Weibel 1963). Macrophages attack and destroy invading bacteria, viruses, and other particles which may become trapped in the alveoli. This is mainly achieved by phagocytosis, which is the cellular ingestion of the offending agent. Neutrophils (a type of white blood cell (WBC)) work in conjunction with macrophages to defend the body; the alveolar surface is the largest epithelial surface area in the body exposed to the outside environment (Hlastala & Berger 2001). Both macrophages and neutrophils are attracted towards inflamed tissue areas by chemotaxis (Guyton & Hall 2000). Macrophages are cleared via the airways and lymphatic system (Hlastala & Berger 2001). There is another very rare cell type, the brush cell, which has been found in some specific regions near terminal bronchioles. These are thought to act as air quality monitoring receptors.

1.2.2.2 Capillary endothelium

The walls of the pulmonary capillaries consist of a single layer of endothelial cells resting on the basement membrane. The endothelium forms a poreless, uninterrupted lining of the capillaries, via cytoplasmic extensions. This endothelial lining consists mainly of a thin layer of cytoplasm, with the cell nucleus bulging into the lumen of the capillary vessels. The cytoplasm layer extends over large areas of the surface and has a thickness of only around 0.2-0.5 μm. Adjacent cells are connected via simple intercellular junctions whereby the two cells often overlap slightly (Weibel 1963). These tight cell junctions do, however, allow transudation of electrolytes and macromolecules from within the blood plasma through the endothelial barrier. There is therefore a relatively free exchange between the plasma and interstitial space. Fortunately the alveolar epithelial junctions are tighter and more selective with the transfer of matter (Weibel 1984). Fluid in the interstitial space is drained via the lymphatic system. The basement membrane consists of a sheet of proteoglycans and a type of collagen which allows solutes and small macromolecules to pass through freely; it forms a continuous lining of the outer endothelium.

The endothelial cells appear to have important pharmacokinetic and metabolic, non-respiratory functions. The lungs contain one half of the entire endothelial cell population in the body, and certain substances in the blood plasma are attacked by enzymes on the endothelial surface (Harris & Heath 1986).

1.2.2.3 Interstitium

The interstitium is enclosed by the endothelial and epithelial basement membranes. Since the pulmonary capillaries are supported by strands of the connective tissue framework of the lung and because of the large alveolar cells, the blood-gas barrier consists of a thin and thick walled region. The thin walled region is concerned with the exchange of respiratory gases, and the thick walled part is involved in tissue fluid transport (Fung 1990, Harris & Heath 1977). In the thinnest part of the blood-gas barrier the endothelial and epithelial basement membranes are so close together that the two separate layers are almost indecipherable. In the thicker parts, the basement membranes follow the bulging of the cells. The interstitial space contains bundles of collagenous and elastic fibres, some fine microfibrils, and fibroblasts. Macrophages (interstitial macrophages) and plasma cells may also be found in the interstitium (Weibel 1963).

1.2.3 Pulmonary capillaries

The pulmonary capillaries form a dense network of interconnecting short capillary segments in the walls of the alveoli. A SEM of a section of the vast pulmonary capillary plexus is shown in Figure 1.4. The alveolar tissue has been removed, but it is still clearly visible how the capillaries wrap over the surface of each alveolus.

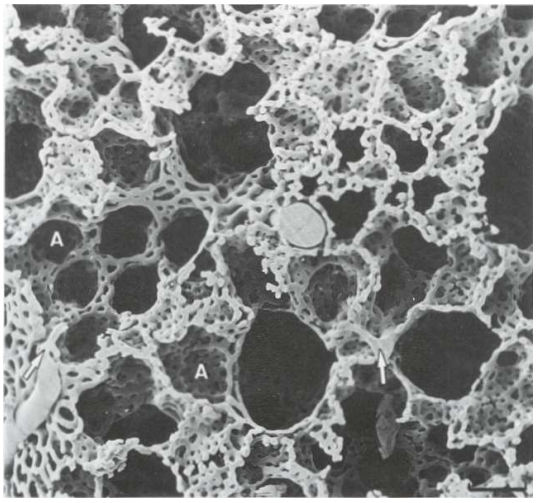

FIGURE 1.4: *SEM of a section of the dense capillary network wrapped over each alveolar unit (A). The arrow illustrates a larger blood vessel feeding into the network. Figure courtesy of E. R. Weibel (Weibel 1984).*

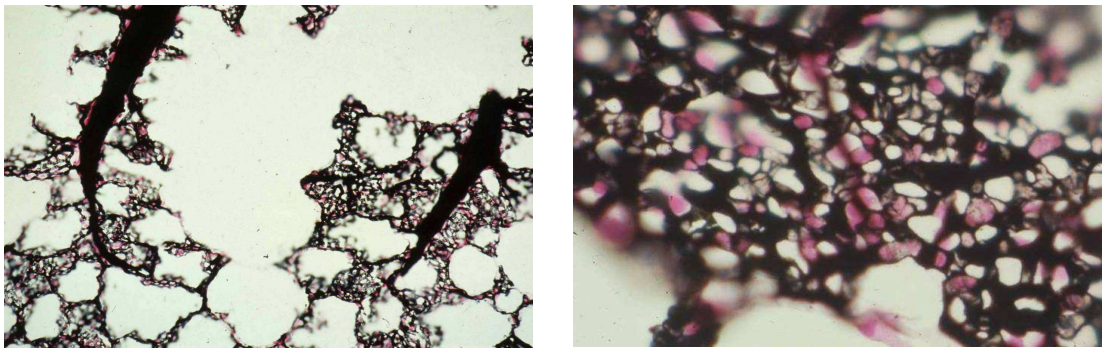

(a) (b)

FIGURE 1.5: *Photomicrograph of a section of the rabbit capillary network (a), close in view of the same network (b). Images courtesy of E. R. Weibel, Institute of Anatomy, University of Berne.*

The pulmonary capillary network forms a much denser network than found in the systemic microcirculation (Figure 1.5). Capillaries found in muscle tissue have

larger diameters, are longer and form a looser network (Weibel 1984). The pulmonary capillary segments are so short that early observations by Fung and colleagues (using relatively low resolution light microscopy) led to the approximation that blood flowed as a sheet through interconnected posts of connective tissue (Fung & Sobin 1969), see Section 1.6.2.1. More detailed, higher magnification SEM analysis later demonstrated that blood does in fact flow though discrete tubules as in the systemic circuit, the only difference being the increased density of tubules in the pulmonary system (Guntheroth, Luchtel & Kawabori 1982).

The capillary wall consists of a layer of endothelial cells resting on the basement membrane layer, as described earlier in Section 1.2.2. In heart failure the pulmonary capillary pressure increases due to the restricted outflow of blood into the left atrium. Fluid is extruded from the capillaries into the interstitial space at a rate in excess of the drainage capabilities. Fluid, therefore, builds up in the interstitial space, firstly in the large connective tissue masses surrounding the blood vessels and bronchi; this condition is termed interstitial edema. In hemodynamic pulmonary edema fluid begins to penetrate though the epithelium into the alveolar spaces. This results in severe respiratory trouble because the flooded alveoli cannot participate in gas exchange (Weibel 1984). Another type of cell found in the pulmonary capillary walls are pericytes. These cells are found between the endothelial layer and the basement membrane. Pericytes contain actin and myosin (contractile proteins), and therefore possess contractile properties and are thought to be a type of smooth muscle, which may provide mechanical support to the thin-walled capillary vessels (Weibel 1984).

Each RBC spends around 1-3 seconds in the capillary network and during this time will traverse around 2-3 alveoli (West 1979). Weibel (1963) conducted a detailed morphometric study of the human alveolar-capillary network; dimensions and estimated numbers of capillary segments were published. The capillary diameters were found to range from 1 to 15μm, with an average internal diameter of 8μm. The average number of capillary segments in a lung was estimated to be around 280 billion and was found to be independent of lung size.

1.2.4 Mechanical support

1.2.4.1 The fibre continuum

As the airways grow during lung development they are surrounded by parenchymal tissue. Within this tissue both the blood vessels and fibre network develop. The

pulmonary fibre system forms a three-dimensional continuum throughout the lung initiating at the hilum (the point of entry for the root of the lung) and extending to the visceral pleura. The fibre skeleton is entangled with the bronchial and vascular systems. On expansion of the chest, and hence the visceral wall, increased tension in the fibre network aids in expansion of the airways and alveoli. The fibre system can be divided into two components; the axial fibre system, which begins at the main stem bronchus and progresses with the airways to the terminal bronchioles, and the peripheral fibre system, which is related to the visceral pleura and enwraps the lobar units. The pulmonary venous network is found to follow the peripheral fibre system (thus in between airways and arteries), while the arterial system closely follows the airways and therefore the axial fibre system. The axial fibre system continues from the terminal bronchioles along the respiratory bronchioles by encircling the alveolar entrances. From here a network of finer fibres extends over the remaining alveolar septal surfaces and weaves through the capillary meshwork, illustrated in Figure 1.6 (Weibel 1984).

FIGURE 1.6: *Schematic of the fibre continuum weaving through the capillary meshwork. Figure courtesy of E. R. Weibel, Institute of Anatomy, University of Berne.*

1.2.4.2 Micromechanical support/corner vessels

The alveolar septum is made of a single capillary network that is interlaced with fibres (Figure 1.6). When the fibres are stretched, the capillaries bulge out alternate sides and cause pits and crevices at the alveolar-capillary intersection. This gives rise to a corrugated surface texture on both sides of the septal wall. A fluid layer coats the surface of the alveoli, and evens out the surface by collecting in the crevices. The fluid consists of an aqueous layer called the hypophase, which is covered with a layer of surfactant. The shape of the interalveolar septum is governed not only by structural factors, but also by mechanical forces. Tissue tension, surface tension, and

capillary distending pressure all interact to mold the malleable structure of the thin septal membrane. Figure 1.7 displays a schematic illustration of these forces. A stable configuration is achieved when all of these forces are in balance. The tissue fibre tension is a function of lung inflation. During inflation the lung expands, thus increasing tension in the fibres; the resulting force acts on the capillary segments pulling them to one side of the septum or the other. Surface tension is exerted normal to the alveolar surface; the size of this force depends on the degree of curvature and the surface tension coefficient (a property of the alveolar fluid). Blood pressure within the capillary vessels causes the capillaries to bulge out. This pressure is determined by arterial and venule pressures, including gravitational forces. The capillary is contained between the fibres and the air-tissue interface whose combined forces tend to squash the capillary flat, into an elliptical shape in cross-section.

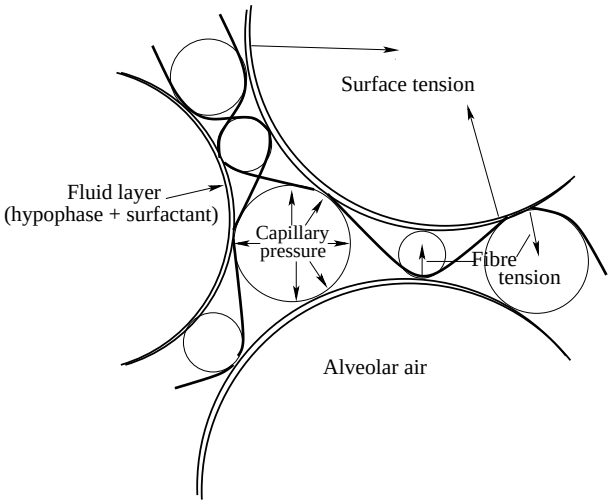

FIGURE 1.7: *Schematic illustration of the balance between alveolar surface tension, fibre tension, and capillary distending pressure, which all play a role in the structure of the alveolar-capillary membrane.*

Alveolar corner vessels are found where three septa meet along a so-called triple line. The surface tension in this region must exert a stronger outward pull on the tissue to balance the negative tissue pressure generated by the highly negative curvature found in this region. This results in fibres being pulled into the alveolar corners, which enables the capillaries in the corners to remain wide open in all conditions, even at high lung inflation and during zone 1 flow (refer Section 1.3.2 for details on zonal flow) (Lamm, Kirk, Hanson, Wagner Jr & Albert 1991). The negative pressure also sucks interstitial fluid from the septum toward the triple line (Weibel 1984). In zone 2 flow the capillaries in the section of septum shared between two adjacent alveoli will be

squashed flat, because the surface and tissue forces exceed the capillary pressure thus collapsing the vessels; but the alveolar corner vessels will remain open, demonstrated in Figure 1.8(a). In zone 3 flow the capillaries are fully perfused and bulging into the air space, because the capillary pressure is greater than alveolar pressure (Figure 1.8(b)).

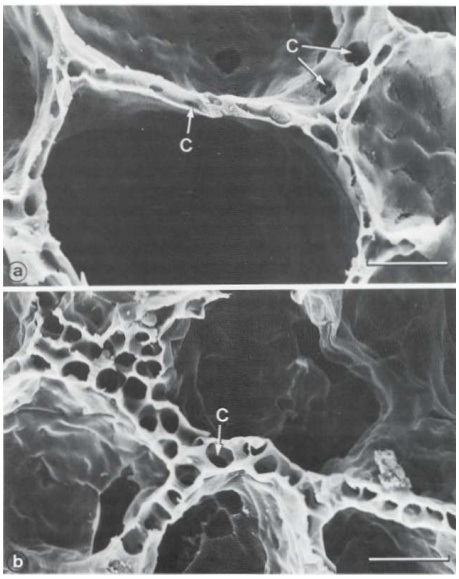

FIGURE 1.8: *SEMs of the alveolar walls in rabbit lungs fixed under (a) zone 2 and (b) zone 3 perfusion conditions. This illustrates that the capillary (C) corner vessels remain patent in both flow zones, even while the septal capillaries under zone 2 flow are collapsed. Figure from (Weibel 1984).*

The parenchymal tissue structure of the lung is such that the mechanical properties of alveolar units are affected by neighbouring alveoli; this is known as interdependence. The woven, tethered structure of the elastin and collagen fibres means that if a single alveolus collapses tension in the surrounding fibres increases, thus preventing collapse of adjacent alveoli. This interdependence extends to the intrapulmonary airways maintaining their patency. The degradation of this fibre network in disease states, such as emphysema, breaks down the interdependence mechanisms and promotes a more heterogeneous ventilation distribution (Hlastala & Berger 2001).

1.3 Capillary blood flow

1.3.1 Properties of blood in the microvascular network

The resistance to flow in microvessels is determined by the topology of the individual vessels and the resulting network, including vessel diameters, length, number and connectivity of vessels, and on the apparent viscosity of the blood.

At the microcirculatory level blood must be considered as a two-phase non-Newtonian fluid: particles suspended in blood, particularly RBCs, strongly influence the apparent viscosity and therefore the blood flow in each segment. The term 'apparent viscosity' simply refers to the viscosity of a non-Newtonian fluid at a certain shear rate. The apparent viscosity of blood varies with several factors, including vessel diameter, hematocrit and blood cell velocity. The hematocrit is the volume fraction of RBCs in blood and is around 0.45 in normal human blood (Guyton & Hall 2000, Pries, Secomb & Gaehtgens 1996).

The basic mechanical properties of RBCs are well established. The cytoplasm is an incompressible, Newtonian fluid. It is surrounded by a thin viscoelastic membrane, which consists of a lipid bilayer and a protein cytoskeleton. The membrane shears and bends easily, but resists area changes. As a consequence of these properties, RBCs are highly deformable, as long as changes in surface area or volume are not required, and they can pass through capillaries with diameters much less than the diameter of an unstressed cell ($\approx$8 μm (Secomb 1995)). Unless fluid flow forces are sufficient to keep RBCs dispersed, they tend to adhere to each other due to bridging by plasma proteins, and lower shear rates increase the aggregation. Blood shows shear thinning properties, that is as the shear rate is increased the progressive breakup of aggregates leads to a decrease in viscosity. WBCs are much stiffer than RBCs and may contribute significantly to microvascular flow resistance. Platelets are much smaller than RBCs and do not contribute significantly to flow resistance (Pries et al. 1996, Skalak & Chien 1987).

In blood vessels smaller than about 300 μm in diameter mechanical interactions between RBCs and the tube wall result in the preferential distribution of RBCs near the vessel centre (Pries et al. 1996, Secomb 1995). This is termed 'axial migration' and has considerable effects in the overall flow behaviour of cells in thin tubes. This creates a layer of zero hematocrit immediately adjacent to the wall, resulting in a reduction in the apparent viscosity of the blood. This phenomenon is known as the Fahraeus-Lindqvist effect (Fahraeus & Lindqvist 1931), whereby apparent viscosity decreases

with decreasing vessel diameter. Fluid flow velocity varies from zero at the wall of a tube to a maximum near the centre of the tube. This means that average RBC velocity is higher than average blood velocity. This leads to a reduction of red cell transit time through a given tube segment, and hence to a reduction in the hematocrit contained in that segment (tube hematocrit) relative to the hematocrit of blood entering or leaving it (discharge hematocrit). This dynamic reduction is known as the Fahraeus effect (Fahraeus 1929), and results in a decreasing blood hematocrit as blood traverses the microvasculature. The existence of a RBC-depleted layer adjacent to the tube wall underlies both the Fahraeus and the Fahraeus-Lindqvist effects. Viscosity has been found to be strongly hematocrit-dependent (Pries et al. 1996, Skalak & Chien 1987).

Another phenomena contributing to RBC distribution is the disproportionate allocation of RBCs and plasma at bifurcations. This phase separation at a junction is proportional to the relative flow rates in the daughter vessels (Pries, Secomb, Gaehtgens & Gross 1990). Combination of the Fahraeus, Fahraeus-Lindqvist, and phase separation effects result in the hematocrit distribution throughout the capillary plexus. The model developed in Chapter 3 incorporates empirically-based equations that calculate the RBC distribution (Section 3.2.4).

1.3.2 Zones of flow

Early experimental studies by West (1979) demonstrated an almost linear increase in blood flow from the top to the bottom of the lung, as would be expected due to the increase in hydrostatic pressure with depth in the blood vessels adjacent to airways in which the pressure is constant with depth. During exercise blood flow in both the upper and lower zones was found to increase resulting in a decrease in the overall distribution differences. These measurements led to the theory of zonal flow which is now wide spread in pulmonary literature.

The difference in pressure between the top and bottom of an average lung (assuming a height of about 30 cm) is about 30 $\mathrm{cm\ H_2O}$ or 23 mmHg (West 1979). The pulmonary capillaries are virtually surrounded by gas and their structure is only supported by a very thin layer of endothelial and epithelial cells lining the alveoli. Due to the lack of support these capillaries are easily collapsed and distended, depending on the magnitude of the pressures in and around them. The effective pressure around the capillaries is alveolar pressure and when this rises above the pressure within the capillaries they collapse. If the external pressure only rises above the tube exit value the Starling resistor phenomenon occurs, also known as the waterfall or sluice gate

effect, whereby the pulmonary capillaries act as a gate to control flow. In collapsible vessels in this state (when alveolar pressure is greater than venule pressure) flow will be governed by the pressure drop between the tube inlet and the external alveolar pressure, rather than the drop between inlet and outlet tube pressures as in normal flow. While alveolar pressure is relatively constant throughout the lung, blood pressure varies due to hydrostatic gradients, resulting from gravitational forces, and because of resistance to flow. The blood pressure is assumed to vary linearly with height due to these effects. This relationship between alveolar and blood pressures led to the classification of West's zonal flow model (West, Dollery & Naimark 1964). A schematic diagram of the four typical zones of flow is illustrated in Figure 1.9.

Zone 1: ($P_{arteriole} < P_{alveolar} > P_{venule}$**)**: Zone 1 flow occurs, if at all, in the least gravitationally-dependent, upper regions of the lung where blood pressure is at its lowest. This zone does not occur under normal lung function conditions. In these regions the alveolar pressure ($P_{alveolar}$) is greater than both the arteriole ($P_{arteriole}$) and venule pressures (P_{venule}), the capillary vessels are therefore collapsed and there will be little or no flow during any part of the cardiac cycle. Lamm and colleagues have shown in rabbit lungs that zone 1 flow utilises alveolar corner vessels, meaning there is not a complete cessation of flow in zone 1 (Lamm et al. 1991). Any zone 1 regions contribute to alveolar dead space because in the unperfused region there will be no gas exchange.

Zone 2: ($P_{arteriole} > P_{alveolar} > P_{venule}$**)**: As the hydrostatic pressure within the blood vessels increases down the lung arteriole pressure will begin to exceed alveolar pressure, this results in zone 2 flow. This zone occurs when venule pressure is still lower than alveolar pressure. Zone 2 may display intermittent blood flow during the cardiac cycle due to the variation in blood pressure. This zone is where the so called 'waterfall effect' occurs, whereby blood flow is governed by the difference in pressure between arterial and alveolar pressure, rather than the difference between arterial and venous pressure as it is in normal flow.

Zone 3: ($P_{arteriole} > P_{alveolar} < P_{venule}$**)**: Zone 2 flow transitions into zone 3 flow as blood pressure increases down the vertical height of the lung. Zone 3 occurs when both the arteriole and venule pressures are greater than alveolar pressure. There is continuous blood flow in this zone. The increasing blood pressure with further descent down the vertical lung results in recruitment of previously collapsed capillaries and distension of perfused capillaries. The majority of the lung is in zone 3 flow.

Zone 4: An additional zone 4 flow region was later defined to account for the decrease in flow observed in the lowest, most gravitationally-dependent regions of the lung (Hughes, Glazier, Maloney & West 1968). Gravitational forces also led to uneven expansion of alveolar units: the least gravitationally-dependent regions are the most expanded at functional residual capacity (FRC), and the dependent regions are the least expanded (Glazier, Hughes, Maloney & West 1967). Zone 4 flow has been attributed to an increased resistance in the extra-alveolar (non-alveolar) vessels in the lower regions because they are less distended due to reduced alveolar expansion (West 1999). The caliber of the extra-alveolar vessels depends on the overall lung volume. Another explanation is that the decreased flow is due to perivascular cuffing resulting from the formation of edema from the high blood pressures (Hlastala & Glenny 1999).

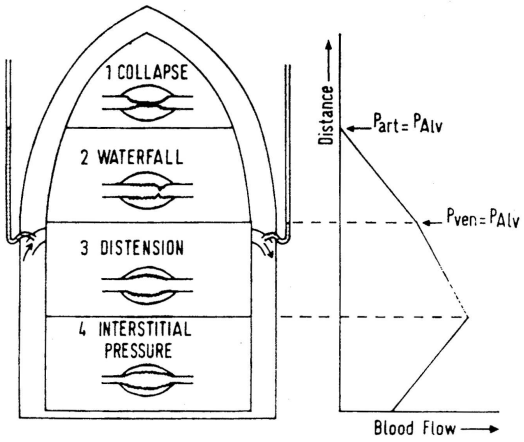

FIGURE 1.9: *Schematic illustration of the different 'zones' of flow in the lung. Figure from (Hughes et al. 1968).*

This zonal model has been used to explain regional differences in blood flow distribution and gas exchange for over three decades. While these zones of flow are still applicable, higher-resolution experimental techniques have brought about new concepts in blood flow distribution and heterogeneity. A more in depth discussion of the changing perspectives and new theories on blood flow distribution in the lung is given in Section 1.5.2.

1.3.3 Capillary perfusion: recruitment versus distension

Under normal blood flow and respiratory conditions not all capillaries are perfused: many are unperfused due to inadequate internal blood pressures (relative to alveolar

pressure). Capillary perfusion switches between segments: some segments are nearly always perfused and form interconnecting pathways across the alveolar wall, while in other capillary regions of the same alveolar wall, the blood frequently switches between segments. These fluctuations in perfusion have been shown to be present even during constant flow conditions (Hanger, Presson Jr, Okada, Janke, Watkins, Wagner Jr & Capen 1997, Wagner Jr, Todoran, Tanabe, Wagner, Tanner, Glenny & Presson Jr 1999). It is not fully known why, but some vessels require higher opening pressures than others, possibly due to high vascular smooth muscle tone or topographical factors which result in preferential perfusion pathways (Levitzky 1990). Another proposal for the existence of uneven opening pressures is based on the non-uniform arrangement of fibres wrapped intimately over the alveolar and capillary surfaces (Godbey, Graham, Presson Jr, Wagner Jr & Lloyd Jr 1995).

The presence of unperfused capillaries implies that there is a large reserve capacity available in the lung for increased flow conditions, such as during exercise. This reserve capacity, via recruitment and distension mechanisms, also inhibits RBC transit time from decreasing below the time needed for complete oxygen saturation (around 0.25 s).

Pulmonary capillaries contain only small amounts of muscle tissue, therefore the opening pressures are relatively small, corresponding to the lower blood pressures present in the pulmonary circuit compared to the systemic circuit. As pulmonary arterial pressure increases these unperfused capillaries may become perfused, thus opening new parallel pathways for blood flow and decreasing the total pulmonary vascular resistance. The perfusion of new capillary segments is known as recruitment. The opposing situation also occurs whereby decreasing blood flow results in derecruitment of pulmonary capillaries (Levitzky 1990). Recruitment of vessels is the dominant mechanism for a reduction in pulmonary vascular resistance as pulmonary arterial pressure rises from lower levels (West 2000). During an increase in pulmonary blood pressure, previously perfused capillaries will increase in caliber, due to their elastic structure; this is known as distension. This is the major resistance reducing mechanism at higher blood pressures. Recruitment and distension often occur together.

In the current model (see Chapter 3) capillary perfusion was determined by the diameter of the vessel, which is a result of the initial geometry and the pressure-flow solution. The minimum capillary diameter that a RBC can pass through is 2.7 $\mu\mathrm{m}$ (Huang, Doerschuk & Kamm 2001), therefore a segment was considered perfused if its height was greater than this value. For diameters smaller than this the segment was

considered unperfused.

1.3.4 Neutrophil Margination

Neutrophils are granular leukocytes (or WBCs) which comprise 50-70% of the total WBC population. Neutrophils originate in the bone marrow and carry out phagocytosis - the engulfing and destruction of foreign materials. Under normal conditions the concentration of neutrophils in the lung is between 40-80 times higher, or around three times the number of cells, than that in circulation (Hogg 1987, Hogg & Doerschuk 1995); this is known as neutrophil margination. In their transit through the capillary bed virtually all neutrophils encounter at least one capillary segment that is too narrow to pass through unimpeded (Doerschuk, Beyes, Coxson, Wiggs & Hogg 1993). Neutrophil transit times through the lung have been shown to range from 2 s to as long as 20 minutes (Hogg, McLean, Martin & Wiggs 1988, Hogg, Coxson, Brumwell, Beyers, Doerschuk, MacNee & Wiggs 1994, Lien, Wagner Jr, Capen, Haslett, Hanson, Hofmeister, Henson & Worthen 1987). An empirically-based model of neutrophil transit, derived from micropipette aspiration studies (Fenton, Wilson & Cokelet 1985, Yeung & Evans 1989), is included in the capillary flow model (Section 3.2.5.2), the results of which are compared with experimental values in Section 3.3.5.

The reason for this margination is the geometry of the pulmonary microcirculatory network, namely the relative diameters of neutrophils to capillaries meaning that the WBCs must deform to squeeze through narrow capillary vessels. Reported values of neutrophil diameters are in the range of 6.8-8.3 $\mu\mathrm{m}$ (Doerschuk 1999), compared to the reported range of capillary diameters of around 4-10 $\mu\mathrm{m}$ (Chang & Paiva 1989). The relative time taken for deformation is proportional to the size the cell must deform to (being relatively quick for small deformations), the stiffness of the cell (activated cells are less deformable), and the driving force pushing the cell through. The sequestering of neutrophils in the lung is thought to play a vital role in host defense, acting as the second line of defense by destroying any unwanted foreign material which may have penetrated the system.

Several mechanisms may increase neutrophil stiffness thus increasing the marginated pool of cells in the lung, for example the activation of cells by inflammatory mediators (Doerschuk 1999, Hogg 1987). Neutrophils in patients with sepsis, cells treated with TNF-α (tumour necrosis factor), and young cells (freshly released from the bone marrow) have all been shown to have longer transit times and are therefore hypothesised to be less deformable (Drost, Kassabian, Meiselman,

Gelmont & Fisher 1999, Gebb, Graham, Hanger, Godbey, Capen, Doerschuk & Wagner Jr 1995, Terashima, Klut, English, Hards, Hogg & van Eeden 1999).

Despite the large concentration of neutrophils effectively blocking capillary segments, experimental studies measuring the effect of leukocyte blockage on arterial pressure have shown that even when all the circulating leukocytes are in the lung the effect on upstream pressure is small (Hogg 1987). This suggests that the large number of parallel pathways can accommodate the diversion of flow from blocked pathways.

1.4 The pulmonary vasculature

The pulmonary vasculature provides a direct route from the heart to the gas exchange surface. In the same way as for the airways, the branching structure of the pulmonary vasculature allows efficient gas exchange by creating a very large alveolar-capillary surface area for gas exchange. After circulating through the systemic circuit, delivering oxygen and nutrients to the body tissue, blood returns to the right atrium of the heart via two large veins known as the venae cavae. The pulmonary trunk emerges from the right ventricle (RV) through the pulmonary valve and conveys deoxygenated blood into the pulmonary circuit. The pulmonary trunk extends only about 5 to 10 cm beyond the right ventricle before dividing into the left and right main pulmonary arteries. The pulmonary trunk is about 3 cm in diameter, and due to the relatively low pressures in the pulmonary circuit has a wall thickness of only around a third that of the aorta and twice that of the venae cavae (Harris & Heath 1986).

The left and right main pulmonary arteries enter into the hila of the lungs and divide into branches accompanying segmental and subsegmental bronchi and lie mostly dorsolateral to them (Hlastala & Berger 2001). The right main pulmonary artery, usually larger and longer than the left, runs horizontally and to the right in the angle between the azygos vein above and the ascending aorta and superior vena cava in front. It is situated anteriorly to the oesophagus and right main bronchus. It travels slightly downwards and then passes transversely to the right hilum where it is situated a little to the right of the spine. This artery divides into two main branches. The larger and lower branch is distributed to the right middle and lower lobes while an upper, smaller branch accompanies the first branch off the right bronchus to the right upper lobe. The left main pulmonary artery runs horizontally from below the aortic arch and crosses the descending aorta. It lies above the left main bronchus until it gives off its first branch. It then runs downwards, behind and laterally to the left main bronchus. It travels in

an oblique course posteriorly to the left hilum where it divides into its lobar branches (Harris & Heath 1986).

Both the left and right main pulmonary arteries show little variation in their positioning and mode of branching. The lobar branches display a comparatively larger variation in their branching pattern (Harris & Heath 1986, Gray 1995). The large pulmonary (accompanying) arteries then proceed in close proximity to the branching of the bronchial tree. Figure 1.10(a) schematically represents the positioning of the main pulmonary arteries in relation to the heart and bronchial system.

The terminal arterioles feed into a dense capillary network within the alveolar walls of an acinus. The end arterioles feed blood into this capillary network and it flows from the centre to the periphery where it then flows into the terminal venules of the pulmonary veins.

The pulmonary arterial branches are relatively short, and all the arteries and arterioles have larger diameters than their systemic counterparts. This fact as well as the fact that the pulmonary arteries are very thin and distensible gives the pulmonary arterial tree a large compliance (averaging 7 ml/mm Hg), similar to that of the entire systemic tree. This compliance allows the pulmonary arteries to hold about two thirds of the stroke volume from the right ventricle. The pulmonary veins are also short but their distensibility is similar to that of the systemic veins, therefore their compliance is not as large (Guyton & Hall 2000).

In general the course and pattern of the pulmonary vasculature resembles that of the airways. The diameter of each pulmonary arterial branch is approximately the same as the bronchus it accompanies. The pulmonary arteries do, however, branch more frequently than the airways (Chang & Paiva 1989), giving rise to supernumerary vessels which do not accompany an airway branch (Section 1.4.1).

Venules arising from the capillary bed combine into larger branches which traverse the lung independently of the arteries and bronchi. Eventually a single main vein emerges from each lobe. The right upper and middle lobar veins usually unite resulting in two main veins from each side of the lung, a superior and inferior vein, which feed into the left atrium. At the hilum of the lung the superior pulmonary vein lies below and in front of the main pulmonary artery (Harris & Heath 1986). Figure 1.10(b) demonstrates the relative positioning of the main venous vessels with respect to the left atrium (LA) and bronchial system.

As well as simply oxygenating blood the pulmonary circuit (sometimes known as the lesser circulation) also has some other not so well known functions. Firstly it may act as a reservoir for blood in the body. An increase in blood pressure

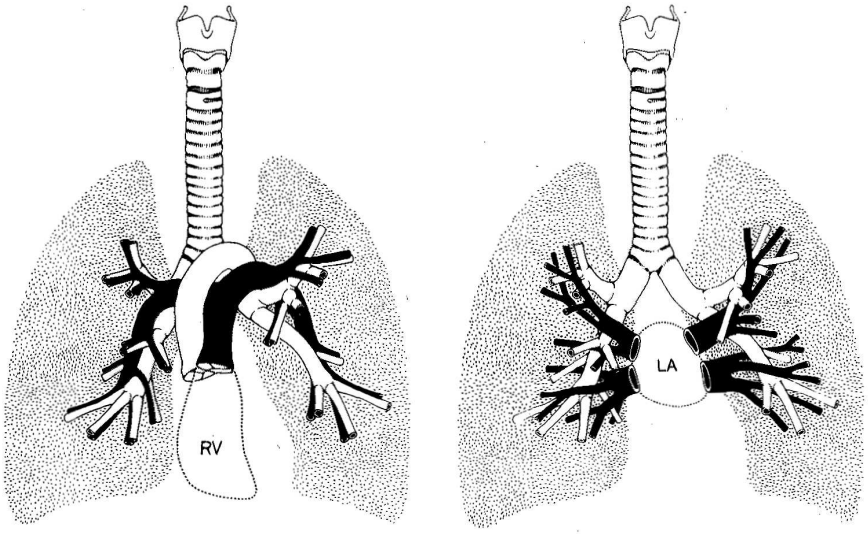

FIGURE 1.10: *Schematic demonstrating locations of the main pulmonary arterial and venous vessels (black) in relation to the bronchial tree (white) emerging from the heart: (a) the pulmonary trunk emerges from the right ventricle (RV) and closely follows the bronchial tree; (b) four main pulmonary veins drain oxygenated blood into the left atrium (LA). Figure from (Weibel 1984).*

allows recruitment and distension of pulmonary capillaries to accommodate the extra blood. Blood also gets filtered as it passes through the pulmonary circulation. Small blood thrombi may be removed to prevent blockage of blood vessels elsewhere in the body. Neutrophil margination also occurs in the pulmonary circulation where there is a concentration of up to fifty times more white blood cells than in the systemic circulation, this increases the ability of host defense in the lung (Section 1.3.4) (West 2000). The lung also plays a role in the metabolisation of substances, for example the conversion of angiotensin I to angiotensin II occurs almost entirely in the lungs, catalysed by converting enzyme present in the endothelium of the blood vessels (Guyton & Hall 2000).

1.4.0.1 Wall structure

The larger muscular arteries continuously divide into smaller vessels with a consequential gradual decrease in the amount of smooth muscle until practically no muscle exists in the very small arterioles. These vessels are narrow, and have a relatively low intravascular pressure therefore only a few smooth muscle fibres are required to regulate flow (Hlastala & Berger 2001). Arterial vessel walls transition

from an elastic structure (vessels down to roughly 3000 μm), through an intermediate transitional stage (vessels ranging from 3000-2000 μm in diameter) into a muscular wall structure (vessels with diameters in the range of 2000-30 μm), followed by partially muscular to non-muscular wall structures (deMello & Reid 1991).

The differences in vessel wall that led to structural and functional heterogeneity is the result of only three different cell types: the endothelial cell creates the inner lining of the vessel, the fibroblast forms the external coating of the blood vessel, in between these two layers is the contractile cell - either the smooth muscle cell or its precursors (the intermediate cell) and the pericyte (deMello & Reid 1991).

1.4.0.2 The bronchial circulation

The bronchial circulation supplies oxygenated blood to the supporting tissue in the lung. The bronchial arteries spring from the systemic circuit and convey an estimated 1-2% of the cardiac output (Guyton & Hall 2000). The bronchial arteries originate from the intercostal arteries and the descending thoracic aorta (Hlastala & Berger 2001). The right bronchial artery usually stems from the third posterior intercostal artery and the upper and lower left bronchial arteries branch separately from the thoracic aorta. Smaller bronchial vessels arise from the descending thoracic aorta (Gray 1995). The bronchial circulatory system supplies the conducting bronchial vessels, bronchial glands, septa, connective tissue, and large pulmonary vessels with oxygen and nutrients. The bronchial vessels supply airway walls down to the level of the respiratory bronchioles (Gray 1995).

There are numerous communication points between the bronchial and pulmonary vessels, known as anastomoses. Bronchial arteries anastomose with pulmonary arterial vessels in the walls of the smaller bronchi and visceral pleura (Gray 1995). The bronchial system proceeds back to the heart in two ways: feeding either into the left or right atrium. Bronchial veins supplying the larger airways feed back into the systemic circuit through the azygos veins into the right atrium. However, the remaining bronchial blood, now deoxygenated, is mixed with blood in the pulmonary circuit (either pre- or post- capillary) and carried back to the left atrium. This is a source of anatomical shunt, whereby deoxygenated blood is mixed with oxygenated blood in the systemic arteries, decreasing the efficiency of the oxygenation system. The total anatomical shunt is about 2-5% of the cardiac output (Hlastala & Berger 2001).

Another function of the bronchial circulation is in humidification of inspired air in the airways. It is also the source of highly soluble gases, such as ethyl alcohol, that

exchange with air in the non-respiratory airways (Hlastala & Berger 2001).

1.4.1 Supernumerary blood vessels

In addition to the accompanying vessels there are many more pulmonary arterial and venous branches. These extra blood vessels, known as supernumerary vessels, are a characteristic feature of the pulmonary vasculature (Takamasa & Nitta 1993) and occur throughout the length of the artery from the hilum to the level of the capillaries, but are more numerous towards the periphery (Elliot & Reid 1965). Figure 1.11 displays a photograph of a cast of the human pulmonary arteries (red) and airways (white) demonstrating numerous small blood vessels branching from a larger stem which ultimately do not accompany an airway branch. Supernumerary vessels have also been identified in rat (Hislop & Reid 1978) and bovine (Shaw, Bunton, Fisher, McGrath, Montgomery, Daly & MacDonald 1999) lungs.

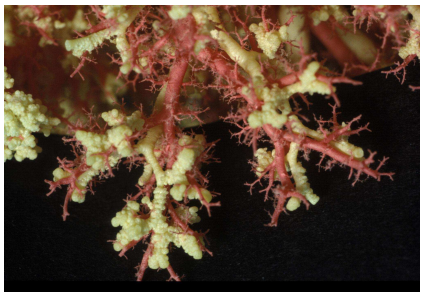

FIGURE 1.11: *Photograph of a cast of the human pulmonary arteries (red) and airways (white), illustrating the presence of supernumerary vessels. Each airway has an 'accompanying' arterial vessel. In addition numerous small supernumerary vessels are seen which diverge from the airways and do not have an accompanying bronchial branch. Photo courtesy of E. R. Weibel, Institute of Anatomy, University of Berne.*

These very small vessels tend to branch off at right angles from the accompanying arterial (or venous) vessel and branch quickly to directly supply (or drain) the closest acinar unit. Supernumerary vessels are not found on angiograms, due to lack of filling, because of the 90^0 angle they make to the axial branch and due to the presence of a sphincter at the entrance (Elliot & Reid 1965, Shaw et al. 1999). It is thought that these vessels provide a reserve capacity during maximal flow, such as during exercise. Also, in the adult, it is these vessels that can provide collateral blood flow if the conventional vessels are occluded (deMello & Reid 1991).

At all ages, the number of supernumerary vessels outnumbers accompanying vessels. Through a combination of measurement and extrapolation, the ratio of

supernumerary to accompanying terminal arteries has been estimated at 2.8:1; the ratio for the venous supernumerary vessels is estimated to be even higher, at 3.5:1 (deMello & Reid 1991). The greater number of venous vessels is thought to contribute to the lower pressure in the venous system, which most likely enhances drainage of fluid from the acinar region (deMello & Reid 1991). An empirically-based technique has been developed to include these vessels into the vascular models, described in Section 4.2.3.

1.4.2 Classification of branches in tree-like systems

The three conducting systems of the lung all form similar topographical tree-like structures. The pulmonary trunk being the stem of the arterial tree, and the four main pulmonary veins leading into the left atrium being the stems of the venous tree. Since these trees are very complex in arrangement and contain so many branches several methods of classifying and simplifying the branching systems have been devised. Such ordering of the tree-like systems also allows vessel segments to be grouped to enable parameters, such as diameter and length of segments, to be defined or analysed. These parameters can be grouped in terms of ”orders” or ”generations”. The most common methods are Weibel generations, Horsfield and Strahler ordering and the more recently developed diameter-defined Strahler ordering method. A simple tree is displayed in Figure 1.12 ordered by application of Weibel generations, Horsfield, and Strahler ordering schemes.

1.4.2.1 Weibel generations

The method of Weibel generations begins system numbering at the stem branch as the first generation, this is a centrifugal system (Dawson, Krenz & Linehan 1998), that is numbering away from the central stem. From here the generation numbering increases towards the peripheral, terminal branches by 1 at each bifurcation (Figure 1.12(a)). The generation number is equal to one plus the number of bifurcations upstream of a particular vessel segment. With increasing asymmetry, classification by generations groups together branches with a large range of characteristics, in terms of dimensional or structural parameters.

The number of vessels in a generation can also be difficult to interpret as the number of generations along a pathway can vary. For example when short pathways are encountered, the number of vessels in a generation in an asymmetrical heterogeneous

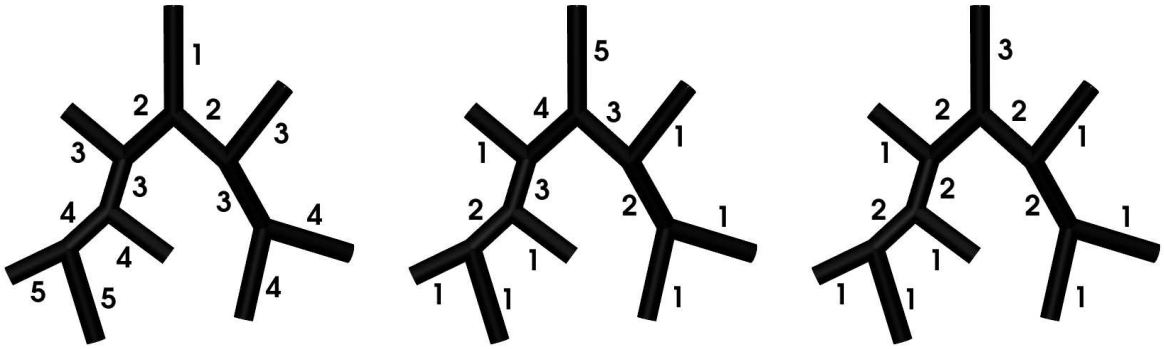

FIGURE 1.12: *Illustration of (a) the generation, (b) Horsfield, and (c) Strahler ordering schemes on a simple tree network. Generation numbering begins at the stem branch and increases by one generation at each branch point. Both the Horsfield and Strahler ordering schemes begin numbering (order 1) at all terminal branches. If two branches of equal order number meet, the parent branch order is incremented by 1. If branches of unequal order meet, the Horsfield order number will increment by 1, but the Strahler order number will retain the highest daughter order number.*

tree can decrease as the generation increases, even though the actual number of vessel segments increases as diameters decrease (Dawson et al. 1998).

1.4.2.2 Horsfield ordering

This method of ordering is based on the Strahler system and was developed by Horsfield & Cumming (1968). Lowest order numbers are assigned to all terminal branches and numbering proceeds towards the main stem, centripetally (Dawson et al. 1998). When two daughter branches meet the Horsfield order number is incremented by one, even if the order numbers are not the same (Figure 1.12(b)).

1.4.2.3 Strahler ordering

Classification of the pulmonary vascular trees via generations or Horsfield ordering would make analysis of the geometry of asymmetric trees difficult, and not necessarily representative. Small supernumerary tributaries would each increment the order and generation number by one. The method of Strahler ordering overcomes this problem.

The Strahler ordering system is derived from a system originally developed to analyse river systems proposed by Horton (1945). This method was modified by Strahler (1953), and redefined as the Strahler ordering scheme. This method has general applicability to branching systems. The lowest order number is allocated to the most

distal, terminal branches. If two branches of the same order meet, the Strahler order number is incremented by one. If two branches of different order converge the parent branch will retain the same Strahler order number as the daughter branch with the highest order number (Figure 1.12(c)). This ordering continues up to the main original stem. Adjacent segments of the same order are merged and considered as a single segment.

This method is found to be useful when several small side branches are found to merge with a larger central branch, as the order number at each junction does not necessarily increase. Due to the high number of supernumerary branches stemming from larger parent branches in the pulmonary arterial and venous trees, the Strahler ordering scheme is particularly appropriate in classification of the pulmonary vasculature. The Strahler ordering method also groups together branches of similar diameter values, which is important in hemodynamic analysis. The diameter-defined Strahler ordering system improves further in this area.

1.4.2.4 Branching ratio

Classification of the pulmonary vascular trees by the Strahler or Horsfield ordering schemes results in a linear relationship between the log of the number of branches in each order versus the order number. This is not the case with generation numbering. The absolute number of the antilog of the least-squares fit of the gradient is known as the branching ratio of the tree. The branching ratio is the factor by which the number of branches increases at each successive order down the system. A symmetric tree will have a Strahler and Horsfield branching ratio of 2, increasing asymmetry will produce a higher Strahler branching ratio and a lower Horsfield branching ratio.

1.4.2.5 Diameter-defined Strahler ordering system

Kassab, Rider, Tang & Fung (1993) developed the diameter-defined Strahler ordering scheme to reduce overlap in the range of diameters of vessels in successive orders. In the diameter-defined ordering method an additional diameter criteria is incorporated into the Strahler ordering scheme. Therefore when branches meet the order number of the parent branch will only increase by one if the vessel diameter is greater than a certain limit (Jiang, Kassab & Fung 1994, Kassab et al. 1993).

The use of this method requires diameter values of all of the vessels in the tree and for this reason the diameter-defined ordering scheme was not used in the current study.

1.5 Pulmonary blood flow

The volume of blood in the lungs is about 450 ml. About 70 ml of this volume (or just less than 20% of the total pulmonary blood volume) is estimated to be in the pulmonary capillaries (Guyton & Hall 2000). The venous system is estimated to contain approximately 60% of the blood volume **??**, leaving only around 20% of the blood volume in the arterial tree. The volume of blood in the lungs can vary significantly. Strong exhalation or loss of blood from the systemic circuit can decrease the blood volume by as much as half. The volume can be increased by up to two times as a result of left heart failure or an increased resistance to blood flow through the mitral valve (the valve between the left atrium and ventricle) (Guyton & Hall 2000).

1.5.1 Pressures in and around the pulmonary blood vessels

The pressures within the pulmonary circulation are much lower than those in the systemic circulation. The mean pressure in the pulmonary trunk is around 15 mmHg, compared to about 100 mmHg in the aorta. The pressure in the pulmonary trunk reaches a value of around 25 mmHg (3.333 kPa) during systole and drops to about 8 mmHg (1.067 kPa) in diastole. The pressure in the right ventricle cycles between about 25 mmHg to 1 mmHg from systole to diastole. The pressure in the left atrium is in the range of 1 to 5 mmHg, with an average of 2 mmHg.

The reason for the low pressures is that as opposed to the systemic circuit the pulmonary circulation does not generally have to direct and control blood flow from one region to another and its arterial pressure needs only be enough to lift blood the height of the lungs. The lower pressure also minimises fluid loss into the alveoli or interstitial space (Hlastala & Berger 2001). Although it is still uncertain, evidence suggests that the pressure in the pulmonary capillaries is about halfway between pulmonary arterial and venous pressure at around 7 mmHg (0.9333kPa). The pressure within the pulmonary capillaries varies considerably throughout the lung as a result of hydrostatic effects (this is investigated in Chapter 3).

The pressure difference between the inside and outside of a blood vessel is known as the transmural pressure, and at the capillary level is equal to the difference between the alveolar and blood pressures. The larger pulmonary blood vessels are pulled open by the radial traction of the elastic lung parenchyma which surrounds them, during inspiration as the lung expands. The caliber of the pulmonary capillaries is determined by the relationship between the alveolar pressure and their internal pressures, whereas

the caliber of the larger pulmonary vessels is influenced by the lung volume, as this determines the extent of distending pressure applied on the vessels by the parenchyma (West 1979).

1.5.2 Changing perspectives on blood flow distribution

Prior to the 1950's it was not possible to obtain quantitative measurements of the distribution of blood flow in the lung (Prisk, Paiva & West 2001). Development of experimental technologies allowed the use of radiolabelled gases to measure regional variations in pulmonary blood flow. As the soluble gases were evolved into the alveolar spaces, the radioactivity could be measured by external radio-activity counters. The counters were placed at different vertical locations adjacent to the chest. Each counter integrated information across the lung and chest wall to extract a single average value for the entire horizontal slice (isogravitational plane). This information cannot represent isogravitational heterogeneity and only displays large scale flow distribution. These earlier analyses led to the well known zones of flow fathered by West (West et al. 1964), described in Section 1.3.2. As mentioned earlier the zonal flow model was not challenged for over three decades.

As experimental technologies have continued to evolve higher resolution information has been extracted from the lung, leading to new insights and controversy involving previous theories. This increased spatial resolution is obtained by injection of microspheres. The microspheres become lodged in the microvasculature in proportion to the amount of blood flow to that region. Information is extracted by measurement of 1-2 cm^3 cubes of dried tissue inflated to near total lung capacity (TLC).

As well as uncovering new features with respect to the relationship between gravity and blood flow distribution, the microsphere injection techniques have illustrated the large scale perfusion heterogeneity within the lung, even within isogravitational planes. Corollary to this analysis of blood flow within small cubes of tissue was the finding that pulmonary blood flow is spatially correlated. These results show that neighbouring regions of lung have similar magnitudes of flow while distant regions negatively correlated, meaning that high flow regions are next to other high flow regions and vice versa - due to the shared history of the vascular pathway used to reach a certain point.

1.5.3 Ventilation-perfusion relationships

The matching of alveolar ventilation and pulmonary capillary perfusion dictate the attainable level of gas exchange in the lung. Ventilation-perfusion (V_A/Q) mismatch is responsible for most of the decreased gas exchange in all pulmonary diseases (West 2000), and is the most important cause of clinically significant arterial hypoxemia. V_A/Q can span from zero, during no ventilation or shunt, to infinity, during no perfusion or dead space, the ideal ratio being 1. Considering the large amount of ventilation and perfusion heterogeneity in the lung, the two are relatively well matched, with a normal range from 0.6-3 and an average of 0.8 (Scharf, Pinsky & Magder 2001). This supposedly stems from the fact that the conducting networks are intimately connected spatially as well as additional active mechanisms which regulate regional air and blood flow conductances. These mechanisms are in place to maintain the required level of oxygen and carbon dioxide exchange. Hypoxic pulmonary vasoconstriction (HPV) is one of the dominant mechanisms controlling V_A/Q matching. HPV diverts blood flow away from hypoxic or atelectic alveoli, and is effective at maintaining arterial oxygenation to a level where about 30% of the lung is hypoxic (Swenson, Domino & Hlastala 1998).

1.6 Previous work

1.6.1 Alveolar-capillary geometric models

Previous modelling of the detailed structure of the alveolar-capillary network has been relatively limited. Previous models are described below.

1.6.1.1 Alveolar models

Weibel (1963) carried out an extremely in depth anatomical analysis of the human lung, and developed early models representing the geometry of the airways and alveolar-capillary units. Alveolar shape can vary considerably, therefore Weibel evaluated several geometric simplifications to represent alveolar geometry. One assumed the alveolus to be a wedge of a hollow cylinder forming a sleeve around the alveolar duct. A more accurate representation was obtained by using two circular cones; an inverted truncated cone to represent the alveolar body, and another cone at the closed end of the alveolus to represent the dome. Lastly, to obtain a smooth surfaced model, 5/6 of a sphere was used requiring only a single dimension to specify its geometry. Other

shapes analysed included an open cube and a dodecahedron with one side open. These shapes were used to empirically estimate the surface-to-volume ratio (σ_A, as calculated using Equation 2.1) that would most appropriately represent that of a real alveolus. The estimated value was σ_A=4.8. The calculated value, from the five lungs in Weibel's study, was σ_A=4.87. Figure 1.13 illustrates an oblique section of a human alveolar duct, including surrounding alveoli. The total depth (A), cone-shaped dome depth (a), and radius (r) were measured for a series of alveoli, these values are compared with model results in Table 2.1.

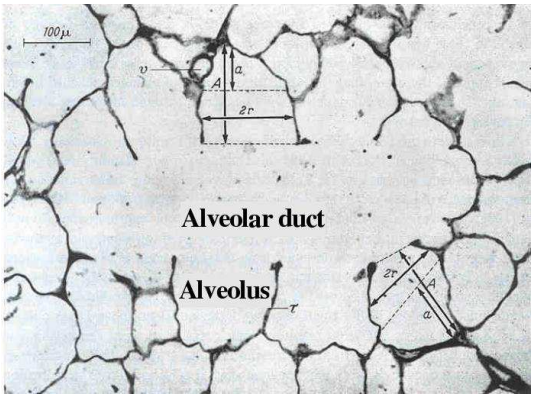

FIGURE 1.13: *Oblique section of a human alveolar duct and surrounding alveoli, used to measure the total depth (A), cone-shaped dome depth (a), and radius (r) for a series of alveoli. Figure courtesy of E. R. Weibel (Weibel 1963).*

In Weibel's model of the full respiratory zone a 5/6 sphere was chosen to represent each alveolus. The surface-to-volume ratio of this sphere is 4.25. To increase this ratio towards the measured value of 4.87, the surface of each alveolus was corrugated, as is introduced in physiology by the bulging of capillaries through to the alveolar surface.

Fung (1988) developed a framework to mathematically describe the structure of the parenchyma in the lung. This work assumed that alveoli are all initially equal in size and shape and are volume-filling. After geometric analysis of all possible uniform space-filling polyhedra to equate the alveolar unit to, a tetrakaidecahedron (14-hedron) was selected. This shape has the minimum surface to volume ratio among all space-filling polyhedra of the same volume. A 14-hedron was used to represent an individual alveolus, and several of these 14-hedron were put together to create a near volume-filling structure. Central faces of all the internal alveolar units were removed to allow aeration. These units are not exactly space filling, but they do compare well with observed data on pulmonary alveolar structure.

Denny & Schroter (1995) created a finite element model of an alveolar duct in

the mammalian lung consisting of a network of adjacent truncated octahedral alveoli surrounding a longitudinal air duct. This model was used to investigate alveolar mechanics by incorporating stress-strain relationships in elastic and collagen fibres and surface tension at the air-liquid interface, and calculating pressure-volume curves.

Denny & Schroter (1996) further developed this alveolar model by developing a method to generate a 3D space-filling model of an acinar ventilatory unit within a cuboidal block. Truncated octahedral were again used to represent individual alveoli with specified faces removed to create ducts and allow ventilation. All alveolar were assumed to be uniform in shape and size. The structure is termed volume-filling in that the polyhedra can pack together without leaving any gaps, but not completely volume-filling in the true sense of the word.

Kitaoka, Tamura & Takaki (2000) developed a simplified 3D model of the human pulmonary acinus. This model was generated using a labyrinth algorithm producing branching ducts that completely fill a volume. This study focussed on the acinar geometry rather than the specific geometry of individual alveolar units. In Kitaoka's model each subacinar unit (the tissue region supplied by the last respiratory bronchiole) was approximated by a set of cubic cells. Individual alveoli were also represented as cubes (with a side dimension of 0.25 mm), whereby 8 alveoli constituted a single cubic cell.

1.6.1.2 Capillary models

Prior modelling of the complex geometry of the pulmonary capillary plexus has been limited; the models which have been developed have only sought to create a simplified representation of the capillary geometry and not an anatomically realistic structure.

Extensive work has been done in development of the sheet-flow model developed by Fung & Sobin (1969), but this model approximated the capillary geometry as a sheet and neglected to define the tubule geometry. Averaged parameters are used to represent the capillary geometry in this approach. The microvascular sheet is characterised by two independent properties: the ratio of the vascular lumen space to the circumscribing tissue space of the network (this quantity has been termed the vascular space tissue ratio, VSTR), and the thickness or height of the microvascular sheet. The sheet-flow model is described in more detail in Section 1.6.2.1.

Weibel (1963) described the geometry of the capillary network as wedged cylinders, whereby three of these cylinders could fit together at a junction. This was acknowledged as an over-simplification of the capillary geometry, because in reality

at capillary junctions the basement membranes of the segments show a smoothly curved transition, rather than a sharp break. As a result of this capillary segments have circular cross-sections at the junctions, and elliptical cross sections everywhere else. In the development of a respiratory zone model the alveolar capillaries were assumed to be cylindrical segments forming a hexagonal mesh-work, with pentagonal meshes inserted to fill the surface of each alveolar sphere. Weibel divided the whole lung into 200-300 million units, each of which contained several alveoli, and each being supplied by a single arteriole and drained by a single venule.

Dhadwal, Wiggs, Doerschuk & Kamm (1997) and Huang et al. (2001) modelled flow through the pulmonary microcirculation within discrete tubes. Dhadwal et al. (1997) represented the capillary geometry in a single alveolar septum as a network of interconnected capillaries arranged into a 6 x 6 square matrix. The network was divided into segments and junctions, whereby a segment was defined as the vessel through which blood flows, and the junction was defined as the connecting region between segments. The length of each capillary segment was equal to the diameter of the tissue space that separated each capillary from its neighbour, and these tissue spaces were all assumed to have equal diameters at a specific lung volume. Anatomical data was used to describe the individual segment geometry, using random variability in vessel size and network compliance.

Huang et al. (2001) further developed Dhadwal's flow and geometric models. A slightly more extensive geometric model was defined; the model consisted of capillary segments randomly generated into a 2D square representing a single alveolar septum. The number of capillary segments, diameters, and level of interconnectedness (number of segments at a junction) were defined from available anatomical data. The square septae were bounded by corner vessels, which are shared by three adjacent intersecting septae. Several of these networks were coupled together to investigate interalveolar flow. Flow entered each septum through a single corner vessel and exited from a single corner vessel on the opposite side of the network. The septae were only lined up one-dimensionally, therefore flow only proceeded from one septum to a single adjacent septum, in reality the capillary network forms a 3D structure and is connected to several adjacent alveolar networks.

The analysis of previous work modelling the geometry of pulmonary capillaries illustrates the advancement of the current model. Previous models have taken a more simplified approach and focussed mainly on the blood flow model rather than capillary geometry. The development of a more detailed, tubular model will aid in analysis of blood cell distributions and interactions within the vast pulmonary microcirculatory

plexus.

1.6.2 Capillary flow models

Microcirculatory blood flow has previously been modelled using two methods, both of which are explained in this section. Capillaries in the systemic microcirculation tend to be longer and wider than those in the pulmonary microcirculation, hence systemic microcirculatory blood flow has previously been modelled within systems of discrete tubules (tube-flow method) (Skalak & Chien 1987, Pries et al. 1990) (Section 1.6.2.2). In contrast, the complexity and density of capillary segments within the pulmonary microcirculation led to development of the sheet-flow model by Fung & Sobin (1969), where blood is represented as a continuous sheet bounded on either side by a compliant endothelium flowing between posts of connective tissue (Section 1.6.2.1). More recent models of pulmonary capillary blood flow have implemented a tube-flow solution method, as described in Section 1.6.2.2.

1.6.2.1 Sheet-flow model

Early morphometric observations of the dense capillary plexus led to the development of the sheet-flow model established by Fung and Sobin (Fung & Sobin 1969, Sobin, Tremer & Fung 1970). This mathematical description approximates blood flow through the pulmonary capillaries as a sheet of fluid flowing around "posts" of connective tissue, bounded on either side by compliant capillary endothelium. The theory behind this model provides a means of analysing the pressure, velocity, thickness and streamline distributions in an interalveolar septum. The distribution and transit times of RBCs can also be determined. This solution requires specification of the geometric boundaries of the sheet, such as the locations of and pressures applied at arterioles and venules. In specifying these boundary conditions approximations are made whereby the flow over a sheet is averaged. This model has shown general agreement with experimental data in terms of flow and resistance.

Although the sheet-flow model oversimplifies the capillary network's anatomic structure by assuming that blood flows in a continuous sheet rather than through discrete tubules (Guntheroth et al. 1982), it has provided a useful description of the general pattern of blood flow through the alveolar walls. The sheet-flow model enables calculation of flow properties in each alveolar sheet, but the effects of individual segment geometry and the two-phase nature of blood is accounted for by an increase in the effective resistance to overall flow. Distributions determined in the sheet-flow

model are averaged over the entire capillary network; segment-to-segment variability in individual capillaries cannot be predicted. The sheet-flow model also cannot predict distributions of cellular transit times from arteriole to venule, only average times can be determined. For these reasons a tube-flow model is implemented in the current study to more realistically represent flow in the pulmonary capillary system.

1.6.2.2 Tube flow models

In these models the network geometry and boundary conditions are defined to determine flow solutions through discrete capillary segments. The simple Poiseuille pressure-resistance-flow relationship, defined in Equation 1.1 is used to determine the pressure and flow distribution throughout a network of tubes.

$$R = \frac{\Delta P}{Q} \tag{1.1}$$

The tube-flow solution procedure is split into three iterative steps:

1. The first step is 'linear analysis' to determine pressure and flow throughout the network. Equation 1.1 is solved for the pressure at every junction and the flow through each segment of the network. A uniform hematocrit distribution is initially assumed.

2. The next step is 'rheological analysis': the distribution of RBCs is calculated, using empirically-derived models which account for the Fahraeus effect (reduction of intravascular hematocrit relative to the inflow hematocrit of a vessel), Fahraeus-Lindqvist effect (dependence of hematocrit on vessel diameter) and phase separation effect (the disproportionate distribution of RBCs and plasma at bifurcations) (Section 1.3.1). Conservation of RBCs and plasma flow is applied at every junction. The apparent viscosity of the blood within each blood vessel is then adjusted accordingly.

3. A diameter relationship is then implemented to calculate the adapted diameters based on variable factors, such as the internal blood pressure, response to mechanical and metabolic stimuli, and alveolar and pleural pressures in the case of the pulmonary system.

The solution procedure repeats these steps until a converged solution is reached. Tube-flow models have been developed to represent flow in both the systemic (Pries

et al. 1990, Pries & Secomb 2000, Fenton et al. 1985, Dawant, Levin & Popel 1986, Skalak & Chien 1987) and pulmonary microcirculatory systems (Dhadwal et al. 1997, Huang et al. 2001).

1.6.2.2.1 Pulmonary tube-flow models With the advent of more sophisticated technologies to view the anatomic structure of pulmonary capillaries, it was apparent that blood does in fact flow through discrete tubes even in the pulmonary microcirculation; the only divergence from the systemic microcirculation is the increased density of capillary vessels in the lung (Guntheroth et al. 1982).

The solution method outlined above in steps 1-3 for tube-flow have been implemented in the pulmonary capillaries by Dhadwal et al. (1997) and Huang et al. (2001). Resistance, rheological, and diameter relationships adapted specifically for the pulmonary microcirculation were implemented in the general solution procedure. These models were developed to enable a more anatomically-realistic description of pulmonary blood flow and a more detailed definition of localised pressure and flow distributions on a segment-by-segment basis than can be provided by the sheet-flow model.

Dhadwal et al. (1997) developed a model of blood flow through a single alveolar septum. The objective of this study was to investigate variation in diameter and compliance of individual vessels on the distribution of pressure and flow in the network. An imposed pressure gradient induces flow across a rectangular 6 x 6 grid representing the capillary geometry. Random variation in parameters (diameter and compliance) showed the existence of preferential pathways through the grid.

Huang et al. (2001) extended the model of Dhadwal et al. (1997) by modelling blood flow through the capillary network of a single alveolar septum and through six consecutive septae. A more detailed description of the capillary geometry was developed in this model (Section 1.6.1.2). A tissue-membrane model was incorporated to describe geometric changes of the capillary cross-section as a function of alveolar, pleural, and capillary pressures to enable the effect of changes in lung volume with transpulmonary pressure (Ptp) on capillary flow to be investigated. The final important extension made was the addition of red and white blood cell transit models, to calculate the passage time from arteriole to venule. Several interesting simulations were carried out in this study including comparison of the transit behaviour of RBCs, WBCs, and rigid microspheres. The incidence of WBC and microsphere stoppage was also predicted. Model transit time predictions were found to compare well with measured *in vivo* transit times. Simulation of the effect of a WBC blockage demonstrated a 100-

300% increase in pressure across a blocked segment causing redistribution of perfusion accordingly.

These discrete tube models allow calculation of the range of cell transit times for discrete pathways, as well as investigation into perfusion patterns in the capillary network; it also provides insight into the distribution and interactions of red and white blood cells within the system. The solution procedures developed in these two pulmonary flow studies have been implemented in the current model, refer to Section 3.2 for more details.

1.6.3 Pulmonary vascular models

Previous evaluations of structure-function relationships in the pulmonary circulation via mathematical techniques have reduced the complexity of the pulmonary vascular tree geometry by, for example, representing the pulmonary arteries and veins as a symmetric tree (Parker, Cave, Ardell, Hamm & Williams 1997), as a self-similar fractal tree (Bennett, Goetzman, Milstein & Pannu 1996, Glenny, Polissar & Robertson 1991, Glenny & Robertson 1991, Krenz, Linehan & Dawson 1992)[1], or by representing an average flow path via summary morphometric parameters (Dawson, Krenz, Karau, Haworth, Hanger & Linehan 1999). These models have been implemented to investigate the effects of large-scale alterations of branching geometry on hemodynamics in the lung, and therefore only represent the average geometry of the branching structure. The models have not been created to accurately reflect the geometry of the vascular structure; they have instead been designed for use in a particular functional investigation. These studies all illustrate the large dependence of flow distribution on network geometry. While these simplified models represent the complicated structure with a small number of parameters and provide useful insights into the relationship between structure and function they do neglect several features known or predicted to be present, such as supernumerary vessels.

1.6.4 Pulmonary blood flow models

There have been two main approaches taken in modelling pulmonary flow, these are: the systems (electrical analogue) approach or a more physiologic approach (as is used in the current study). The systems approach simplifies the physiology of the

[1] A fractal structure or process has the quality of self-similarity or scale-independence. This means that it is repeatable over a range of spatial or time scales (Glenny & Robertson 1998)

system by creating a lumped parameter type model where components of resistance and compliance are joined in series or parallel to represent the flow circuit (Huang, Tian, Gao & Yen 1998). While this method can provide reasonable estimates of global perfusion these models cannot capture the complex geometry of the system and therefore cannot be used to investigate, for example, relationships between the vascular branching structure and flow distribution.

Physiologically based modelling solves flow equations within a more realistic geometry; this approach is adopted in the current study. Flow equations solved include Poiseuille type power law equations (Zhuang, Fung & Yen 1983) or nonlinear fluid flow equations representing conservation of mass and momentum (Collins & Maccario 1979, Li & Cheng 1993). While these models are similar to the model developed in the current study, they lack detailed anatomically-based vascular geometries. These models are discussed further in Section 5.5.

Chapter 2

Geometric modelling of the pulmonary microcirculation

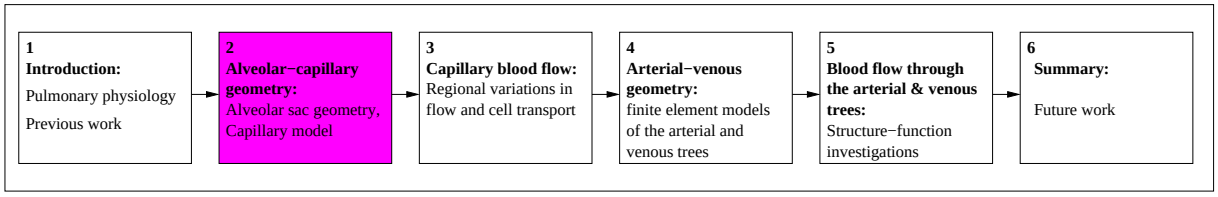

This chapter describes the development of an anatomically-based finite element model of the human pulmonary microcirculation, including alveolar and capillary geometries. This geometric model has been created to enable a detailed description of blood flow through the complex microcirculatory system in the human lung (Chapter 3). An initial overview of the anatomy and physiology of the system is contained in the previous chapter in Section 1.2. A Voronoi meshing technique is used to describe both the alveolar and capillary geometries (Section 2.2). These models are found to compare well with available anatomical data (Section 2.3).

2.1 Introduction

The complexity of the pulmonary microvasculature geometry arises from its vast number of component capillary segments. The density of the pulmonary microcirculation far exceeds that found in the systemic circuit (Guntheroth et al. 1982, Weibel 1984). A single RBC traveling from an arteriole to a venule via the pulmonary capillaries will pass through around 40-100 (90 on average) capillary segments in the human lung (Hogg 1991), over a distance of between 600-800μm in

cats and dogs (about 60 segments (Wagner Jr et al. 1999)), and between 550-650μm (about 45 segments) in rabbits (Doerschuk, Coxson & Hogg 1989, Staub & Shultz 1968).

The majority of pulmonary capillaries have similar or smaller diameters than both RBCs and neutrophils. Neutrophils are a type of WBC, comprising around 50-70% of the WBC population. They have a spherical shape and higher viscosity than RBCs and therefore deform more slowly (Hanger, Wagner Jr, Janke, Lloyd Jr & Capen 1993). This causes the neutrophils to effectively "block" some capillary segments while they deform and increases the concentration of neutrophils in the pulmonary network by more than 50 times that in the systemic microcirculation (Huang et al. 2001, Wiggs, English, Quinlan, Doyle, Hogg & Doerschuk 1994). This phenomenon is known as neutrophil margination and is thought to be a means by which the body can retain a reservoir of neutrophils in the lung to aid in host defense (Huang et al. 2001). This is discussed further in Section 1.3.4. However, the multisegmented geometry of the capillary bed allows the RBCs to move freely through unblocked parallel pathways in the network.

Accurate representation of the pulmonary capillary geometry and its boundary conditions is essential for investigating complex flow phenomena and cellular interactions in the pulmonary microvasculature. The geometry of the model described in this chapter consists of a capillary network continuous over 19 adjacent alveoli, which together form a single alveolar sac. Finite element meshes are developed using two and three-dimensional Voronoi meshing techniques for the capillaries and alveoli, respectively. This new method produces meshes of the alveolated airways that are space-filling and have similar geometric properties to alveoli in nature. The meshing procedure produces a continuous capillary model that enwraps the surface of each individual alveolar unit, closely replicating *in vivo* structures.

2.2 Methods

2.2.1 Voronoi diagrams and Delaunay triangulation

The Voronoi meshing technique has been used in the development of both the alveolar and capillary geometric models presented in Chapter 2. Given a collection of points within a certain host space or volume, a Voronoi diagram partitions the space into smaller 'cells' or regions, each enclosing a point. The property of these Voronoi cells is that the space within each cell is closer to the point it contains than to any other points. The Delaunay triangulation of the same set of points is the geometric dual of

the Voronoi diagram (Okabe, Boots & Sugihara 1992).

The Voronoi meshing procedure implemented in this study builds the Voronoi data structure from the Delaunay triangulation. The Delaunay triangulation has the additional property that for each triangle (in two dimensions 2D), or tetrahedra (in three dimensions 3D), the circumcircle, (or circumsphere in 3D), of that triangle does not contain any other points. These closely related data structures have been utilised extensively in the fields of computational geometry, astronomy, archaeology, geography, as well as many more (Okabe et al. 1992).

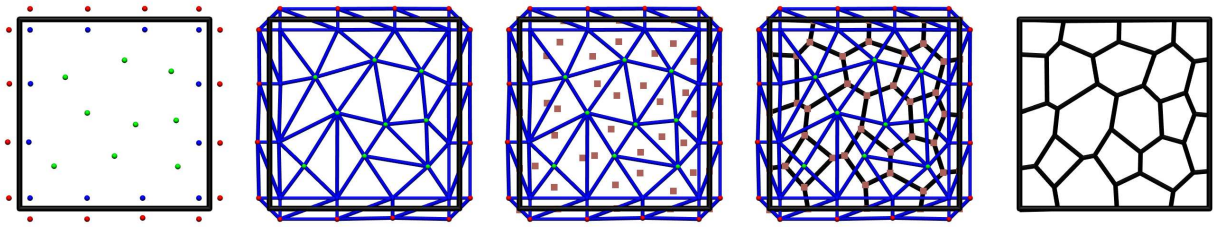

FIGURE 2.1: *Illustration of Delaunay triangulation and Voronoi meshing technique in 2D. (a) Data points generated into host space; (b) Delaunay triangulation created; (c) circumcentres of triangles located; and (d), (e) adjacent circumcentres connected to create the Voronoi mesh.*

The Voronoi meshing procedure used in this work is illustrated schematically in 2D in Figure 2.1. Seed points are generated within the given host volume (Figure 2.1(a)). This collection must include boundary points (shown in red) and internal boundary points (shown in blue) placed orthogonal to each other across the host boundaries. This technique ensures that the host boundaries will be accurately represented in the resulting Voronoi tessellation. Internal points are also generated (shown in green). To create the Delaunay triangulation proximal points are grouped to form triangles (in 2D) or tetrahedra (in 3D) (Figure 2.1(b)), such that the resulting triangulated mesh has the fundamental property of Delaunayism: no circumsphere defined by the four vertex points of a tetrahedra contains any other vertex point. Once the Delaunay tessellation has been formed it is relatively simple to create the Voronoi structure. The circumcentres of each of the Delaunay triangles becomes a node in the Voronoi mesh (Figure 2.1(c)). Nodes of adjacent triangles are joined to form the elements of the mesh (Figures 2.1(d) and (e)). In the case of the alveolar model, two-dimensional surface elements are created, and for the capillaries one-dimensional line elements result from

the Voronoi meshing procedure.

2.2.2 The alveolar geometric model

A volume-filling model of the alveolar structure is created within a cube. In the current study a single alveolar sac is isolated from the more extensive model. The alveolar sac model consists of 19 adjoining polyhedra with selected faces 'open' to the central duct. The technique for generating the model is shown in Figure 2.2, illustrated for a two-dimensional mesh.

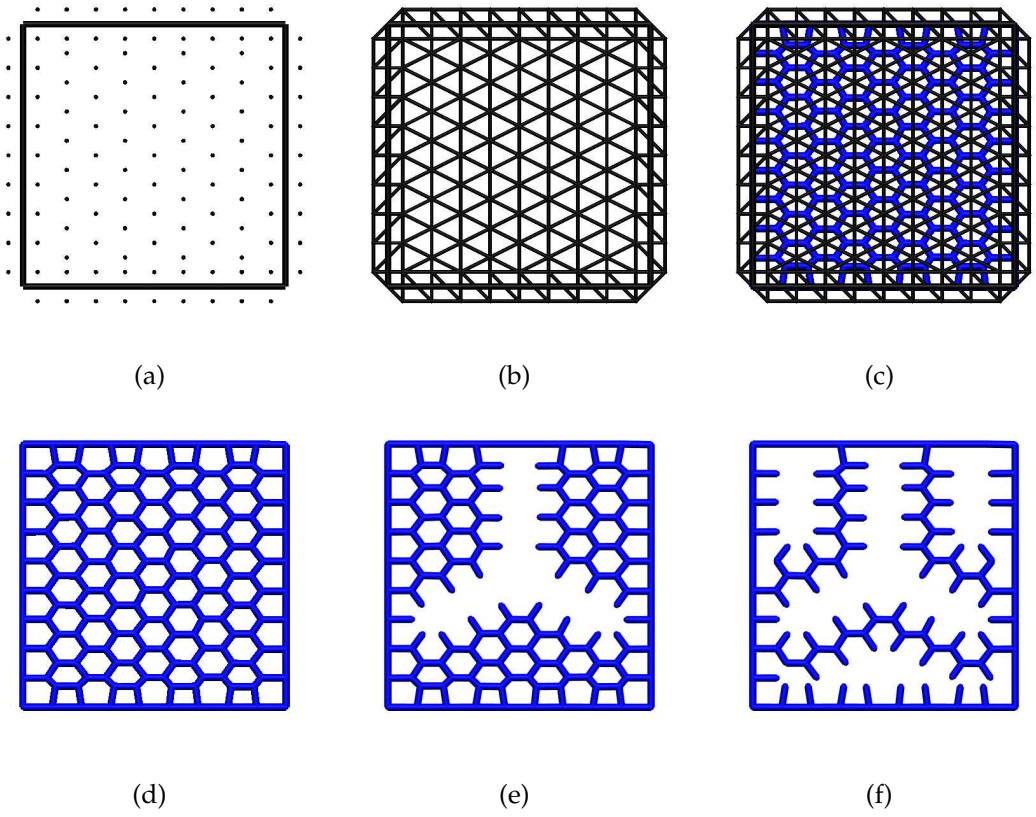

FIGURE 2.2: *Alveolar mesh generation using a Voronoi meshing technique in 3D, process illustrated here in 2D. (a) Points generated into host space; (b) Delaunay triangulation of the point set is formed; (c), (d) Adjacent circumcentres are joined to form the Voronoi diagram. (e), (f) Voronoi duct cells are removed leaving open alveolar Voronoi cells. Figure courtesy of Burrowes et al. (2004).*

In the alveolated airway model seed points are generated uniformly within the host volume, which is a cube in the current model generation (Figure 2.2(a)). The points are triangulated (Figure 2.2(b)), and as noted in Section 2.2.1, this Delaunay

triangulation forms tetrahedra in 3D, such that the sphere passing through the four tetrahedra nodes does not contain any other seed points. The Voronoi 'dual' of the triangulation are adjacent polyhedral 'cells' with vertices at the circumcentre of neighbouring tetrahedra (Figure 2.2(c) and (d)). Specific Voronoi cells are allocated as airway duct cells, and these Voronoi faces are then removed and any adjacent cells become alveoli. The remaining system forms a volume-filling honeycomb-like mesh (Figure 2.2 (e)). Aeration of each Voronoi cell is ensured by removal of obstructing Voronoi edges (Figure 2.2(f)). These final cells form the 'clusters of alveoli' observed during morphometric studies (Haefeli-Bleuer & Weibel 1988). This method provides a relatively simple way to create alveolated airway structures within general host volume shapes.

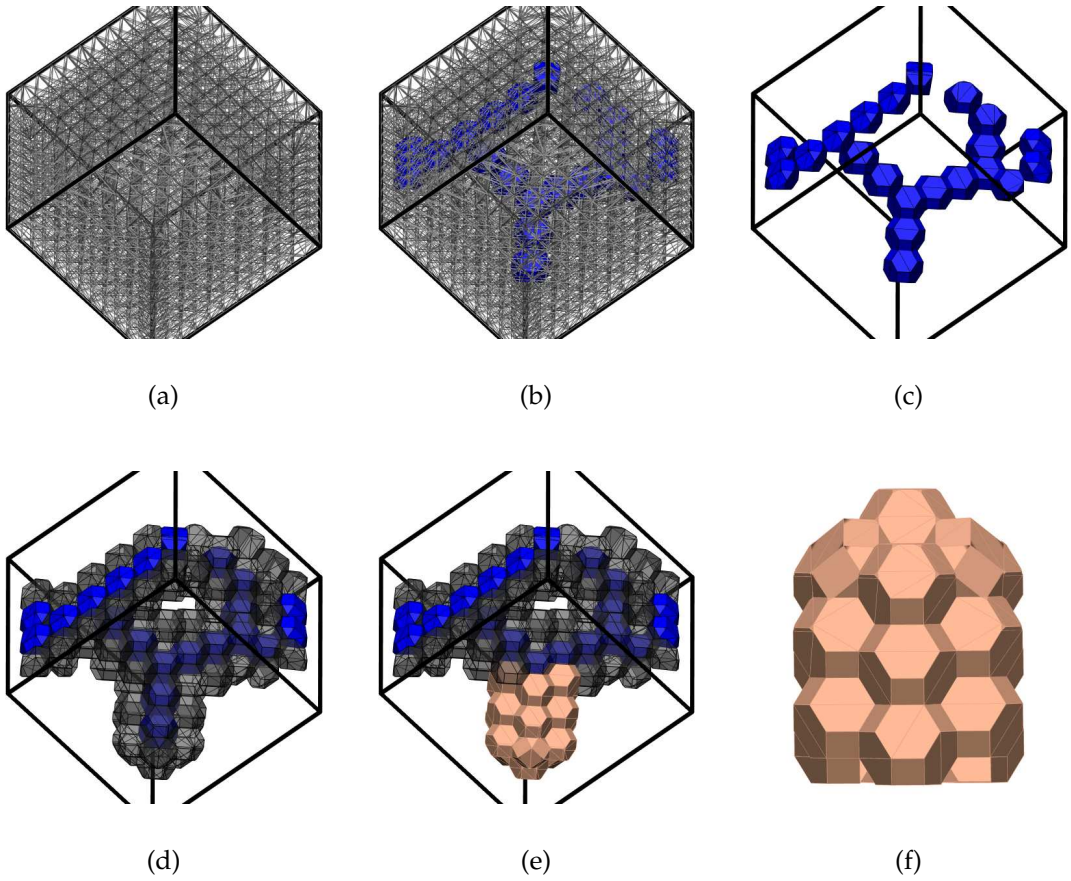

FIGURE 2.3: *Development of the alveolar sac model, illustrated in 3D. (a) shows the full Voronoi mesh within a cube; (b),(c) selected Voronoi cells (selection criteria explained further in text) are allocated as duct cells (blue); (d) all adjacent Voronoi cells become alveoli (gray); (e),(f) a single alveolar sac is selected for use in the current study (pink).*

The progression of alveolar model development is illustrated for the actual 3D model in Figure 2.3. The full Voronoi mesh within a unit cube is displayed in Figure 2.3(a). All of the internal Voronoi cells are very similar in size and shape, but the edge cells are variable. From this full Voronoi tessellation selected cells must be allocated as duct cells (to allow aeration), and the remaining cells become alveoli. Each alveolus must be adjacent to a duct cell. The algorithm used to determine which Voronoi cells become alveolar duct or alveolar cells proceeds as follows:

1. The required number of alveolar duct generations is input into the model.
2. The algorithm is initiated at a peripheral Voronoi cell, which is allocated as the first alveolar duct cell.
3. From here a specified number of adjacent, axial Voronoi cells are designated as duct cells.
4. At a bifurcation two daughter Voronoi cells are selected as duct cells. The first one is chosen to be the Voronoi cell making the largest angle (while still less than 90^0) with the parent cell. The second daughter branch is selected as the Voronoi cell making the greatest angle (while still less than 90^0) with the sister cell.
5. This procedure continues until either the specified number of duct generations have been executed or until a peripheral Voronoi cell is reached.

Figure 2.3(b) and (c) show the alveolar duct cells (blue) within the unit cube. The alveolar cells are specified as any Voronoi cell in contact with a duct cell, shown in Figure 2.3(d) in gray. The alveolar duct or sac, including the surrounding alveoli, has been proposed as the basic mechanical and gas-exchanging unit of the lung (Hoppin & Hildebrandt 1977), because it represents a distinct functional pulmonary unit. Hence, a single alveolar sac, highlighted in pink (Figure 2.3(e) and (f)) is isolated from this more extensive model, to be used in the current capillary flow study.

2.2.3 The capillary geometric model

The capillary model is generated to cover the 2D alveolar septae of the sac model shown in Figure 2.5 using the following steps (the procedure is demonstrated over the surface of a simplified alveolar geometry in Figure 2.4):

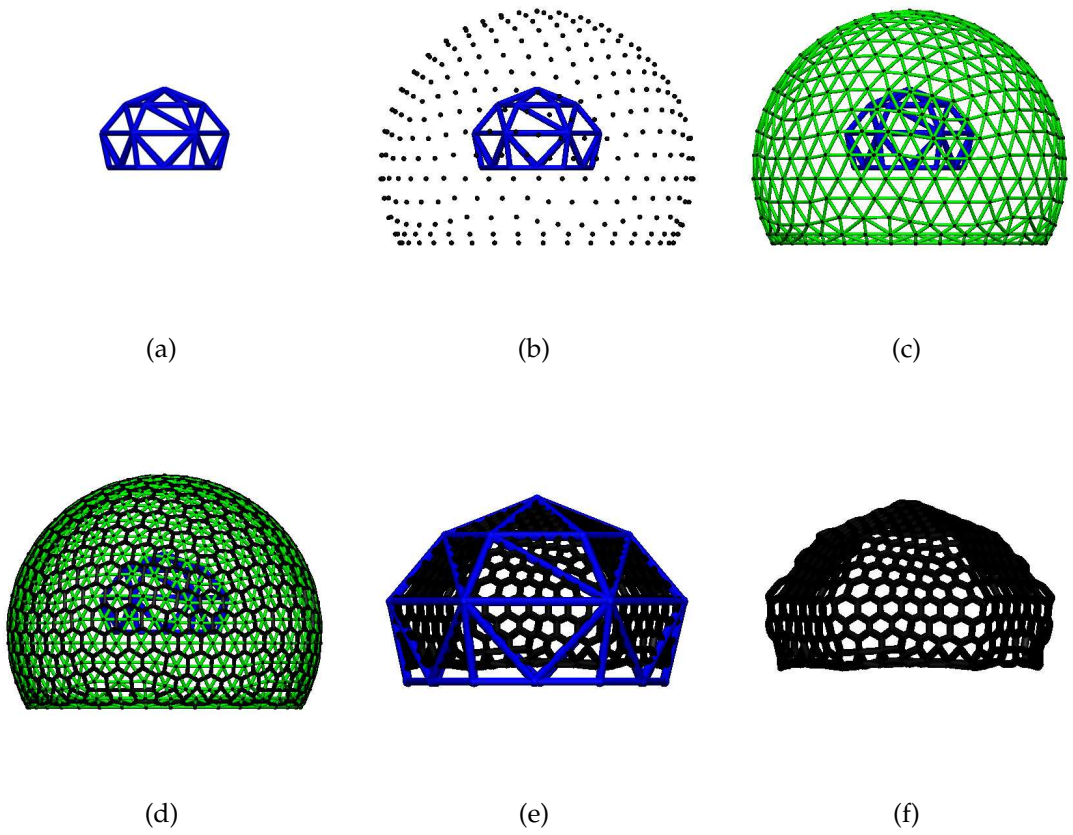

FIGURE 2.4: *Generation of the capillary model using a 2D Voronoi meshing technique, over the surface of a simplified alveolar geometry (a). (b) Points are generated on the surface of a unit sphere, (c) the Delaunay triangulation is formed (d) and the Voronoi mesh is generated. (e) This mesh is projected onto the alveolar surface geometry to create the capillary mesh, shown in (f). Figure courtesy of Burrowes et al. (2004).*

1. Regularly spaced points are generated over the surface of a portion of a unit sphere, (the orifice of the sphere is defined by an orifice angle), Figure 2.4(b).

2. The points are triangulated using an algorithm for 2D Delaunay triangulation over a unit sphere, Figure 2.4(c).

3. The capillary segments are created from the one dimensional (1D) lines that join the circumcentres of neighboring Delaunay triangles. These are the 'edges' of Voronoi cells in 2D, Figure 2.4(d).

4. The points are projected onto the surface of a single alveolus, Figure 2.4(e) and the resulting capillary mesh is obtained, Figure 2.4(f).

5. For shared faces (between adjacent alveoli) the points on the shared face are replaced with the points from the neighbouring previously triangulated alveolus. In this way a continuous capillary network is generated, with only a single capillary layer between adjacent alveoli.

At the acinar level the arteries still closely follow the airways while the veins drain from the acinar periphery (Haefeli-Bleuer & Weibel 1988). Based upon measurements from human data (Weibel 1963, Horsfield 1978, Horsfield & Gordon 1981) a total of 4 arterioles are used in the current model to centrally feed the alveolar-capillary plexus, and 5 venules to drain at the network perimeter.

The capillary cross-section is represented as an ellipse, with the major and minor elliptical dimensions being defined initially from randomly selected values within a physiological range and recalculated throughout the solution procedure using a dimensional model (Huang et al. 2001) (described in more detail in Section 3.2.1).

2.3 Results

2.3.1 Alveolar geometry

The resulting alveolar sac model is shown in Figure 2.5. Each alveolus surrounding the alveolar duct consists of 19-21 two-dimensional (bi-linear) finite elements. Together these triangular, square, and pentagonal elements form a polygon with square and hexagonal faces, with pentagonal (truncated hexagonal) faces at the alveolar opening.

Average dimensions of the alveoli in the alveolar sac model are compared with published anatomical values, displayed in Table 2.1. The average volume, surface area, diameter, surface area to volume ratio, and depth are compared in this table. The diameter is calculated as the average of several lines dissecting the cross-section of the model alveoli. The depth value is the maximum depth, calculated as the distance from the alveolar entrance plane to the furthest point in the alveolus. The computational spatial scale was transformed to standard units (mm) by using a volume based scale factor from anatomical measurements (Weibel 1963); the value used is the model volume in Table 2.1. The volume value was selected, from a measured range, such that the capillaries generated over the surface geometry were in close accordance with anatomical values.

The average surface area (s_A) to volume (v_A) ratio ($\overline{\sigma}_A$) for the 19 alveoli in the model alveolar sac was 4.74, as calculated using Equation 2.1 (Weibel 1963).

$$\overline{\sigma}_A = \frac{s_A}{v_A^{\frac{2}{3}}} \tag{2.1}$$

Anatomical investigation by Hansen & Ampaya (1975) gave average results for the alveolar orifice diameter, depth, surface area, and volume. Two different average values were recorded. The first was calculated using only the mean dimensions for each of the six shapes used to qualitatively describe the structure (described in Section 1.2). The second average was calculated using mean dimensions for each shape and distribution coefficients. The values displayed in Table 2.1 are those determined using the latter method.

2.3.2 Capillary geometry

The resulting capillary mesh generated over an entire alveolar sac model is shown in Figure 2.6.

Measurement	Model	Published values
Volume (mm^3)	0.00744	0.00480 (Hansen & Ampaya 1975), 0.0105 (Weibel 1963)
Surface Area (mm^2)	0.1806	0.119 (Hansen & Ampaya 1975), 0.234 (calculated from (Weibel 1963))
Diameter (mm)	0.246	0.244 (Weibel 1963), 0.3 (West 2000)
Surface Area to volume ratio	4.74	4.87 (Weibel 1963)
Depth (mm)	0.228	0.238 (Weibel 1963), 0.238 (Hansen & Ampaya 1975)

TABLE 2.1: *Comparison of model alveolar dimensions with published anatomical data.*

Table 2.2 compares values from the generated model, at mid-lung height (15 cm), with published anatomical data. The total capillary volume was calculated by scaling the volume of the alveolar sac model to full human lung size, based on the total number of alveoli (300 million) in an adult lung.

Parameter	Model	Published values
Hydraulic diameter ($\mu\mathrm{m}$)	6.78	6 (Chang & Paiva 1989), 8 (Weibel 1963)
Diameter range ($\mu\mathrm{m}$)	5.75-7.87	4-10 (Chang & Paiva 1989), 6.3-9.9 (Weibel 1963)
Capillary length ($\mu\mathrm{m}$)	11.92	12 (Chang & Paiva 1989), 12 (Weibel 1963)
No. segments per alveolus	1109	1000 (Chang & Paiva 1989)
No. segments per pathway	85	90 (Hogg 1991)
Mean path length (mm)	1.10	0.6-0.8 (in dog) (Staub & Shultz 1968), 1.08 (Hogg 1991, Weibel 1963)
Total capillary volume (ml)	149.0	100-200 (average 153) (Weibel 1963), 178 (Hogg et al. 1994)

TABLE 2.2: Comparison of model generated dimensional data with published anatomical data. (These values determined at $P_{pleural}$=-5.75, $P_{alveolar}$=0, $P_{arteriole}$=15, and P_{venule}=7, all in $\mathrm{cm}H_2O$).

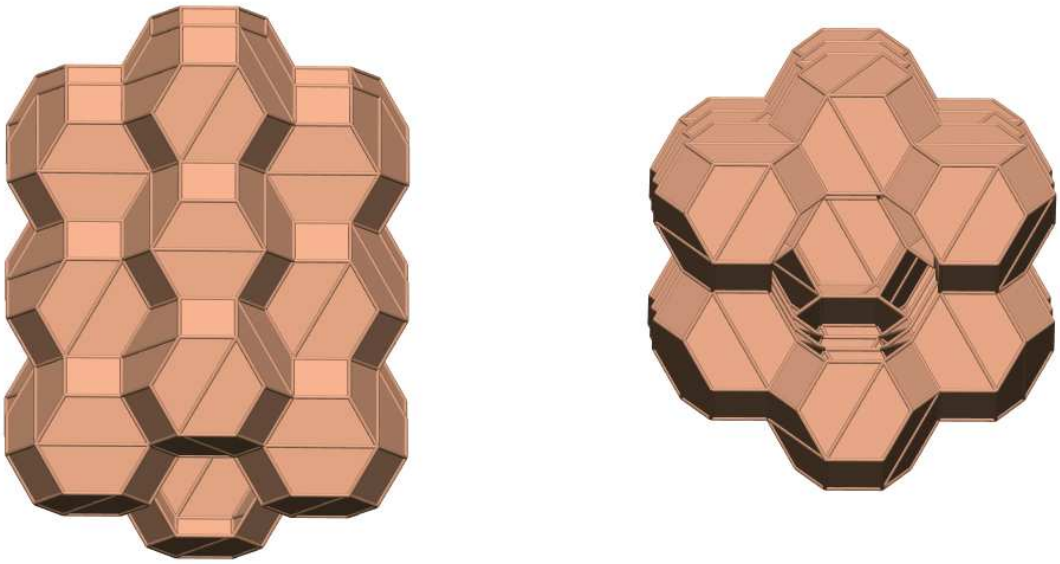

(a) (b)

FIGURE 2.5: *Finite element computational Voronoi alveolar mesh, (a) front view (b) end on view.*

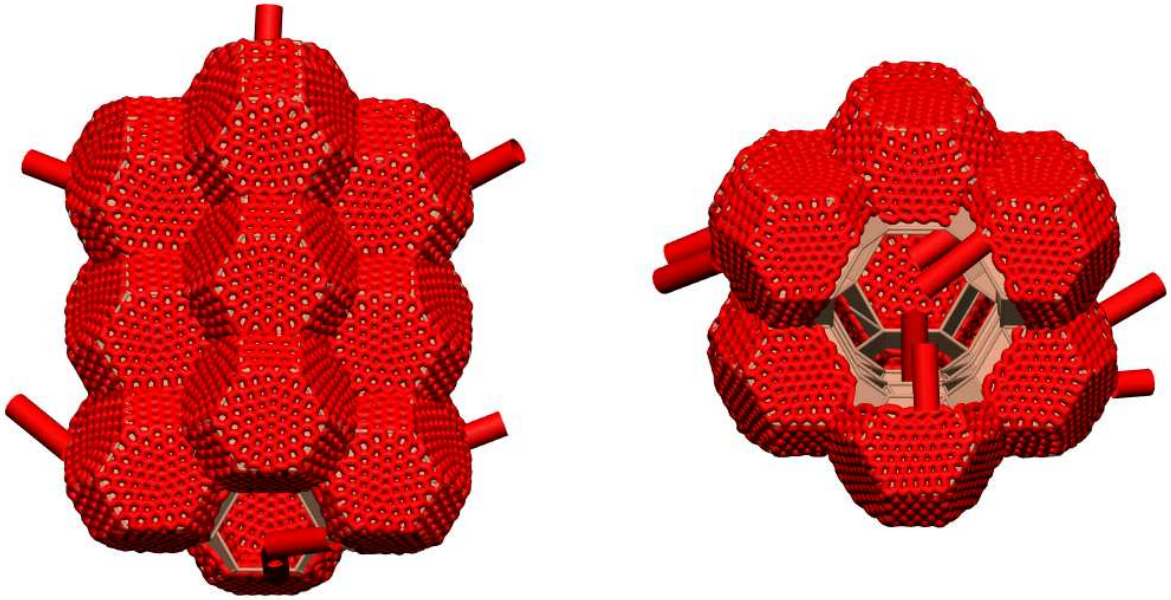

(a) (b)

FIGURE 2.6: *Finite element computational Voronoi capillary mesh, (a) front view, (b) end-on view.*

2.4 Discussion

2.4.1 Alveolar model

An efficient algorithm has been developed to mimic the *in vivo* geometric structure of alveoli in the human lung. The alveolar model is able to create an entirely volume-filling model into any reasonably defined host volume. The Voronoi concept of equally partitioning space around a collection of points replicates the human alveolar structure effectively. Certain measurable geometric parameters (volume, surface area, diameter, surface area to volume ratio, and depth) were compared to published anatomical data and found to be in good agreement (refer Table 2.1). The surface area to volume ratio calculated for the model alveolar sac was 4.74, which was within 2.7% of the published value of 4.87 from anatomical results (Weibel 1963).

The individual alveolar geometry in the current model is similar to previous models of alveolar geometry (Fung 1988, Denny & Schroter 1995, Denny & Schroter 1996), but the geometry of individual alveoli may vary from each other. These previous models assumed each alveolus to have an identical geometry.

An advantage of the current alveolar model generation, as compared with previous models (refer Section 1.6.1), is the true volume-filling nature of the Voronoi technique. Polyhedrons will be created to fill the entire host volume of any defined shape. Another advantage of this model is in the ability of the alveolar units to be of varying size, more realistically replicating anatomical geometry. In the current model a uniform grid of points was used, therefore all alveoli were of very similar geometry, except the peripheral alveoli. However, by using a more random grid of points a heterogeneous alveolar meshwork could be constructed. This meshing technique could be used for future investigation into the effect of alveolar geometry on function in the lung, as it has been shown that there is a distribution of alveolar sizes in the vertical lung (Glazier et al. 1967).

The development of this alveolar model will also enable investigation into other areas of pulmonary function, such as air flow distribution. The alveolar structure in a larger block of lung tissue will be able to be constructed relatively easily subject to computational constraints using the Voronoi meshing technique. Future directions involving this alveolar model may include coupling of the parenchymal structure to models of soft-tissue mechanics and air flow, in order to create a deforming, interacting alveolar structure which could provide boundary conditions for an air flow model. This model may also be of use in investigating particle deposition in the alveolated airways.

2.4.2 Capillary model

This study is the first attempt to accurately model the relationship between the segmented geometry of the pulmonary microcirculation and the space-filling alveoli over which they lie. Previous models have used a more simplified geometry, or represented only smaller units of the dense capillary plexus. This method produces a more extensive model than has been developed in previous studies.

Capillary continuity is found at least throughout the acinus, between adjacent acini and possibly extends throughout the lobule. The observation of collateral ventilation across pulmonary segments implies pulmonary parenchyma continuity and suggests that capillary continuity over this large area is possible (Weibel 1963). A complete alveolar sac was used in the current study because it represents a distinct pulmonary structure over which it is most likely that the capillary network is continuous. This capillary model can be extended to cover many more alveolar units. Given the alveolar geometry, capillary segments will be generated over the surface of each individual alveolus and any shared alveolar faces will be enveloped by only a single capillary network. The ability of the algorithm to be extended to larger blocks of parenchymal tissue while only creating a single capillary layer between adjacent alveoli is a unique feature of the model.

The Voronoi meshing technique is advantageous in representing the alveolar and capillary structures as it is a space-filling, efficient algorithm. It is a relatively simple method used to reproduce the complex anatomical structure found in the mammalian lung.

The Voronoi-based capillary model shares some geometric characteristics with those observed in the pulmonary microcirculation: both model and *in vivo* capillary junctions usually comprise, but are not restricted to, three segments (Weibel 1963); and the rings formed by both model and *in vivo* adjoining capillary segments form predominantly pentagons and hexagons (Weibel 1963, Guntheroth et al. 1982, Horsfield & Woldenberg 1989). This method has reproduced capillary vessels of comparable length to vessels *in vivo* (Weibel 1963, Chang & Paiva 1989).

Detailed histological measurements of cat lungs by Zhuang, Yen, Fung & Sobin (1985) have shown that each terminal precapillary vessel (arteriole) supplies, on average, 24.5 pulmonary alveoli and each terminal postcapillary vessel (venule) drains an average of 17.8 alveoli. The predictions of Horsfield (1978) and Horsfield & Gordon (1981) are that a single arteriole and venule each supply (on average) 4.11 alveoli in the human lung (these figures are based on their calculation of the number of order

1 arterioles and venules, and assuming 300 million alveoli in the human lung). The difference in the numbers predicted by Zhuang et al. (1985) and Horsfield (1978), Horsfield & Gordon (1981) are thought to be due to the classification of order 1 vessels. Zhuang et al. (1985) believes that the order 1 vessels that Horsfield classified, were in fact sprouts of the capillary sheet belonging to the capillary network. The current capillary model is supplied by four arterioles and drained by five venules to be consistent with human data. Model flow results indicate that this is a reasonable number of vessels to use (Section 3.3).

2.5 Conclusions

This chapter describes the development of an anatomically-based finite element model of the microcirculatory geometry. A Voronoi meshing technique is used to develop both the alveolar and capillary models which efficiently represent the structure found *in vivo*.

The geometric model developed in this study is the first anatomically-based representation of the segmented pulmonary microvasculature. This geometric model is used for the flow simulation studies which follow in Chapter 3.

A summary of this work can be found in Burrowes et al. (2004) and Tawhai & Burrowes (2003).

Chapter 3

Microcirculatory blood flow

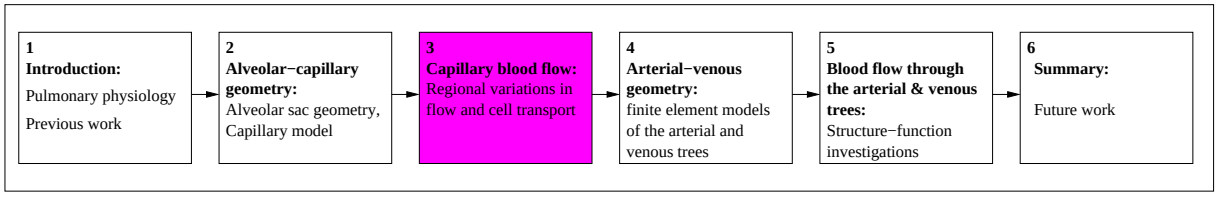

3.1 Introduction

A Poiseuille-type flow model, previously implemented by Huang et al. (2001), is solved within the geometric capillary model (continuous over a single alveolar sac) developed in Chapter 2 to simulate microcirculatory blood flow. In order to evaluate the blood flow relationships in a microvascular network several factors relating to the property of blood and RBCs in vessels of this size must be considered, an introduction was given in Section 1.3.1. A mathematical equation describing the shear-thinning properties of blood due to the presence of RBCs is included in the flow model (refer Section 3.2.2) and a hematocrit model is used to calculate the distribution of RBCs within the system in Section 3.2.4. Empirically-based relationships describing red and white blood cell transit are incorporated to determine the transit times from arteriole to venule within the network (Section 3.2.5). The resulting flow model is used to investigate cell transit time distributions and other regional variations in blood flow in the upright human lung (Sections 3.3.7 and 3.3.8), respectively. Regional flow is investigated by imposing gravity dependent transpulmonary and transmural pressure boundary conditions.

3.2 Methods

The blood flow model of Huang et al. (2001) and Dhadwal et al. (1997) has been implemented in the geometry of the alveolar-capillary mesh developed in Chapter 2. This model uses the tube-flow method, the general procedure of which is described in Section 1.6.2.2. In summary, the resistance in each vessel can be calculated - initially assuming a uniform hematocrit - (Section 3.2.2), and an initial linear pressure-flow solution is calculated for the entire network (Section 3.2.3). The RBC (Section 3.2.4), and diameter (Section 3.2.1), values for each segment are then calculated based on the pressure-flow distributions. The hematocrit, flow rate and dimensions of each segment are interdependent, hence an iterative procedure is implemented to reach a converged solution.

Empirically-based relationships in combination with the pressure-flow solution are used to calculate the transit time of RBCs and WBCs from arteriole to venule. This procedure is described in Section 3.2.5.

3.2.1 Dimensional changes of the capillary cross-section

Huang et al. (2001) developed a tissue-membrane structural model whereby each capillary circumference is assumed to be made up of two parts, illustrated in Figure 3.5. One part is tethered to the septal fibre network therefore expanding and contracting with alveolar septal dimension changes (length a). The other portion makes up the blood-gas barrier and is relatively thin and compliant (length C). A transpulmonary pressure (alveolar minus pleural pressure) (Ptp) dependent elastic coefficient is determined and used to calculate the alveolar volume and capillary perimeters. The geometric parameters of the capillary segments, which are assumed to have an elliptical cross-section, are hence dependent on transmural pressure (capillary minus alveolar gas pressure) (Ptm) and Ptp. The dimensional model calculates the radius (R), height of the capillary (h), and the perimeter of the capillary cross-section.

Additional assumptions made in the derivation of this model were as follows:

1. changes in Ptm only affect the septal dimension (a);

2. these changes are proportional to the total change in alveolar septal length (L);

3. the length of the blood-gas barrier portion (C) increases linearly with increasing tension around the capillary circumference (T_c);

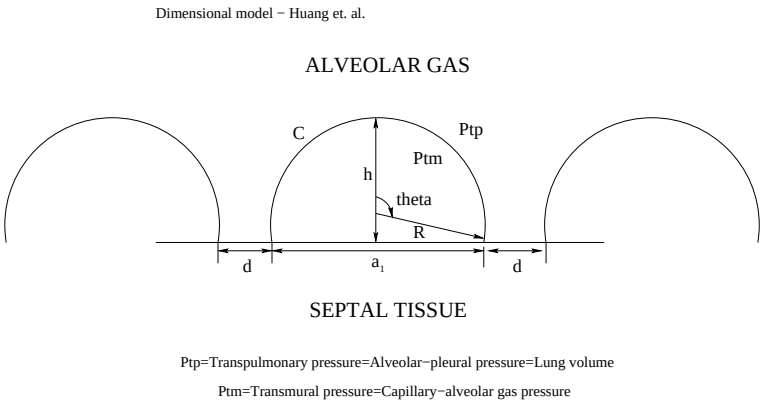

FIGURE 3.1: *Schematic of capillary cross-section, illustrating dimensional model development. The capillary circumference is divided into a septal portion (a_1, NB/ a_1=a when Ptm=0) and a membrane portion (C). The capillary height (h), radius (R), and the angle theta (θ) are calculated in the dimensional model. d is the distance between adjacent capillaries. Figure reconstructed from (Huang et al. 2001)*

4. a single alveolar septum is approximated as a square plane and an alveolus as a cube.

Initially Ptm is set equal to zero and only the effects of Ptp are evaluated. The change in septal dimension a is proportional to the change in alveolar volume which is a function of Ptp (or lung volume). The following relationship between alveolar volume (V) and Ptp was derived from measurements on rat alveolar volumes during inflation and deflation from Mercer, Laco & Crapo (1987):

$$V = V_0 + (A - V_0)e^{(-\frac{B}{Ptp})^M} \tag{3.1}$$

where A, B, and M are empirically determined constants. For inflation $A = 2.90\text{x}10^5 \mu\text{m}^3$, $B = 6.43\text{cmH}_2\text{O}$, and $M = 2.14$, for deflation $A = 3.07\text{x}10^5 \mu\text{m}^3$, $B = 3.42\text{cmH}_2\text{O}$, and $M = 1.03$. Assuming the side length of an alveolus varies as $V^{1/3}$, we can obtain the following relationship:

$$\frac{L}{L_0} = \left[1 + \left(\frac{A}{V_0} - 1\right)e^{(-\frac{B}{Ptp})^M}\right]^{\frac{1}{3}} \tag{3.2}$$

Where L_0 is the initial alveolar septum length at Ptp=0; a value of 70 μm is used derived from rat data (Huang et al. 2001). The new capillary septal dimension a is then equal to:

$$a = a_0 \frac{L}{L_0} \tag{3.3}$$

Where a_0 is the initial a at Ptp=0. Therefore, given V_0 (the alveolar volume at zero Ptp) and L_0 the length a (the length of tissue portion of the circumference of a capillary cross-section at zero Ptm) can be calculated. For simulations in the current study V_0 was set equal to $20.7\text{x}10^3$ μm^3 (Mercer et al. 1987) (for rat alveolar volume at zero Ptp).

Applying a force balance in the alveolar septum and rearranging to give the equation in a stress-strain form gives the following equation:

$$T_s = E(Ptp)\left(\frac{L}{L_0} - 1\right) \tag{3.4}$$

where T_s is the force per unit length in the septal wall, and $E(Ptp)$ is the elastic coefficient of the capillary wall as a function of Ptp, defined as:

$$E(Ptp) = \frac{\frac{1}{2}PtpL}{\frac{L}{L_0} - 1} \tag{3.5}$$

When changes in Ptm are also incorporated the length of the septal portion will increase further from a to a_1, and the membrane portion length will increase from C_0 to C. The following equations (from Huang et al. (2001)) defining a force balance and geometric relationships yield the following equations:

$$Ptmh = T_c + E(a_1 - a)\left(\frac{1}{a} + \frac{1}{d-a}\right) \tag{3.6}$$

$$T_c = PtmR \tag{3.7}$$

$$T_c = k_c(C - C_0) \tag{3.8}$$

$$a_1 = 2Rsin\theta \tag{3.9}$$

$$h = R(1 - cos\theta) \tag{3.10}$$

$$C = 2R\theta \tag{3.11}$$

where d is the distance between two capillaries, taken as the average distance of all surrounding capillaries, R is the radius and h is the height of the capillary cross-section, k_c is the stiffness of the capillary wall, and θ is the angle as shown in Figure 3.5.

Combining equations 3.7, 3.8, and 3.11 enables calculation of R:

$$R = \frac{C_0}{2\theta - \frac{Ptm}{k_c}} \tag{3.12}$$

Combination and rearrangement of equations 3.6, 3.7, 3.9, 3.10, and 3.12 gives an expression to determine the angle θ:

$$c_1\theta + c_2 cos\theta + c_3 sin\theta + c_4 = 0 \tag{3.13}$$

where

$$\begin{aligned} c_1 &= 2aE^* \\ c_2 &= -C_0 Ptm \\ c_3 &= -2C_0 E^* \\ c_4 &= -\frac{aE^* Ptm}{k_c} \\ E^* &= E\left(\frac{1}{a} + \frac{1}{d-a}\right) \end{aligned}$$

The bisection method is used to determine θ from the above equations. On calculation of θ the remaining parameters R, C, a_1, and h can be determined. The perimeter of an ellipse, P (=C+a_1), can be approximately represented by:

$$P \approx \pi\sqrt{2(a^{*2} + b^{*2})} \tag{3.14}$$

The following two equations are then used to determine the major and minor elliptical parameters a^* and b^*, respectively:

$$b^* = \frac{h}{2} \tag{3.15}$$

$$a^* = \sqrt{\left(\frac{P^2}{2\pi^2} - b^2\right)} \tag{3.16}$$

This dimensional model was validated by Huang et al. (2001) by comparison against experimental data of Fung and Sobin (Fung & Sobin 1972*b*, Fung & Sobin 1972*a*), in the estimation of capillary sheet height. A good correlation was shown.

3.2.2 Flow in a single vessel

Each capillary segment is represented by a single one-dimensional (1D) element joined at either end by a node, which represents a junction. The following equation from Dhadwal et al. (1997) is used to calculate the approximate resistance in each individual segment:

$$R_{seg} = \frac{\Delta P}{\dot{Q}} = \int_0^l \frac{\mu_{app} Re_{Dh} f d}{2 A_c D_h^2} ds \tag{3.17}$$

where ΔP is the pressure difference between the inlet and outlet of the segment (Pa), $\dot{Q}$ is the volumetric flow rate ($\mu\mathrm{m}^3\ \mathrm{s}^{-1}$), μ_{app} is the apparent viscosity (Pas), A_c is the local cross-sectional area of the segment at location s along the vessel axis ($\mu\mathrm{m}^2$), D_h is the vessel hydraulic diameter (μm), $Re_D h$ is the Reynolds number, based on D_h, and finally, f_d is the Darcy friction factor. D_h, which is the equivalent circular diameter (D_h=4 times A_c divided by the wetted perimeter of the vessel) is calculated from the elliptical dimensions, a^* and b^*. The Darcy friction factor is a dimensionless number expressing the linear relationship between mean flow velocity and pressure drop. Under the approximation of an elliptical cross-section $Re_{D_h} f_d$ can be approximated by the following polynomial:

$$Re_{Dh} f_d = 80.2 - 30.3 \left(\frac{b^*}{a^*}\right) + 3.45 \left(\frac{b^*}{a^*}\right)^2 + 10.6 \left(\frac{b^*}{a^*}\right)^3 \tag{3.18}$$

This term depends on the aspect ratio of the elliptical vessels, being 63.95 when a vessel is circular in cross-section and varying between 63 and 73 in the current models' range of vessel shapes. The variation in $Re_{Dh} f_d$ influences the resistance value by less than $\pm$ 2%. Therefore the ellipticity of the vessels plays only a small role in this flow model.

μ_{app} represents the increased resistance to flow produced by the deformation of RBCs that occurs at the microcirculatory level. This term is calculated for each individual segment, initially assuming a uniform distribution of RBCs. A semi-empirical model describing the dependence of blood viscosity on vessel diameter and blood discharge hematocrit adapted by Kiani & Hudetz (1991) is used to calculate μ_{app}, Equation 3.19:

$$\mu_{app} = \frac{\mu_p}{\left[1 - \left(1 - \frac{\mu_p}{\mu_c}\right)\left(1 - 2\frac{D^*}{D_h}\right)^4\right]\left(1 - \left(\frac{D_m}{D_h}\right)^4\right)} \tag{3.19}$$

The cytoplasmic viscosity (μ_c) and the parameter D^* are functions of the hematocrit (H_d), as defined by Equations 3.20 and 3.21, respectively. The diameter of the smallest vessel that a RBC can pass through (D_m) is 2.7 μm and μ_p is the blood plasma viscosity (=0.012Pas) (Huang et al. 2001). The apparent viscosity relationship is based on experimental work carried out in glass tubes of circular cross-section and is assumed to be approximately valid in the current model, as used by Huang et al. (2001). Since the capillary vessels are elliptical the hydraulic diameter is used in the calculation.

$$\mu_c = exp(0.48 + 2.35H_d) \quad \text{cP} \tag{3.20}$$

$$D^* = 2.03 - 2.0H_d \quad \mu\text{m} \tag{3.21}$$

Pries, Secomb, Geβner, Sperandio, Gross & Gaehtgens (1994) developed a hematocrit model via *in vivo* experimental techniques in rat mesentery capillaries. Their studies showed that the resistance to flow in small vessels <40 μm was much higher than previously predicted by experiments carried out in glass tubes. The mechanisms for this were proposed as interactions between the capillary endothelium and blood components. Huang et al. (2001) implemented this model and compared the results obtained with results using the hematocrit model from Kiani & Hudetz (1991) derived from experiments in glass tubes. Huang found a significant decrease in flow (-58.5%) and corresponding increases in RBC (+146.7%) and WBC (+107.5%) transit times. This increases RBC transit times to values much longer than observed *in vivo*. The conclusion reached was that this raises issues with regard to blood-endothelial interactions in the lung as compared to in the systemic circuit. The model of Kiani & Hudetz (1991) was therefore used for the final results of Huang et al. (2001) and is used in the current model.

After evaluating the flow relationships in individual segments, the effect of a junction on flow dynamics must also be considered. Due to the small size of the microvascular network it is difficult to evaluate the resistance at a junction. An approximation to calculate the resistance at a junction was formulated by Huang et al. (2001) and is shown in equation 3.22. This relation assumes that the flow resistance associated with a capillary, including the segment and connecting junctions at either end, is proportional to the total surface area. This total surface area of the capillary is scaled using the segmental resistance calculated in equation 3.17.

$$R = R_{seg} + R_{junc1} + R_{junc2} = \left(1 + \frac{S_{junc1} + S_{junc2}}{S_{seg}}\right) R_{seg} \tag{3.22}$$

A difference in the current model was that the capillary segments overlapped at junctions, therefore a slightly new method to account for this overlap was incorporated into the capillary flow model developed in this study. The capillary diameter protrudes from the nodal point which is the intersection of the multiple segments. Therefore the resistance of a segment is over estimated. Using the same assumption that the resistance of a segment is proportional to the surface area of it a similar relationship as Equation 3.22 can be obtained. For the element in which the resistance is being calculated, the effective surface area is the total surface area (length x perimeter) less the surface area of each overlapping triangular wedge. Considering the intersection of two segments, the overlapping surface area is equal to half of the surface area of half of the elliptical segment, i.e. one quarter of the surface area calculated using the perimeter at the end of the segment and the overlapping length of the segment. The resistance is scaled to obtain the actual resistance for the element R_{seg} using the following equations:

$$R_{seg} = 1 - \left(\frac{SA_{junction}}{SA_{total}}\right) R_{seg} \tag{3.23}$$

$$SA_{junction} = \frac{1}{4} P \sum_{j=1}^{j=n} L_{overlap} \tag{3.24}$$

where SA_{total} is the total surface area of the current element (=Px$length$), $L_{overlap}$ is the overlapping length of each element at the junction, n is the total number of overlapping portions at the junction, and the perimeter P is calculated using Equation 3.14.

So for each neighbouring segment at a junction the branching angle and major elliptical axis are used to calculate the length of the overlapping portion of the segment, and from this the effective surface area and resistance of the segment is calculated.

Analysis of the effect of this scaling was carried out on a regular hexagonal mesh. The difference in resistance and solution values were compared before and after the overlap at junctions was considered. This regular hexagonal mesh consisted of each element connected at an angle of 120^o to each adjacent element. With two segments overlapping, a decrease in resistance of approximately 0.5% was calculated. This resulted in an increase in flow of 1.16%, a decrease in pressure solution of approximately 0.013% and no significant change in the hematocrit values. Segments overlapping with three other segments experienced a 0.79% reduction in resistance

when the overlapping portions were removed. This led to an increase in flow solution of 1.16% and a decrease in pressure of 0.012%; again no significant change in the hematocrit was observed. The removal of overlap when four neighbouring segments overlapped at a junction demonstrated a decrease in resistance of 1.05%. This increased both the flow and hematocrit solutions by approximately 1.38% and 0.08%, respectively, and decreased the pressure solution by 0.009%.

3.2.3 The network flow model

After constructing the flow relationships in a single capillary segment the next step is to consider the flow relations through a network model consisting of n capillary segments and m junctions. The network flow model is developed by applying conservation of mass at each junction, Equation 3.25:

$$\sum_{p=1}^{q(i)} \dot{Q}_{ip} = 0 \qquad \text{i=1,2,...,m} \tag{3.25}$$

where $\dot{Q}_{ip}, p$=1,2,...,$q(i)$ are the flow rates in each segment connected to junction i. The pressure-resistance-flow relationship is applied within each segment, resulting in the following equation:

$$\frac{P_{j1} - P_{j2}}{\dot{Q}_j} = R_j \qquad \text{j=1,2,...,n} \tag{3.26}$$

where P_{j1} and P_{j2} are the pressures at either end of the jth segment. This will involve solution of m nodal unknowns, which are the pressure values, P_i, i=1,2,..,m, and n element unknowns, which are the flow values, Q_j, j=1,2,...,n. This results in n + m unknowns which require n + m equations to solve. Allocation of pressure or flow boundary conditions at each tributary branch reduces the number of variables to provide a solvable system of equations.

3.2.4 Hematocrit distribution

At the microcirculatory level blood must be considered as a two-phase non-Newtonian fluid. The preferential distribution of RBCs at a tubes' central axis means that RBCs tend to travel at a higher velocity than plasma leading to a nonuniform hematocrit (H_d) distribution. The H_d values in a segment influence the apparent viscosity of the blood, which affects the resistance and therefore the pressure and flow within a

capillary. A model adapted by Levin, Dawant & Popel (1986) is implemented with this flow model to calculate hematocrit (or RBC concentration) in each capillary segment. The volumetric flux of RBCs in a vessel segment (the volume of RBCs traversing a cross-section of a vessel per time), f is defined as:

$$f = H_d \dot{Q} \tag{3.27}$$

Where H_d is the discharge hematocrit and $\dot{Q}$ is the volumetric flow rate in a segment. The total blood flow rate and the RBC volumetric flow rate can be balanced at each junction, where index 0 is the parent branch, supplying flow into the junction, and indices 1 and 2 are the two daughter branches. These balances give the following equations:

$$\dot{Q}_0 = \dot{Q}_1 + \dot{Q}_2 \tag{3.28}$$

$$f_0 = f_1 + f_2 \tag{3.29}$$

Therefore, substituting Equation 3.27 into Equation 3.29 provides the following expression:

$$H_{d0}\dot{Q}_0 = H_{d1}\dot{Q}_1 + H_{d2}\dot{Q}_2 \tag{3.30}$$

The flow rates in each segment at a junction are known, assuming a uniform hematocrit for the initial solution. The inlet hematocrit value f_0 must be specified enabling H_{d0} to be calculated. In order to solve for the last two unknowns (f_1 and f_2) an additional relationship between the RBC fluxes and the flows is required. Equations 3.31 and 3.32 are adapted from the experimental studies of Schmid-Schoenbein, Skalak, Usami & Chien (1980) and Klitzman & Johnson (1982):

$$\frac{f_i}{f_0} = \begin{cases} G\left(\frac{\dot{Q}_i}{\dot{Q}_0}\right) & \text{if} \quad G\left(\frac{\dot{Q}_i}{\dot{Q}_0}\right) \leq \frac{\dot{Q}_i}{f_0} \\ \frac{\dot{Q}_i}{f_0} & \text{if} \quad G\left(\frac{\dot{Q}_i}{\dot{Q}_0}\right) > \frac{\dot{Q}_i}{f_0} \end{cases} \tag{3.31}$$

The function G has the following sigmoidal form:

$$G\left(\frac{\dot{Q}_i}{\dot{Q}_0}\right) = \begin{cases} 0 & \text{if} \quad 0 \leq \frac{\dot{Q}_i}{\dot{Q}_0} \leq r \\ \left[1 + \left(\frac{1-\left(\frac{\dot{Q}_i}{\dot{Q}_0}+r\right)}{\frac{\dot{Q}_i}{\dot{Q}_0}-r}\right)^b\right]^{-1} & \text{if} \quad r \leq \frac{\dot{Q}_i}{\dot{Q}_0} \leq 1-r \\ 1 & \text{if} \quad 1-r \leq \frac{\dot{Q}_i}{\dot{Q}_0} \leq 1 \end{cases} \tag{3.32}$$

where i is the daughter vessel index, r, the flux cut-off parameter, has a value of 0.05 (Pries et al. 1990) and b, the preferential flux parameter, has a value of 1.15 (Levin et al. 1986, Klitzman & Johnson 1982) in these simulations. b was included to account for factors, other than flow rate, that affect RBC partitioning at bifurcations, such as the radial position of the RBC (Schmid-Schoenbein et al. 1980). Equation 3.32 was used by Huang et al. (2001) to describe the sigmoidal hematocrit relationship. It differs from the equation printed in the original manuscript [Eqn(27)] due to a typographical error. This error has been corrected in Equation 3.32, and a corrigendum will be published by the authors.

Since the hematocrit in any segment cannot be greater than unity Equation 3.31 was included in the model to modify the results obtained from equation 3.32 to satisfy this criteria. It follows then that the vessel hematocrit H_d for vessel i is calculated using:

$$H_d = \frac{f_i}{\dot{Q}_i} \tag{3.33}$$

These equations enable calculation of H_d for all daughter vessels providing the other parameters are known. The above equations are also applicable to converging bifurcations given that the inflow data, $\dot{Q}_1$, $\dot{Q}_2$, f_1, f_2, H_{d1} and H_{d2} are all known. The network hematocrit model therefore initiates at the inlet capillary vessels and proceeds through the network, thereby ensuring that the upstream blood and RBC volumetric flow rates at a junction are always known.

The parameter b may vary at different bifurcations and with vessel diameter, but experimental data is limited in this area. Therefore in the current model the values of b=1.15 and r=0.05 from Levin et al. (1986) and Huang et al. (2001), respectively, are assumed to be constant throughout the network. Investigation into the effect of the dispersion of parameter b on the mean capillary discharge hematocrit showed that the variation in hematocrit was very small (Levin et al. 1986). The effect of a normal distribution of b with a mean of 1.5, and a coefficient of variation of 0-0.3 was investigated and found to only increase the normalised hematocrit from 0.69 to 0.71. The effect of variation of the flux cut-off parameter, r, was also investigated by Levin et

al. (1986). The mean capillary discharge was found to be more sensitive to variations in r, with a variation in r from 0 to 0.15 decreasing the normalised hematocrit from 0.87 to 0.59.

3.2.5 Cell transit time models

RBC and WBC transit times are calculated within each segment and for entire pathways from arteriole to venule. Due to the vast number of possible pathways through the capillary network only 50,000 randomly selected pathways from arteriole to venule are selected for analysis of the transit time distributions.

Once the converged flow solution is reached the RBC transit time through each individual segment can be calculated, using Equation 3.34. The WBC transit time is calculated on-the-fly as we proceed through a pathway, described in this section. The total number of desired pathways to be sampled is first split between the number of inlet vessels, in proportion to the fraction of total blood flow going through each. Cell transit times are then summed along a flow pathway from arteriole to venule. Depth first analysis is carried out (Strang 1986) whereby an entire pathway from arteriole to venule is sought before moving onto the next one. The algorithm begins at the inlet node and the next node is selected randomly from all possible nodes in the forwards flow path (the pressure must decrease from node 1 to node 2 for flow to exist). The pathway terminates when an outlet vessel is reached. Both the RBC and WBC average transit times are weighted according to the amount of blood flowing through each pathway, to more accurately reflect the transit of blood cells.

3.2.5.1 RBC transit time

RBC transit time (t_i), through a vessel i of volume V_i, is calculated using Equation 3.34 (Huang et al. 2001):

$$t_i = \frac{V_i}{\dot{Q}_i C_{tt}} \tag{3.34}$$

where $\dot{Q}_i$ is the flow rate in the vessel, and C_{tt} the ratio of plasma transit time to RBC transit time has a value of 1.4 as derived via experimental studies by Presson, Graham, Hanger, Godbey, Gebb, Sidner, Glenny & Wiltz (1995). As the transit time model randomly proceeds along pathway j from arteriole to venule, each segmental transit time in that path $t_{i,j}$ is summed, from segment i to the total number of segments in the pathway n, to yield the total transit time for that pathway t_j:

$$t_j = \sum_{i=1}^{n} t_{i,j} \tag{3.35}$$

The fraction of blood flowing through each pathway ($\dot{Q}_j$) is calculated as a pathway progresses from arteriole to venule using the product of the fraction of blood flowing through each vessel in the pathway, using Equation 3.36:

$$\dot{Q}_j = \prod_{i=1}^{n} \frac{\dot{Q}_i}{\dot{Q}_{in}} \tag{3.36}$$

where $\dot{Q}_{in}$ is the total amount of blood flowing into segment i. This flow fraction can be used to investigate the distribution of RBC transit times through the network. The total length and number of segments in each pathway was also calculated for comparison with anatomical data, shown in Table 2.2.

3.2.5.2 WBC transit time

A WBC transit model, derived empirically from leukocyte aspiration studies into micropipettes (Fenton et al. 1985, Yeung & Evans 1989), is incorporated into the model. WBC transit is more complex than that of RBCs due to the slower deformation of cell cytoplasm. WBC transit time depends on the aspect ratio of the cell to vessel diameter, and the resistance of the cell to deformation. The entrance diameter of WBCs varies depending on the diameters of capillaries it has previously "squeezed" through. A WBC will only be able to pass through a segment if the pressure drop across that segment exceeds a critical pressure P_{cr}, calculated as:

$$P_{cr} = 2\frac{\tau_0}{R_{WBC}}\left(\frac{R_{WBC}}{R_p} - 1\right) \tag{3.37}$$

where τ_0=3.5x10^{-5} N m^{-1} is the average tension in the cell cortex, R_{WBC} and R_p are the radii of the cell (before deformation) and the tube, respectively (Huang et al. 2001). The WBC transit time is calculated in two parts: the entrance time t_e and the passage time t_p:

$$t_{WBC} = t_e + t_p \tag{3.38}$$

t_e is the time taken for a neutrophil to enter a capillary segment, calculated using Equation 3.40. t_p is the time taken for a neutrophil to pass through a segment, calculated using Equation 3.47. If the vessel diameter if less than the cell diameter then the time

taken for the cell to deform to enter the cell is usually significantly larger than the time taken for it to pass through once deformed. A WBC is considered 'stopped' if its entrance time into a capillary is greater than 1 second. Neutrophils are assumed to be spherical, and the vessel radius (R) is approximated using Equation 3.39:

$$R = \frac{\sqrt{a^* b^*} + b^*}{2} \tag{3.39}$$

The vessel radius value was selected to be the average between two different approximations: using the height of the capillary h (=b^*) as the radius, and using the effective circular radius (conserving cross-sectional area) of the elliptical vessel (=$\sqrt{(a^* b^*)}$). These two different radius values represent the minimum and maximum radius of the vessel, respectively, therefore the average value was used in WBC transit time calculations. Yeung & Evans (1989) developed a model relating neutrophil aspiration time to pressure and the ratio of the cell radius to vessel radius. This theory was developed from micropipette aspiration studies where the cell was modelled as a uniform liquid core encapsulated by a distinct cortical shell. Huang et al. (2001) combined relationships from Yeung & Evans (1989) and Fenton et al. (1985). While both studies agree that the aspiration time of a WBC depends on the ratio of cell to vessel ratio, Fenton et al. (1985) concluded that entrance time was not dependent on aspiration pressures. A pressure-dependent entrance time model related to R_0^* (defined in Equation 3.42) was developed by Huang et al. (2001) and is used in the current study, Equation 3.40:

$$t_e = \left\{ \begin{array}{ll} \frac{\mu}{\Delta P - P_{cr}} t_e^* & \text{if } R_0^* < 1.2 \\ \\ 0.107 \frac{m\mu}{\Delta P - 33} 10^{3.68(R_0^* - 1.2)} & \text{if } R_0^* \geq 1.2 \end{array} \right\} \tag{3.40}$$

where t_e^* is defined as:

$$\begin{aligned} t_e^* = & m \left[\frac{1}{3} + \frac{2}{3} R_0^{*3} - R_0^{*2} + \frac{2}{3} (R_0^{*2} - 1)^{3/2} + (R_0^{*2} - 1)^{1/2} - R_0^{*2} sin \left[arccos \left(\frac{1}{R_0^*} \right) \right] \right. \\ & \left. + ln \left[\frac{R_0^* sin\big(arccos\big(\frac{1}{R_0^*}\big)\big) + R_0^*}{R_0^* + (R_0^{*2} - 1)^{1/2}} \right] \right] \end{aligned} \tag{3.41}$$

where m, a coefficient in the linearised model of neutrophil deformation, is equal to 6, and R_0^* is defined as follows (Huang et al. 2001):

$$R^* = R_0^* = \frac{R_{WBC}}{R} \quad \text{at } t^* = 0 \tag{3.42}$$

$$R^* = 1 \quad \text{at } t^* = t_e^* \tag{3.43}$$

where R^*=r_c/R and r_c is the instantaneous radius of a portion of the cell lying outside the vessel. Given a capillary with radius R_1 at the entrance and radius R_2 at the exit, assuming that the radius varies linearly along the segment the following expression can be written:

$$R(x) = R_1 + \frac{R_2 - R_1}{l}x \tag{3.44}$$

where l is the capillary length and x is the position along the vessel. The following equation is from Fenton et al. (1985) and describes the ratio of neutrophil velocity u_{WBC} to bulk blood velocity u_{blood}:

$$\frac{dx}{dt} = \frac{\dot{Q}}{\pi R^2(x)}\left[\frac{2}{1 + \left(\frac{R_{WBC(in)}}{R(x)}\right)^{2.42}}\right] \quad t(x=0) = 0, \quad t(x=l) = t_p \tag{3.45}$$

where $R_{WBC(in)}$ is the radius of the neutrophil inside the capillary segment:

$$R_{WBC(in)} = R_{WBC} \quad \text{if} \quad R_{WBC} \leq R_1$$

$$R_{WBC(in)} = R_1 \quad \text{if} \quad R_{WBC} > R_1 \tag{3.46}$$

In the current capillary model each segmental radius is assumed to remain constant over the length of the capillary, therefore $R_1 = R_2 = R(x)$. Combining Equations 3.44 and 3.45, and integrating over the length of the segment the WBC passage time t_p can be determined using Equation 3.47 which is valid if R_1=R_2:

$$t_p = \frac{\pi l R_1^2}{2\dot{Q}}\left[1 + \left(\frac{R_{WBC(in)}}{R_1}\right)^{2.42}\right] \tag{3.47}$$

Equation 3.47 differs from the equation published by Huang et al. (2001) [Eqn(47)] due to a typographical error in their paper. A corrigendum will be published by the authors correcting this error. This model assumes that when a cell is deformed the time taken for the cell to return to its initial shape is sufficiently long such that when a neutrophil passes through a capillary segment with a radius smaller than that of

the cell, the neutrophil will retain the smaller radius value for the remainder of the pathway. The WBC transit time model calculates the total time for a neutrophil to pass through a given pathway from arteriole to venule. The model also records the number of times the neutrophil will become 'stopped' (that is when $t_e > 1\,\mathrm{s}$), and the percentage of pathways in which a WBC will become stopped. This model can be easily adapted to incorporate vessels with variable radii, refer to Huang et al. (2001) for details.

3.2.6 Parameters used in the model

Table 3.1 displays the parameters used in the model for the simulations published in this thesis. The parameter values are listed and the source from which they were obtained are listed in the final column. The blood pressure conditions in this table apply to a mid height in a vertical human lung (15 cm), blood pressures used in height simulations are shown in Table 3.3.

Parameter	Value	Source
a_0	6 μm	(Huang et al. 2001)
b	1.15	(Levin et al. 1986)
H_d (at inlet)	0.4	(Huang et al. 2001)
k_c	15 (normal range 15-30) $\mathrm{cm\ H_2O}$	(Huang et al. 2001)
$P_{arteriole}$	20 $\mathrm{cm\ H_2O}$	(Huang et al. 2001)
P_{venule}	12 $\mathrm{cm\ H_2O}$	(Huang et al. 2001)
$P_{alveolar}$	0 $\mathrm{cm\ H_2O}$	(Guyton & Hall 2000)
$P_{pleural}$	-4.25 $\mathrm{cm\ H_2O}$	(Guyton & Hall 2000)
r	0.05	(Levin et al. 1986)
μ_c	135 Pas	(Needham & Hochmuth 1990)
μ_p	0.012 Pas	(Fung 1990)
τ_0	3.5x10-5 $\mathrm{N\ m^{-1}}$	(Huang et al. 2001)

TABLE 3.1: *Parameters used in the capillary model, the source of which is included in the final column.*

3.2.7 Normal simulation conditions

Unless otherwise stated, all results are obtained using boundary conditions and pressure settings at a height of 14 cm in a vertical human lung. Therefore the inlet blood pressure is set to 20 $\mathrm{cm\ H_2O}$, outlet blood pressure to 12 $\mathrm{cm\ H_2O}$, pleural pressure is equal to -4.25 $\mathrm{cm\ H_2O}$, and alveolar pressure is 0 $\mathrm{cm\ H_2O}$, and an initial hematocrit value of 0.4. Other material parameters are set as specified in Table 3.1.

3.2.8 Cell transit time distributions in the upright lung

Regional results of cell transit time distributions were studied for the upper (lung height, 28 cm), middle (14 cm), and lower (2 cm) regions of a vertical human lung by setting appropriate pressure boundary conditions for these 3 different 'zones', as defined in Table 3.2. The alveolar pressure remained constant at atmospheric pressure (0 $\mathrm{cm}H_2O$) in the simulations.

Pressure Boundary Conditions ($\mathrm{cm}H_2O$)			
Upper lung (28 cm)	$P_{pleural} = -7.75$	$P_{arteriole} = 6$	$P_{venule} = 0$
Mid lung (14 cm)	$P_{pleural} = -4.25$	$P_{arteriole} = 20$	$P_{venule} = 12$
Lower lung (2 cm)	$P_{pleural} = -1.25$	$P_{arteriole} = 32$	$P_{venule} = 24$

TABLE 3.2: *Pressure boundary conditions used in regional variation simulations, $P_{alveolar}$=0 $\mathrm{cm}H_2O$ as at functional residual capacity (FRC). Note: 1 $\mathrm{cm}H_2O$=0.09806*kPa.

3.2.9 Variation in blood pressure in the upright lung

The capillary model is used to investigate the effect of regional variations in pressure on microcirculatory blood flow in the lung. Published data of intrapleural pressure suggests an increase down the lung of about 0.25 $\mathrm{cm}H_2O$ per cm of lung height, and an increase in blood pressure of 1 $\mathrm{cm}H_2O$ per cm of lung height (West 1995), while alveolar pressure is 0 $\mathrm{cm}H_2O$ throughout the lung when there is no flow (for example, at FRC). A linear pressure gradient is assumed down the lung height for both the pleural and blood pressures. In the upper regions of the lung the venous pressure drops below alveolar pressure, known as the zone 2 region (as discussed in Section 1.3.2). In this region the flow is governed by the pressure difference between the arteriole and alveolar pressures (West 1995), and therefore the venule pressure is set equal to alveolar pressure.

These idealised pressure gradients were used to prescribe pressure boundary conditions for simulations at 2cm intervals over the height of a 30cm vertical lung. A table of the pressure boundary conditions applied at the pleural surface, arterial and venous tributaries at each 2cm interval is shown in Table 3.3.

Pressure Boundary Conditions ($\mathrm{cm}H_2O$)			
Height (cm)	$P_{pleural}$ **(**$\mathrm{cm}H_2O$**)**	$P_{arteriole}$ **(**$\mathrm{cm}H_2O$**)**	P_{venule} **(**$\mathrm{cm}H_2O$**)**
30	-8.25	4	0
28	-7.75	6	0
26	-7.25	8	0
24	-6.75	10	2
22	-6.25	12	4
20	-5.75	14	6
18	-5.25	16	8
16	-4.75	18	10
14	-4.25	20	12
12	-3.75	22	14
10	-3.25	24	16
8	-2.75	26	18
6	-2.25	28	20
4	-1.75	30	22
2	-1.25	32	24
0	-0.75	34	26

TABLE 3.3: *Pressure boundary conditions applied in simulations of flow at 2* cm *height intervals over the vertical height of a 30* cm *lung.*

3.3 Results

3.3.1 Blood flow results

Figure 3.2 shows the flow rate solution on the full alveolar sac capillary model using two different spectrums to illustrate the solution. Cylinders are drawn around each of the one-dimensional elements using the diameter solution field. Figures 3.2(b) and (d) show the spectrums used to illustrate the flow rate values ($\mathrm{mm}^3\ \mathrm{s}^{-1}$) for Figures 3.2(a) and (c), respectively. The flow rates span a large range, therefore Figure 3.2 (c) uses a narrower solution spectrum range to illustrate more detail in the flow solution. The highest flow rates are seen at the inlet and outlet vessel locations where the flow must converge to enter and exit the network. These vessels also have larger diameters and therefore a lower resistance to flow. The highest flow rate in the feed vessels is about 0.0027 $\mathrm{mm}^3\ \mathrm{s}^{-1}$; the spectrums extend above to this value. There are several unperfused segments where the pressure drop across the vessel is insufficient to exceed the resistance to flow. Preferential pathways can be seen in various locations, especially at the septal boundaries where adjacent capillary networks converge. Areas of low flow can also be seen, especially in regions furthest from inlet and outlet vessels. This

illustrates the large reserve capacity available for high flow conditions.

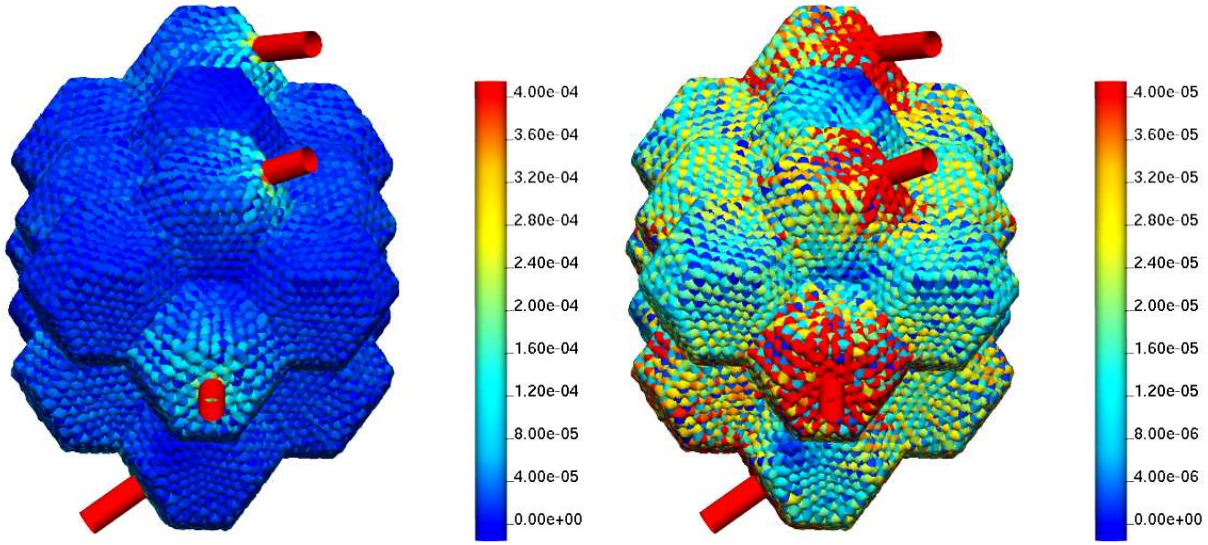

FIGURE 3.2: *Flow solution in the alveolar sac model at a vertical human lung height of 14* cm*, two different spectrums are used to illustrate the range of flow values. Spectrums shown in (b) and (d) have flow units* $\mathrm{mm}^3\ \mathrm{s}^{-1}$*. Highest flow rates are in the venule vessels which drain the converged capillary flow at the periphery of the alveolar sac model.*

Figure 3.3(a)-(c) illustrates the pressure solution (Pa) at each nodal location in the alveolar-capillary network, from two different view points, (b) and (c). The spectrum used to represent the pressure values is shown in Figure 3.3(c). A relatively uniform decreasing pressure gradient from inlet to outlet is displayed.

The RBC distribution (hematocrit) results obtained in the capillary network are presented in Figure 3.3(d)-(e). The hematocrit values are found to range from 0 to 0.78. The inlet and initial hematocrit value was set to 0.4. The large range of hematocrit values is due to the uneven partition of RBCs at bifurcations, where RBCs travel in proportion to flow fractions. Several vessels can be seen to have a 0 hematocrit fraction (that is, contain no RBCs), this is due either to plasma skimming, where a vessel contains only plasma, or to the segment being completely unperfused.

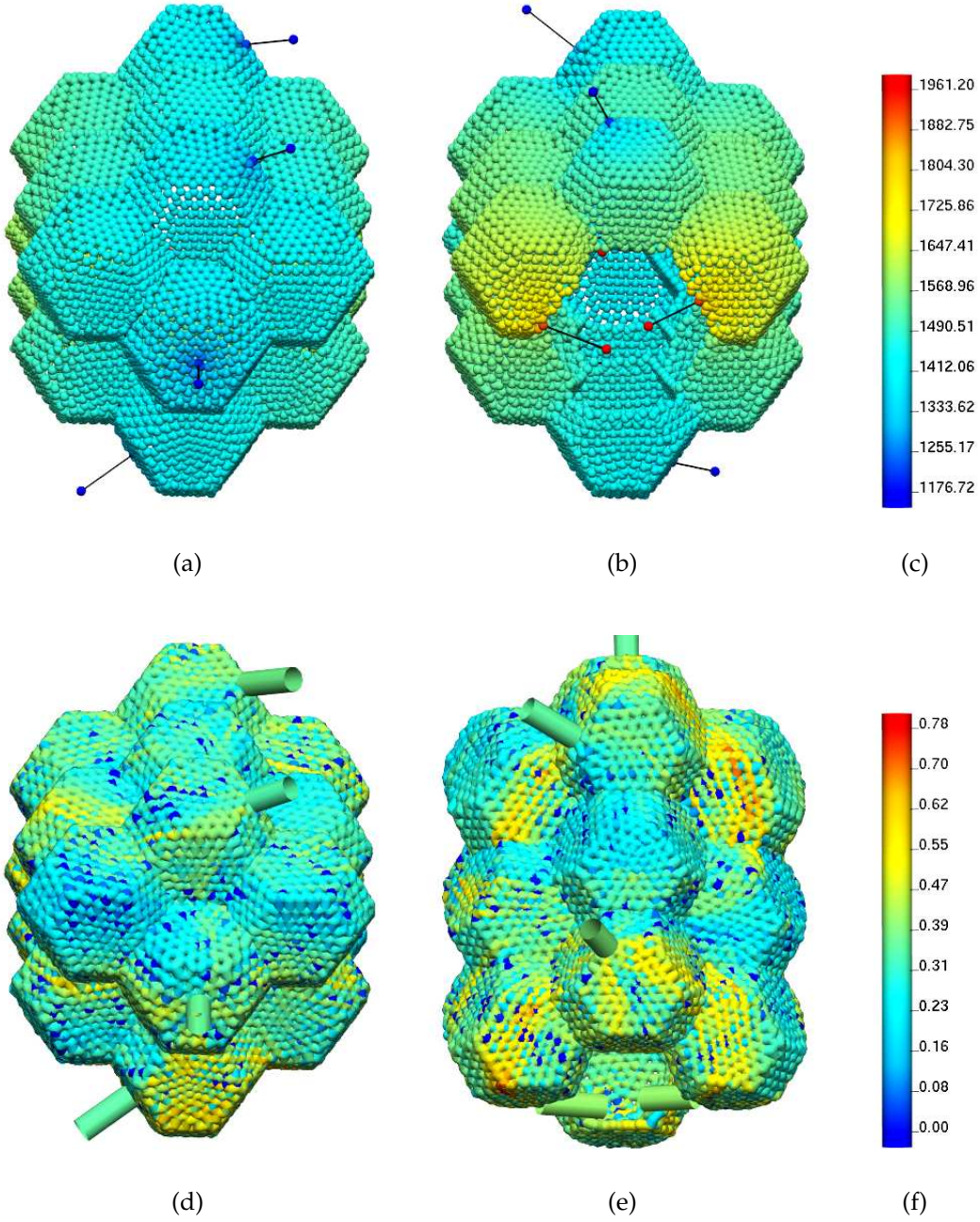

FIGURE 3.3: *Pressure and hematocrit solutions displayed in the alveolar sac model at a vertical human lung height of 14* cm *from two different view points. (a), (b) display the pressure solution ranging from 1176* Pa *(12* cm H_2O*) to 1961* Pa *(20* cm H_2O*), (c) solution spectrum in pressure units of* Pa*. (d), (e) illustrate the hematocrit solution within each capillary vessel ranging from 0 to 0.78, (c) solution spectrum (dimensionless).*

Figure 3.4 displays flow (Q), hydraulic diameter (D_h), and hematocrit (H_d) distributions with respect to the percentage of capillary segments with each value. Bin intervals of $1\text{x}10^{-7}$, $5\text{x}10^{-6}$, and 0.01 are used for each plot, respectively. Figure 3.4(a) displays flow values dominating the left side of the plot, illustrating that only very few vessels have flow rates greater than $1\text{x}10^{-4}\ \text{mm}^3\ \text{s}^{-1}$. Figure 3.4(b) demonstrates a relatively uniform distribution of diameters ranging between 6.75 μm and 9.75 μm. The hematocrit plot shows a normal distribution, with a mean of around 0.35, apart from an addition peak at a hematocrit value of 0 where about 2.75% of segments contain no RBCs.

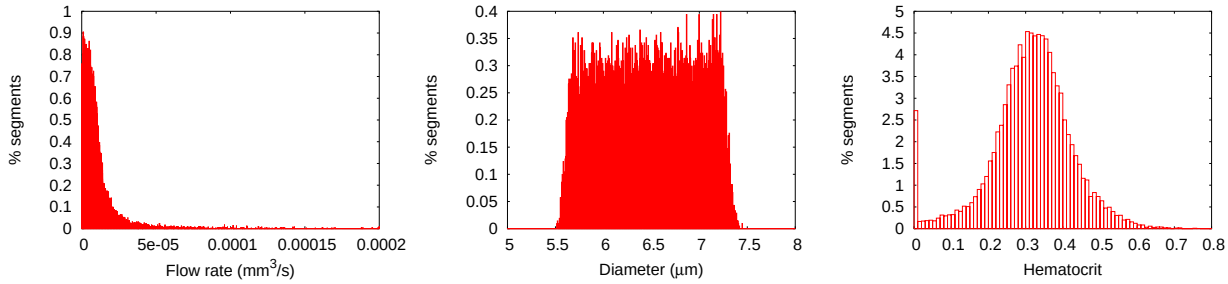

(a) (b) (c)

FIGURE 3.4: *(a) Flow, (b) diameter, and (c) hematocrit distributions throughout the alveolar-capillary network.*

3.3.2 Analysis of the flow model

This section looks at the various components of the flow model and their effect on the flow solution. After the initial linear pressure-flow solution is determined the solution procedure calculates the resultant capillary dimensions and RBC distribution as a function of the pressure-flow solution.

3.3.2.1 Dimensional model

The alveolar pressure-volume relationship used in the dimensional model was derived from experimental studies on rat lung tissue during inspiration and expiration. The hysteresis relationship results in different parameter values during inflation and deflation. Figure 3.5(a) plots the calculated alveolar volume versus Ptp, for the relationship in Equation 3.1. The range of Ptp in the current study on regional

variations (refer Section 3.3.8) is from 0.75 $\mathrm{cm\ H_2O}$ in the lowest regions of the lung, to 8.25 $\mathrm{cm\ H_2O}$ at the top of the lung. This relationship demonstrates that a limiting alveolar volume of about $250\text{x}10^3\ \mu\mathrm{m}^3$ is reached as Ptp increases. An initial volume value (V_0) of $20.7\text{x}10^3\ \mu\mathrm{m}^3$ was used based on rat data from the study of Mercer et al. (1987) with which the empirical relationship is derived. Figure 3.5(b) illustrates the relationship between E, the elastic coefficient of the alveolar septal wall, and Ptp, as defined by Equation 3.5, during inspiration and expiration. A rapid increase in E is displayed at low Ptp during inspiration. In all other regions E varies within a narrow range of about 0.3 to 1.3 $\mathrm{cm\ H_2O\ mm}$. All simulations conducted at zero alveolar pressure fall on the expiration curve.

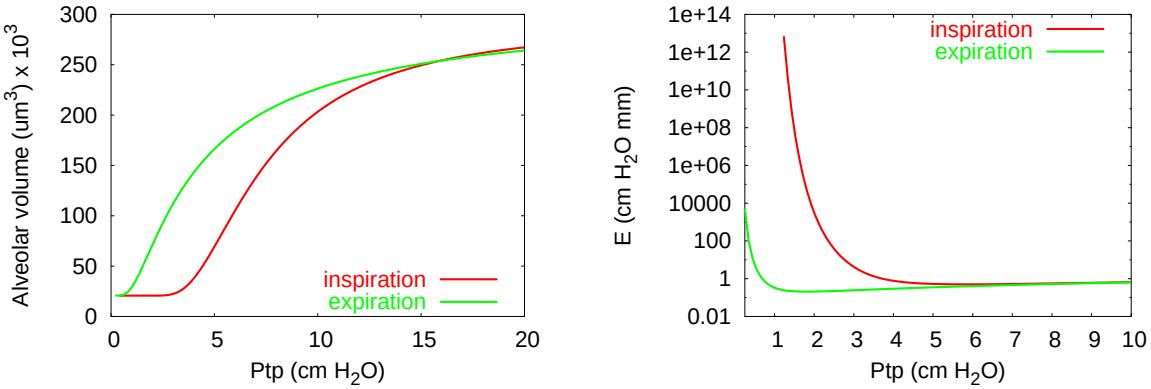

FIGURE 3.5: *Plot of (a) alveolar volume and (b) septal wall elasticity coefficient E versus Ptp during inspiration and expiration, determined using alveolar dimensional model, Equation 3.1.*

3.3.2.2 Vessel ellipticity

The capillary cross-sections were assumed to be elliptical, prescribed by a major (a^*) and minor (b^*) axis. These elliptical parameters are used in the polynomial approximation for the calculation of $Re_{D_h} f_d$, the Reynolds number times the friction factor, as defined by Equation 3.18. This term depends on the aspect ratio of the elliptical vessels, being 63.95 when the vessel cross-section is cylindrical. The variation in vessel shapes in the model geometry leads to only a very small change in resistance of less than $\pm$ 2%.

3.3.2.3 Viscosity model

The μ_{app} of blood at the capillary level is a function of the vessel diameter, as described in Equation 3.19. The effect of this relationship on the resistance term (R_{seg}), as calculated by Equation 3.17, was investigated by comparing the use of this non-linear viscosity model with a simpler uniform viscosity assumption. Figure 3.6 demonstrates the relationship between (a) μ_{app} and (b) resistance versus hydraulic diameter (D_h). Two solutions are shown: one assuming a uniform viscosity value for all diameters and the second using the non-linear viscosity model implemented in the solution procedure. These plots illustrate that as vessel diameter decreases, towards the minimum diameter vessel which will accommodate the passage of a RBC (D_m=2.7 μm), μ_{app} and therefore the resistance to flow increases rapidly. This will result in smaller vessels being much less likely to receive any blood flow, and thus leads to unperfused segments. Parameter values used in Figure 3.6 are H_d=0.4, $Re_{D_h} f_d$=64, $length$=12 μm, and other values as in Table 3.1.

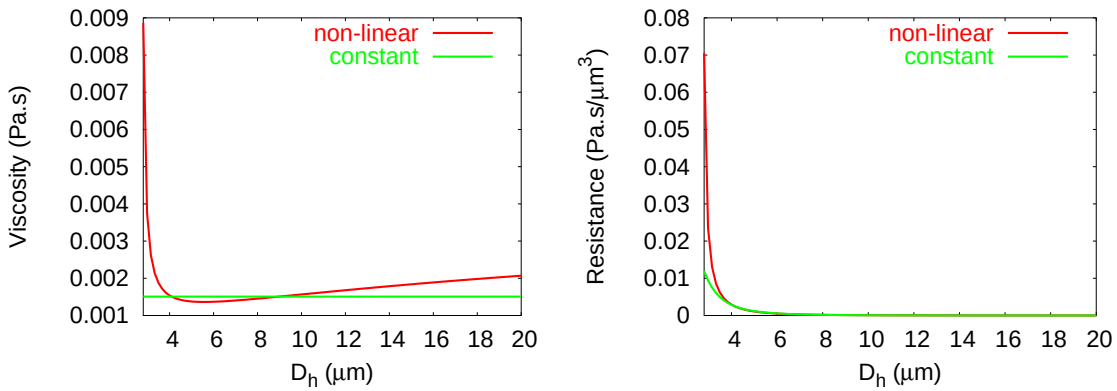

FIGURE 3.6: *Comparison of constant versus non-linear viscosity models: μ_{app} and resistance (R_{seg}) versus hydraulic diameter (D_h).*

3.3.2.4 Hematocrit model

Figure 3.7 illustrates the sigmoidal function G specifying the relationship between RBC fluxes and blood flow rates Q_i/Q_0 at a bifurcation point as defined by Equation 3.32, for (a) different values of the flux cut-off parameter r, while maintaining the preferential flux parameter b at 1.15, and (b) variations in b while holding r constant

at 0.05. When b=1 and r=0 the hematocrit in each branch at a bifurcation will be equal. When b increases above unity the proportion of RBCS going into the higher flow segment increases disproportionately. As b approaches infinity all RBCs flowing into a junction should flow into the segment with higher flow (Levin et al. 1986), however the hematocrit in any branch may not exceed 1. This restriction is incorporated via Equation 3.31.

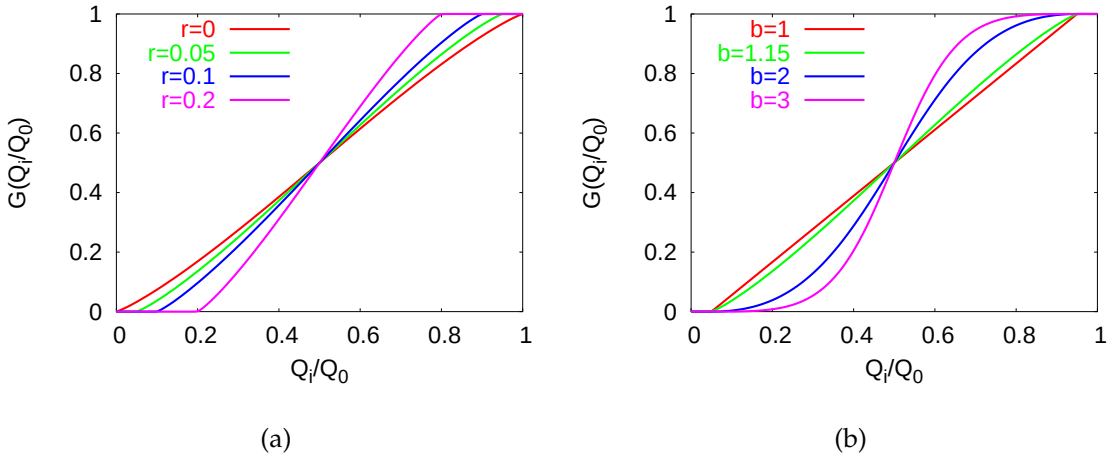

(a) (b)

FIGURE 3.7: *Relationship between RBC fluxes and flow rates Q_i/Q_0 at a bifurcation as defined by the sigmoidal function G, investigating changes in (a) the flux cut-off parameter r and (b) the preferential flux parameter b.*

Comparisons were made between solutions in the capillary model with and without the hematocrit model, by assuming a uniform hematocrit throughout the network. Figure 3.8 illustrates the different red and white blood cell transit time distributions obtained in the two simulations. These plots both show longer cell transit times when the hematocrit model is not used. The distribution of RBC transit times are more spread out with the RBC standard deviation increasing from 2.6 to 17.5 s. The WBC transit time standard deviation remained fairly constant, decreasing a small amount from 48.3 to 44.0 s. Summary results are displayed in Table 3.4. The overall average RBC transit time increased from 0.62 s to 0.70 s (-12.9%) when the hematocrit model was excluded. The hematocrit model accounts for the Fahraeus effect which results in an increased velocity of RBCs relative to plasma and therefore reduces the transit time of RBCs through the capillaries, therefore this increase in transit time when the hematocrit model is removed is as expected. The overall average WBC transit time actually decreased from 1.57 s to 1.46 s (7.0%). The passage time increased from 0.56 s to 0.64 s, but the entrance time decreased from 1.0 s to 0.82 s, due to the small increase (-0.1%) in average diameter of

the vessels when the hematocrit model is excluded.

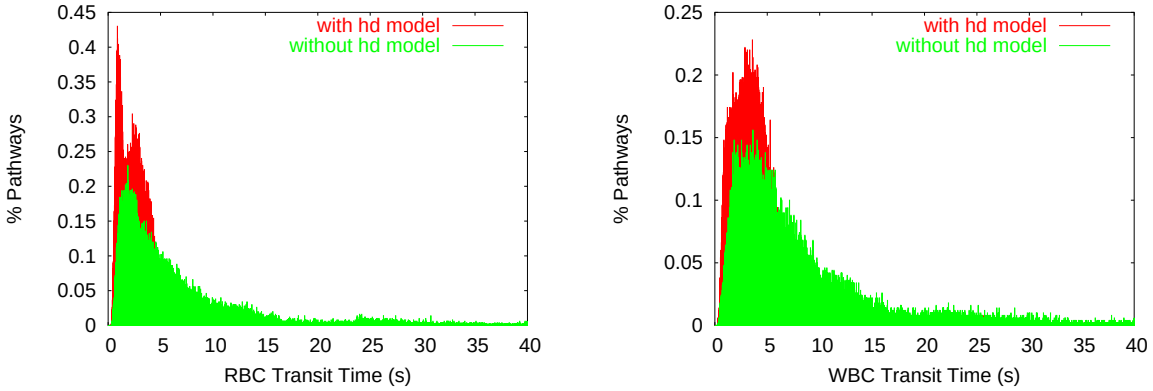

(a) (b)

FIGURE 3.8: *Cell transit time results with respect to the percentage of pathways with and without hematocrit model: (a) RBC transit times; (b) WBC transit times.*

Parameter	With Hd model	Without Hd model	% difference
D_h (μm)	8.45	8.46	-0.1
t_{RBC} (s)	0.62	0.70	-12.9
t_{WBC} (s)	1.57	1.46	+7.0
t_e (s)	1.00	0.82	18.7
t_p (s)	0.56	0.64	-13.9
$\dot{Q}$ ($\mathrm{mm}^3\ \mathrm{s}^{-1}$)	0.64	0.62	1.8

TABLE 3.4: *Comparison of model results with and without hematocrit model.*

Simulations were also carried out setting different initial hematocrit values of 0.2 and 0.6 as compared to the standard value of 0.4. The red and white cell transit time distributions with respect to the percentage of pathways are shown in Figures 3.9(a) and (b), respectively. As H_d increased from 0.2 to 0.4 to 0.6 the average RBC transit time increased from 0.55 s to 0.62 s to 0.97 s. This was a consequence of the decreasing flow rate which receded from 0.72 to 0.64 to 0.52 $\mathrm{mm}^3\ \mathrm{s}^{-1}$ as the hematocrit increased. This is a direct result of the increasing viscosity of blood as the concentration of RBCs increases, which consequently increases the resistance to flow.

The effect of a variation in the initial hematocrit by $\pm$ 10% is also shown in Table 3.7 (Section 3.3.6).

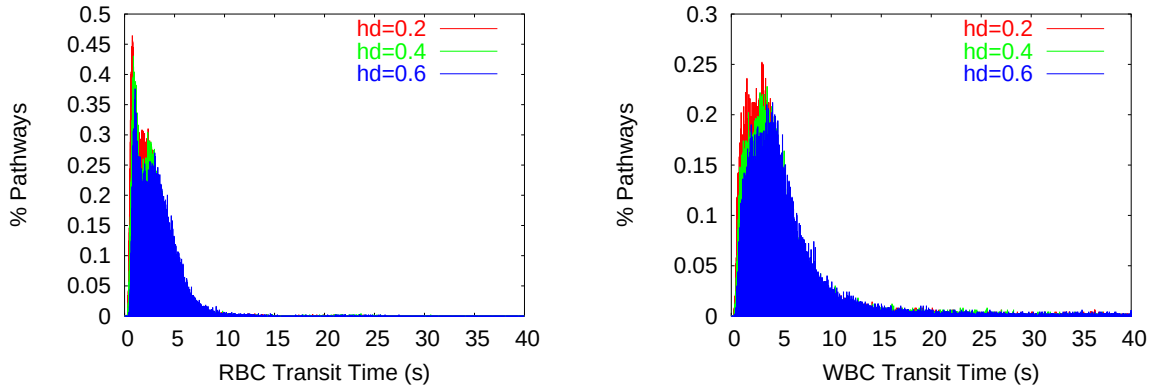

(a) (b)

FIGURE 3.9: *Cell transit time results with respect to the percentage of pathways with different initial hematocrit values, 0.2, 0.4, 0.6: (a) RBC transit times; (b) WBC transit times.*

3.3.3 Corner vessels

At the intersection of three adjacent alveolar septae excess fibres exert a strong outward pull resulting in a negative tissue pressure in this region. This effect allows alveolar corner vessels to remain patent in all conditions (Lamm et al. 1991, Weibel 1984), and also results in vessels with larger diameters than septal capillaries. A more detailed description is given in Section 1.2.4. Model simulations were carried out incorporating the geometric differences of corner vessels in order to investigate the effect of these vessels on overall results. Huang et al. (2001) incorporated the effects of alveolar corner vessels into their flow model. Due to lack of anatomical data on the dimensions and behaviour of corner vessels they assumed that corner vessels were of circular cross-section, and that each corner vessel conveyed an amount of blood flow equal to the average flow rate in the septal capillaries (Q_{mean}) multiplied by the number of adjoining septae. There are typically three septae sharing each corner vessel, therefore the following equation is developed to represent flow in a corner vessel, Q_{cv}:

$$Q_{cv} = 3Q_{mean} \quad or \quad R_{cv} = \frac{1}{3}R_{mean} \tag{3.48}$$

where R_{cv} is the resistance in the corner vessel per unit length of the vessel, and R_{mean} is the average resistance per unit length of septal capillaries. Assuming a circular cross-section, the resistance in a tube is proportional to D^4, therefore the diameter of a corner vessel D_{cv} was determined as:

$$D_{cv} = 1.32 D_{mean} \tag{3.49}$$

Huang's assumptions were implemented in the current model for analysis. Inclusion of the corner vessel anatomical structure resulted in an overall increase in average flow (over the height of the lung) of 5.57%, and an increase in average RBC transit time of 12.35%. Results were qualitatively similar with and without corner vessel effects.

The physiological effects of corner vessels result from micromechanical interactions of the septal corners. There is currently not sufficient information to accurately incorporate corner vessels into the current geometric flow model. Therefore the results in this study relate to the model without including the effects of corner vessel behaviour. Future coupling with models of micromechanics could more accurately include the effects of corner vessels in the blood flow simulations.

Solution results in the current study demonstrated a natural occurrence of increased flow at the septal boundaries due purely to the geometry of the capillary network and the resulting convergence of vessels and therefore flow at these locations. More simplified models not considering the merging of capillary vessels at all alveolar septal boundaries would not automatically take this into account.

3.3.4 Breathing cycle

The capillary cross-sectional area is a function of Ptp (=alveolar-pleural pressure) and Ptm (=blood-alveolar pressure). Alveolar pressure oscillates between around -1 and +1 $\mathrm{cm\ H_2O}$ from inspiration to expiration, respectively. Similarly pleural pressure follows an oscillatory pattern during the breathing cycle with the pleural pressure fluctuating between approximately -7.5 and -5 $\mathrm{cm\ H_2O}$ from inspiration to expiration (Guyton & Hall 2000). Model simulations were carried out using the pressure conditions defined in Table 3.6 specifying both alveolar and pleural pressure to mimic the *in vivo* respiratory patterns. The effect on capillary flow properties including RBC and WBC transit times, hematocrit distributions, WBC stoppage, and capillary diameters was investigated.

Figure 3.10 illustrates the effect of alveolar and pleural pressures on (a) RBC transit, (b) flow, and (c) H_d distributions with respect to the percentage of pathways. Table 3.6 displays average model values at rest, during inspiration and expiration. WBC transit time and stoppage results can be seen in Figure 3.11. These results show that the model was not very sensitive to variations in pleural and alveolar pressures. This indicates

	$P_{alveolar}$ (cm H_2O)	$P_{pleural}$ (cm H_2O)
Rest	0	-4.25
Inspiration	-1	-7.5
Expiration	+1	-4

TABLE 3.5: *Alveolar and pleural pressure conditions at different stages of breathing, for comparisons of WBC stoppage at different stages of respiration.*

that further development of the dimensional model may be required to more accurately represent flow during the breathing cycle. The current model does not incorporate the axial deformation (change in length) of the vessels, which may also have a significant effect on flow during the breathing cycle. In reality, during inspiration the alveoli expand and compress the capillary vessels which would result in lower flows.

Parameter	**Rest**	**Inspiration**	**Expiration**
D_h (μm)	8.45	8.56	8.26
t_{RBC} (s)	0.62	0.63	0.50
t_{WBC} (s)	1.57	1.38	1.33
t_e (s)	1.00	0.79	0.89
t_p (s)	0.56	0.58	0.45
$\dot{Q}$ (mm^3 s^{-1})	0.64	0.65	0.60

TABLE 3.6: *Average model results at different stages of the respiratory cycle (rest, inspiration, and expiration).*

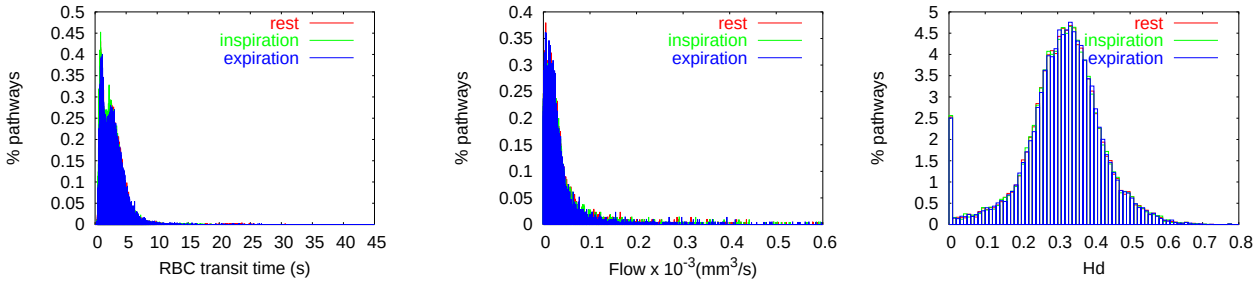

(a) (b) (c)

FIGURE 3.10: *Model results at different stages of breathing (rest, inspiration, expiration): (a) RBC transit time distribution, (b) flow distribution, (c) H_d distribution with respect to % pathways.*

3.3.5 Neutrophil traversing

The neutrophil transit time model calculates the entrance time t_e and the passage time t_p of a WBC travelling through the capillary network, as explained in Section 3.2.5.2. If t_e is greater than 1 s the WBC is considered 'stopped'. The normal results show that from the 50,000 pathways sampled 62.5% of pathways would not stop a WBC, 29.3% of pathways would stop a WBC once, 7.1% twice, and 1.1% of pathways would stop a WBC three times or more. These results compare well with *in vivo* observations in dogs made by Hanger et al. (1993) which demonstrated that about 46% of neutrophils proceeded from arteriole to venule unimpeded, around 24% were stopped once, and about 30% were stopped twice. The model of Huang et al. (2001) predicted that 46% of neutrophils would not stop, 51% would stop once and 3% would stop twice or more (when Ptp=5 $\mathrm{cm\ H_2O}$ and Ptm=10 $\mathrm{cm\ H_2O}$ in the arteriole).

The incidence of WBC stoppage at different stages of respiration was investigated by setting the appropriate alveolar and pleural pressure values (for use in the dimensional model) as defined in Table 3.6. All other parameters were set as for the normal mid human lung height - 14 cm- condition. Figure 3.11(a) compares the WBC transit time distributions during inspiration, expiration and at FRC. This illustrates only a very small change in the WBC transit time distribution. Figure 3.11(b) demonstrates the number of times a WBC becomes blocked in a pathway during the different stages of breathing.

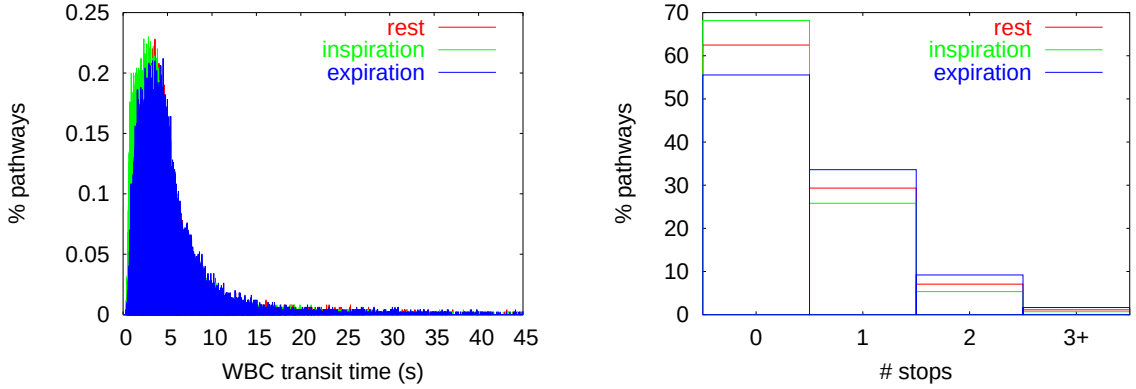

FIGURE 3.11: *WBC transit time model results at different stages of breathing (rest, inspiration, expiration): (a) transit time distributions and (b) WBC stopping frequency.*

Simulations were carried out varying the tension in the neutrophil cell cortex, τ_0,

which is proportional to the critical entrance pressure (P_{cr}) of a WBC as described by Equation 3.37. The normal τ_0 value used is 3.5x10^{-5} $\mathrm{N\,m^{-1}}$, this value is varied by $\pm$ 10%, and +50% to investigate the effects on WBC transit. The WBC transit time distributions for the three different cases are shown in Figure 3.12(a). The incidence of WBC stoppage in the three cases are compared in Figure 3.12(b). Increasing τ_0 effectively makes the WBCs stiffer, or less deformable, therefore an increase in τ_0 was expected to increase WBC transit times and increase the number of times a WBC is stopped in passage from arteriole to venule. The transit time distributions do not show much change as a result of the variation in τ_0. The average alveolar-sac WBC transit time increases from 2.89 to 2.96 to 2.99 s when τ_0 is increased from -10% to +10% to +50%, respectively. The incidence of stopping increases slightly in frequency with the average number of stops in all pathways increasing from 0.96 to 0.99 to 1.04. These differences are only very small, illustrating that the WBC transit model is fairly insensitive to changes in τ_0.

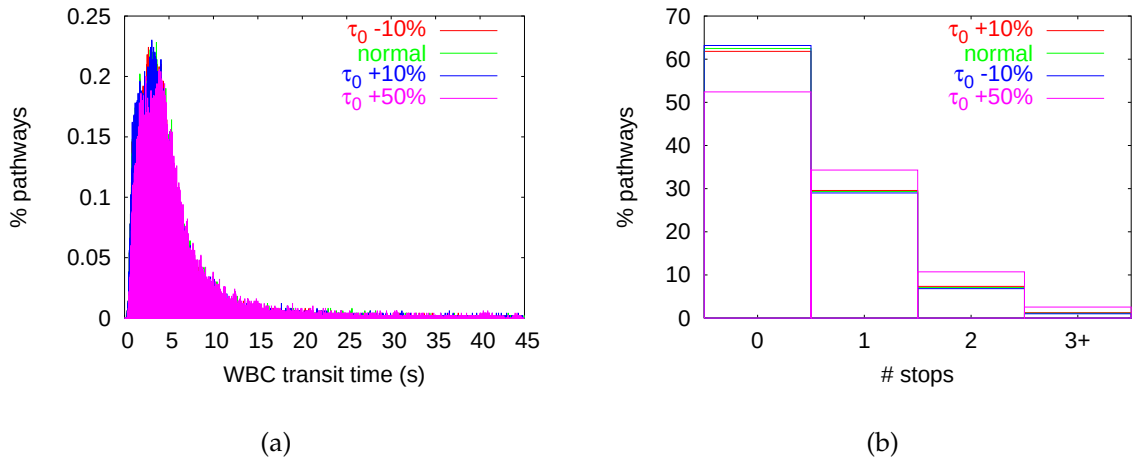

FIGURE 3.12: *WBC transit time model results with varying cell cortex tension τ_0: (a) transit time distributions and (b) WBC stopping frequency.*

The most noticeable difference in WBC stoppage was in different 'zones' of the lung. Comparison of WBC stopping frequency is demonstrated in the upper, mid, and lower regions of the lung in Figure 3.13. This shows that in the lower regions of the lung the WBCs travel through the capillaries without being trapped. In the upper lung 87.2% of WBCs are stopped three or more times.

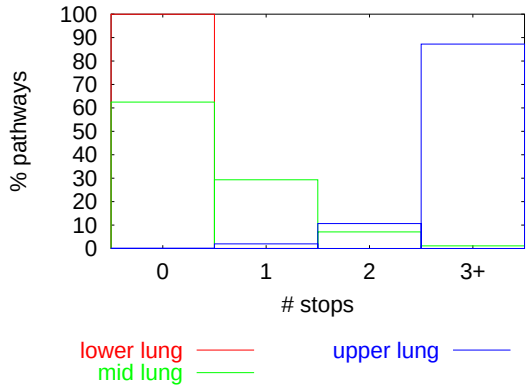

FIGURE 3.13: *Comparison of WBC stopping frequency in upper, mid, and lower regions of the lung.*

3.3.6 Sensitivity analysis

A sensitivity analysis of the important model parameters has been conducted. Parameters were varied by $\pm$ 10% and the effects on flow ($\dot{Q}$), hydraulic diameter (D_h), RBC (t_{RBC}), and WBC (t_{WBC}) transit times are shown in Table 3.7. These results indicate that the inlet pressure boundary condition applied and the diameters allocated to the vessels had the largest effect on results. The outlet pressure also had a large effect on the cellular transit times, with a 10% decrease in pressure decreasing the red and white blood cell transit times by more than 30%. This suggests that the model will be made more realistic when it is coupled with a model of flow in the arterial and venous systems to provide better pressure boundary conditions. Information on capillary vessel diameters is more established than the pressure boundary conditions. The average capillary diameter in the model is 8.45 μm which fits in well with anatomical information. The hydraulic diameter of the vessels was relatively insensitive to parameter changes. Variation of the vessel elasticity did alter the vessel diameters by around $\pm$ 4% which had a significant effect on the WBC transit time results. The most sensitive model output was the WBC transit time, due to the empirical nature of the WBC transit model and the complex interactions of WBCs in the network.

3.3.7 Cell transit time distributions in the upright lung

Illustrations of the blood flow solutions ($\mathrm{mm}^3\ \mathrm{s}^{-1}$) in the alveolar-capillary sac model are shown in Figure 3.14 in (a) the upper, (b) mid, and (c) lower regions of the lung.

Model cell transit time frequency distributions are presented in Figures 3.15 and 3.16. The transit time distributions are plotted against the percentage of pathways

		Effects, %			
Parameter	**% Variation**	$\frac{\Delta \dot{Q}}{\dot{Q}_0}$	$\frac{\Delta t_{RBC}}{t_{RBC0}}$	$\frac{\Delta t_{WBC}}{t_{WBC0}}$	$\frac{\Delta D_h}{D_{h0}}$
Elasticity k_c (cmH_2O)	-10	14.53	-9.33	-23.13	4.36
	10	-11.06	-1.03	49.94	-3.53
Inlet pressure (cmH_2O)	-10	-30.93	26.05	58.81	-2.31
	10	35.71	-24.99	-20.06	2.46
Outlet pressure (cmH_2O)	-10	9.72	-31.77	-34.96	-1.47
	10	-11.11	15.84	-3.32	1.59
Pleural pressure (cmH_2O)	-10	-1.70	-2.79	-10.60	-0.26
	10	1.34	-5.97	-6.98	0.22
Initial hematocrit (H_d)	-10	3.00	-2.47	-4.61	0.04
	10	-3.17	5.33	-3.15	-0.05
Tissue part of capillary x-section (μm)	-10	-7.15	12.20	11.85	-1.27
	10	6.85	3.79	4.71	0.99
Alveolar part of capillary x-section (μm)	-10	-25.23	12.69	57.46	-8.87
	10	28.59	-24.05	-58.65	8.63

TABLE 3.7: *Sensitivity analysis of model parameters and boundary conditions. Simulations carried out at a vertical human lung simulation height of 14* cm*, with corresponding boundary conditions. These results indicate that the model flow results are most sensitive to variations in the applied inlet pressure boundary conditions and the diameter distribution of the capillary vessels.*

sampled with these transit times, and the actual percentage of sampled blood flow with these transit times. The sample bins were 0.1s wide.

Figure 3.15 plots transit times against percentage of pathways, for (a) RBC and (b) WBC transit results. These plots display relatively smooth curves as they do not reflect the distribution of flow. The RBC transit time frequency distributions show a more homogeneous distribution in the lower lung, and a faster mean transit time. Increasing in height to the mid and upper lung regions results in a widening of the transit time distribution and a lengthening of the transit times. The distributions are slightly skewed to the right. The WBC transit time frequency distribution was also narrowest for the lower lung zone, and skewed to the right. The peak decreased for the mid and upper zones, and the right skew increased.

Figure 3.16 displays the distribution of transit times with respect to the actual percentage of blood flow through each path, (a) illustrates the RBC distribution and (b) the WBC transit distributions. This distribution is much more heterogeneous, with large peaks seen in certain time brackets. The large peaks represent the occurrence of preferential pathways where large portions of the blood flow pass through the lowest resistance pathways. In the lower lung a RBC transit time of 0.58 s occurred in 18.2%

of the flow, with a narrow distribution around this peak. The average transit time in this region was 0.42 s. The distribution was wider in the middle zone, and peaked with 6.9% of the flow having a RBC transit time of 0.46s. The average transit time in this region was 0.61 s. The distribution in the upper lung was far more heterogeneous due to uneven perfusion and showed several peaks over a range of times. The average transit time was 2.46 s, with a peak at 3.75 s with 7.8% of flow. The WBC distributions in all regions were more heterogeneous than the RBC distributions. In the lower lung a peak occurred at 0.33 s with 21.6% of the flow, and the average WBC transit time was 0.39 s. The mid lung showed a peak where 9.3% of the flow passed with a WBC transit time of 1.19 s, and the average time was 1.90 s. The upper lung showed a very wide distribution of WBC transit times with a mean of 32.40 s, and the highest peak at 14.60 s for 7.8% of the flow.

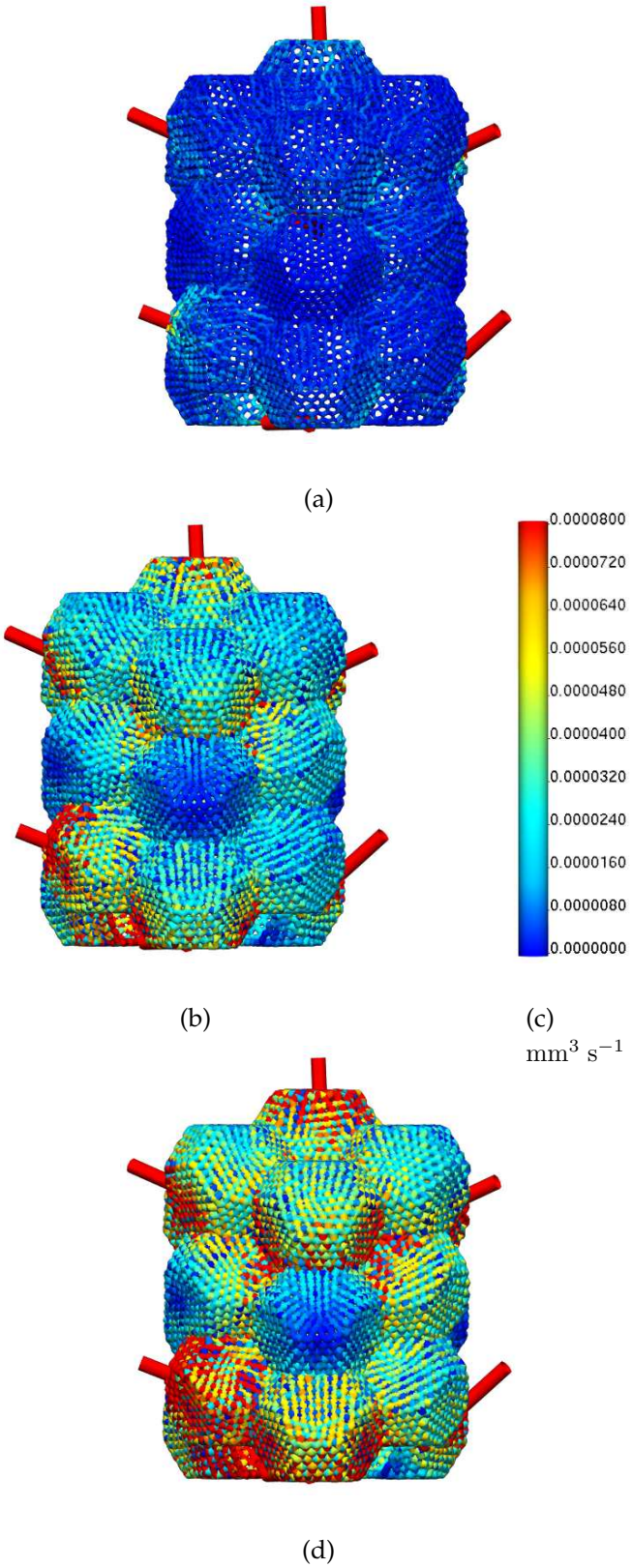

(a)

(b)

(c)
$\mathrm{mm}^3\ \mathrm{s}^{-1}$

(d)

FIGURE 3.14: *Blood flow solutions in the alveolar-capillary model in (a) the upper (28* cm*), (b) mid (14* cm*), and (d) lower (2* cm*) regions of a vertical human lung. Solution spectrum illustrated in (c) units* $\mathrm{mm}^3\ \mathrm{s}^{-1}$*. Results in the upper lung demonstrate lower flow rates as well as smaller diameters, on average, as a result of the lower pressures in these regions. The lower lung region demonstrates the opposite behaviour, higher flow and larger capillary diameters.*

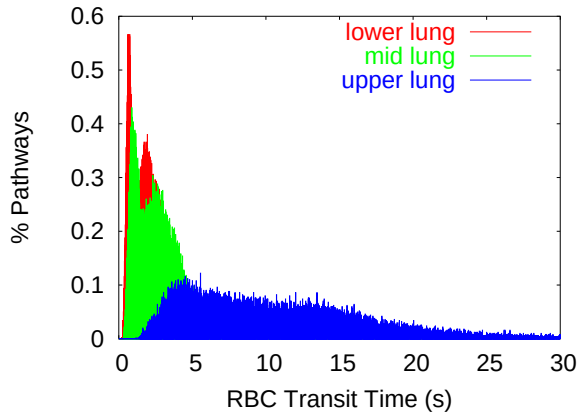

(a)

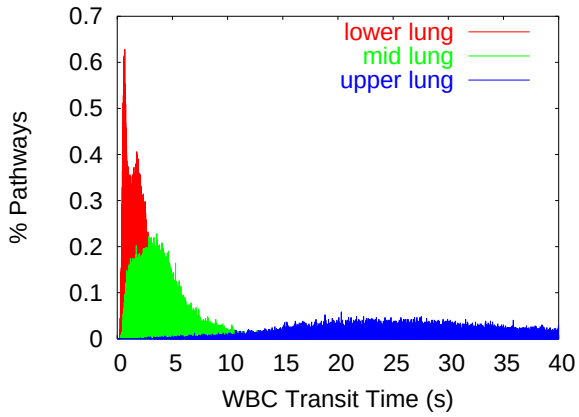

(b)

FIGURE 3.15: *Simulation results for cell transit time frequency distributions, with respect to the percentage of pathways: (a) RBCs, (b) WBCs, for the upper (28*cm*), middle (14*cm*) and lower (2*cm*) lung zones. Sample intervals 0.1*s.

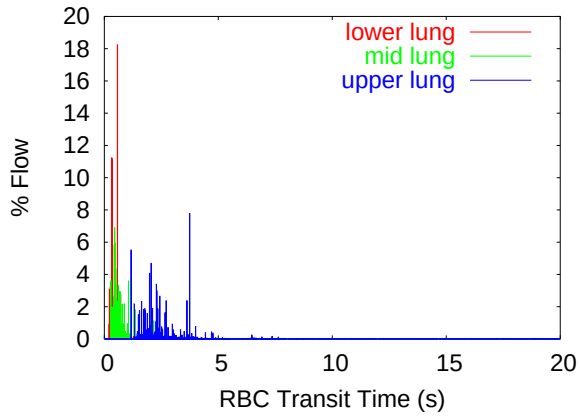

(a)

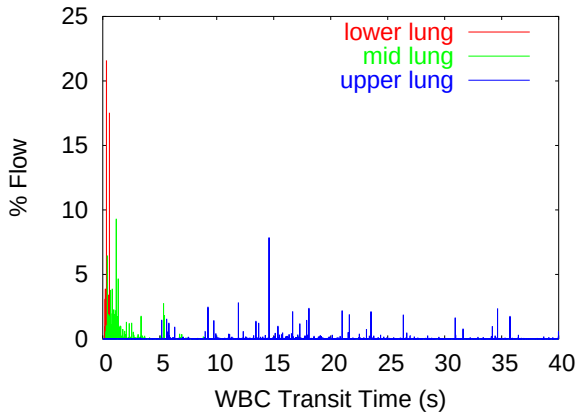

(b)

FIGURE 3.16: *Simulation results of cell transit time frequency distributions, with respect to the percentage of flow: (a) RBCs, (b) WBCs, for the upper (28*cm*), middle (14*cm*) and lower (2*cm*) lung zones, sample intervals 0.1*s.

3.3.8 Variation in blood pressure in the upright lung

Figure 3.17(a) shows the average capillary diameter (D_h) versus height up the lung, resulting from distension or compression of the elastic capillaries via the combination of local Ptp and Ptm. This plot demonstrates an increase in diameter from the apical region downwards. The capillaries generally become more distended down the vertical lung due to an increase in the arteriole, venule and pleural pressures. In the lowest regions of the lung a decrease in the average D_h is displayed. This is due to the relatively low Ptp (where pleural pressure$\approx$1 $\mathrm{cm\ H_2O}$) at the very bottom of the lung. Ptp is equal to only 0.75 $\mathrm{cm\ H_2O}$ at the 0 cm height simulation, Figure 3.5 displays a large increase in E, the septal wall elasticity coefficient, at this very low Ptp, which is why the decrease in D_h is observed.

Figure 3.17(b) demonstrates the effect of lung height on blood flow in the single alveolar sac. Flow increases towards the lower regions of the lung, which relates directly to the capillary diameter plot in Figure 3.17 (a): as the average capillary hydraulic diameter increases, resistance to flow is decreased, thereby elevating the volumetric flow rate. In the very lowest regions of the lung a decrease in volumetric flow rate can be seen as a function of the decreasing capillary diameters. This region of decreased flow has been observed in experimental observations and is typical of the so called 'zone 4' flow region. Zone 4 was recognised more recently, as it is absent in measurements carried out above FRC. This zone occurs in the most gravitationally-dependent regions of the lung at lower lung volumes, or arguably in all peripheral regions of the lung (Hakim, Lisbona & Dean 1987). At a vertical height of 30 cm the arteriole pressure is inadequate to open any of the capillary vessels for perfusion; the vessels are therefore collapsed and there is no flow. The flow transitions from zone 2 to zone 3 flow between the heights of 24 and 26 cm. A smooth transition is displayed and a linear flow gradient is maintained.

Figure 3.18(a) shows average cell transit times generated in the model with respect to lung height, for both RBCs and WBCs. These plots show experimentally consistent trends, namely decreasing average transit times towards the basal regions of the lung where the flow is higher (Hogg, Martin, Lee & McLean 1985, MacNee, Martin, Wiggs, Belzberg & Hogg 1989, Wagner Jr, Latham, Hanson, Hofmeister & Capen 1986, Presson Jr, Hanger, Godbey, Graham, Lloyd & Wagner Jr 1994). Figure 3.18 (a) also shows the standard deviation of the RBC transit time distribution with respect to lung height. The standard deviation decreases with decreasing lung height, consistent with experimental observations (Presson Jr et al. 1994), due to more uniform perfusion

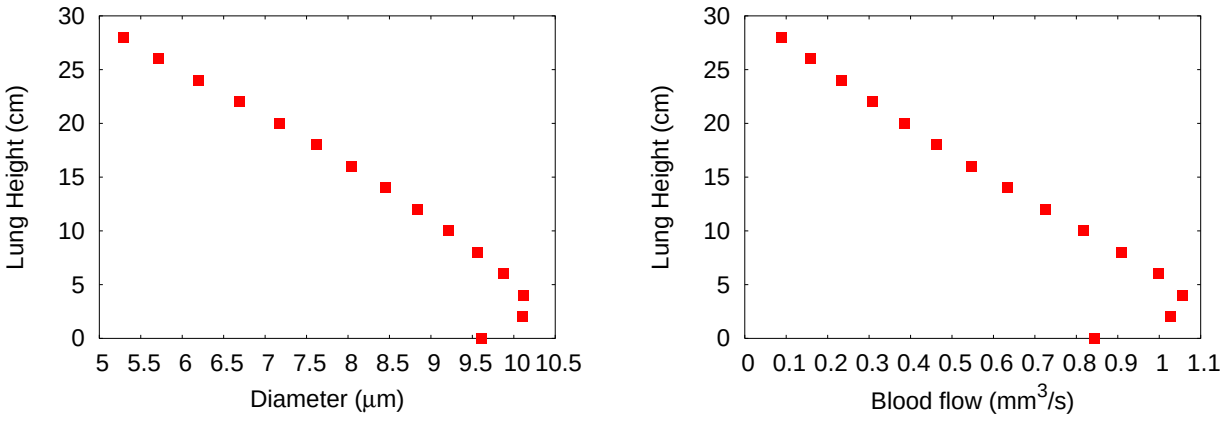

(a) (b)

FIGURE 3.17: *Average capillary results in alveolar sac model in relation to lung height: (a) capillary diameters (μm) and (b) volumetric blood flow rate ($\mathrm{mm}^3\ \mathrm{s}^{-1}$).*

as a result of increased flow. The model produced longest transit times in the upper lung, and demonstrated that expansion of lung blood volume due to recruitment and distension as flow increased down the lung prevented an excessive shortening of the transit time. A very large difference in the cell transit times and relative dispersion are seen in the very top regions of the lung, due to the decrease in flow and diameters of the capillary vessels and the increased stoppage of WBCs as shown in Figure 3.18(b).

Figure 3.18(b) shows the percentage of pathways that will stop a WBC. There is limited data in the literature to compare with these model results, however the model does show a logical trend in that the more basal regions have less WBC stoppage due to increased flow and larger diameter of vessels.

Figure 3.19(a) plots RBC transit time with respect to lung height for model results and published experimental data (Hogg et al. 1985, MacNee et al. 1989, Wagner Jr et al. 1986). To allow comparison with the experimental data from different regions of the lung, the positioning of the lower, middle and upper regions of the lung were assumed to be 16, 50, and 83% of lung height, respectively. Results from (Hogg et al. 1985) are from supine dogs; the two sets of data displayed are the fastest and slowest transit time data from experiments on 9 dogs. Experimental data from (Wagner Jr et al. 1986) studied the same area of lung, in mongrel dogs, but oriented the dogs in three different positions with respect to gravity to obtain regional transit times. Data from (MacNee et al. 1989) are from humans, pre- and post-operatively in the lateral decubitus position, and in normal subjects sitting in the upright position. The model results display the

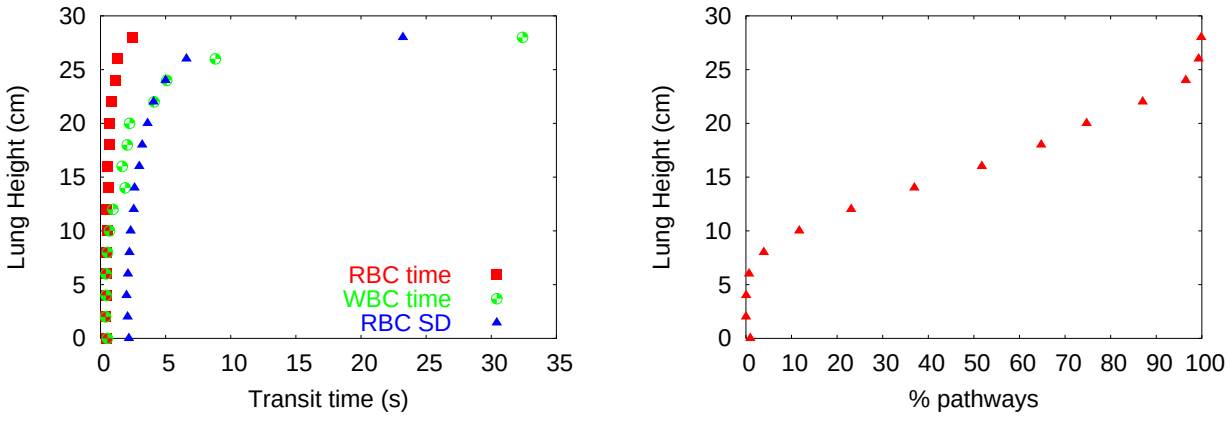

FIGURE 3.18: *Cell transit time results for simulation at 2* cm *intervals over the height of a 30* cm *lung. (a) RBC and WBC mean transit times and standard deviation values of RBC transit times, and (b) percentage of paths stopping WBCs.*

same trend as the published data; the transit times do, however, appear to be shorter than the limited human experimental data available for comparison. Experimentally measured transit times from Hogg et al. (1985) and MacNee et al. (1989) are for the full pulmonary circuit. These have been scaled to represent capillary transit times (refer Section 3.4.2) which may contribute to the discrepancy between model and experimental transit times. The differences in transit times could also be due to the definition of pressure boundary conditions, or factors not accounted for in the current model, such as variation in alveolar size within the height of the lung (discussed further in Section 3.4.2).

Figure 3.19(b) compares published flow results with model results, plotting blood flow relative to the mean against percentage of lung height. This plot includes experimental perfusion data from upright baboons (Glenny, Bernard, Robertson & Hlastala 1999), reprinted in (Prisk et al. 2001). Results from (Glenny, Lamm, Bernard, An, Chornuk, Pool, Wagner Jr, Hlastala & Robertson 2000) are from supine pigs in normal gravity (1G). The model demonstrates the same qualitative behaviour as the experimental data, and fits well quantitatively with results from (Glenny et al. 1999). The model does display a small decrease in blood flow in the lowest regions of the lung as found in all of the animal studies, excluding the baboon. The baboon data included is only the best fit line for the portion of increasing flow, though not shown in this plot, the baboon does display a region of decreasing flow in the basal regions of the

lung (Glenny et al. 1999). The capillary model simulations could have been conducted assuming a supine posture (for better comparison with supine measurements), but since the pressure boundary conditions applied simply varied linearly with height, similar results would have been obtained over a narrower height range.

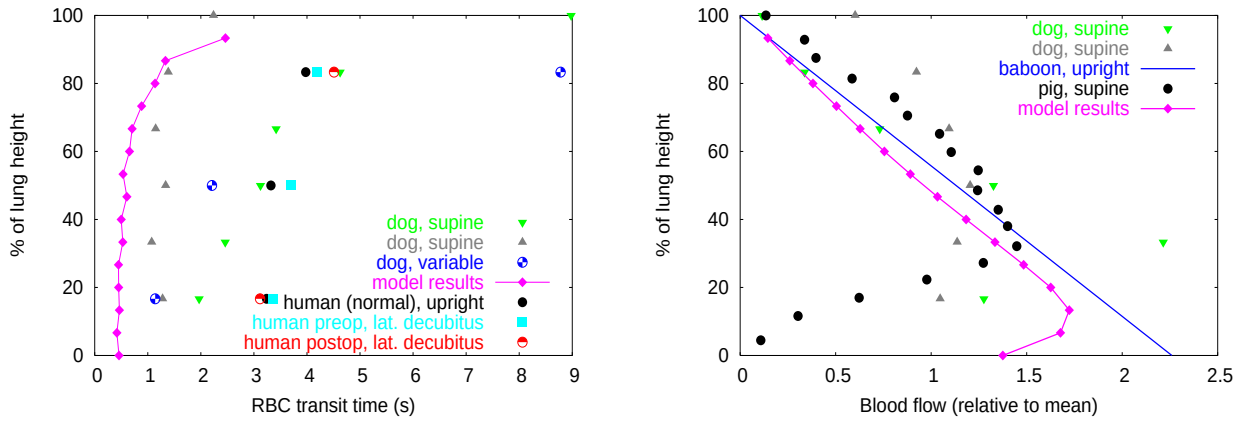

(a) (b)

FIGURE 3.19: *Comparison of model results with measured experimental values of (a) RBC transit time, and (b) blood flow (relative to mean) with respect to gravitationally-dependent height. Experimental data is shown in supine dogs (Hogg et al. 1985), dogs in 3 different positions with respect to gravity (Wagner Jr et al. 1986), humans, pre- and post-operatively in the lateral decubitus position, and in normal subjects sitting upright (MacNee et al. 1989), upright baboons (Glenny et al. 1999), and supine pigs (Glenny et al. 2000).*

Figure 3.20(a) shows the effect of lung height on the total alveolar sac capillary volume. The volume of the capillaries increases due to increased hydrostatic forces down the lung, consistent with Figures 3.17(a) and 3.20(b) showing an increase in the diameter and cross-sectional "sheet" height of the vessels, respectively.

Figure 3.20(b) plots the average sheet height with respect to lung height. The sheet height value is determined in the dimensional model (refer (Huang et al. 2001)), from which the elliptical dimensions (a^*, b^*) of the capillary vessels are calculated. This plot shows a similar increase in sheet height with descending lung height as does Figure 3.17(a), with a small decrease in height in the lowest regions of the lung.

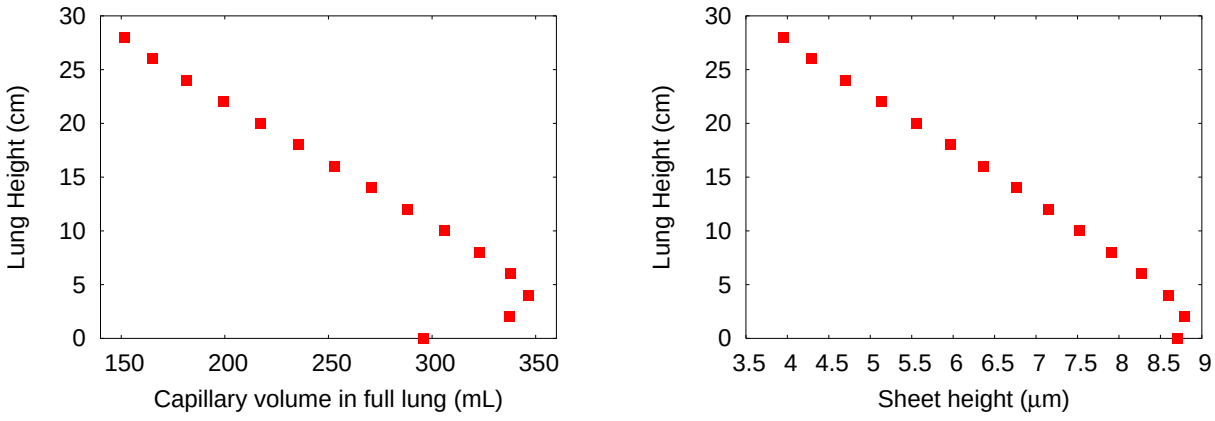

(a) (b)

FIGURE 3.20: *(a) Total alveolar sac capillary volume* (ml) *and (b) average capillary "sheet" height in relation to vertical position in the lung.*

3.4 Discussion

3.4.1 Cell transit time distributions in the upright lung

Fluorescence videomicroscopy has shown that a decrease in RBC transit time caused by an increase in flow is partially offset by capillary recruitment and distension, therefore leading to a narrowing of the transit time distribution (Presson Jr et al. 1994, Presson et al. 1995, Presson Jr, Todoran, Witt, McMurtry & Wagner Jr 1997). This design property is thought to be a stabilising feature to prevent RBC transit time from decreasing below the theoretical minimum time of 0.25 s for complete oxygen saturation (Presson et al. 1995). The regional variation simulations in the current study can be used to look at the effect of increasing flow on the cell transit time distributions, as blood flow increases in the lower regions of the lung.

Figure 3.15 plots RBC transit time versus the percentage of pathways with these transit times. This plot shows smooth distributions and clearly represents the effect of increased flow, namely a decrease in average transit time and a narrowing of the distribution. This plot represents the distribution of transit times of certain pathways, which does not necessarily represent the flow in this case. At maximal capacity flow patterns may tend more towards this representation, as recruitment and distension reach their limit. Figure 3.16, plotting the percentage of blood flow versus transit time, shows a more scattered distribution. The high percentage of flow in particular transit

time intervals indicates the presence of preferential pathways where the bulk flow passes. Certain pathways have a lower overall resistance than others, therefore a higher proportion of flow passes through them. This phenomenon has been documented experimentally by Okada, Presson Jr, Godbey, Capen & Wagner Jr (1994). As the flow increases, however, it becomes more homogeneously distributed as the resistance in intermittently perfused pathways decreases, and the dispersion of transit times narrows as shown in the lower lung region simulations.

Transit time distributions in the lower lung show, on average, shorter transit times and a more homogeneous distribution due to higher flow, while in the upper lung the opposite was observed. This narrowing in distribution is due to recruitment of new capillaries and distension of previously recruited segments. Vessels which were previously intermittently perfused become continuously perfused and have similar resistance and flow to other perfused segments, thereby increasing the homogeneity of perfusion and transit time distributions. Model results have reproduced the RBC transit time phenomena observed in these experimental studies (Presson Jr et al. 1994, Presson Jr et al. 1997), namely by illustrating that as flow increases the average transit time decreases and the transit time distribution becomes more homogeneous due to distension of vessels.

Terashima et al. (1999) investigated the effect of cigarette smoke on neutrophil sequestration in the lung. Experimental results demonstrated an increase in the amount of neutrophils sequestered in the lungs of animals exposed to smoke. Smoke exposure causes an increased release of WBCs from the bone marrow, and these freshly released cells are less deformable, and therefore become lodged in the small capillary vessels. Model simulations with varying WBC cell cortex values (Figure 3.12) demonstrated only a small influence of cell deformability on WBC transit times and stoppage.

Terashima et al. (1999) also showed that the percentage of neutrophils sequestered in the gravity-independent regions (upper lung) was higher than in the gravity-dependent regions. This study also speculated that these trapped WBCs, as a result of increased elastase release, may contribute to the alveolar wall damage associated with smoke-induced lung emphysema. Centriacinar (centrilobular) emphysema characteristically affects the upper lobes and upper parts of the lower lobes of the lung (Bourke & Brewis 1998). *In vivo* studies by Wiggs et al. (1994) have also demonstrated higher WBC transit times in the upper lung, due to an increased frequency of vessels with smaller diameters in these regions. The current model agrees with these measurements and demonstrates that WBCs have a much longer transit time in the upper lung (Figure 3.18(a)) and are trapped more frequently (Figure 3.18(b)) in this

region.

3.4.2 Variation in blood pressure in the upright lung

It is a well known phenomenon that significant regional variations in ventilation, perfusion, gas exchange, intrapleural pressure, alveolar expansion, and parenchymal stresses exist in the upright mammalian lung. One school of thought is that these differences are a result of the effects of hydrostatic pressure gradients (from gravity) acting on the relatively large height of the lung and emphasised by the presence of an extremely thin blood-gas barrier (West 1977, Prisk et al. 2001).

Controversy remains over the predominant origin of regional perfusion heterogeneity. Early investigations using isolated perfused animal lungs concluded that the major contribution to the distribution of blood flow was due to gravity; the discrepancy between the hydrostatic pressure gradient in the blood vessels and the absence of a gradient in the alveolar airways (West et al. 1964). More recent high-resolution studies, using microsphere deposition techniques, have shown that these regional blood flow variations can be maintained even under zero gravity conditions, with the conclusion that gravity is an important but secondary determinant of regional pulmonary blood flow (Glenny, Polissar & Robertson 1991, Glenny, Lamm, Albert & Robertson 1991, Glenny et al. 1999, Glenny et al. 2000). These studies focused on the effect of gravity on blood flow redistribution independent of lung compression and concluded that the perfusion heterogeneity stems primarily from structural factors and, to a lesser extent, from gravitational forces. Objections have been raised about the lung volumes used at the time of microsphere injection (West 1992). The regional differences of lung expansion caused by its weight were not taken into account and the distribution of microspheres were measured after the lung was removed from the chest and uniformly expanded to total lung capacity (TLC), with consequent changes to regional lung volumes (West, Glenny, Hlastala & Robertson 2002). Despite continued debate, it is still acknowledged that regional gradients exist, and gravity contributes to them.

The persistence of a non-gravitational gradient has bearing on inter-species comparisons made throughout the current study. Most of the experimental studies used for comparison with the modelling results were from animals in which the lung orientation *in vivo* is usually prone-inclined. In contrast the modelling study considered an erect human lung, with uniform tissue properties. Experimental measurements from the upright baboon lung (Glenny et al. 1999) are the most

comparable anatomically to that of the human lung, and model results compare well with the limited experimental results available for this animal. Model simulations utilising a human lung in the supine posture could have been carried out, but since the pressure boundary conditions applied assumed a linear gradient of pressure with respect to gravitationally-dependent height, similar results would have been obtained within a narrower height range.

Perfusion experiments have demonstrated that capillary perfusion always began as the capillary pressure exceeded airway pressure, and that recruitment was purely due to capillary pressure (Godbey et al. 1995). At low airway pressures the capillary bed recruited over a narrow capillary pressure range, acting like a sheet. Increased lung distension (via increased airway pressure) caused capillary distension to occur over a wider range of pressures, in a more segment-by-segment basis. They hypothesised that this was due to the increased tension of the fibre network, and the non-uniform distribution of fibres resulting in non-uniform compression of capillaries leading to more heterogeneous opening pressures. This sudden collapse of capillaries in the zone 2 region was displayed in the model. During simulations carried out in the upper (zone 2) flow regions of the lung convergence problems were encountered. If the venule boundary pressure was less than alveolar pressure, capillary pressures would drop below alveolar pressure and the vessels would collapse. Solutions fluctuated between vessel collapse and vessel re-opening, due to pressure build up. Thus the solution was not able to converge. Fung & Sobin (1977) indicated that if venule pressure is below alveolar pressure there will be vessel collapse, the arteriole pressure will then prevail and the vessels will be opened again. Previous studies have indicated that a "flutter" condition occurs (Permutt, Bromberger-Barnes & Bane 1962), but, Fung & Sobin (1977) states that this is not possible due to the small inertial forces relative to the elastic, pressure and viscous forces in the capillaries. In zone 2 the flow is thought to be governed by the difference between arterial and alveolar pressures (West 1995), therefore the alveolar pressure was prescribed as the venule boundary condition in the zone 2 region simulations.

Hogg et al. (1985) investigated regional differences in RBC transit in supine dog lungs, and MacNee et al. (1989) measured the frequency distribution of RBC transit times in the upper and lower regions of human lungs in the lateral decubitus position. Both studies calculated RBC transit times for the entire pulmonary circuit. The time spent in the microvasculature is approximately 82% of the total time (Clough, Haworth, Hanger, Wang, Roerig, Linehan & Dawson 1998), therefore transit time values for the full pulmonary circuit have been scaled for comparison with simulation

results. The shortest mean transit time from (Hogg et al. 1985) was 1.62s (range 0.41 to 6s) adjusted to 1.33s, the longest mean transit time was 4.6s (range 0.9 to >20s), adjusted to 3.77s. The overall mean transit time was 2.86s, adjusted to 2.35s, which is quite a bit longer that the model average of 0.77 s over all height simulations. The model result is also shorter than the experimental values of 1.6s and 3.0s in human (Hogg et al. 1994) and 1.37s in dog (Hogg et al. 1988). The adjusted values from (MacNee et al. 1989) are even longer than these transit times; adjusted average values of 3.24s, 3.32s, and 3.98s were measured in the apical, mid, and basal regions, respectively. RBC transit time predictions made based on measurements of the diffusing capacity of the lung for carbon monoxide to measure capillary volume and then dividing this volume by cardiac output, give a better overall estimation of average transit in the entire lung. RBC transit times measured using this technique have been found to lie in the range of 0.75-1 s (Hill, Power & Longo 1973, Hlastala 1972, Hlastala & Robertson 1998), these values do compare well with the overall model prediction.

Wagner Jr et al. (1986) studied the vertical gradient of pulmonary capillary transit times in anesthetized dogs. Transit times and perfusion indices were measured on the surface of the "upper", "middle" and "lower" lung by following the passage of fluorescent dye through the capillaries using *in vivo* television microscopy. In these investigations a window was inserted in the left lower lobe. The same area of lung was studied but the dogs were oriented in three different positions with respect to gravity. To simulate the "upper" lung, measurements were done with the dog in the right lateral decubitus position. The "mid lung" was studied by placing the dogs on a 20^o sloped platform in the head-up semirecumbent position. Finally the "lower" lung was studied with dogs in the left lateral decubitus position. This investigation assumed that the plasma dye bolus measurement was a reasonable approximation of RBC transit time, however it has subsequently been shown that plasma takes about 1.4 times longer to traverse the capillary bed than RBCs (Presson et al. 1995). Adjusting for this phenomenon, the RBC transit times from (Wagner Jr et al. 1986) are therefore 8.78s in the upper lung (12.3s for plasma), 2.21s in mid lung (3.1s plasma) and 1.14s in the lower lung (1.6s plasma). These transit time results are compared with model results in Figure 3.19(a). The results from Wagner Jr et al. (1986) are from subpleural capillary networks and are therefore not necessarily quantitatively representative of the internal capillary network. The subpleural capillary network is less dense, the capillaries are longer and wider, and the distance from arteriole to venule is shorter than for internal capillaries. The subpleural capillary mechanics may also differ as they are exposed to pleural forces on one side and alveolar on the other, as opposed to internal capillaries

which are exposed to alveolar pressures on both sides (Godbey et al. 1995). Lamm & Albert (2000) made observations of vessels directly beneath the pleura and in the interior regions of rabbit lungs in different positions. They concluded that flow through subpleural capillaries is less than that which occurs deeper in the interior, but that the regional distributions of flow and the effects of zonal conditions are similar in the two regions. Therefore results from subpleural networks are qualitatively representative, but may not be so quantitatively accurate.

The blood cell transit time results presented in Figures 3.19(a) and 3.18(a) show a wide variation in transit times from the apical to basal regions of the lung. As the vessel diameters decrease with height up the lung resistance is increased. The transit time range may be larger than expected due to the nonlinear relationship between the apparent viscosity of the blood and vessel diameter (see Equation 3.19 and Figure 3.6). As vessel diameters approach the minimum vessel diameter a RBC can pass through (2.7 μm) the apparent viscosity of the blood rapidly increases reflected by a large increase in resistance.

Figure 3.19(b) compares published flow results with model results. The model results compare reasonably well with all of the experimental results. The experimental data shown in Figure 3.19(b) is the line of best fit through a high-resolution data set (Prisk et al. 2001). All other experimental data in Figure 3.19 (b) are from lower resolution studies, and show average blood flow within isogravitational planes.

The model transit time results presented in Figure 3.19(a) are quite a lot shorter than the published experimental data. There are known weaknesses in the capillary model, a major one being the assumption of structural uniformity within the lung, for example the current model does not incorporate forces provided by the fibre network, and all alveoli are roughly of equal size. Recent studies have argued that regional variations in flow are largely due to structural factors (Hlastala & Glenny 1999). The current model only investigates the influence of gravity on capillary blood flow. There is limited experimental data describing structural changes with respect to lung height making it difficult to include in the model. Future coupling of the capillary flow model to models of blood flow in the larger vessels and soft-tissue mechanics may be able to represent structural differences through functional properties, for example variation in alveolar size and shape and inlet/outlet boundary conditions prescribed by the arterioles/venules. Another possibility for the discrepancy of model results versus experimental data is the influence of *in vivo* tissue remodelling. Quantification of this has not been experimentally verified rendering it difficult to include in the current model. As more physiological detail becomes available the current model could be

extended to more realistically represent *in vivo* conditions.

The classic 'zonal model' of pulmonary blood flow (West et al. 1964, Prisk et al. 2001) includes a more recently described zone 4 of reduced flow found in the basal and peripheral regions of the lung. This zone is demonstrated in the model, but is purely due to the effects of the dimensional model. The high septal elasticity results in smaller average diameter vessels in the very lowest regions of the lung, which reduces flow. In reality zone 4 may be produced due to the relatively poor expansion of the lung parenchyma and therefore of the extra-alveolar vessels, leading to higher resistance and lower flow at a level higher up than the capillaries. Changes in the extra-alveolar vessels were not included in the model at this stage, and resistance in the tributary arteriole and venule vessels remained constant for all simulations. The effect of variation in alveolar volume distributions in the lung may also play a role in the development of the zone 4 flow region. Alveoli in the lower regions of the lung are more compressed, due to gravity, and therefore are generally smaller than alveoli in the upper lung region. Equivalent alveolar volumes were used for all of the simulations in this chapter. Differences in alveolar size would be interesting to examine with an extended model. This could be approached by coupling the current model with a model of soft-tissue mechanics to better prescribe pressure boundary conditions and deformation of the alveolar structure.

The variations shown in Figure 3.19 may also be due to species-related differences. The model is based on human data, while the published results are from upright baboons (Glenny et al. 1999), supine dogs (Hogg et al. 1985) and pigs (Glenny et al. 2000). Dogs in the supine position had a total vertical height 12 cm, and pigs approximately 18 cm as opposed to the 30 cm height of an upright human lung. The baboon lung is the most comparable anatomically to that of the human lung, with an upright vertical height of about 25 cm.

The empirically-based relationship, implemented in the capillary dimensional model, between alveolar volume and Ptm was derived from experimental studies on rat lungs (Mercer et al. 1987). This use of this relationship assumes that human lungs have a similar alveolar response to changes in Ptm. Measurements such as this would be very difficult to obtain from human tissue, due to ethical issues, and it is believed that this model is a valid approximation for the current model.

This flow model neglects the effect of WBCs on blood viscosity, due to lack of available models to represent this. Future improvement of the model could include an empirically-based relationship to reflect the effect of WBCs on blood viscosity in the microcirculatory network.

3.5 Conclusions

This chapter describes the development of an alveolar-capillary flow model, verifies and confirms model results, and investigates the parameter sensitivity of the microcirculatory model. Future applications of this model could include coupling with models of gas exchange, soft-tissue mechanics, blood flow in the conducting arterial and venous vessels, and air flow in the bronchial system.

The current model is limited by the difficulty of prescribing realistic pressure boundary conditions. Accurate pressure measurements at the microvasculature level are hard to obtain. Coupling this model with the model of blood flow in the conducting arteries and veins will allow more physiologically-realistic pressure boundary conditions to be applied at the capillary level. This will also incorporate the impact of the larger vessel flow on the results at the microcirculatory level to be more representative of experimental results. Hydrostatic pressure gradients in the lung will also be more realistically represented: in the current study the pleural pressure, arteriole and venule boundary pressures are assumed to vary linearly with height.

Blood flow has been modelled in the microcirculatory alveolar sac geometry developed in Chapter 2 and used to investigate flow phenomena in different regions of the lung. Comparisons of red and white blood cell transit times in the upper, mid, and lower lung show physiologically consistent trends of a decreasing average transit time and an increased homogeneity of transit time distributions as a result of increasing average capillary diameter and flow down the height of a vertical lung. The model was found to reproduce experimentally consistent trends in red blood cell transit times and relative blood flows with respect to lung height. This model enables flow properties and cell transit time behaviour in the pulmonary microcirculation under varying conditions, for example in different 'zones' of the lung, to be explored.

A summary of this work can be found in Burrowes et al. (2004) and Tawhai & Burrowes (2003).

Chapter 4

Geometric modelling of the large pulmonary vessels

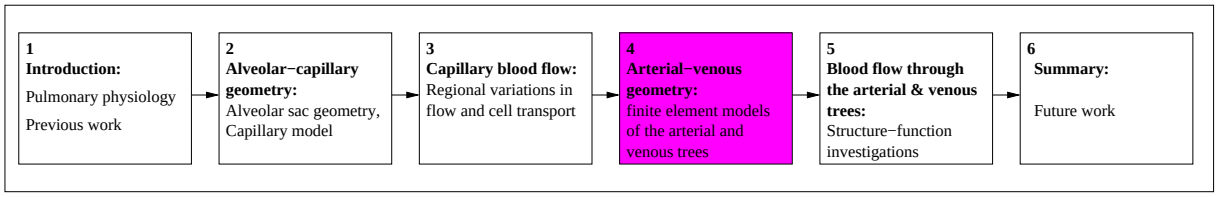

To enable detailed investigation of structure-function relationships in the pulmonary circulation an anatomically-based finite element model of the arterial and venous networks has been developed to more accurately reflect the geometry found *in vivo*. This chapter describes the development of this model. Geometric models of the arterial and venous tree structures are created using a combination of multi-detector row x-ray computed tomography (MDCT) imaging to define around 2500 vessels from each tree (Section 4.2.1), a volume-filling branching algorithm to generate the remaining accompanying conducting vessels (Section 4.2.2), and an empirically based algorithm to generate the supernumerary vessel geometry (Section 4.2.3). The explicit generation of supernumerary vessels is a unique feature of the computational model. Analysis of branching properties and geometric parameters demonstrates close correlation between the model geometry and anatomical measures of human pulmonary blood vessels. A total of twelve Strahler orders for the arterial system and ten Strahler orders for the venous system are generated, down to the equivalent level of the terminal bronchioles in the bronchial tree. This model has been constructed to accurately represent available morphometric data derived from the complex asymmetric branching structure of the human pulmonary vasculature in a

form that will be suitable for application in functional simulations in Chapter 5.

4.1 Introduction

Experimental studies to investigate the origin of pulmonary blood flow heterogeneity (Glenny et al. 1999, Glenny, Polissar & Robertson 1991, Hlastala & Glenny 1999) have suggested that non-gravitational mechanisms play a far greater role than was suggested by earlier studies (West et al. 1964). Normal variations in lung tissue material properties, the branching vascular tree, regional gas volumes, and the position of the heart are just a few of the interacting components influencing blood flow distribution in the lung. The contribution of the structure of the pulmonary vascular tree to blood flow heterogeneity has previously been investigated using computational models (Dawson et al. 1999, Glenny, Polissar & Robertson 1991, Krenz et al. 1992, Parker et al. 1997).

Each bronchial airway is accompanied by an arterial vessel, but there are many more pulmonary arterial vessels than there are branches in the bronchial tree; the same is true for the venous system. These vessels, which do not have a corresponding bronchial airway, have been termed 'supernumerary' blood vessels. These very small vessels tend to bud at right angles from the accompanying blood vessels and branch rapidly to directly supply the closest pulmonary acinus. Previous models of the pulmonary vascular trees (Dawson et al. 1999, Glenny, Polissar & Robertson 1991, Krenz et al. 1992, Parker et al. 1997) have not explicitly differentiated the supernumerary vessels from the accompanying vessels, yet these vessels have unique structural and functional differences that may prove to be particularly important in computational studies that investigate perfusion heterogeneity in the normal lung, during exercise, or when a vessel is occluded.

In the current study geometric models of the pulmonary arterial and venous trees are constructed using a combination of multi-detector row computed tomography (MDCT) to identify the largest vessels, a volume-filling branching (VFB) algorithm (Tawhai, Pullan & Hunter 2000) to generate the vessels that accompany airways to the level of the respiratory bronchioles, and a vessel-specific algorithm that incorporates the supernumerary arteries and veins. The focus of this study is on creating a representative geometric model for use in several possible functional investigations. This study develops the framework for creating patient-specific models derived from MDCT scans.

4.2 Methods

4.2.1 Vessels from MDCT images

Grayscale bitmap masks segmented from MDCT data of a normal unsedated human male in the supine posture, with lungs inflated to (and held at) 90% vital capacity (7.05 L), were obtained from the Department of Physiological Imaging at the University of Iowa. The masks are a resource from the Lung Atlas (Li, Christensen, Hoffman, McLennan & Reinhardt 2003), and are the same data set used in derivation of models of the conducting airways by Tawhai, Hunter, Tschirren, Reinhardt, McLennan & Hoffman (2004). A pitch of 1.5, collimation of 1.2, 100 mAs, 120 kV, slice thickness of 1.3 mm, slice increment of 0.65 mm, reconstruction matrix size of 512 x 512, and a field of view of around 35 cm was used for the spiral scanning in a Marconi MX8000 MDCT scanner. Vessel bifurcation points and 1D lines supplying connectivity information were also accessed from the Lung Atlas resource, details on the skeletonisation techniques can be found in (Palagyi, Sorantin, Balogh, Kuba, Halmai, Erdohelyi & Hausegger 2001).

Use of a contrast agent allowed automatic identification of numerous vessels in both the arterial and venous trees (Figure 4.1), but the vessels were not automatically differentiated as arterial or venous vessels. This differentiation was performed manually by first identifying the largest pulmonary arteries and veins, and then following the connectivity of each tree while tagging each successive vessel as either an artery or vein. In many locations the arterial and venous trees passed so closely to each other that the skeletonisation software (Palagyi et al. 2001) was unable to identify them as separate trees. In this case the tree connectivity revealed many more than three vessels converging at a bifurcation point. In most cases the correct classification of the vessels was clear from their orientation or from the relationship between the vessels in the next generation, but for locations where it was not clear no further classification of vessels was made beyond that point.

Each vessel segment (the portion of vessel between two branch divisions) was modeled as a 1D linear finite element through the centre of the vessel. A finite element node was placed at each bifurcation point (at the intersection of 1D centrelines) in the segmented (and classified) tree and the tree connectivity was described by joining elements at the appropriate nodes.

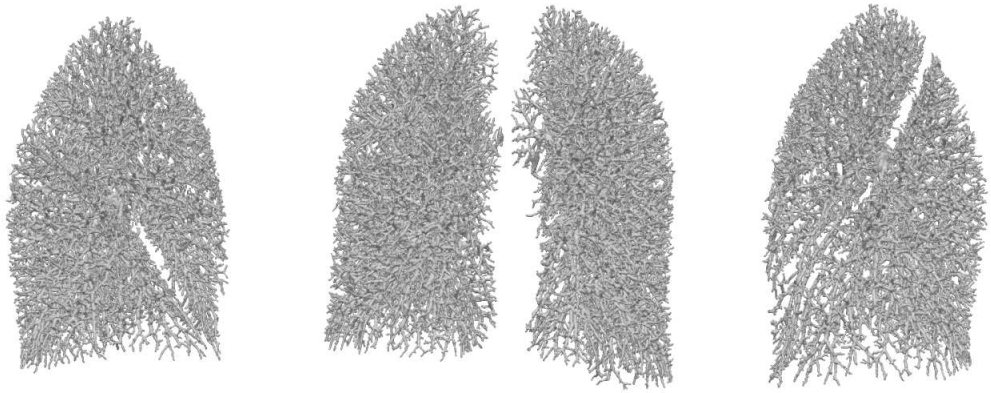

(a) (b) (c)

FIGURE 4.1: *Grayscale bitmap masks of the large arterial and venous vessels segmented from MDCT data of a normal human male: (a) right side view, (b) front view, (c) left side view. The use of contrast agent allows identification of numerous blood vessels, however the arteries and veins are unidentifiable from each other, these masks therefore include both arterial and venous trees. This data was provided by the Department of Physiological Imaging at the University of Iowa, from the Lung Atlas project (Li et al. 2003).*

4.2.2 Accompanying vessels

Anatomical studies have identified a characteristic relationship between the airway, venous, and arterial trees: each airway is 'accompanied' by an artery (Elliot & Reid 1965, Maina & van Gils 2001, Weibel 1963), and is more loosely followed by veins that bifurcate between neighbouring airway and arterial bifurcations (Weibel 1984), as illustrated in the schematic diagram in Figure 4.2. The branching geometry of the accompanying vessels is therefore very similar to the branching geometry of the airway tree. The volume-filling branching (VFB) algorithm - previously developed to model the conducting airway tree (Tawhai et al. 2004, Tawhai et al. 2000) - was therefore used in the current study to generate accompanying arterial and venous vessels such that the models are continuous with the MDCT-derived model trees.

4.2.2.1 Host mesh

The volume-filling algorithm generates a branching tree into a constraining host volume, in this case the pleural cavity. The same pleural volume geometry as defined by Tawhai et al. (2004) was used to generate the blood vessel structure in the current study. Finite element volume meshes of each of the five lobes (Figure 4.3(c)) were fitted

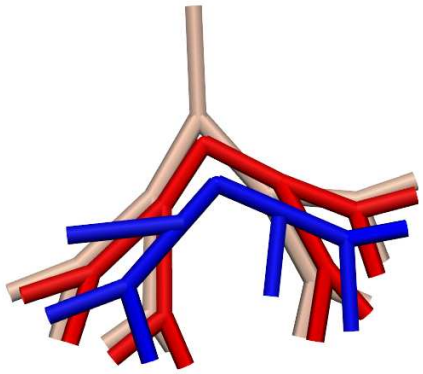

FIGURE 4.2: *Schematic diagram illustrating the relationship between the three conducting trees in the lung; the arteries (red) closely follow the airways (pink), while veins are found to be positioned half way between arterial-airway pairs.*

to data point clouds (Figure 4.3(b)), generated via grayscale information provided by lung surface masks (also obtained from the Lung Atlas) (Figure 4.3(a)) using a geometry fitting procedure (Fernandez, Mithraratne, Thrupp, Tawhai & Hunter 2004). Initial linear elements were fitted to the cloud of data points by minimizing the distance between each data point and the projection of the data point onto the element surface.

Cubic Hermite basis functions are used in the mathematical description of the lobar surfaces, this enables a more accurate description of curved surfaces more efficiently, with a relatively small number of elements (Bradley, Pullan & Hunter 1997).

4.2.2.2 Volume-filling branching algorithm

A VFB (volume-filling branching) algorithm developed in 3D by Tawhai et al. (2000) is implemented in the current study from the MDCT vessel end points to create arterial and venous trees into the MDCT derived pleural host volume.

Each lobe was filled with a grid of uniformly spaced seed points (illustrated schematically in 2D in Figure 4.4(a) which were subdivided according to which MDCT-based vessel they were closest to (N MDCT-model terminal vessels = N sets of seed points) (Figure 4.4(b)). Each set of points was further divided by the plane that contained the centre of mass of the points and the MDCT-model parent branch (2N sets of seed points) (Figure 4.4(c)). The first VFB vessels were generated starting at the end of the corresponding MDCT-model vessel, directed towards the centre of mass of the subset of points, and terminating 40% of the distance to the centre of mass (Figure 4.4(c)) (Tawhai et al. 2004, Tawhai et al. 2000). This generated 2N new model

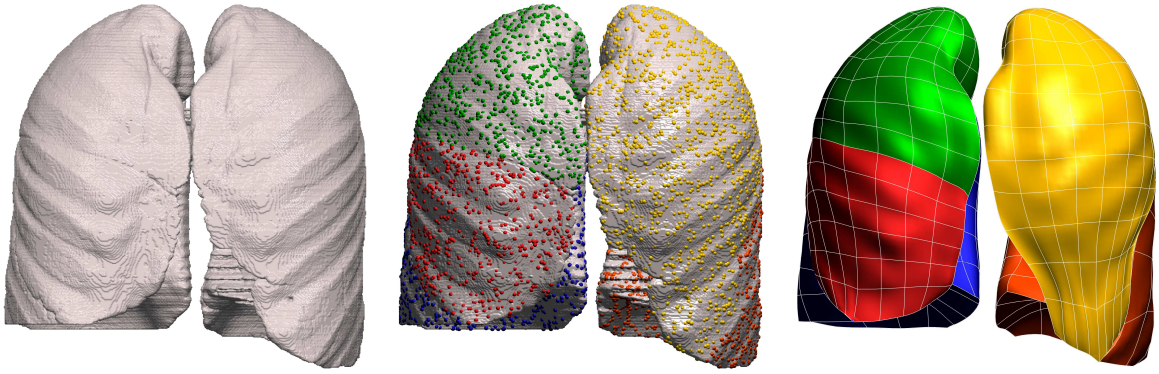

(a) (b) (c)

FIGURE 4.3: *Finite element model of each of the five lobes typical of the human lung (illustrated in different colours): (a) Rendered volumetric image reconstruction from the Lung Atlas (Li et al. 2003); (b) data points created on the surfaces of each of the lobes, a minimisation technique is then used to fit initially linear finite elements to these data points. (c) The final finite element surface model used in the current study obtained using a geometry fitting procedure (Fernandez et al. 2004).*

vessels. The point reassignment (to closest terminal branch), plane splitting, and branch generation steps were repeated (Figure 4.4(d),(e)) until either the generated length was less than a minimum length, or else the new branch supplied only a single seed point. For paths that terminated by length limit, all but the closest seed point to the end of the generated branch were reassigned to the global set of seed points for further branch generation. The VFB algorithm is described in more detail in Tawhai et al. (2004). Figure 4.4(f) displays the final branching structure generated into the simplified 2D rectangle.

Arterial and venous trees were generated using the same seed point density (30,000 terminal bronchioles / 7.05 L (Haefeli-Bleuer & Weibel 1988)), branching fraction (distance to centre of mass = 40%), and angle limit (180^o) as used by Tawhai et al. (2004) for modelling the human conducting airway tree. Minimum vessel lengths of 1.4 mm and 1.8 mm were used for the arterial and venous trees, respectively. These values were chosen using the criteria that the mean length of the generated terminal branches was consistent with anatomical measurements of 1.38 mm (arteries) and 1.34 mm (veins) for the lowest order accompanying vessels (Strahler order 7) (Horsfield 1978, Horsfield & Gordon 1981).

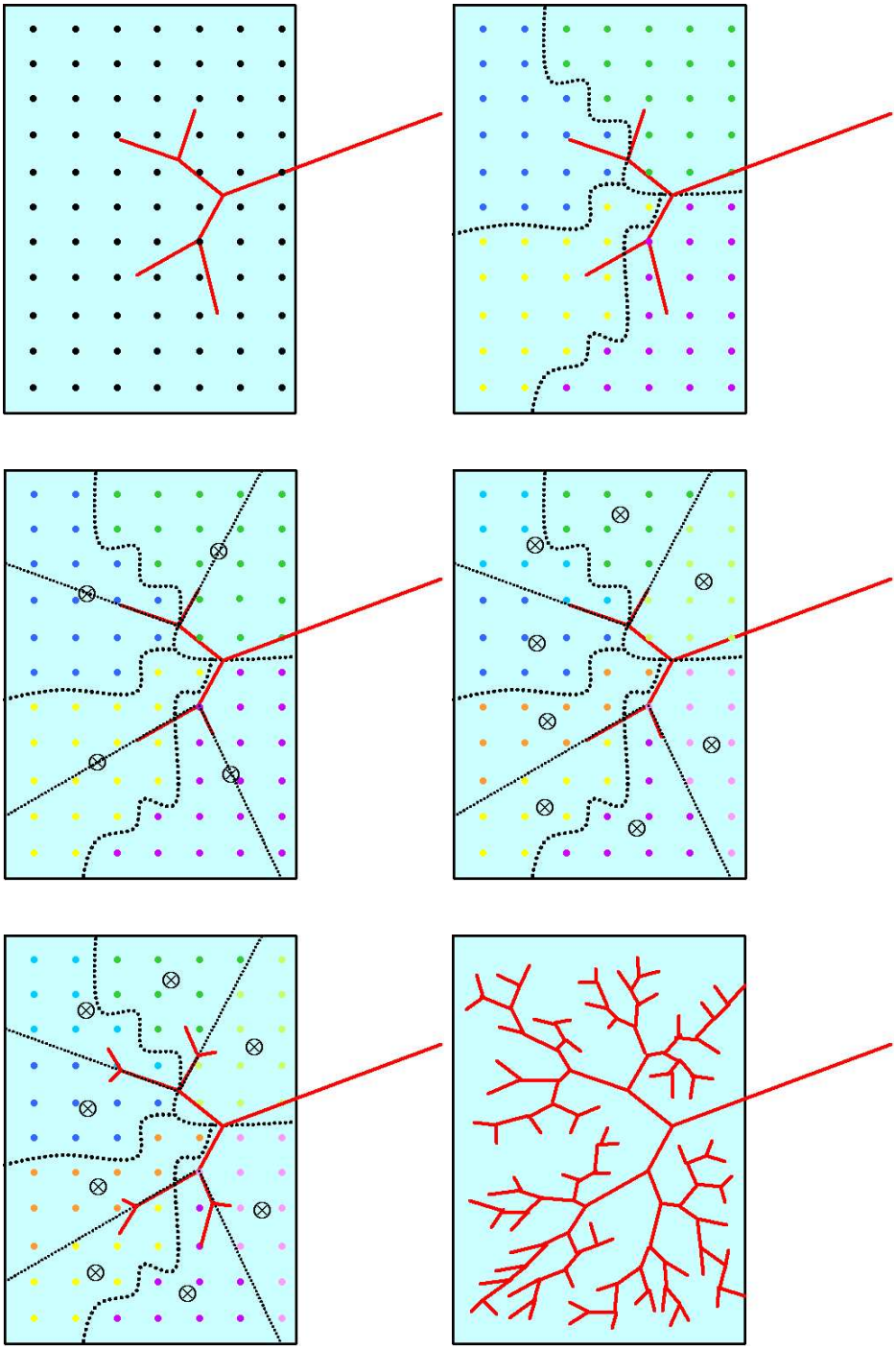

FIGURE 4.4: *Demonstration of the 3D volume-filling branching (VFB) algorithm (represented in 2D) developed by Tawhai et al. (2000) used to generate the geometry of the accompanying (branches accompanying airways) arterial and venous vessels. (a) Evenly space seed points generated within host volume, initial MDCT-derived blood vessels illustrated in red; (b) data points allocated to closest MDCT vessel branch; (c) data set split by plane containing centre of mass of points and MDCT parent branch, new vessel created 40% of distance to centre of mass; (d),(e) this process is repeated either until the branch length is less than a length limit or until the branch supplies a single seed point. (f) Resulting volume-filling branching structure. Images courtesy of M. H. Tawhai, the University of Auckland.*

Diameters for the MDCT-based and VFB-based trees were allocated using anatomically-based Strahler diameter ratios (R_d) (Horsfield 1978, Horsfield & Gordon 1981), such that:

$$logD(x) = (x - N)logR_d + logD_N \tag{4.1}$$

where D is the computed diameter for any vessel of order x, x is the Strahler order, N is the highest vessel order, and D_n is the diameter of the vessel of highest order. Values of R_d = 1.6 (Horsfield 1978) and 1.7 (Horsfield & Gordon 1981) were used for the arterial and venous trees, respectively.

4.2.3 Supernumerary vessel algorithm

An algorithm was developed to mimic the limited known geometric characteristics of supernumerary vessels, and to produce models of the full venous and arterial trees with anatomically-consistent geometry. The following criteria or anatomical information was used:

- Weibel (Weibel 1963) estimated that supernumerary branches begin to emerge when the main tract vessel has a diameter of less than 1.5 mm (beyond approximately the eighth generation). Supernumerary vessels were therefore added to branches of generation 8 and higher in the MDCT- and VFB-based models.
- Supernumerary vessels emerge at roughly 90^o from the accompanying branch and branch rapidly to supply the closest parenchymal tissue;
- The final tree was required to have R_b close to 3.0 and 3.3 for the arterial and venous trees, respectively.

The following steps were used to generate the supernumerary vessels; this procedure is represented schematically in Figure 4.5:

1. The mean ratio of supernumerary vessels to accompanying vessels is specified. For each vessel, the number of local supernumerary branches is calculated as the integer value 1 (i.e. if the overall ratio is 2.7 there will be a 70% chance of having 3 supernumerary vessels per accompanying vessel, and a 30% chance of having 2 supernumeraries per accompanying vessel). Values of 2.5:1 (arterial) and 3.0:1 (venous) were used to produce appropriate branching ratios.

2. The starting point of each supernumerary vessel is located at an evenly spaced position along the length of the accompanying vessel (i.e. if there is one supernumerary vessel it is located half way along the accompanying vessel), and the closest adjacent seed point from the VFB model generation (representing a single acinus) is calculated. The angle this point makes to the parent vessel is checked to ensure it is close to 90^o, if not the next closest point is found.

3. A new branch is created from the accompanying branch towards the closest acinus (seed point). The diameter of the vessel is defined as a fraction of the parent branch diameter (0.3 in the current model for both the arterial and venous systems). The length of the vessel is calculated using length to diameter ratios of 6:1 for the arteries (Horsfield 1978) and 8:1 for the veins (16).

4. The diameter-based Strahler order of each new vessel is determined based upon typical diameter ranges from anatomical data (Horsfield 1978, Horsfield & Gordon 1981). If it is not a terminal branch (Strahler order 6 for the current model) the algorithm proceeds to step 5.

5. If the vessel is to bifurcate the order number is decreased by 1, and the two closest data points are found (limited by an angle specification of between 20^o and 160^o), and each branch then extends towards its closest data point (which is different for each daughter). The diameter is allocated as the average anatomical diameter value for the new Strahler order number of the vessel; the length is set as specified in step 3. The supernumerary vessel successively bifurcates in this manner until a terminal order vessel is obtained, or until the vessel reaches a VFB seed point.

4.2.4 Analysis of branching geometry

Each full model tree (MDCT-based, accompanying, and supernumerary vessels) was classified by Strahler order. The branching, diameter, and length ratios (R_b, R_d, and R_l, respectively) were calculated for each of: MDCT vessels only, MDCT plus accompanying vessels, MDCT plus accompanying plus supernumerary vessels. Branching angles were calculated for the complete model, where θ_{branch} is the angle between a parent and a child branch, and γ (rotation angle) is the angle between the plane containing the parent branch and its sibling and the plane containing the two daughter branches. The angles between the parent and the major (θ_{major}) and minor (θ_{minor}) child branches were also calculated, where the minor branch is classified as the

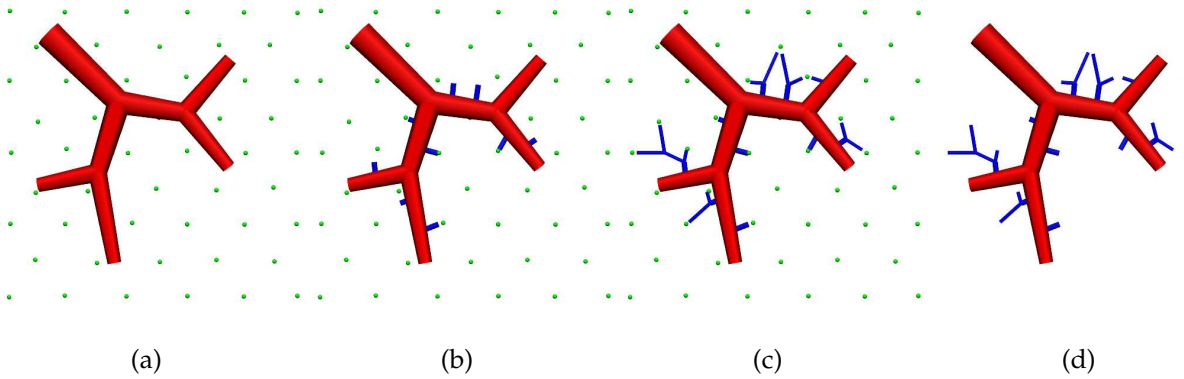

FIGURE 4.5: *Schematic illustration of the supernumerary algorithm: (a) Starting with the accompanying blood vessels and a uniformly distributed grid of points (generated in the VFB algorithm) within the lung volume (each point representing an acinar unit); (b) supernumerary branches emerge at right angles from the accompanying branch and grow towards the closest point; (c), (d) vessels branch and continue to grow towards the closest point, until the point is reached or an order 6 (terminal order) vessel is obtained.*

branch with the smallest diameter, or if both daughter branch diameters are equal the minor branch is defined as the branch with the largest branch angle; the major branch is the other branch of the two.

4.3 Results

4.3.1 Vessels from MDCT

Approximately 2500 branches in each of the arterial and venous trees were manually differentiated from the 1D skeleton of the arterial and venous trees derived from volumetric MDCT images. Arterial paths were identified to between generations 6 and 26 (mean 18), and venous paths were identified to between generations 6 and 23 (mean 15). The isolated MDCT-based vessels had equivalent to 7 (incomplete) Strahler orders in the arterial tree and 6 (incomplete) Strahler orders in the venous tree (note that the venous tree has two less bifurcations at the heart inlet). Figure 4.1 shows the rendered iso-surfaces for the segmented blood vessels (both arterial and venous) from MDCT images. Figure 4.6 displays the separated arterial (red) and venous (blue) vessels extracted from the 1D skeleton derived from MDCT data. Each vessel segment is represented by a 1D line (or finite element), joined by a node at either end of the segment. Diameters are allocated based on Strahler order number and cylinders are

drawn to represent these diameter values.

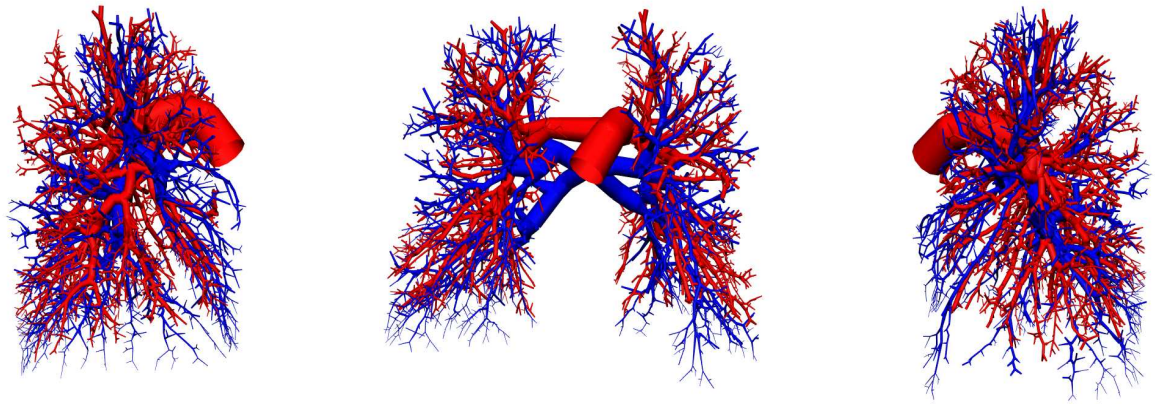

(a) (b) (c)

FIGURE 4.6: *Arterial (red) and venous (blue) vessels obtained from the 1D skeleton information generated from MDCT scan data. Approximately 2500 branches from each of the trees were separated from the MDCT data. 1D lines are used to represent the vessels, joined by a node at either end. Cylinders are drawn using the Strahler order based diameter values. Views shown: (a) right, (b) front, (c) left.*

4.3.2 Accompanying vessels

Generation of accompanying vessels to the level of the respiratory bronchioles produced just more than 57,000 additional branches in each tree, resulting in trees with nearly 60,000 vessels each. The MDCT plus accompanying vessel arterial tree had a total of 11 Strahler orders, compared with 9 Strahler orders for the venous tree. Figure 4.7 shows the MDCT-based and accompanying vessel models for the arterial (red) and venous (blue) models. R_b for the arterial tree was 2.78, and for the venous tree was 2.93 (Table 4.1).

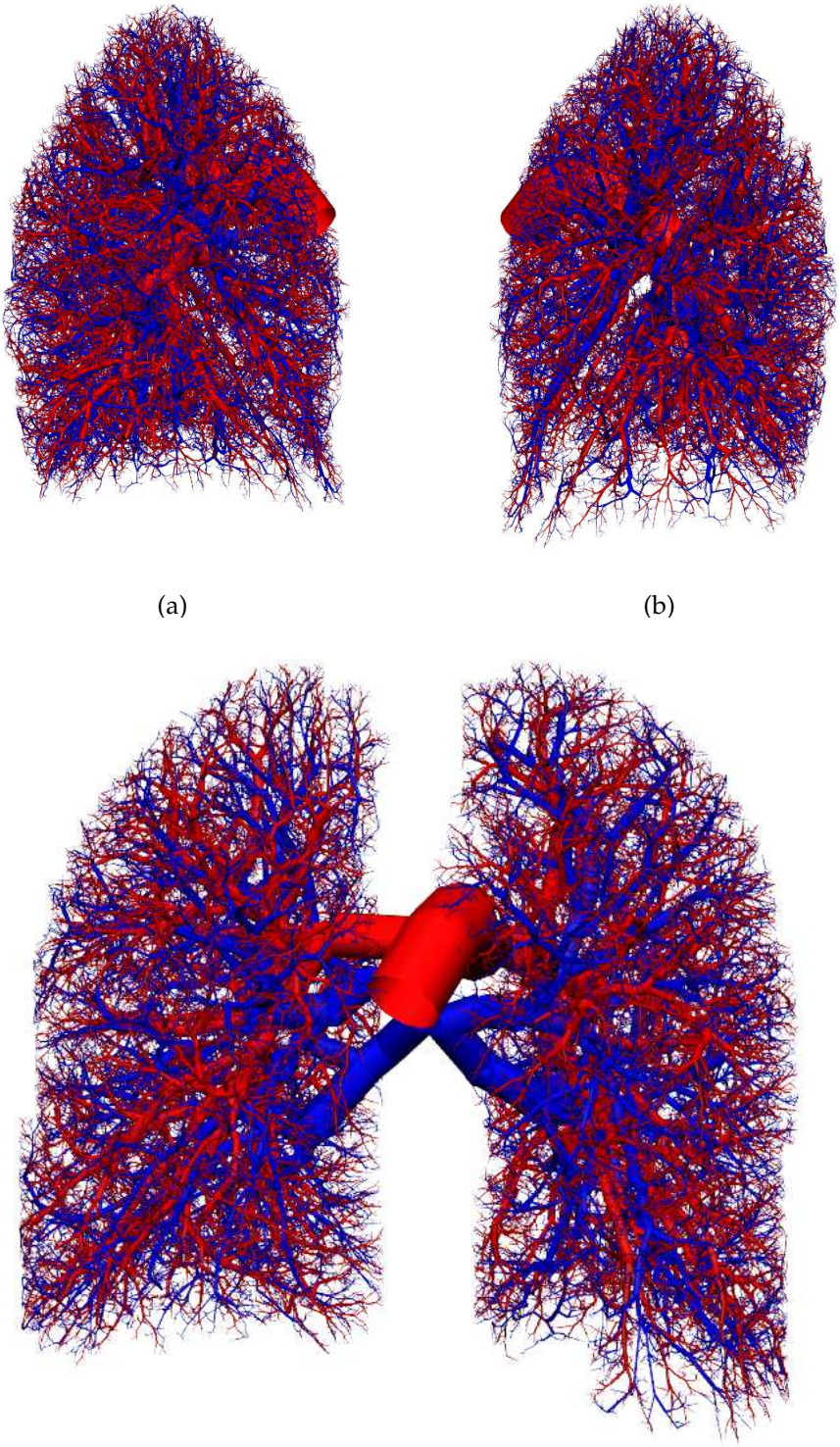

(a) (b)

(c)

FIGURE 4.7: *Resulting arterial (red) and venous (blue) models generated using the volume-filling branching (VFB) algorithm (Tawhai et al. 2000), including major vessels from MDCT scan data. Each tree consists of approximately 60,000 vessels. Each vessel represented by a 1D finite element, with a finite element node at either end. Cylinders drawn representing the Strahler order based diameter values.*

4.3.3 Supernumerary vessels

Addition of the supernumerary vessels increased the total number of vessel segments in the arterial model to approximately 375,000, and the total number in the venous tree to approximately 497,000. A close in view of the supernumerary and accompanying vessels is shown in Figure 4.8. The complete model comprised a total of 12 arterial Strahler orders and 10 venous Strahler orders; that is, addition of the supernumerary vessels increased each tree by only 1 Strahler order. The Strahler R_b increased from 2.8 to 3.0 for the arterial tree, and from 2.9 to 3.4 for the venous tree (Table 4.1), which is much closer to the anatomical values than the MDCT-based plus accompanying vessel models.

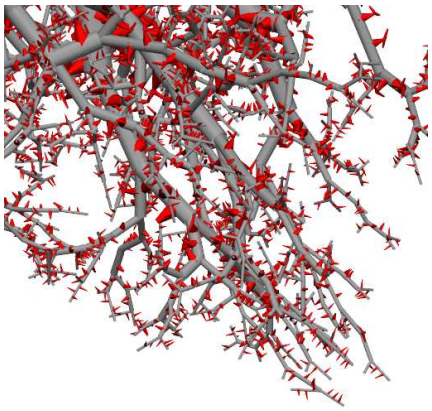

FIGURE 4.8: *Close in view of the model supernumerary arterial blood vessels (red) emerging from the larger accompanying blood vessels (gray). This image demonstrates the vast number of supernumerary blood vessels compared to the number of accompanying vessels, the ratio being 2.5 supernumerary arteries for each accompanying arterial vessel in the final model.*

4.3.4 Geometric analysis

Branching angles calculated for the full vessel model, for the conducting airway model from Tawhai et al. (2004), and from anatomical studies of the airway tree are listed in Table 4.2. Branching angles (branching angle θ_{branch} and rotation angle γ) for the accompanying arterial and venous trees are very similar to those for the conducting airway network. The addition of supernumerary vessels increases θ_{minor} and decreases θ_{major}.

Figure 4.9 plots Strahler order against number of branches for the model at all three stages of development (MDCT, plus accompanying vessels, plus supernumerary

	MDCT vessels	+VFB vessels	+Supernumerary	Anatomical data
R_b arteries	1.29 (R^2=0.16)	2.78 (R^2=0.99)	3.04 (R^2=1.00)	3.03 (6-17) [a], 3.36 (1-15) [b]
R_d arteries	1.57 (R^2=1.00)	1.57 (R^2=1.00)	1.57 (R^2=1.00)	1.60 (1-17) [a], 1.56 (1-15) [b]
R_l arteries	1.42 (R^2=0.77)	1.52 (R^2=0.92)	1.50 (R^2=0.95)	1.49 (1-14) [a], 1.49 (1-15) [b]
R_b veins	1.82 (R^2=0.94)	2.93 (R^2=0.99)	3.41 (R^2=1.00)	3.30 (1-17) [c], 3.33 (1-15) [b]
R_d veins	1.70 (R^2=1.00)	1.65 (R^2=0.99)	1.66 (R^2=1.00)	1.69 (7-14) [c], 1.58 (1-15) [b]
R_l veins	1.83 (R^2=0.98)	1.65 (R^2=0.89)	1.64 (R^2=0.94)	1.68 (7-14) [c], 1.50 (1-15) [b]

TABLE 4.1: *Strahler-based branching, diameter, and length ratios for the three stages of model development: MDCT vessels, plus VFB vessels, plus supernumerary vessels, compared with anatomical data.*

a b c d

[a] (Horsfield 1978)

[b] (Huang, Yen, McLaurine & Bledsoe 1996)

[c] (Horsfield & Gordon 1981)

[d]The numbers in brackets in the anatomical data list represent the Strahler order number range for which the ratio was determined. The data from (Huang et al. 1996) used the diameter-defined Strahler ordering method, therefore the main comparative data considered is that of (Horsfield 1978, Horsfield & Gordon 1981), which is based on the Strahler ordering system.

vessels) and compares with estimated numbers of branches from anatomical studies (Horsfield 1978, Horsfield & Gordon 1981). Figures 4.10 and 4.11 similarly plot the diameter and length values as a function of Strahler order. The different stages of model development are included and compared with anatomical data (Horsfield 1978, Horsfield & Gordon 1981).

	Full arterial model	Full venous model	MDCT + VFB arteries	MDCT + VFB veins	Airway model[a]	Published airway data
θ_{branch}	$47.29^o \pm 42.88^o$	$51.52^o \pm 42.50^o$	$49.37^o \pm 29.04^o$	$50.79^o \pm 29.39^o$	$50.31^o \pm 28.92^o$	37.28^o [b], 39^o, 43^o [c]
γ	$83.27^o \pm 55.58^o$	$81.93^o \pm 53.52^o$	$89.24^o \pm 45.86^o$	$89.91^o \pm 44.60^o$	$89.99^o \pm 43.28^o$	79^o [c], 90^o [d]
θ_{minor}	$83.25^o \pm 19.71^o$	$83.19^o \pm 18.68^o$	$53.32^o \pm 29.45^o$	$54.35^o \pm 29.57^o$	$53.00^o \pm 20.02^o$	-
θ_{major}	$11.23^o \pm 26.50^o$	$19.85^o \pm 35.46^o$	$45.41^o \pm 28.08^o$	$47.23^o \pm 28.77^o$	$47.63^o \pm 28.56^o$	-

TABLE 4.2: *Branching angles of the model generated using a combination of MDCT-derived vessels, VFB algorithm, and supernumerary vessel algorithm, compared with model and anatomical data for the conducting airways.*

a b c d e

[a] (Tawhai et al. 2000)
[b] (Horsfield & Cumming 1967)
[c] (Sauret, Halson, Brown, Fleming & Bailey 2000)
[d] (Horsfield 1985)
[e] Results are mean ± standard deviation. Values from anatomical studies in the final column are followed by their reference in brackets.

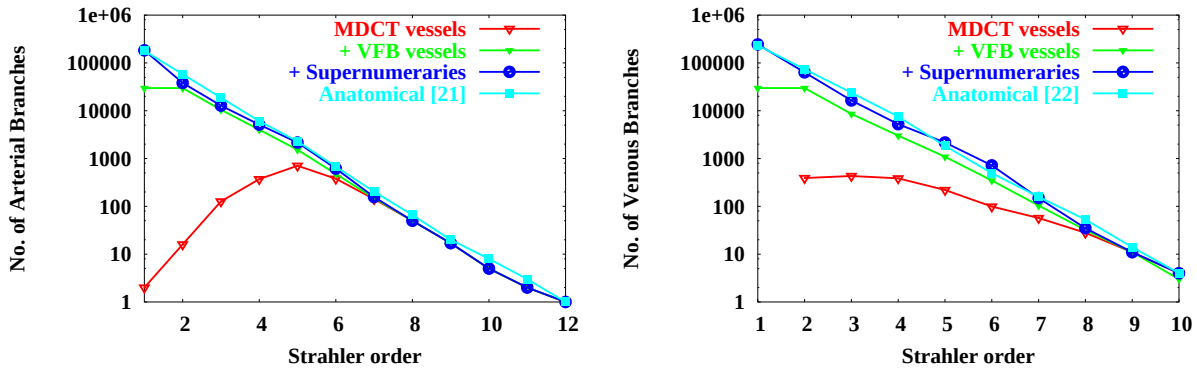

(a) (b)

FIGURE 4.9: *Strahler order number versus number of branches showing the progression of the model towards anatomical data for (a) the arterial and (b) the venous network. Plots show the number of branches from MDCT data, plus VFB vessels, and plus supernumerary vessels.*

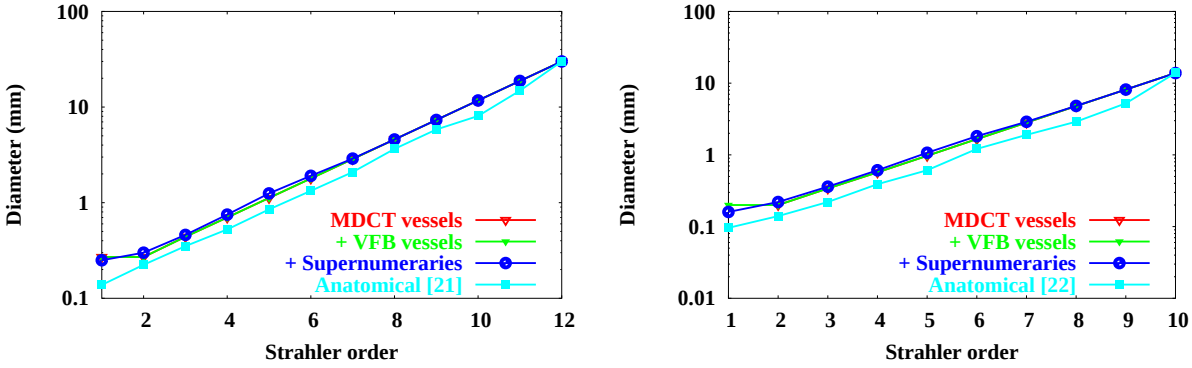

(a) (b)

FIGURE 4.10: *Strahler order number versus branch diameter for different stages of model development for (a) the arterial and (b) the venous network. Plots show the average diameter per Strahler order from MDCT data, plus VFB vessels, and plus supernumerary vessels. Diameters were allocated on the diameter ratio derived from these studies, therefore a good match is shown.*

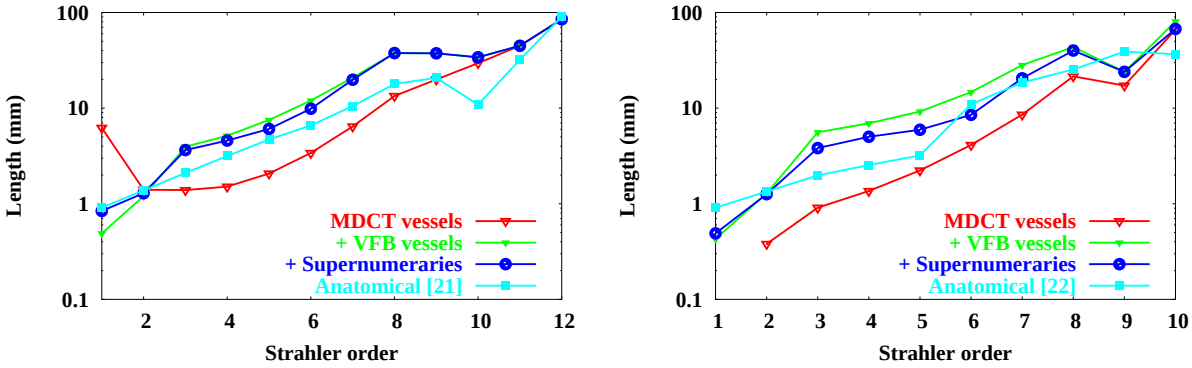

(a) (b)

FIGURE 4.11: *Strahler order number versus branch length showing the different stages of model development for (a) the arterial and (b) the venous network. Plots show the average vessel length per Strahler order from MDCT data, plus VFB vessels, and plus supernumerary vessels.*

4.4 Discussion

Studies into the origin of blood flow heterogeneity in the lung have highlighted the prominent functional significance of the asymmetric branching structure of the pulmonary vasculature, suggesting that gravitational factors are a minor determinant of flow distribution (Glenny et al. 1999). Previous studies have highlighted the intimate relationship between structure and function in the pulmonary circulatory system through both computational (Dawson et al. 1999, Krenz et al. 1992, Parker et al. 1997) and experimental investigations (Glenny et al. 1999, Glenny, Polissar & Robertson 1991). Although these previous models have been based on anatomical measures, they cannot represent the geometry of an individual subject, nor do they provide accurate spatial information. This limits their application in computational studies where the vessel's 3D orientation is important, for example, if correlations between imaging data and model results need to be made. 'Anatomically-based' models - such as presented by Tawhai et al. (2000) for the human bronchial airways, and developed further by Tawhai et al. (2004) for the human and ovine airway tree - are derived from medical imaging and have subject-specific 3D branching geometry. This type of model accurately represents the measured average geometry of the airway tree and has a further advantage of relating individual airways to their location in the lung. The vascular models created in this study are of the same nature, whereby the future possibilities of coupling structural or functional imaging information to computational modeling will allow specific structure-function relationships to be investigated.

The development of a computational model of normal human pulmonary vascular structure can be applied to understanding normal hemodynamics, and investigating the functional changes occurring in pulmonary vascular diseases as a result of vascular remodeling. The current study has developed an anatomically-based finite element model of the human pulmonary macro-circulation that is suitable for application in such studies. The largest arterial and venous vessels were identified from multi-detector row x-ray computed tomography (MDCT) scans from the Lung Atlas (Li et al. 2003). This technique enables a more accurate description of vessel geometry and allows patient- and species-specific models to be generated. A volume-filling algorithm (Tawhai et al. 2000) was initiated from the MDCT-derived vessel endpoints to create a mathematical representation of the smaller accompanying blood vessels unidentifiable from MDCT images. The algorithm 'grows' these vessels into an MDCT defined pleural host volume down to the equivalent level of the respiratory bronchioles. This creates arterial and venous trees which are somewhat governed by the shape of the lobe

surfaces and the positions of the initial MDCT derived vessels, thereby producing a more realistic, integrated model.

4.4.1 MDCT vessels

The MDCT imaging used contrast agent injected into the pulmonary circulation to enhance the contrast between the blood vessels and surrounding tissue. This, however, resulted in an augmented arterial-venous data set from which it was very difficult to extract the separate trees. The segmented images, shown in Figure 4.1, contain both the arterial and venous vessels. There were several points where the two trees met and appeared to join. The two trees were separated by visually predicting which vessels belonged to which system, therefore some uncertainty remains over whether each of the vessels distinguished is correctly allocated to the arterial or venous system. The algorithm used to generate the centreline data in this study resulted in centrelines which were not always accurately located. The complex, intertwining nature of the pulmonary vasculature meant that several of the centrelines went outside of the vessel boundaries and crossed over to meet adjacent vessels. The centreline algorithm also superimposed several bifurcation points on top of each other, so it appeared as if there were multiple branches emerging from a single branch point. In reality it is most likely that the system forms only bifurcations in close succession, and possibly trifurcations, but not higher orders than this, corrections were made to reflect this and ensure no vessels overlapped. On inspection of the actual MDCT segmented vessel surfaces it was apparent that most junctions were bifurcations, and for these reasons the vessels were selected manually. Diameter values for the larger vessels were not able to be derived via MDCT due to the same issues explained above, as the amount of uncertainty was too high. Segmentation algorithms and reconstruction techniques are constantly being improved, and in the near future it should be possible to use automated techniques to obtain more extensive MDCT-derived, patient-specific models of the arterial and venous trees (Shikata, Sonka & Hoffman 2004). MDCT imaging enables the pulmonary vessels to be located and measured in vivo, thereby avoiding any vessel deformation that may occur during casting. The use of high resolution imaging data also provides greater scope for establishing normative ranges of variation in geometry and vessel distension in different orientations or at different blood pressures - which is the goal of the Lung Atlas (Li et al. 2003).

4.4.2 Accompanying blood vessels - VFB algorithm

Tawhai et al. (2004) investigated the influence of lobar geometry and the effect of using MDCT derived vessels as starting points as opposed to lobar branches when using the VFB algorithm on the branching ratio of the conducting airway model. The VFB algorithm was generated into the left and right lung volumes, as opposed to the five separately defined lobes; this caused the Strahler based branching ratio to decrease by 7.5%, demonstrating that the lobar constraining surfaces contribute to the asymmetry of the pulmonary trees. Generation of the VFB vessels from lobar branches decreased the branching ratio a further 5.3% from the initial branching ratio, indicating that the more accurate definition of large vessels via MDCT also increased the asymmetry of the tree. Tawhai shows that the branching geometry of the airway tree (and hence the geometry of the accompanying vessels) is modeled well by the VFB algorithm, regardless of the initial number of MDCT vessels. These comparisons were not sought to be reproduced in this study, however similar behavior has been observed in the current vascular model. This may have implications for generating vascular models for different species, where the shape of the lung is significantly more asymmetric than the human lung.

4.4.3 Supernumerary vessels

Each airway is known to have an accompanying artery and vein, but in addition to these vessels there are also many extra blood vessels unaccompanied by airways - the 'supernumerary' vessels (Elliot & Reid 1965). Morphological studies have shown that pulmonary vascular branching is not a classical dichotomy and that the supernumerary vessels are a characteristic feature of pulmonary arterial and venous trees (deMello & Reid 1991, Elliot & Reid 1965). Supernumerary vessels are not found on angiograms, due to lack of filling, because of the 90^0 angle they make to the axial branch (Elliot & Reid 1965) and the presence of a sphincter, which has been found at the entrance of bovine supernumerary vessels (Shaw et al. 1999). It is thought that these vessels provide a reserve volume during increased cardiac output, such as during exercise (Shaw et al. 1999). Also, in the adult, it is these vessels that can provide collateral blood flow if the conventional vessels are occluded (deMello & Reid 1991). The limited known characteristics of the supernumerary vessels were exploited to develop a computational algorithm to incorporate these vessels into the model. The development of this algorithm was based on the small amount of available

anatomic data. The representation of these vessels is therefore very dependent on the accuracy of measurements from casts. It is very likely that many of these vessels were not adequately perfused during the casting procedure, or that some of these vessels may have been removed in the trimming routine. It can be seen in Figure 4.9 that the addition of the supernumerary vessels increases the number of branches in the last few Strahler orders of the model, bringing the branch number per Strahler order close to the anatomical data. This algorithm may be easily adapted in the future, by modifying the diameter ratio of accompanying to supernumerary vessel, frequency of supernumerary vessels to accompanying vessels, or by modifying the length to diameter ratio, as more measured data becomes available. The frequency values determined to produce the most accurate model, 2.5:1 for the arteries and 3:1 for the veins, are relatively close to the predicted ratios of accompanying to supernumerary vessels of 2.8:1 and 3.5:1 for the arteries and veins, respectively.

4.4.4 Geometric analysis

The current model allocates diameters based on the Strahler order number of each branch. For future functional investigations the diameter relationships may be applied differently to achieve the desired tree qualities. As image processing technologies advance it will be possible to obtain diameter values of the largest vessels via MDCT images, providing a much more accurate model by enabling in vivo data to be used directly as opposed to information derived from casts. Pulmonary arterial diameters have previously been obtained via CT (Karau, Lothen, Dhyani, Haworth, Hanger, Roerig, Johnson & Dawson 2001, Liu, Hoffman & Ritman 1987, Wood, Zerhouni, Horford, Hoffman & Mitzner 1995), but relatively few vessels were measured in these studies.

Figures 4.9(a) and (b) clearly show that the vessel set extracted via MDCT was not complete. Anatomical measures have shown that there is a linear relationship between the Strahler order number and the log of the number of branches in each order. For example, it appears that the vessel set is complete in the arterial network from orders 7 through to 12, and for the venous tree only from Strahler orders 8 to 10. After these points the line in the semi-logarithmic plot of Strahler order versus branch number delineates from the expected straight line.

The Strahler based branching ratios (Table 4.1) are compared with ratios calculated from anatomical data. Only the Strahler ratios are calculated - not Horsfield based ratios - because the Strahler ordering system better describes the asymmetric blood

vessel geometry. The branching ratios increase from relatively low values at the MDCT vessel start point to values very close to the anatomical values for the complete model. The model diameter and length ratios are all within 2.5% of the anatomical values. The asymmetry of the full model arterial and venous trees is therefore closely representative of the measured asymmetry of the human pulmonary vascular trees.

The full model branch angles (Table 4.2) are compared with published values from the conducting airway model developed by Tawhai et al. (2004) and anatomical values for the conducting airways. The branch angle in the MDCT plus accompanying vessel model is higher than the published airway branch angles due to increasing branching angles towards the tree periphery, as explained in (Tawhai et al. 2004). Addition of supernumerary vessels increases the minor branch angle and decreases the major branch angle with respect to the MDCT plus accompanying vessel model, by approximately 30^o for each angle, and for each of the arterial and venous models. This large change in major and minor branch angle reflects the difference in branching geometry of the supernumerary vessels. That is, the minor branch angle in the full model is heavily weighted by supernumerary branching angles close to 90^o, and the major branch angle now includes 'zero' branch angles comprising the continuation of the parent vessel.

4.5 Conclusions

This model has been developed to represent the complex geometry found in the pulmonary circulatory system, for application in structure-function investigations in Chapter 5. The methods for coupling structure and function are well established: the model is simply a finite element mesh within which a system of mathematical equations can be solved, as has previously been demonstrated for blood flow through the pulmonary capillary (Burrowes et al. 2004) and coronary vessels (Smith, Pullan & Hunter 2002). Solution of flow equations through the geometric models developed in this chapter are presented in Chapter 5.

The derivation of lobar and large vessel geometry from MDCT enables the creation of subject-specific anatomically-based models of the pulmonary system with relatively low effort. As imaging and image processing techniques improve it will be possible to derive an increasing amount of information from imaging modalities such as CT. The increasing spatial and temporal resolution of CT imaging will enable unification of structure-to-function correlations via imaging and computational techniques. This

amalgamation provides potential applications in tracking structural changes via imaging (remodeling, vasoconstriction), and investigating the consequences on global lung function via modeling. This is the first known attempt to explicitly incorporate the supernumerary vessels into a vascular model; it is hoped that the development of this model will aid in future computational investigations to determine the functional significance and behavior of these vessels.

A summary of this work can be found in (Burrowes, Tawhai & Hunter 2005*a*).

Chapter 5

Blood Flow in the Large Vessels

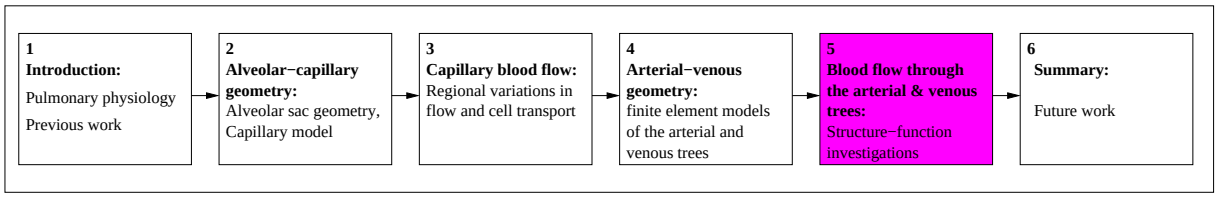

This chapter details the techniques used and results obtained by solution of blood flow equations through the vascular geometries defined in Chapter 4. The Lax-Wendroff numerical technique is used to solve a reduced form of the Navier-Stokes equations within the arterial and venous networks to yield pressure, radius and velocity solutions throughout the system, described in Section 5.2. Hemodynamic structure-function relationships are investigated by comparing the relative influences of the vascular branching structure (Section 5.4.1) and gravity (Section 5.4.2) on blood flow distribution in the lung. Flow results are analysed within different slice 'thicknesses' to illustrate the effect of different resolution data on the interpretation of flow results (Section 5.4.3). Flow distributions in different postures are compared (Section 5.4.5), and the effect of variation in several model parameters, such as pleural pressure (Section 5.4.4), and vessel elasticity (Section 5.4.6) on flow distribution. Transit time results (Section 5.4.7) and pulsatile solutions (Section 5.4.8) are also included in the chapter. The flow solution technique is also applied to a sheep arterial tree geometry and results are compared to the human flow results (Section 5.4.10).

5.1 Introduction

Perfusion of the pulmonary circulation has previously been investigated via direct experiment (West et al. 1964, Glenny et al. 1999, Glenny et al. 2000) or through imaging studies (Levin, Chen & Zhuang 2001, Musch, Layfield, Harris, Melo, Winkler, Callahan, Fischman & Venegas 2002, Jones, Hansell & Evans 2001, Won, Chon, Tajik, Tran, Robinswood, Beck & Hoffman 2003). Although such studies have increased our understanding of both the anatomy and functional mechanisms in the lung, such as the effect of body posture and the relative contribution of gravity to blood flow distribution, the underlying structure-function relationships that result in clinical or experimental observations are not entirely understood.

Evolution of concepts with regard to pulmonary blood flow distribution initiated with the belief of uniform perfusion within the lung. Experimental observations by West et al. (1964) revealed a vertical gradient of reducing blood flow from the least (gravitationally-) dependent to the most dependent regions with the conclusion that hydrostatic pressure differences were the main determinant of blood flow distribution within the lung; this led to the well known zonal flow model (Section 1.3.2). The most recent stage in these changing perspectives has strongly suggested that gravity plays only a minor role in the distribution of blood flow, with non-gravitational components, such as vascular branching structure, playing a more dominant role (Glenny et al. 1999, Glenny, Polissar & Robertson 1991, Hlastala & Glenny 1999).

In order to investigate the relative influences of branching structure and gravity on blood flow distribution in the lung a computational model of flow through the human pulmonary arterial and venous trees has been developed. A reduced form of the Navier-Stokes equations, representing Newtonian fluid flow, are solved within the vascular networks defined in Chapter 4 to yield pressure, radius and velocity distributions. A two step Lax-Wendroff finite difference solution technique is used to solve the flow equations. Simulations are conducted to investigate structure-function relationships in the pulmonary circulation, namely to investigate the following points:

- To evaluate the influence of the asymmetric branching vascular structure on blood flow distribution in the human lung;
- To assess the influence of gravity on blood flow distribution in the human lung;
- To illustrate the effect that different resolution data may have on the interpretation of flow distribution results;

- To investigate the influence of pleural pressure changes during breathing on blood flow distribution in the human lung;
- To investigate the effect of posture on blood flow distribution;
- To evaluate transit times through the pulmonary vasculature, for comparison of model results with experimental data and to increase understanding of the factors governing blood flow distribution;
- To investigate pulsatile flow solutions through the arterial tree;
- To compare model results with experimental measures obtained from functional imaging studies;
- To compare human arterial model flow distributions with flow results obtained in a model of the sheep arterial tree;

5.2 Methods

The solution procedure initially formulated by Hunter (1972) and developed further by Smith (1999) to model three-dimensional pulsatile blood flow with an efficient one dimensional numerical scheme is used to model flow in the pulmonary arterial and venous networks. This section develops a set of nonlinear equations (Equations 5.2, 5.1, and 5.4) relating pressure, velocity, and vessel radius for pulsatile flow through elastic vessels.

5.2.1 Navier-Stokes flow equations

Equations describing fluid motion are in accordance with basic laws of physics which prescribe that mass and energy are conserved, and that Newton's second law (force=mass·acceleration) is obeyed. These principles define the continuity, momentum and energy equations.

The current study models blood flow within the finite element geometric models of the larger pulmonary arterial and venous vessels (Strahler orders 7-11) developed in Chapter 4, as an incompressible, homogeneous, Newtonian fluid, flowing in a laminar state. The flow is also assumed to be axisymmetric. Although studies have predicted that the Reynolds number (=$(2 \cdot \rho \cdot V \cdot R)/\mu$) may exceed 2,000 (the approximate limit for laminar flow) in the largest pulmonary arterial vessels, turbulent flow probably

does not occur, and certainly does not occur in smaller vessels where the Reynolds number is much lower (Horsfield & Woldenberg 1989). Results from the current model display a maximum Reynolds number in the pulmonary trunk of only 587, therefore the assumption of laminar flow appears to be valid. The effect of red blood cells (RBCs) on blood viscosity only becomes significant in the smaller microcirculatory vessels (less than about 300 μm in diameter (Pries et al. 1996)), when the size of the vessels approaches the diameter of RBCs ($<\approx$8 μm (Pries et al. 1996)). The distensibility of the vessel walls is assumed to dominate any effects due to the compressibility of blood (Smith et al. 2002).

By constraining the velocity profile over the cross-section of each vessel, a reduced form of the Navier-Stokes equations can be derived (more details of this derivation may be found in (Smith et al. 2002, Smith 1999, Hunter 1972)). The current study has extended this flow model by the addition of a gravitational component, due to the relatively large hydrostatic pressures exerted over the height of the lung. These equations govern the conservation of mass (Equation 5.1) and momentum (Equation 5.2) of a Newtonian fluid.

$$\frac{\partial R}{\partial t} + V\frac{\partial R}{\partial x} + \frac{R}{2}\frac{\partial V}{\partial x} = 0 \tag{5.1}$$

(see Equation 2.16 in (Smith et al. 2002))

$$\frac{\partial V}{\partial t} + (2\alpha - 1)V\frac{\partial V}{\partial x} + 2(\alpha - 1)\frac{V^2}{R}\frac{\partial R}{\partial x} + \frac{1}{\rho}\left[\frac{\partial p}{\partial x} + \rho g cos(\Theta)\right] = -2\frac{\nu\alpha}{\alpha - 1}\frac{V}{R^2} \tag{5.2}$$

(see Equation 2.22 in (Smith et al. 2002))

where the unknown variables p, R, and V represent the transmural pressure (where transmural pressure is equal to the difference between blood and pleural pressures), vessel radius, and the mean axial velocity. t denotes time, Θ is the vertical angle between the gravitational vector and the vector of the vessel centreline, and g is the acceleration due to gravity (g=9.81 $\mathrm{m\ s^{-2}}$ (1G) or 0 $\mathrm{m\ s^{-2}}$ (0G)). The gravitational effect on pleural pressure is also included, whereby the lung tissue density is assumed to be equal to one-quarter that of the blood density (that is a pressure change of 0.25 $\mathrm{cm\ H_2O}$ per cm height (West 1995)). The term ρ (blood density) has a value of 1.05x10^{-6} $\mathrm{kg\ mm^{-3}}$, and ν (the kinematic viscosity of blood) has a value of 3.2 $\mathrm{mm^2\ s^{-1}}$ for all simulations in this study.

The vessel cross-section velocity profile parameter, α, defines a velocity profile, such

that α=1 corresponds to a flat, uniform profile and the profile becomes more parabolic as α is increased. The velocity profile has the following form:

$$v_x(r) = \frac{\alpha}{2-\alpha} V \left[1 - \left(\frac{r}{R} \right)^{\frac{2-\alpha}{\alpha-1}} \right] \tag{5.3}$$

(see Equation 2.20 in (Smith et al. 2002))

where V is the mean axial velocity. The simulations in this study use a value of α=1.1 (assumed to be constant throughout the network), as fitted to experimental data (Smith et al. 2002, Hunter 1972). The velocity profile for various values of α is displayed in Figure 5.1.

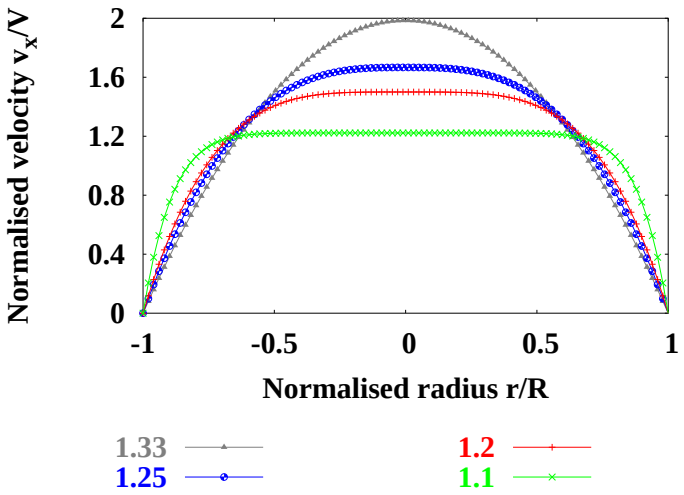

FIGURE 5.1: *The velocity profile across a vessel cross-section (as defined by Equation 5.3), normalised by the mean axial velocity, for various values of α (α values are specified in key).*

The arterial and venous walls are assumed to be elastic, but the viscoelastic properties are ignored in this model. The flow model therefore requires a description of the relationship between pressure and vessel wall radius. An empirically-based relationship between transmural pressure (p) and vessel radius (R) was chosen to best fit available experimental data (Smith et al. 2002), as follows:

$$p(R) = G_0 \left[\left(\frac{R}{R_0} \right)^{\beta} - 1 \right] \tag{5.4}$$

where G_0 and β are constants fitted to experimental data, having values of 5 kPa and 3.2 (dimensionless), respectively, for the arteries and 7.5 kPa and 1.2 for the venous vessels from pulmonary elasticity measures (Yen, Fung & Bingham 1980, Yen

& Foppiano 1981, Krenz & Dawson 2003). These values are assumed to be uniform throughout the network. R_0 denotes the unstrained vessel radius value at p=0 kPa. The pressure-radius relationship is plotted in Figure 5.2 with various values of G_0 and β to display the form of the relationship (where the maximum pressure in this study is 2 kPa). The effect of varying values of G_0 and β on model results is presented in Section 5.4.6.

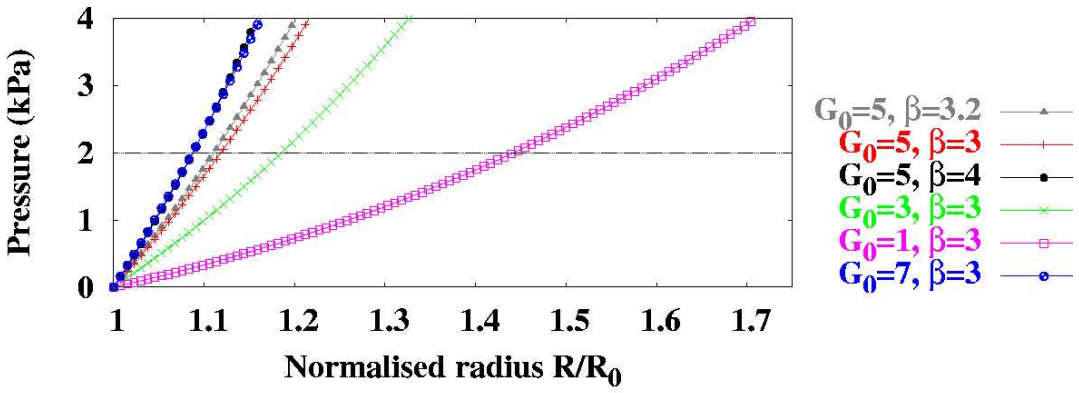

FIGURE 5.2: *Plot of pressure versus radius demonstrating the form of the pressure-radius relationship incorporated into the Navier-Stokes flow solution with various values of G_0 and β.*

Equations 5.1 and 5.2 form a set of two non-linear, first order differential equations, which, with the inclusion of Equation 5.4 can be used to solve for p, R, and V within the pulmonary arterial and venous networks. A steady-state analytic solution for flow through a single vessel is derived (Section 5.2.2.1) and the solution compared with the numerical solution technique developed in Section 5.2.2.

5.2.2 The Lax-Wendroff numerical scheme

The two step Lax-Wendroff explicit, finite difference solution technique is used to solve the Navier-Stokes flow equations (Equations 5.1, 5.2, 5.4). A finite difference grid is generated over the finite element arterial and venous meshes, and solutions are obtained at half and full time steps. The first step computes a set of intermediate points with first order accuracy, the second step calculates second order accurate solutions in both space and time. The general two step Lax-Wendroff procedure is fully outlined in Smith (1999), this work does not seek to replicate the derivation of equations.

Equations 5.5, 5.6, and 5.7 are used to calculate V, p, and R at intermediate or half step points. Superscript k represents a grid point at time step k, and subscript i represents a grid point at a spatial location i.

$$V_{i+\frac{1}{2}}^{k+\frac{1}{2}} = \frac{1}{2}(V_{i+1}+V_i)^k - \frac{\Delta t}{2\Delta x}\left[\frac{2\alpha-1}{2}(V_{i+1}+V_i)(V_{i+1}-V_i)+ \right. \tag{5.5}$$
$$\left.(\alpha-1)\frac{(V_{i+1}+V_i)^2}{R_{i+1}+R_i}(R_{i+1}-R_i)+\frac{1}{\rho}(p_{i+1}-p_i+\Delta x\rho g cos(\Theta))\right]^k - 2\Delta t\nu\frac{\alpha}{\alpha-1}\left[\frac{V_{i+1}+V_i}{(R_{i+1}+R_i)^2}\right]^k$$

$$R_{i+\frac{1}{2}}^{k+\frac{1}{2}} = \frac{1}{2}(R_{i+1}+R_i)^k - \frac{\Delta t}{2\Delta x}\left[\frac{1}{4}(R_{i+1}+R_i)\right. \tag{5.6}$$
$$\left.(V_{i+1}-V_i)+\frac{1}{2}(V_{i+1}+V_i)(R_{i+1}-R_i)\right]^k$$

$$p_{i+\frac{1}{2}}^{k+\frac{1}{2}} = \frac{1}{2}(G_{0_{i+1}}+G_{0_i})\left[\left(\frac{2R_{i+\frac{1}{2}}^{k+\frac{1}{2}}}{R_{0_{i+1}}+R_{0_i}}\right)^\beta - 1\right] \tag{5.7}$$

(see Equations 2.31-2.33 in (Smith et al. 2002))

where Δx is the distance between grid points. Final or full step values are calculated using Equations 5.8, 5.9, and 5.10.

$$V_i^{k+1} = V_i^k - \frac{\Delta t}{\Delta x}\left[\frac{2\alpha-1}{2}\left(V_{i+\frac{1}{2}} + V_{i-\frac{1}{2}}\right)\left(V_{i+\frac{1}{2}} - V_{i-\frac{1}{2}}\right)\right. \tag{5.8}$$
$$\left. + (\alpha-1)\frac{\left(V_{i+\frac{1}{2}} + V_{i-\frac{1}{2}}\right)^2}{R_{i+\frac{1}{2}} + R_{i-\frac{1}{2}}}\left(R_{i+\frac{1}{2}} - R_{i-\frac{1}{2}}\right) + \frac{1}{\rho}\left(p_{i+\frac{1}{2}} - p_{i-\frac{1}{2}} + \Delta x \rho g cos(\Theta)\right)\right]^{k+\frac{1}{2}}$$
$$- 4\Delta t\nu\frac{\alpha}{\alpha-1}\left[\frac{V_{i+\frac{1}{2}} + V_{i-\frac{1}{2}}}{\left(R_{i+\frac{1}{2}} + R_{i-\frac{1}{2}}\right)^2}\right]^{k+\frac{1}{2}}$$

$$R_i^{k+1} = R_i^k - \frac{\Delta t}{\Delta x}\left[\frac{1}{4}\left(R_{i+\frac{1}{2}} + R_{i-\frac{1}{2}}\right)\left(V_{i+\frac{1}{2}} - V_{i-\frac{1}{2}}\right) + \right. \tag{5.9}$$
$$\left.\frac{1}{2}\left(V_{i+\frac{1}{2}} + V_{i-\frac{1}{2}}\right)\left(R_{i+\frac{1}{2}} - R_{i-\frac{1}{2}}\right)\right]^{k+\frac{1}{2}}$$

$$p_i^{k+1} = G_{0_i}\left[\left(\frac{R_i^{k+1}}{R_{0_i}}\right)^{\beta} - 1\right] \tag{5.10}$$

(see Equations 2.34-2.36 in (Smith et al. 2002))

The finite difference equations outlined above provide a means of calculating the values V_i^{k+1}, R_i^{k+1}, and p_i^{k+1} for i=2,N, where N is the total number of grid points. A boundary condition scheme is required to calculate solutions at all peripheral locations at $i = 1$ and N. Initial values are set such that at k=0 V_i^k=0, R_i^k=R_0, and p_i^k=0. Pressure boundary conditions are applied at all inlet and outlet sites. Equation 5.4 can then be used to calculate the radius values at these points. By considering the difference representations for the conservation of mass and momentum equations centred at $(\frac{3}{2}, k+\frac{1}{2})$, the following equation can be derived to determine V_1^{k+1}:

$$V_1^{k+1} = V_2^k + \frac{\Delta t}{2\Delta x}\left[2\alpha\frac{(V')^2}{R'}\left(R_2^{k+1} + R_2^k - R_1^{k+1} - R_1^k\right) - \right.$$
$$\left.\frac{1}{\rho}\left(p_2^{k+1} + p_2^k - p_1^{k+1} - p_1^k + 2\Delta x\rho g cos(\Theta)\right)\right] - 2\Delta t\nu\frac{\alpha}{\alpha-1}\frac{V'}{(R')^2} \tag{5.11}$$
$$+ \frac{1}{R'}\left(\frac{\Delta x}{\Delta t} + 2\alpha V'\right)\left(R_1^{k+1} + R_2^{k+1} - R_1^k - R_2^k\right) - \frac{2V'}{R'}\left(R_1^{k+1} - R_2^k\right)$$

(see Equation 2.45 in (Smith et al. 2002))

where V', R', and p' refer to the points $V_{3/2}^{k+1}$, $R_{3/2}^{k+1}$, and $p_{3/2}^{k+1}$, respectively. An equation to calculate V_N^{k+1} can similarly be derived:

$$V_N^{k+1} = V_{N-1}^k + \frac{\Delta t}{2\Delta x}\Bigg[2\alpha\frac{(V')^2}{R'}\big(R_N^{k+1} + R_N^k - R_{N-1}^{k+1} - R_{N-1}^k\big) - \frac{1}{\rho}\big(p_N^{k+1} + p_N^k - p_{N-1}^{k+1} - p_{N-1}^k + 2\Delta x\rho g cos(\Theta)\big)\Bigg] - 2\Delta t\nu\frac{\alpha}{\alpha-1}\frac{V'}{(R')^2} + \frac{1}{R'}\bigg(-\frac{\Delta x}{\Delta t} + 2\alpha V'\bigg)\big(R_{N-1}^{k+1} + R_N^{k+1} - R_{N-1}^k - R_N^k\big) + \frac{2V'}{R'}\big(R_{N-1}^k - R_N^{k+1}\big) \tag{5.12}$$

Pressure boundary conditions for the pulmonary circuit are applied by the heart at the inlet of the arteries (right ventricle) and at the outlet of the veins (left atrium). In the current model pressure boundary conditions also need to be applied at all terminal arterioles and venules. For most simulations in this study (except Section 5.4.8 where pulsatile flow is investigated) steady-state flow solutions are obtained whereby the inlet pressure is increased to a certain value and held constant until a steady-state flow solution is reached. The normal pressure boundary conditions for the arterial system simulations was 2 kPa at the inlet (pulmonary trunk) and 1.25 kPa at all peripheral branches. For the venous system the normal pressure values were 0.7 kPa at all peripheral branches and 0.2 kPa at the venous exit into the left atrium. The inlet into the two trees was considered the reference height, all peripheral pressure boundary conditions included a gravitational term added to the applied pressure value.

5.2.2.1 Analytic solution for single vessel

In order to validate the numerical solution technique, comparison with an analytic solution for steady state flow in a single vessel can be made. This section derives the analytic equations for flow through a single vessel (again extended from Smith et al. (2002) only by the inclusion of a gravitational component). At steady state all transient terms are equal to zero. Equation 5.2 then reduces to:

$$\alpha V\frac{dV}{dx} + \frac{1}{\rho}\left[\frac{dp}{dx} - \rho g cos(\Theta)\right] = -2\pi\frac{\nu\alpha}{\alpha-1}\frac{V}{S} \tag{5.13}$$

where S is the cross-sectional area of the vessel ($S = \pi R^2$). Given that the velocity V=$\frac{Q}{S}$, and conservation of mass implying a constant flow rate along the vessel, the following expression can be written:

$$\begin{aligned} \alpha V \frac{dV}{dx} &= \alpha \frac{Q}{S} \frac{d\left(\frac{Q}{S}\right)}{dx} \\ &= \alpha \frac{Q^2}{S} d \frac{\left(\frac{1}{s}\right)}{dS} \frac{dS}{dx} \\ &= \frac{-\alpha Q^2}{S^3} \frac{dS}{dx} \end{aligned} \tag{5.14}$$

From the pressure-radius relationship:

$$p(S) = G_0 \left[\left(\frac{S}{S_0} \right)^{\frac{\beta}{2}} - 1 \right] \tag{5.15}$$

therefore:

$$\frac{1}{\rho} \frac{dp}{dx} = \left[\frac{G_0^{\frac{\beta}{2}}}{\rho S_0^{\frac{\beta}{2}}} S^{\frac{\beta}{2}-1} \right] \frac{dS}{dx} \tag{5.16}$$

By substituting Equation 5.14 and Equation 5.16 into Equation 5.13 the following expression can be obtained:

$$\frac{-\alpha Q^2}{S^3} \frac{dS}{dx} + \frac{G_0 \frac{\beta}{2}}{\rho S_0^{\frac{\beta}{2}}} S^{\frac{\beta}{2}-1} \frac{dS}{dx} - g cos(\Theta) = -2\pi \frac{\nu \alpha}{\alpha - 1} \frac{Q}{S^2} \tag{5.17}$$

This is now rearranged and integrated as follows:

$$\frac{dS}{dx}\left[\frac{-\alpha Q^2}{S^3}+\frac{G_0\frac{\beta}{2}}{\rho S_0^{\frac{\beta}{2}}}S^{\frac{\beta}{2}-1}\right]=-2\pi\frac{\nu\alpha}{(\alpha-1)}\frac{Q}{S^2}+gcos(\Theta) \tag{5.18}$$

$$\Rightarrow\frac{dS}{dx}\left[\frac{-\alpha Q^2}{S}+\frac{G_0\frac{\beta}{2}}{\rho S_0^{\frac{\beta}{2}}}S^{\frac{\beta}{2}+1}\right]=\frac{-2\pi\nu\alpha Q+gcos(\Theta)S^2(\alpha-1)}{(\alpha-1)}$$

$$\Rightarrow\int\left[\frac{-\alpha Q^2(\alpha-1)}{-2\pi\nu\alpha QS+(\alpha-1)gcos(\Theta)S^3}+\frac{(\alpha-1)G_0^{\frac{\beta}{2}}S^{\frac{\beta}{2}+1}}{-2\rho S_0^{\frac{\beta}{2}}\pi\nu\alpha Q+(\alpha-1)\rho S_0^{\frac{\beta}{2}}gcos(\Theta)S^2}\right]dS$$

$$=\int 1\quad dx$$

$$\Rightarrow-\alpha Q^2(\alpha-1)\left[\frac{-ln(S)}{2\pi\nu\alpha Q}+\frac{ln\left(2\pi\nu\alpha Q-(\alpha-1)gcos(\Theta)S^2\right)}{4\pi\nu\alpha Q}\right]+$$

$$\frac{(\alpha-1)G_0^{\frac{\beta}{2}}S^{\frac{\beta}{2}+2}{}_2F_1\left[\frac{\beta}{4}+1,1,\frac{\beta}{4}+2,\frac{(\alpha-1)gcos(\Theta)S^2}{2\pi\nu\alpha Q}\right]}{-2\rho S_0^{\frac{\beta}{2}}\pi\nu\alpha Q\left(\frac{\beta}{2}+2\right)}=x+C$$

Where ${}_2F_1[a,b,c,z]$ is the hypergeometric function and has the series expansion defined by Equation 5.19.

$${}_2F_1(a,b,c,z)=\sum_{k=0}^{\inf}(a)_k(b)_k/(c)_kz^k/k! \tag{5.19}$$

The constant of integration C can be determined from Equation 5.18 by substituting the boundary condition of vessel area at the entry point (where x=0) S_i:

$$C=-\alpha Q^2(\alpha-1)\left[\frac{ln(S_i)}{2\pi\nu\alpha Q}+\frac{ln(2\pi\nu\alpha Q-(\alpha-1)gcos(\Theta)S_i^2)}{4\pi\nu\alpha Q}\right] \tag{5.20}$$
$$+\frac{(\alpha-1)G_0^{\frac{\beta}{2}}S_i^{\frac{\beta}{2}+2}{}_2F_1\left[\frac{\beta}{4}+1,1,\frac{\beta}{4}+2,\frac{(\alpha-1)gcos(\Theta)S_i^2}{2\pi\nu\alpha Q}\right]}{-2\rho S_0^{\frac{\beta}{2}}\pi\nu\alpha Q}$$

By substituting Equation 5.20 into Equation 5.18 an equation specifying the steady-state relationship between vessel area S and distance along a vessel x for a given flow rate Q can be obtained.

Figure 5.3 compares the analytic and numerical solutions within a single vessel 50 mm in length. An unstrained radius (R_0) of 1 mm was used, with G_0 and β values of 5 kPa and 1.2, respectively, and inlet and outlet pressures of 2 and 1.25 kPa. The resulting

radius value is plotted with respect to distance along the vessel x, for the solution in a vessel in four different orientations: horizontally (Θ=$\pi/2$), vertically (Θ=0), and with angles of Θ=$\pi/3$ and Θ=$\pi/6$. These results show an ideal match between the analytic and numerical solutions.

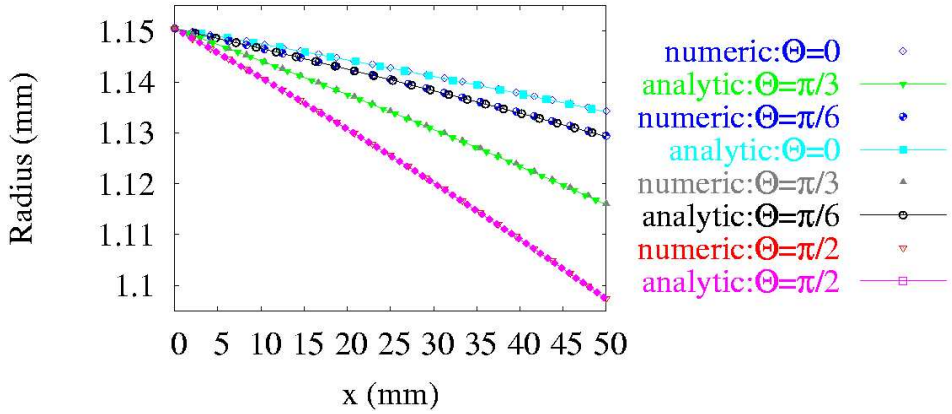

FIGURE 5.3: *Comparison of analytic solution versus numerical Navier-Stokes solution in a single vessel in four different orientations to validate the inclusion of the gravity term: horizontally ($\Theta = \pi/2$), vertically ($\Theta = 0$), and at angles of $\Theta = \pi/3$ and $\Theta = \pi/6$, in a 50 mm vessel with R_0=1 mm, with an inlet pressure of 2 kPa and outlet pressure of 1.25 kPa.*

5.2.2.1.1 Stability In order to maintain the stability of an explicit finite difference scheme the numerical velocity $\frac{\Delta x}{\Delta t}$ must not exceed the wave speed of the governing equations. Given a certain time discretisation (Δt), this criteria can be used to estimate the largest useable spatial discretisation to achieve an accurate, stable solution. This improves the efficiency of computation. An expression to calculate the theoretical wave speed of the numerical solution can be derived from the boundary condition scheme (Smith et al. 2002):

$$\lambda = \frac{dx}{dt} = \alpha V \pm \left[\alpha(\alpha-1)V^2 + \frac{\beta G_0 R^\beta}{2\rho R_0^\beta} + \frac{\Delta x \rho g R cos(\Theta)}{2}\right]^{\frac{1}{2}} \tag{5.21}$$

This expression defines the characteristic directions along which information travels in (x,t) space. Smith (1999) carried out a detailed stability analysis and demonstrated that the stability criteria (Δx and Δt) as defined from the characteristic slope (Equation 5.21) was a good approximation to the von Neumann stability criteria. In the current study Equation 5.21 was used to determine the appropriate grid spacing (Δx) and time discretisation (Δt).

5.2.3 Calculating flow through bifurcations

So far a numerical technique for solving flow through individual vessels has been developed. A separate scheme is required for calculation of flow parameters at a bifurcation. The more empirically-based bifurcation solution scheme was implemented by Hunter (1972) and Smith et al. (2002) and will be explained only briefly in this work. The equations have been modified to include gravitational forces. The forces of gravity on these very small portions of a vessel will most probably be negligible, but the term has been added to ensure accuracy and consistency in the governing equations.

The bifurcation model approximates a junction as three short elastic tubes, sufficiently short such that velocity can be assumed to be constant through each of the tubes. Mass is conserved at the bifurcation, and it is assumed that no fluid is stored in the junction. There are three grid points situated at each vessel bifurcation. A schematic diagram of the bifurcation nomenclature is illustrated in Figure 5.4 (Smith 1999).

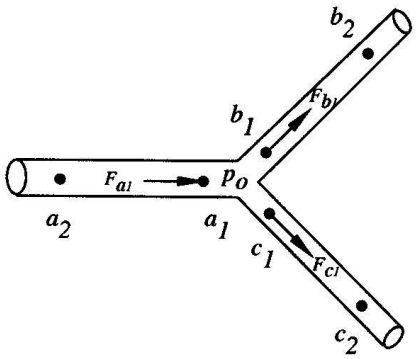

FIGURE 5.4: *Schematic diagram of a vessel junction showing grid point locations (a_1, a_2, b_1, b_2, c_1, c_2), flows (F_{a_1}, F_{b_1}, F_{c_1}), and pressure at the junction (P_0). Figure from (Smith 1999).*

Flow equations coupling boundary conditions of individual vessels ensuring conservation of mass and momentum at each bifurcation are incorporated into the solution procedure. Equation 5.22 represent conservation of mass, and Equation 5.23 governs conservation of momentum for tube a and a bifurcation point.

$$F_{a1}^{k+1} - F_{b1}^{k+1} - F_{c1}^{k+1} = 0 \tag{5.22}$$

$$\pi R_a^2 (p_a - p_0 + \rho g cos(\Theta_a) l_a) = \rho l_a \pi \frac{\partial R_a^2 V_a}{\partial t} \tag{5.23}$$

where subscripts a, b, and c represent the three different segments at a junction, and the indices 1 and 2 represent the location at the junction and adjacent to the junction (that is at the other end of the segment), respectively. Similar conservation of momentum equations can also be written for tubes b and c. A central difference representation about the $(k+\frac{1}{2})$ time step is used to expand Equation 5.23, and results in the following equations:

$$p_{a_1}^{k+1} + p_{a_1}^{k} - p_0^{k+1} - p_0^k + 2\rho g cos(\Theta_a) l_a = \frac{2L_a}{\Delta t}(F_{a_1}^{k+1} - F_{a_1}^k) \tag{5.24}$$

$$p_0^{k+1} + p_0^{k} - p_{b_1}^{k+1} - p_{b_1}^k - 2\rho g cos(\Theta_b) l_b = \frac{2L_b}{\Delta t}(F_{b_1}^{k+1} - F_{b_1}^k) \tag{5.25}$$

$$p_0^{k+1} + p_0^{k} - p_{c_1}^{k+1} - p_{c_1}^k - 2\rho g cos(\Theta_c) l_c = \frac{2L_c}{\Delta t}(F_{c_1}^{k+1} - F_{c_1}^k) \tag{5.26}$$

where F=$\pi R^2 V$, and

$$L_a = \frac{\rho l_a}{\pi R_a^2}, \qquad L_b = \frac{\rho l_b}{\pi R_b^2}, \qquad L_c = \frac{\rho l_c}{\pi R_c^2} \tag{5.27}$$

These lumped parameter constants have a set value of 1x10^{-9} for all simulations in this study (as set by (Smith et al. 2002)). By combining Equations 5.22 and 5.24-5.26 the following equation is constructed to calculate the pressure at a junction at the $k+1$ time step (p_0^{k+1}):

$$p_0^{k+1} = -p_0^k + \frac{\frac{p_{a1}^{k+1}+p_{a1}^k+2\rho g cos\Theta_a l_a}{L_a} + \frac{p_{b1}^{k+1}+p_{b1}^k+2\rho g cos\Theta_b l_b}{L_b} + \frac{p_{c1}^{k+1}+p_{c1}^k+2\rho g cos\Theta_c l_c}{L_c}}{\frac{1}{L_a}+\frac{1}{L_b}+\frac{1}{L_c}} \tag{5.28}$$

where the p_{a1}^{k+1}, p_{b1}^{k+1}, p_{c1}^{k+1}, and p_0^{k+1} are all unknown. By considering the conservation of mass equation (Equation 5.1) and the pressure-radius relationship (Equation 5.4), and using the chain rule to describe $\frac{\partial R}{\partial t}$ as $\frac{\partial p}{\partial t}\frac{dR}{dp}$ and $\frac{\partial F}{\partial x}$ as $2\pi V R\frac{\partial R}{\partial x} + \pi R^2 \frac{\partial V}{\partial x}$ the following equation can be constructed:

$$\frac{\partial p}{\partial t} + \frac{1}{2\pi R}\frac{dp}{dR}\frac{\partial F}{\partial x} = 0 \tag{5.29}$$

Again expanding this using a central difference scheme about the $(k+\frac{1}{2})$ time step yields equations describing the unknown pressures p_{a1}^{k+1}, p_{b1}^{k+1}, and p_{c1}^{k+1} in terms of the known up/downstream values p_{a2}^{k+1}, p_{b2}^{k+1}, and p_{c2}^{k+1}:

$$p_{a_1}^{k+1} + p_{a_2}^{k+1} - p_{a_1}^{k} - p_{a_2}^{k} - A_a \frac{\Delta t}{\Delta x}\left(F_{a_2}^{k+1} + F_{a_2}^{k} - F_{a_1}^{k+1} - F_{a_1}^{k}\right) = 0 \tag{5.30}$$

$$p_{b_1}^{k+1} + p_{b_2}^{k+1} - p_{b_1}^{k} - p_{b_2}^{k} - A_b \frac{\Delta t}{\Delta x}\left(F_{b_2}^{k+1} + F_{b_2}^{k} - F_{b_1}^{k+1} - F_{b_1}^{k}\right) = 0 \tag{5.31}$$

$$p_{c_1}^{k+1} + p_{c_2}^{k+1} - p_{c_1}^{k} - p_{c_2}^{k} - A_c \frac{\Delta t}{\Delta x}\left(F_{c_2}^{k+1} + F_{c_2}^{k} - F_{c_1}^{k+1} - F_{c_1}^{k}\right) = 0 \tag{5.32}$$

where:

$$A_a = \frac{\beta(G_{0_{a1}} + G_{0_{a2}})\left[\frac{2R_{N-1/2}^{k+1/2}}{R_{0_{a1}}+R_{0_{a2}}}\right]^{\beta-1}}{2\pi R_{N-1/2}^{k+1/2} + (R_{0_{a1}} + R_{0_{a2}})} \tag{5.33}$$

Similar expressions can be derived for branches b and c. By using Equation 5.24 to eliminate F_{a1}^{k+1} from Equation 5.30 an expression describing $p_{a_1}^{k+1}$ is terms of interior values which are calculated using the single vessel solution technique. The following equation differs from Hunter (1972) and Smith et al. (2002) due to typographical errors in those references:

$$p_{a_1}^{k+1} = \frac{p_{a_1}^{k} + p_{a_2}^{k} - p_{a_2}^{k+1} + A_a \frac{\Delta t}{\Delta x}\left[F_{a_2}^{k+1} + F_{a_2}^{k} - 2F_{a_1}^{k} - \frac{\Delta t}{2L_a}\left(p_{a_1}^{k} - p_0^{k+1} - p_0^{k}\right)\right]}{1 + \frac{A_a \Delta t^2}{2\Delta x L_a}} \tag{5.34}$$

Corresponding expressions can be written to represent $p_{b_1}^{k+1}$ and $p_{c_1}^{k+1}$. Since p_0^{k+1} is a function of the unknown pressures p_{a1}^{k+1}, p_{b1}^{k+1}, and p_{c1}^{k+1}, an iterative procedure is required to solve the system of equations. Initial pressure estimates are obtained using the explicit scheme outline above. Then, to reduce errors introduced by the terms F_{a1}^{k+1}, F_{b1}^{k+1}, and F_{c1}^{k+1}, a Newton-Raphson iterative scheme is used to simultaneously satisfy conservation of mass and momentum as defined by Equations 5.22, and 5.30-5.32. In most cases the Newton-Raphson bifurcation solution converges in only three iterations. After calculation of the pressure values at a junction the boundary condition scheme (described in Section 5.2.2, Equations 5.10, 5.11 and 5.12) can be used to calculate velocity and radius values.

5.3 Single vessel results

Implementation of the two step Lax Wendroff technique was analysed within a single vessel before applying the numerical technique to a full bifurcating network.

5.3.0.1 Flow profiles

Flow profiles within a single vessel oriented vertically with and without gravity are compared (Figure 5.5). These solutions were obtained within a vessel 50 mm in length with an unstrained radius of 1 mm. The density of blood (ρ) is 1.05x10^{-6} $\mathrm{kg\ mm^{-3}}$ and blood viscosity (ν) is 3.2 $\mathrm{mm^2\ s^{-1}}$. The vessel wall elasticity constants G_0 and β are 5 kPa and 1.2, respectively. The pressure is stepped up at the left end (x=0 mm) of the vessel from an initial pressure value (at both ends) of 1.75 kPa to 2 kPa from time t=0 to t=0.1 s. The pressure at the right end (x=50 mm) is held fixed at 1.75 kPa. Space (Δx) and time (Δt) are discretised by 2.08 mm and 0.1 ms, respectively. Pleural pressure is not included in these solutions.

Figure 5.5 displays pressure, radius, and velocity solutions with respect to distance along the vessel (where x runs from top to bottom) with and without gravity at times t=0, 0.01, 0.02, 0.05, 0.1, and 1 s (at t=1 s the solution was steady-state). Equivalent pressure and therefore radius values are present at the inlet for the two solutions, because the inlet pressure is set as a boundary condition and the inlet is the reference height for gravity (that is, there is no effect of gravity at this point). The solution without gravity displays an initially uniform pressure along the tube; as time progresses inlet pressure increases, resulting in a pressure gradient from 2 to 1.75 kPa from the top to the bottom of the vessel. This results in a decreasing tube radius along the vessel. In contrast, the solutions with gravity display an increasing pressure along the tube at all times, due to the influence of gravity. The outlet boundary condition includes a hydrostatic pressure head of approximately 0.25 kPa meaning that the outlet pressure is fixed at about 2.25 kPa. The increasing pressure is reflected by an increasing radius along the tube length. The resulting velocity profiles are less different than the respective pressure and radius solutions. The velocity wave propagates along the vessel with time. The steady-state velocity without gravity (displayed more clearly in Figure 5.6) displays a slight increase along the vessel, due to the decreasing radius value. The solution with gravity shows the reverse trend, that is a decreasing velocity along the vessel due to an increasing vessel radius. The solution with gravity results in a higher velocity of 126 $\mathrm{mm\ s^{-1}}$, compared to 112 $\mathrm{mm\ s^{-1}}$ without gravity.

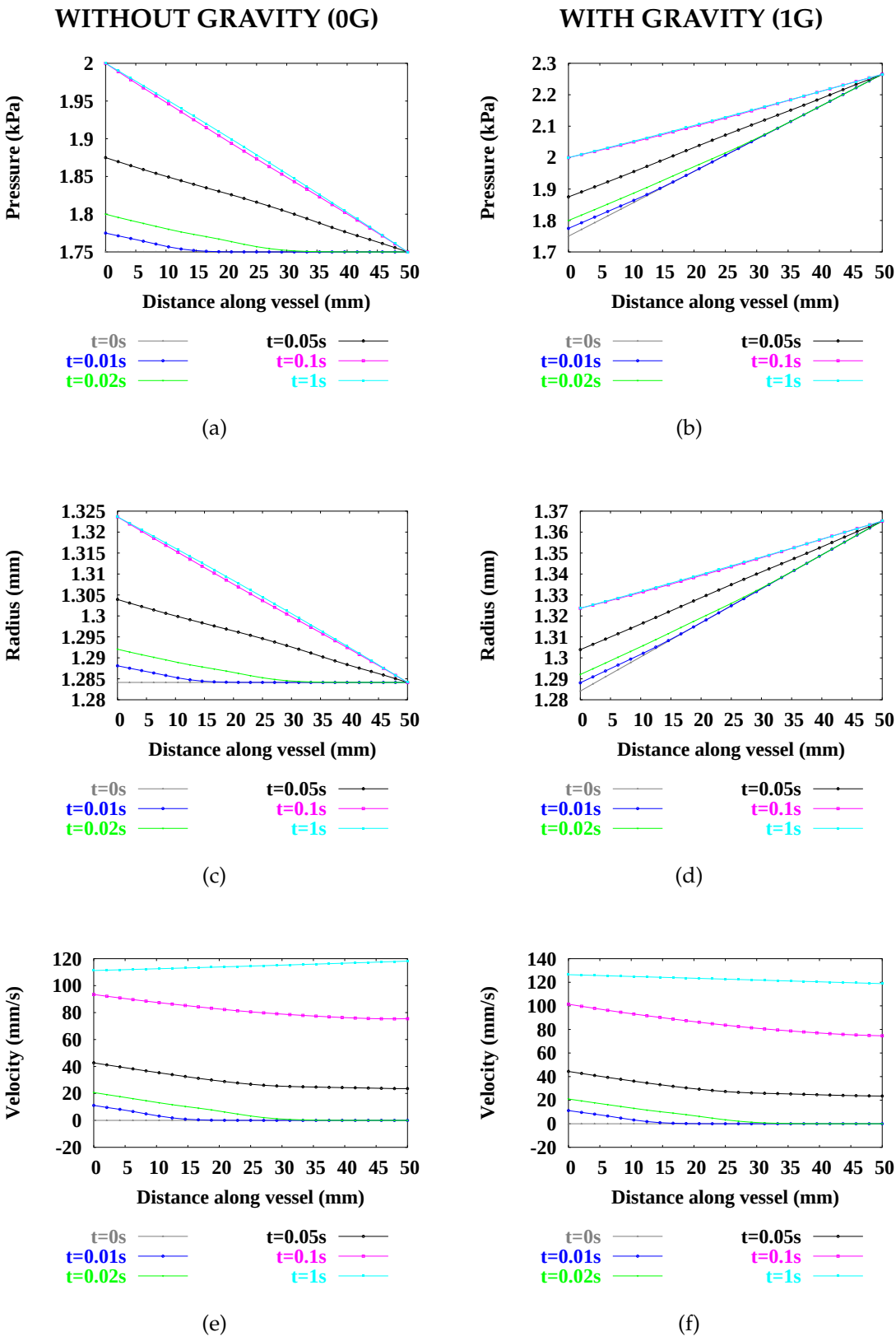

FIGURE 5.5: *Single vessel solution profiles: (a,b) pressure, (c,d) radius, and (d,e) velocity profiles within a single vessel oriented vertically with (g=9.81 $\mathrm{m\ s^{-2}}$) and without (g=0 $\mathrm{m\ s^{-2}}$) gravity, respectively. NB/ x runs from top to bottom.*

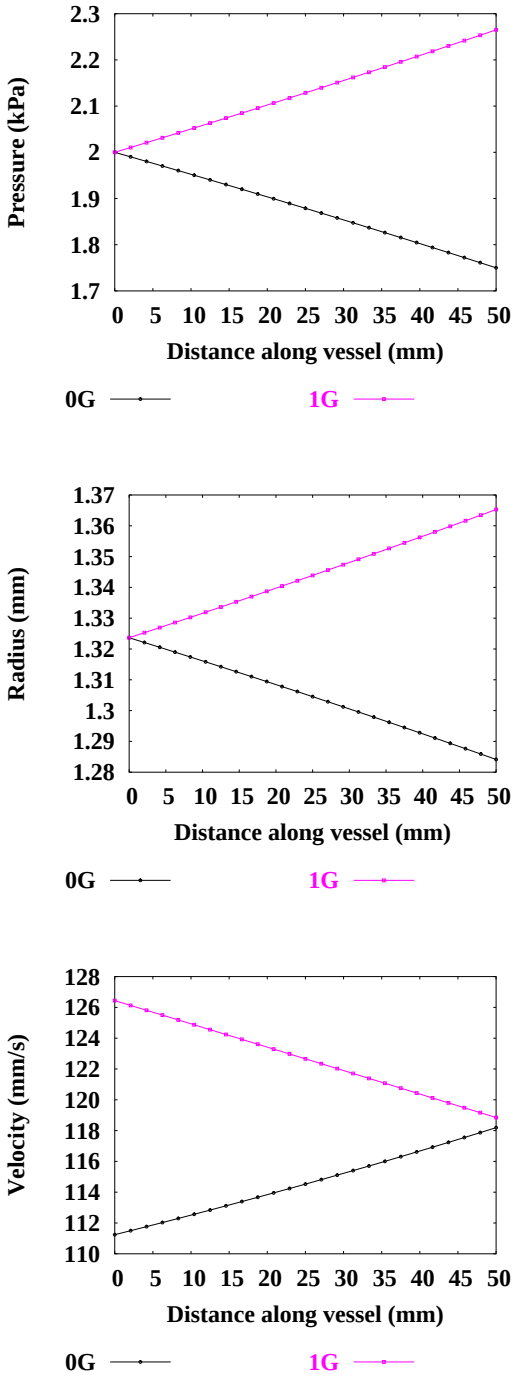

FIGURE 5.6: *Comparison of steady-state (a,b) pressure, (c,d) radius, and (d,e) velocity profiles with respect to distance along a single vessel (x) oriented vertically with and without gravity. NB/ x runs from top to bottom.*

5.3.0.2 Solution convergence

Simulations were conducted within a single vessel (of the same specifications as in Section 5.3.0.1) with various grid spacing values (Δx) to test the convergence of the numerical scheme. Both transient and steady-state velocity profiles along the vessel are presented. Figure 5.7(a) plots the transient velocity solution at t=0.02 s along the length of the vessel. These results show that the transient solutions differ only a small amount for a wide range of Δx values. The steady-state solutions (Figure 5.7(b)) are not significantly different.

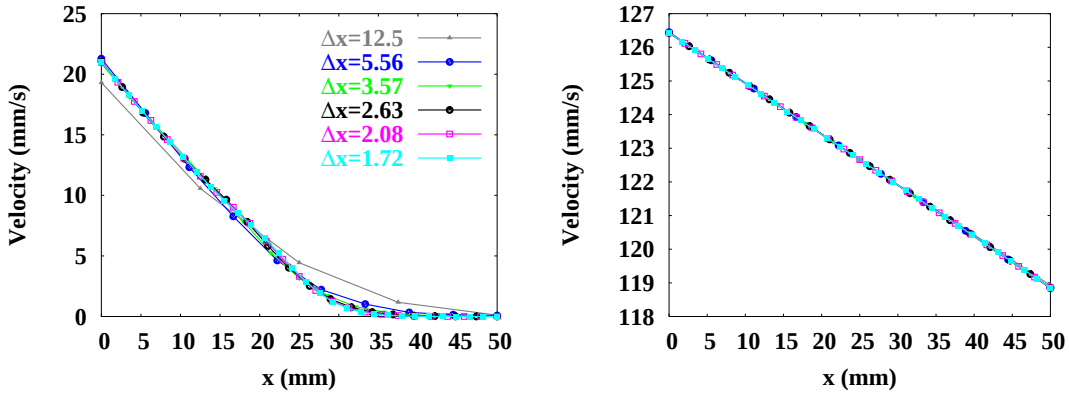

FIGURE 5.7: *Convergence analysis in a single vessel (including gravity): velocity with respect to distance along the vessel x. (a) Displays a transient velocity solution at t=0.02 s, (b) displays the steady state velocity solution ($\mathrm{mm\ s^{-1}}$) for various grid spacings (Δx).*

5.4 Full model results

The full conducting arterial and venous models consist of just over 210,000 grid points each, with 29,818 terminal grid locations in each tree. This grid was created using a Δx discretisation of 2 mm (smaller grid spacings did not give significantly different full model steady-state results). The results included in this section were obtained by applying a steady-state pressure boundary condition, whereby the pressure was linearly increased from t=0 to 0.1 s to the specified value. For all simulations blood was assumed to have a density and viscosity of 1.05x10^{-6} $\mathrm{kg\ mm^{-3}}$ and 3.2 $\mathrm{mm^2\ s^{-1}}$, respectively. The velocity profile parameter α used for all simulations was 1.1 (Hunter 1972, Smith 1999). All simulations in this section assume an upright posture,

unless otherwise stated. Vessel elasticity parameters G_0 and β were set to 5 kPa and 3.2, respectively, for the arterial tree, and 7.5 kPa and 1.2 for the venous tree, respectively.

5.4.1 Blood flow distribution as a function of vascular branching

- To investigate the influence of the anatomically-based asymmetric vascular branching structure on blood flow distribution in the human lung without gravity.

Flow solutions within a symmetric arterial model were compared with solutions in the anatomically-based arterial model (constructed in Chapter 4) in order to assess the influence of the asymmetric vascular branching structure on blood flow distribution in the human lung. Lobar branches (with equal lengths and diameters) were used as the starting points for the symmetric model, and in this respect the model is not entirely symmetric. Each branch in the same generation has the same length and diameter, and each generation is complete. Each bifurcation has a branch angle of 30^o. Daughter branches are rotated by 90^o in the parent plane at each bifurcation. The symmetric model was made to be as similar as possible to the anatomically-based model by aiming to maintain the same number of generations, same total number of branches and approximately the same gravitationally-dependent height (although this was the hardest factor to satisfy). The average lengths and diameters of branches in each Strahler order were also maintained at equivalent values to those used in the anatomically-based model.

The symmetric model has a total of 15 generations. The total number of branches was 32,769 with 16,384 terminal branches. The finite difference grid generated for the flow solution consisted of 115,462 grid points (Δx=2 mm, as was used for the anatomical model). The Strahler branching, length, and diameter ratios were 2.0 (symmetric branching), 1.22, and 1.38, respectively.

Figure 5.8 compares pressure, velocity, and flow solutions in the symmetric and anatomically-based pulmonary arterial models. The pressure solutions range from 1.25 to 2 kPa in both the symmetric model (Figure 5.8(a)) and the anatomically-based model (Figure 5.8(b)), as defined by the inlet and outlet pressure boundary conditions. The simulations in this section exclude gravitational forces and therefore all terminal pressure values have a consistent value of 1.25 kPa. A much narrower velocity range is displayed in the symmetric model between 24.76 to 47.12 $\mathrm{mm\ s^{-1}}$ (Figure 5.8(c)), as opposed to 0.93 to 208.55 $\mathrm{mm\ s^{-1}}$ in the asymmetric model (Figure 5.8(d)).

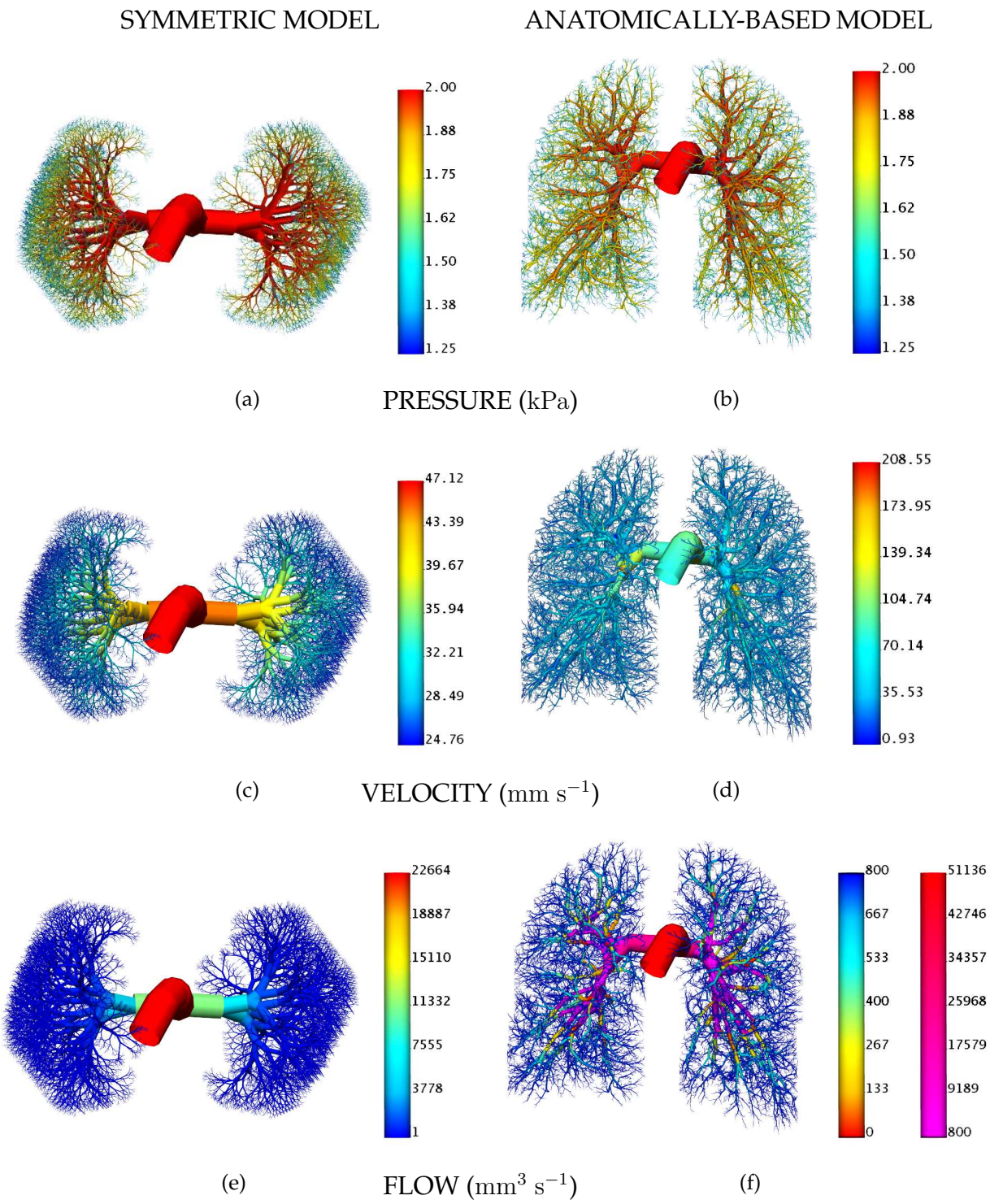

FIGURE 5.8: *(a,b) Pressure (*kPa*), (c,d) velocity (*mm s^{-1}*), and (e,f) flow (*mm^3 s^{-1}*) solutions in the symmetric and anatomically-based arterial models, respectively, without gravity (0G), to evaluate the influence of branching structure on blood flow distribution. Flow values are calculated from radius and velocity solutions.*

Flow values (Q) were calculated from the radius and velocity solution fields (Q=$V\pi R^2$), the symmetric flow rates ranging from 1.38 to just over 22,663 $\mathrm{mm}^3\ \mathrm{s}^{-1}$ in the largest vessel (Figure 5.8(e)), and from approximately 0.05 to 51,135 $\mathrm{mm}^3\ \mathrm{s}^{-1}$ in the anatomically-based model (Figure 5.8(f)). Due to the large range of flow rates in the anatomic model, two spectrums were used to illustrate the flow solution. The highest flow rate values were present in the largest vessels, due to the relative size of the vessel cross-sections.

All terminal grid points were extracted from the models and solution averages were obtained within slices of 1 and 50 mm in thickness from the top to the bottom of the vertical lung. Pressure, radius, velocity, and flow values are plotted in Figure 5.9 with respect to the normalised vertical position in the lung for the two geometric models.

All terminal locations have a pressure value of 1.25 kPa, defined by the outlet pressure boundary condition. The terminal nodal radius values were 0.1317 mm (unstrained radius, R_0=0.1200 mm) and 0.1259 mm (R_0=0.1146 mm) in the symmetric (S) and anatomical (A) models, respectively (Figure 5.9(a)). Both velocity (Figure 5.9(b)) and flow (Figure 5.9(c)) solutions within the symmetric model at a certain height are homogeneous, as opposed to results in the asymmetric model with 1 mm averages showing marked heterogeneity. Flow solutions in the anatomically-based model averaged within 50 mm slices show a clearer relationship between velocity and flow and vertical position in the lung, with the lowest flow being present in the very lowest regions of the lung. The symmetric model displays no gradient with respect to velocity or flow and vertical position in the lung.

Transit time information for each pathway can also be extracted from the model. Figure 5.10 plots path lengths (averaged within 1 mm slices) and transit time results with respect to the normalised vertical position in the respective arterial models. The symmetric model displays a uniform path length for all pathways of about 220 mm, while the anatomically-based model displays longer path lengths over the whole lung. The longest path lengths are present in the upper and lower regions of the anatomically-based model. All pathways in the symmetric model have a blood transit time of approximately 5.5 s, while the asymmetric model displays a range of transit times from 3.5 s (in the mid region of the lung) to 7.3 s in the bottom of the lung.

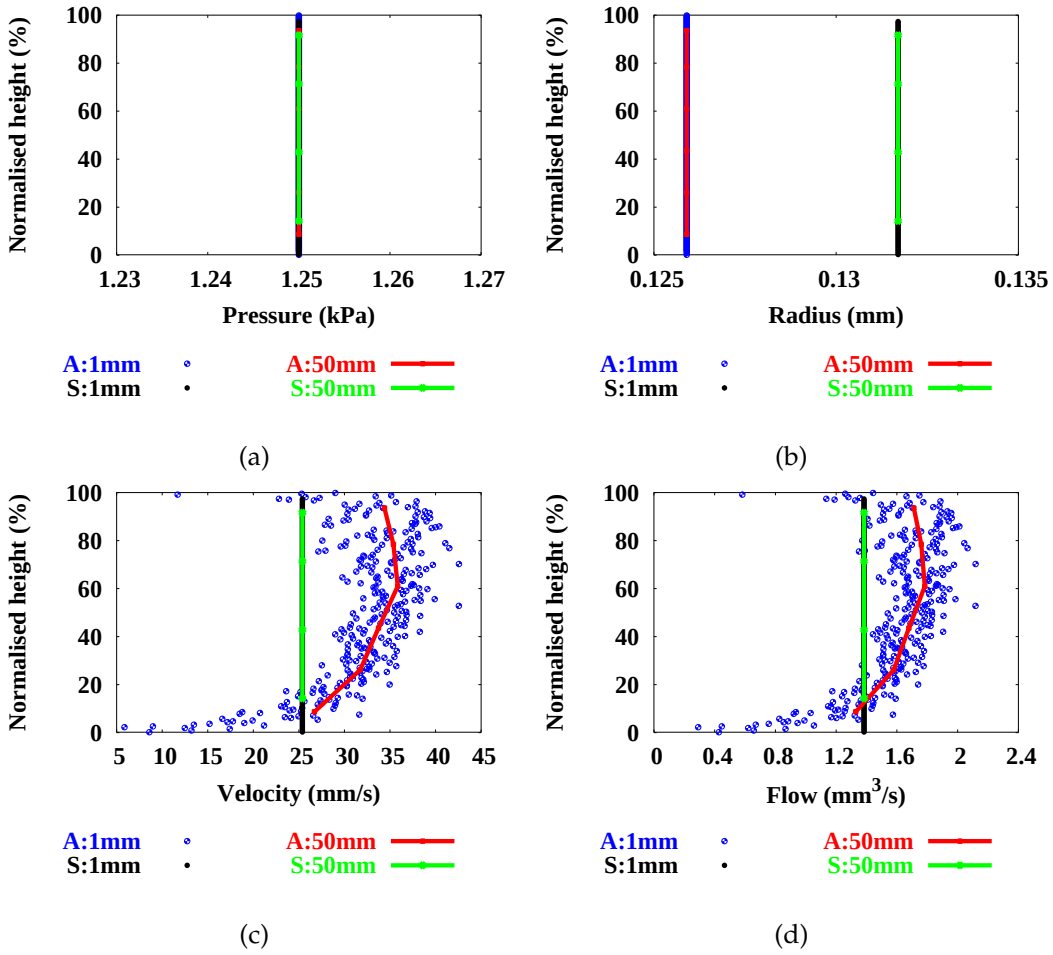

FIGURE 5.9: *Comparison of flow solutions in the symmetric (S) versus anatomically-based (A) arterial models without gravity at all terminal nodal locations averaged within 1 and 50* mm *slices: (a) pressure* (kPa)*, (b) radius* (mm)*, (c) velocity* (mm s^{-1})*, and (d) flow* (mm^3 s^{-1}) *values, all plotted with respect to the normalised vertical height (%) in the lung.*

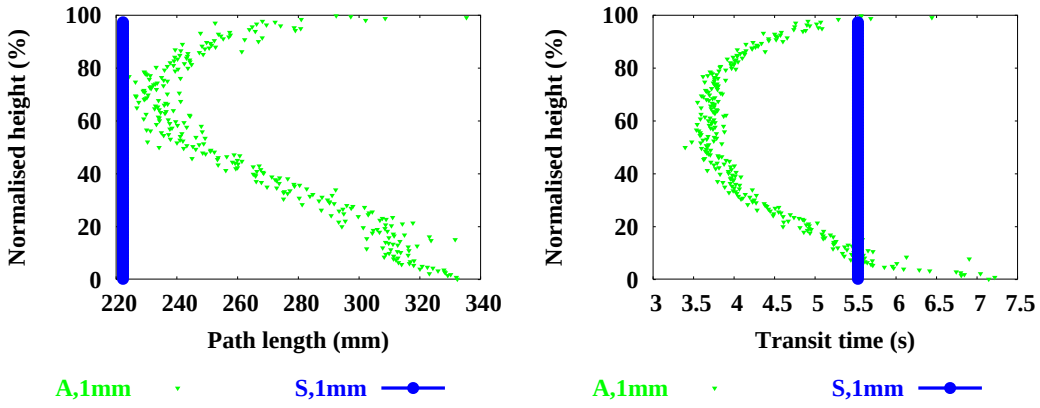

(a) (b)

FIGURE 5.10: *Comparison of (a) path lengths* (mm) *and (b) transit time* (s) *solutions in the symmetric versus anatomically-based arterial model plotted with respect to normalised height in the lung (%). Solutions are averaged within 1* mm *slices and are without gravity.*

5.4.2 Blood flow distribution as a function of gravity

- To assess the influence of gravity on blood flow distribution in the human lung.

5.4.2.1 Symmetric versus anatomically-based arterial flow (with gravity)

The simulations in this section incorporate a gravitational component, where g=9.81 $\mathrm{m\ s^{-2}}$ is equal to 1G. Solutions in the symmetric model are again compared with flow solutions in the anatomically-based arterial model, including gravity.

Pressure in the symmetric model ranges from 0.23 to 2.48 kPa (Figure 5.11(a)), and from 0 to 3.2 in the more realistic asymmetric model (Figure 5.11(b)). The larger pressure range in the anatomically-based model is due to the greater vertical height of the model, and therefore a larger hydrostatic pressure difference due to gravity. The velocity values range from 22.97 to 47.17 and 0.97 to 212.61 $\mathrm{mm\ s^{-1}}$ in the symmetric (Figure 5.11(c)) and anatomical models (Figure 5.11(d)), respectively. The range of flow rate values is also narrower in the symmetric model, where flow ranges from approximately 1 to 22,254 $\mathrm{mm^3\ s^{-1}}$ (Figure 5.11(e)), as opposed to 0.05 to 51,587 $\mathrm{mm^3\ s^{-1}}$ in the more realistic arterial model (Figure 5.11(f)).

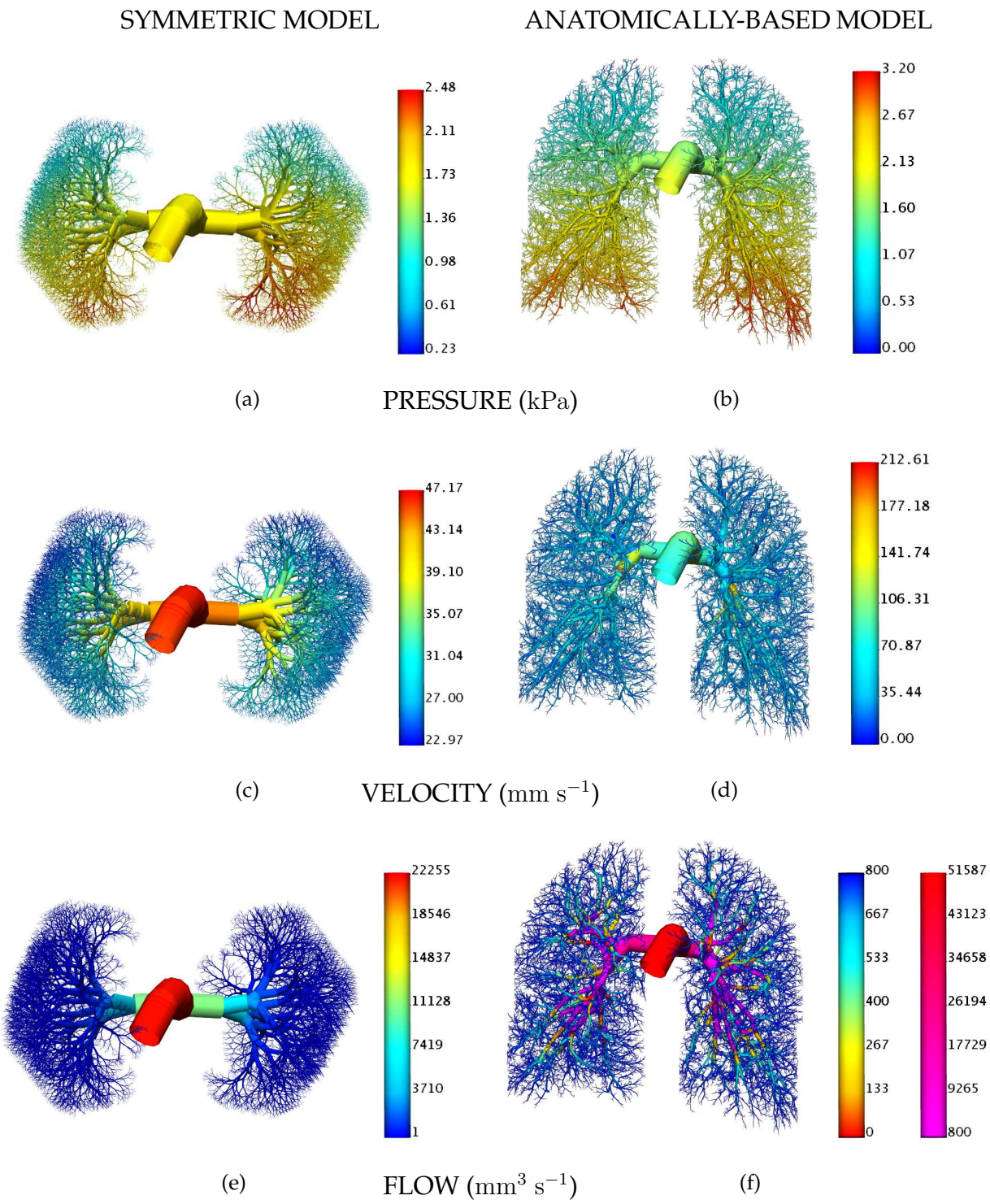

FIGURE 5.11: *(a,b) Pressure* (kPa)*, (c,d) velocity* (mm s^{-1})*, and (e,f) flow* (mm^3 s^{-1}) *solutions in the symmetric and anatomically-based arterial models, respectively, with gravity (1G), to evaluate the influence of branching structure on blood flow distribution. Flow values are calculated from radius and velocity solutions.*

Figure 5.12 compares flow results in the symmetric (S) versus anatomically-based (A) models at terminal locations with (1G) and without (0G) gravity. Pressures range from approximately 0.2 to 2 kPa in the symmetric model with gravity (1G - Figure 5.12(a)). The initial radius values of the terminal symmetric nodes (at time=0) were equal to the radius values in the asymmetric model at time=0. The final radius results at terminal positions are all slightly larger in the symmetric model. This leads to a slight offset in the velocity and flow solutions, but the trends can be compared. The radius values range from 0.127 to 0.135 mm in the symmetric model, as opposed to 0.12 to 0.133 mm in the anatomically-based model (Figure 5.12(b)). Both models display the same trend in pressure and radius with respect to vertical position in the lung, that is, increasing pressure and radius from the top to the bottom of the lung.

Velocity (Figure 5.12(c)), and therefore flow (Figure 5.12(d)), solutions in the symmetric model are much more homogeneous than in the asymmetric model. All path lengths in the symmetric model were equal (Figures 5.10 and 5.13), the diameters and therefore resistance in each pathway was also equal, resulting in homogeneous solutions at all terminal locations with respect to vertical height. All terminal velocities in the symmetric model without gravity are 25.4 $\mathrm{mm\,s^{-1}}$, when gravity is included the velocity solutions have only a narrow range roughly between 23.6-26.1 $\mathrm{mm\,s^{-1}}$, indicating that gravity has only a small influence on terminal velocity solutions. Similar results are displayed with flow rate values, where there is a flow range of approximately 1.2-1.5 $\mathrm{mm^3\,s^{-1}}$ with gravity, as opposed to a constant of 1.38 $\mathrm{mm^3\,s^{-1}}$ without gravity.

Transit time results are again compared between the two different models (Figure 5.13). The path length data will be the same as the solutions without gravity (displayed in Figure 5.10(a), but this information is again displayed in Figure 5.13(a)) because the model geometry has not changed. The transit time results of the symmetric (S) versus asymmetric (A) models with and without gravity are compared in Figure 5.13(b). With gravity included, the symmetric model results display a slight gradient of decreasing transit time from the top to the bottom of the lung, consistent with an increasing velocity (Figure 5.12(c)). The transit time results in the anatomically-based model are similar with and without gravity.

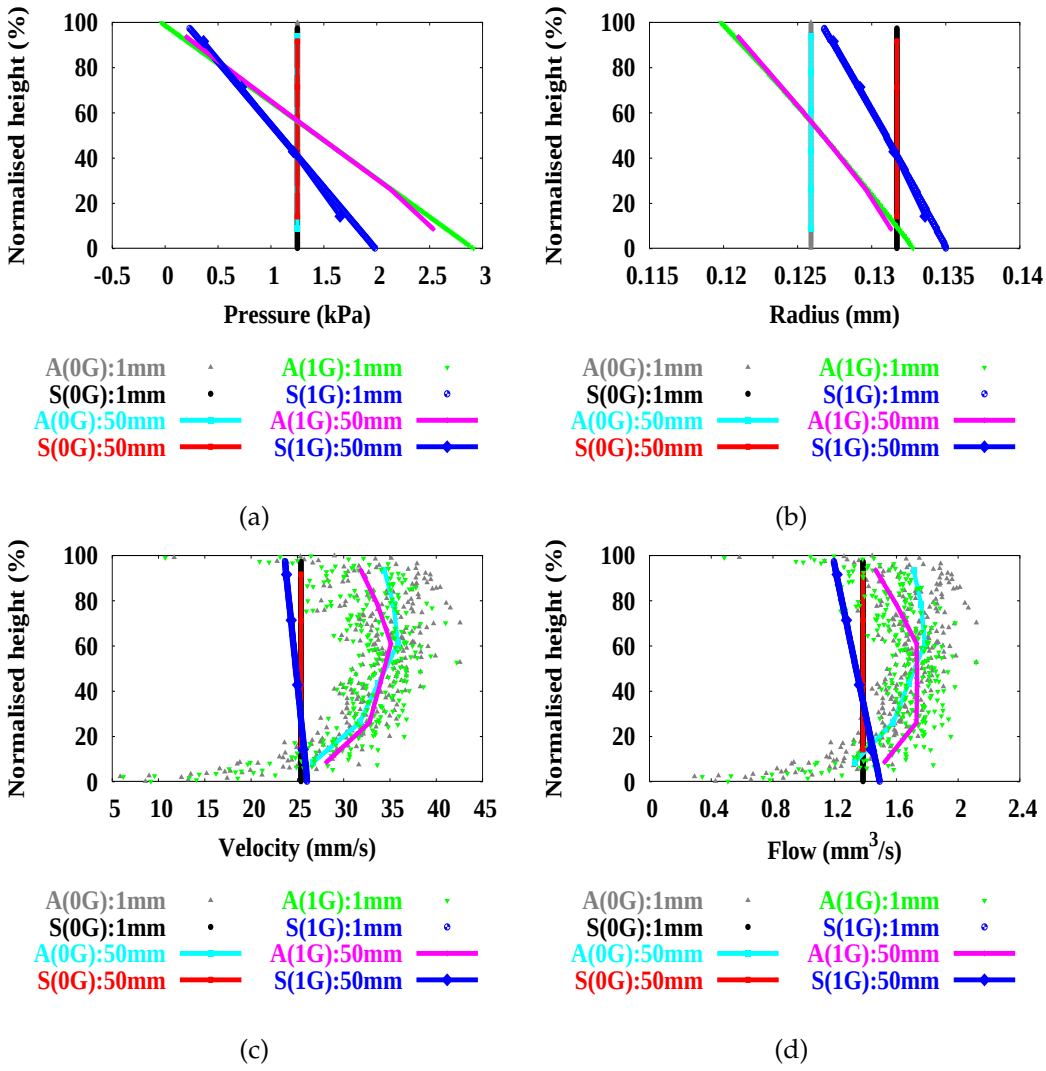

FIGURE 5.12: *Comparison of flow solutions in the symmetric versus anatomically-based arterial models with respect to gravitationally-dependent height with (1G) and without (0G) gravity at all terminal nodal locations averaged within 1 and 50* mm *slices: (a) pressure* (kPa)*, (b) radius* (mm)*, (c) velocity* (mm s^{-1})*, and (d) flow* (mm^3 s^{-1})*values.*

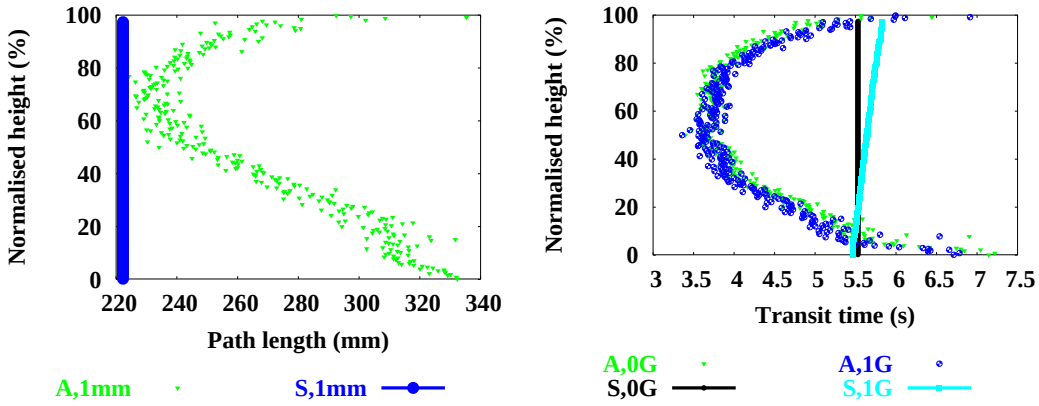

(a) (b)

FIGURE 5.13: *Comparison of (a) path lengths* (mm) *and (b) transit time* (s) *solutions in the symmetric versus anatomically-based arterial models plotted with respect to normalised height in the lung (%). Transit time results with and without gravity are included in (b). Solutions are averaged within 1* mm *slices and include gravity.*

5.4.2.2 Effect of gravity in the anatomically-based arterial model

In order to evaluate the effect of gravity on blood flow distribution in the arterial tree, comparisons are made between solutions with and without gravity. The pressure at all terminal vessels was fixed at 1.25 kPa and the inlet pressure was increased from 1.25 to 2 kPa from t=0-0.1 s. The results presented here are steady-state solutions.

Pressure, velocity and flow results in the anatomically-based arterial model with (1G) and without (0G) gravity are displayed in Figure 5.14. Without gravity all terminal pressure values are constant. When gravity is included in the solution a clear gradient of increasing pressure from top to bottom is seen in the arterial model. The effect of gravity on the velocity and flow solutions is less clear. The highest velocity values in the arterial model (Figure 5.14(c,d)) are within branches of about the fourth generation of branching. These high velocities result from a relatively large drop in branch radius at the bifurcation points. Since flow must be conserved, a drop in radius results in a consequential increase in velocity. Attempts were made to include tapering of vessels into the model, but results could not be achieved under these conditions due to stability issues. Relatively high velocities are also present in the terminal vessels. Flow values (Figure 5.14(e,f)) are calculated from the radius and velocity solutions. The highest flow rates are in the largest vessels and flow decreases towards the peripheral branches as individual vessel cross-sectional area decreases. The peak velocity and flow values increased by only 1.9 % and 0.9 % with the addition of gravity.

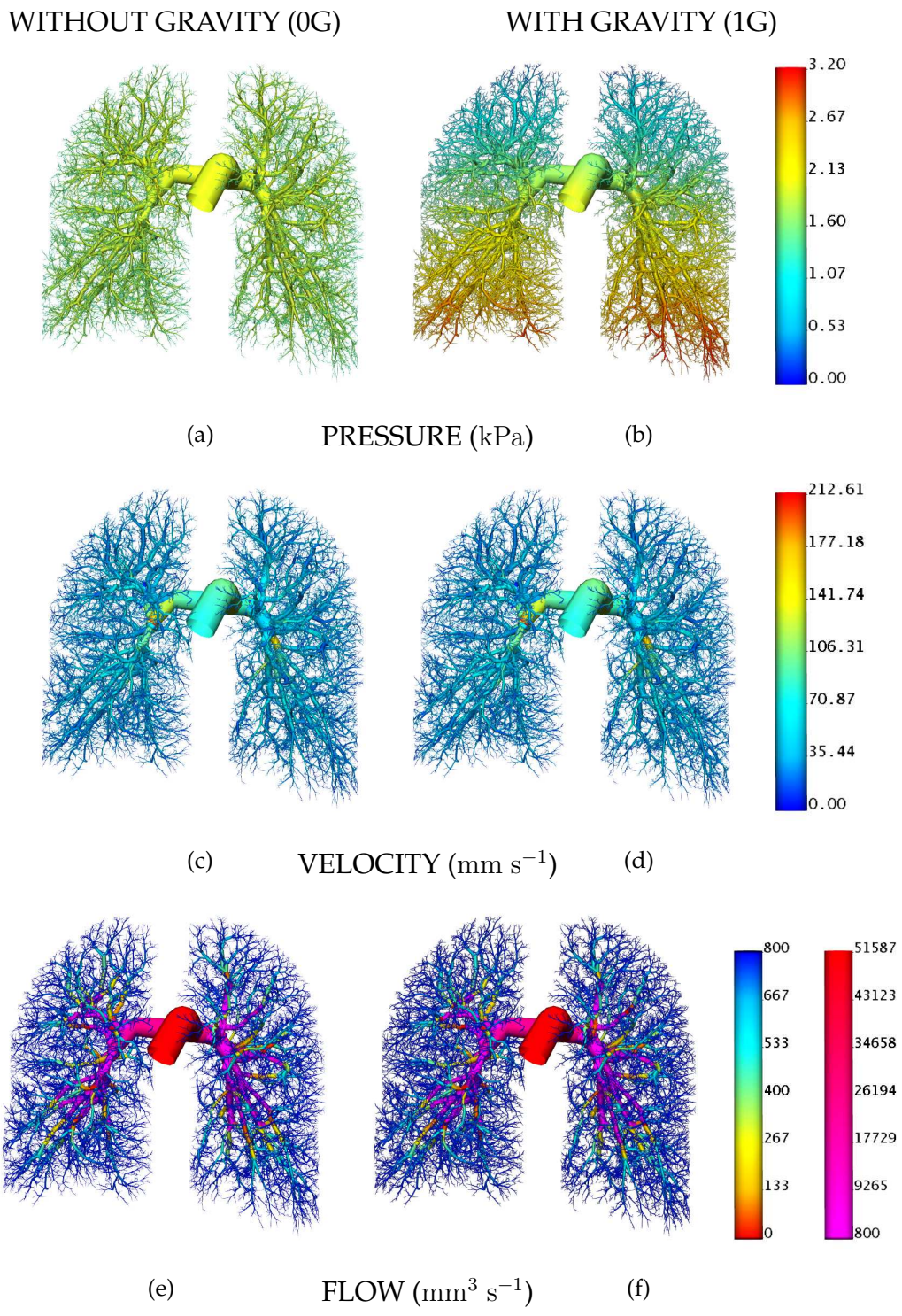

FIGURE 5.14: *(a,b) Pressure* (kPa)*, (c,d) velocity* (mm s^{-1})*, and (e,f) flow* (mm^3 s^{-1}) *solutions in the anatomically-based arterial model with and without gravity, respectively. Inlet and outlet pressure boundary conditions were set to 2 and 1.25* kPa*, respectively, these images display the steady-state solution.*

Solution values at all terminal locations were extracted and compared. These results were averaged within 1 and 50 mm slices to mimic different resolution data. Without gravity, all terminal nodal pressure values were uniform, as defined by the pressure boundary condition of 1.25 kPa (Figure 5.15(a)). When gravity was included a linear relationship between pressure and height was exhibited (Figure 5.15(a)). The percentage change in radius from the initial unstrained radius (R_0) value is plotted with respect to vertical height in Figure 5.15(b). In accordance with pressure, the radius values at all terminal nodes without gravity are constant having radius values approximately 10 % higher than the unstrained values. With gravity the radius values range from 5-16 % greater than R_0. The effect of gravity on velocity (Figure 5.15(c)) and flow (Figure 5.15(d)) results may be easily seen in the solutions within 50 mm slices, this trend is less clear in the higher resolution data within 1 mm slices. Flow rate values, and to a lesser extent velocity, shows an increased gradient with respect to vertical height with the addition of gravity. Results, both with and without gravity, display decreasing velocity and flow rates in the most peripheral upper and lower regions of the lung.

The effect of gravity was assessed in more detail by using linear regression to determine the gradient of flow with respect to vertical height (Figure 5.16). Flow results with gravity showed a gradient of flow of -0.019 (increasing flow from top to bottom) relative flow units/cm height, with r^2=0.41, where r^2 denotes the goodness of fit of the regression. Without gravity the flow gradient decreased to -0.006 relative flow units/cm height, with r^2=0.05. These gradients were only determined for the portion of increasing flow - within the height range of 12-30 cm. High resolution measures of blood flow in the upright baboon lung (via microsphere injection) (Glenny et al. 1999) displayed a flow gradient of -0.088 and -0.020 relative flow units/cm height with and without gravity, respectively. Measured values of flow in the supine pig lung (Glenny et al. 2000) are compared with model results in Figure 5.17 with and without gravity, where the corresponding flow gradients were -0.109 and -0.086 relative flow units/cm, respectively. The best fit lines from the upright baboon data (Glenny et al. 1999) is also included in these plots. The measured pig data also displays a decrease in flow in the upper and lower regions of the lung, as has been shown in the model results. The model results agree relatively well with the measurements without gravity, but measured gradients of flow with gravity are higher than estimates from the arterial model. More realistic results may be obtained through the model when the system is coupled to form a complete flow loop (see Chapter 6 for details).

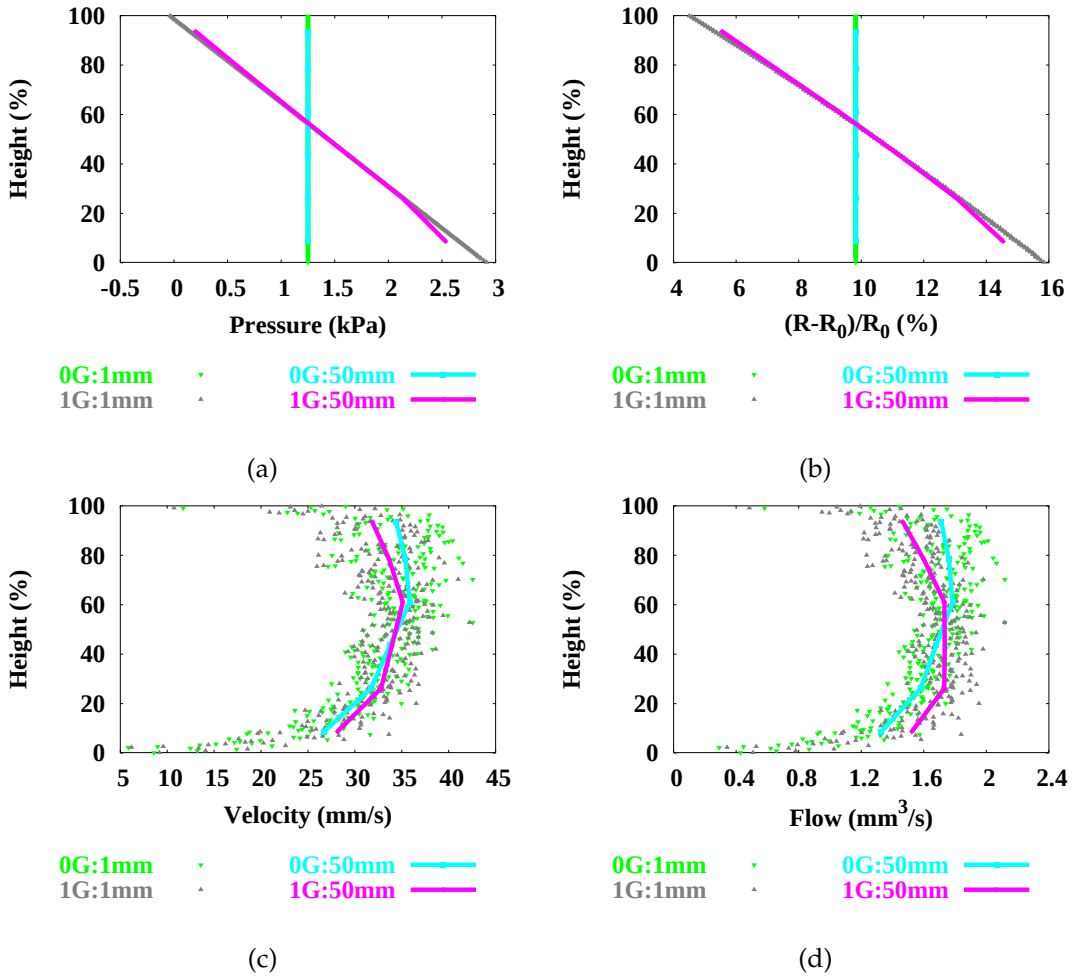

FIGURE 5.15: *Comparison of flow solutions at terminal nodes in the anatomically-based arterial model with respect to gravitationally-dependent height with (1G) and without (0G) gravity, averaged within 1 and 50* mm *slice thicknesses: (a) pressure* (kPa)*, (b) radius* (mm)*, (c) velocity* (mm s^{-1})*, (d) flow* mm^3 s^{-1}.

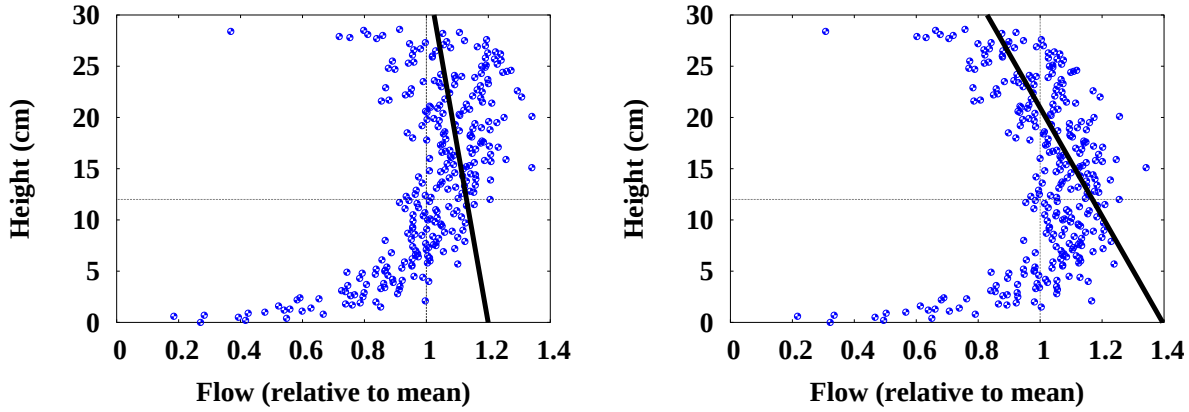

(a) Flow(0G)=-0.006xheight+1.2

(b) Flow(1G)=-0.019xheight+1.4

FIGURE 5.16: *Flow (relative to mean) with respect to vertical position in the lung in the arterial model, including least squares regression line of flow as a function of gravitationally-dependent height (cm): (a) without gravity: flow=-0.006xheight+1.2 (r^2=0.05), (b) with gravity: flow=-0.019xheight+1.4 (r^2=0.41). Goodness of fit is denoted by r^2. NB: Linear regression only includes data for region of increasing flow from 12-30* cm *height.*

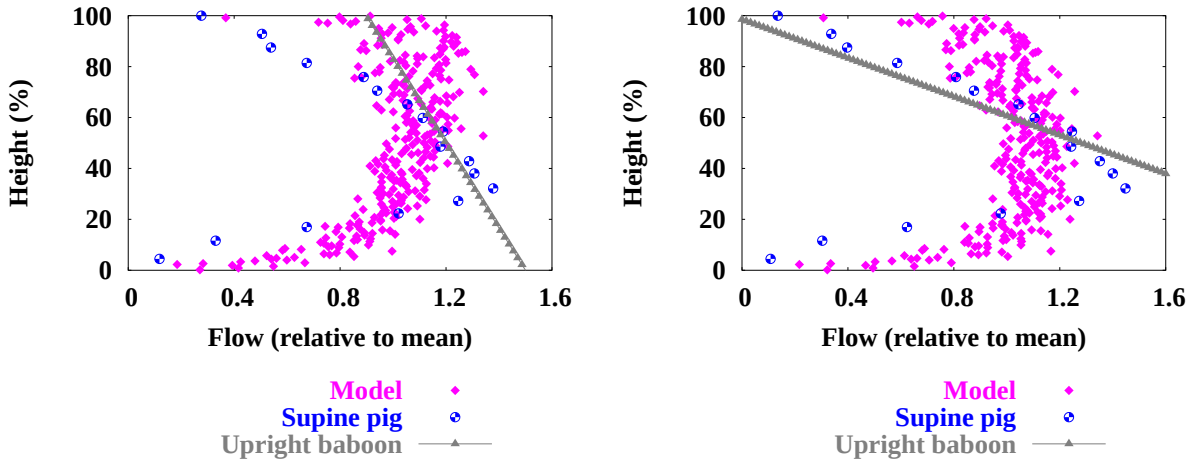

(a)

(b)

FIGURE 5.17: *Comparison of model flow results (relative to mean) with respect to gravitationally-dependent height with experimental measurements of blood flow in the supine pig (Glenny et al. 2000) and upright baboon lungs (Glenny et al. 1999). Flow (relative to mean) plotted with respect to vertical position in the lung. (a) without gravity (0G), (b) with gravity (1G).*

5.4.2.3 Effect of gravity in the anatomically-based venous model

Comparison between solutions with and without gravity were also made within the venous finite element model. The pressure was linearly increased from 0.2 kPa at all terminal branches to 0.7 kPa from t=0-0.1 s while holding the pressure at the outlet constant at 0.2 kPa until a steady-state solution was reached. A pleural pressure of -5 $\mathrm{cm\ H_2O}$ (-0.4903 kPa) was applied.

Similar results to those presented for the arterial model were found. With the addition of gravity a clear gradient of increasing pressure from the top to the bottom of the venous tree was present (Figure 5.18(b)), while the effect of gravity on velocity (Figure 5.18(d)) and flow (Figure 5.18(e)) solutions was less distinct. Pressure values at the very top of the venous tree experienced negative pressures. These vessels were able to remain open due to a retarding factor in the pressure-radius relationship which enables pressure within a vessel to be slightly negative without collapsing. This effectively mimics the tethering effect of fibres in the pulmonary system.

All terminal points were extracted from the venous model. Terminal solution values were averaged within slices of 1 and 50 mm thickness to display different resolution data. The pressure, radius, velocity, and flow results with and without gravity are plotted with respect to vertical position in the lung in Figure 5.15. A clear gradient of pressure (Figure 5.15(a)) and radius (Figure 5.15(b)) with respect to vertical height is displayed in the solutions with gravity. The velocity (Figure 5.15(c)) and flow (Figure 5.15(d)) solutions are more heterogeneous and the relationship between velocity or flow and height is less clear, The 50 mm averages produce less heterogeneous values and display a clearer trend of an increasing velocity and flow from the top to the bottom of the lung in the presence of gravity. Decreasing velocity and flow values are present in the upper and lower regions of the lung, due to the longer path lengths (as displayed in Figure 5.35(c)).

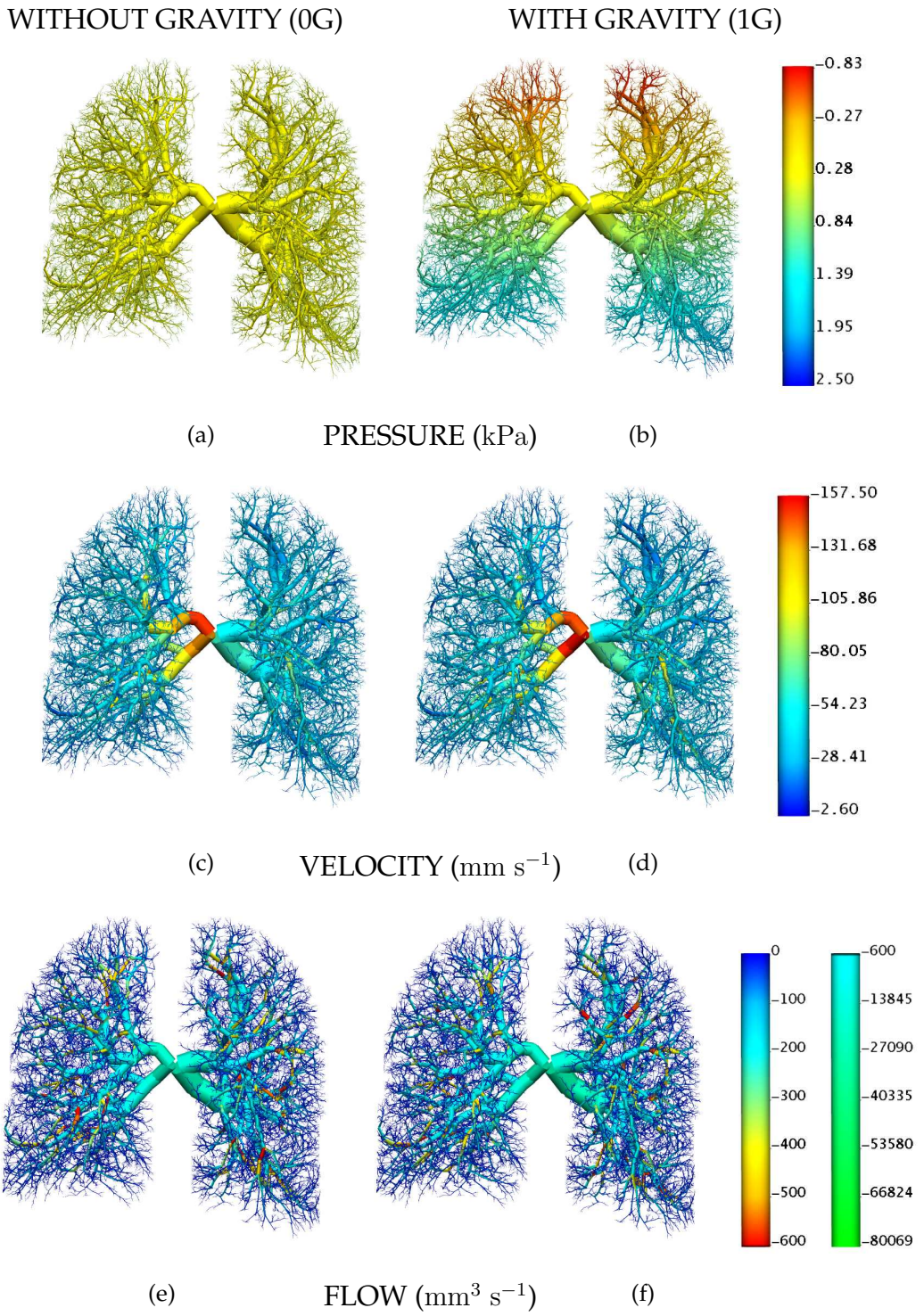

FIGURE 5.18: *Comparison of pressure, velocity, and flow solutions in the venous model with and without gravity: (a,b) pressure (*kPa*), (c,d) velocity (*mm s^{-1}*), (e,f) flow solutions without (0G) and with (1G) gravity in the anatomically-based venous model. Inlet and outlet pressure boundary conditions were set to 0.7 and 0.2* kPa*, respectively, and a steady-state solution was obtained.*

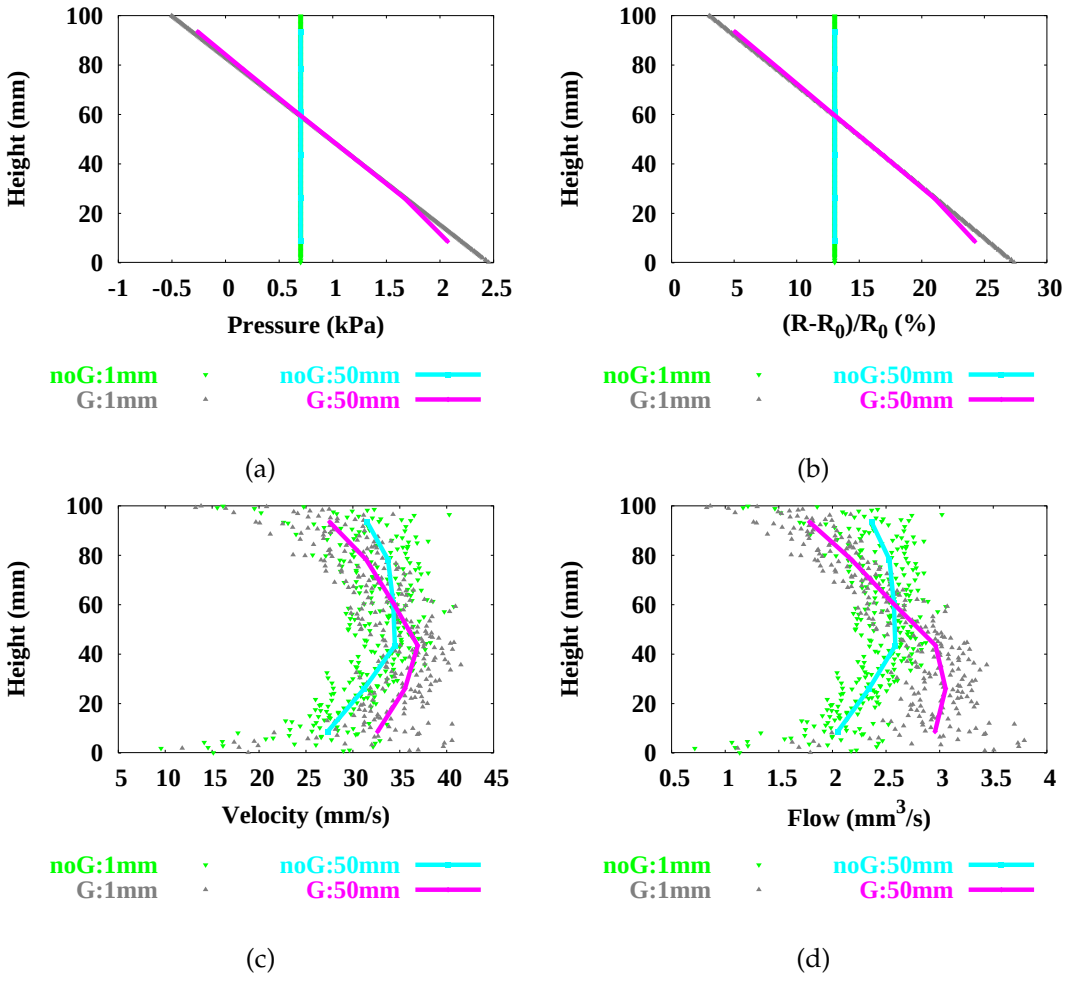

FIGURE 5.19: *Comparison of flow solutions at terminal nodes with respect to gravitationally-dependent height in the anatomically-based venous model with and without gravity, averaged within 1 and 50* mm *slice thicknesses: (a) pressure* (kPa)*, (b) radius* (mm)*, (c) velocity* (mm s^{-1})*, (d) flow* mm^3 s^{-1}.

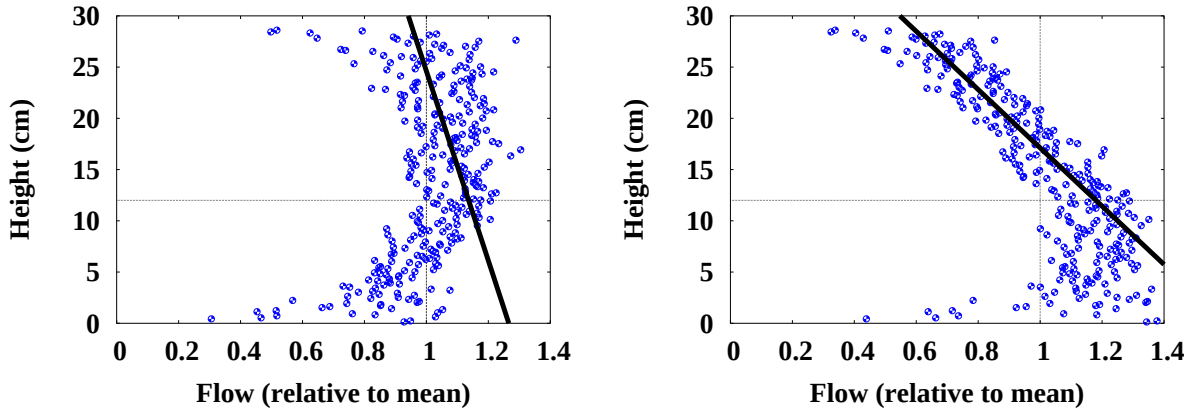

(a) Flow(0G)=-0.011xheight+1.3

(b) Flow(1G)=-0.035xheight+1.6

FIGURE 5.20: *Flow (relative to mean) with respect to vertical position in the lung, including least squares regression line of flow as a function of gravitationally-dependent height (cm): (a) without gravity: flow=-0.011xheight+1.3 (r^2=0.16), (b) with gravity: flow=-0.035xheight+1.6 (r^2=0.78). Goodness of fit is denoted by r^2. NB: Linear regression only includes data for region of increasing flow from 12-30* cm *height.*

Linear regression was again carried out to determine the relationship between flow and vertical position in the lung (Figure 5.20). The venous network displayed a slightly stronger gradient of flow with respect to height with and without gravity. Without gravity the gradient of flow was -0.011 relative flow units/cm height (r^2=0.16), showing a persistent gradient of flow in the absence of gravity. With gravity the flow gradient increased to -0.035 relative flow units/cm height (r^2=0.78).

5.4.2.4 The effect of increased gravity on flow solutions in the anatomically-based arterial and venous models

West's zonal flow model (Section 1.3.2), where gravity is the main determinant of blood flow distribution in the lung, predicts that as gravity is increased the gradient of flow with respect to gravitationally-dependent height increases proportionally. To test this assumption flow results were obtained in the arterial and venous models with an increased gravity of 1.8 times normal gravity (1.8G: g=17.66 $\mathrm{m\,s^{-2}}$, chosen to be consistent with experimental measurements in the upright baboon lung (Glenny et al. 1999)). Results with these varying amounts of gravity (0G, 1G, and 1.8G) were compared in the arterial (Figure 5.21) and venous (Figure 5.22) models with solutions

averaged within 1 and 50 mm slices. The pressure, and therefore radius, gradient increases in proportion to the amount of gravity (Figure 5.22(a)) due to the direct relationship between gravitational force and pressure. The velocity and flow solutions also show a increasing gradient as the gravitational force is increased. Results at all levels of gravity show a relatively large amount of heterogeneity within isogravitational regions. Solutions averaged within 50 mm slices show a clear relationship between velocity or flow and gravity.

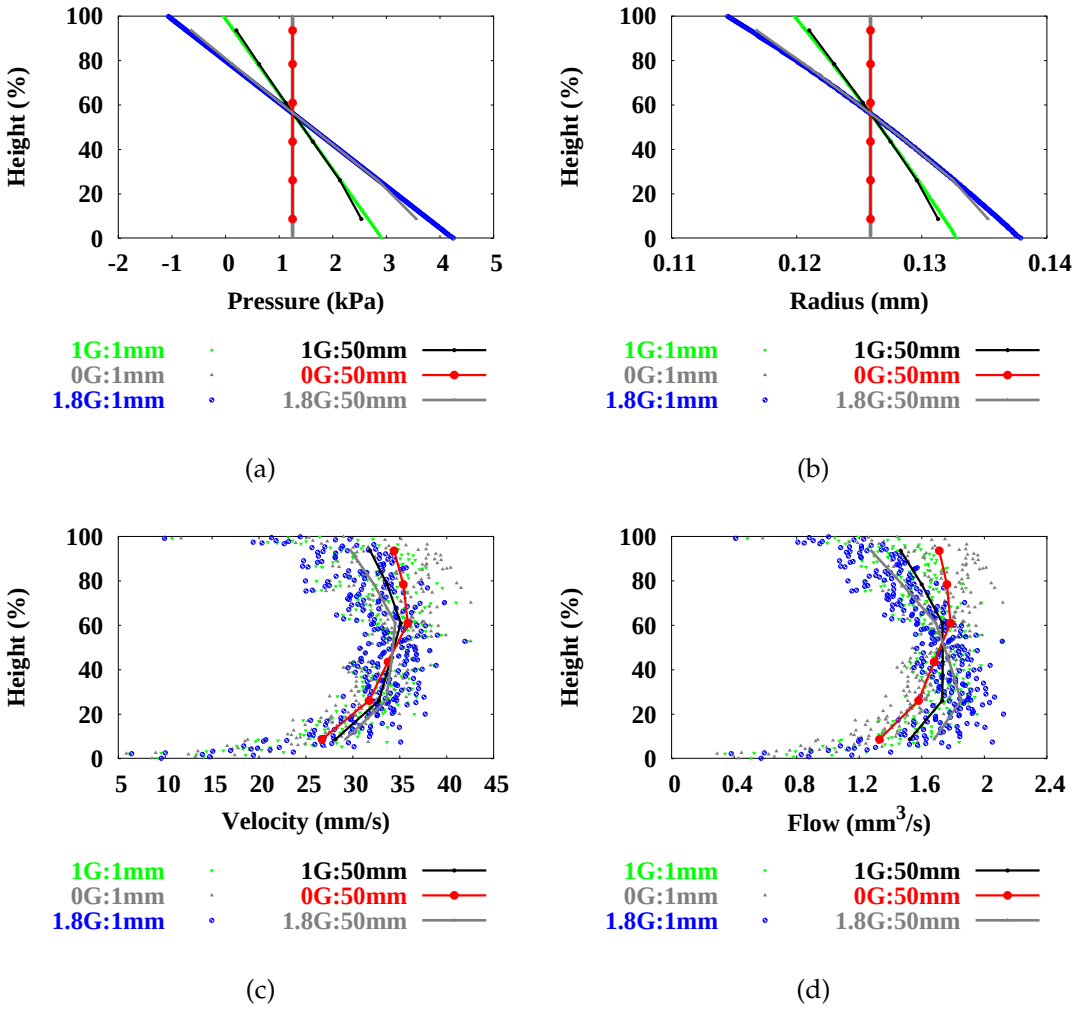

FIGURE 5.21: *Comparison of (a) pressure, (b) radius, (c) velocity and (d) flow solutions with increasing amounts of gravity (0G, 1G, 1.8G) in the anatomically-based arterial model averaged within slice thicknesses of 1 and 50* mm.

Linear regression was used to determine the relationship between flow and gravitationally-dependent height with an increased gravity of 1.8G. Again the gradient

was only determined for flow data between the heights of 12-30 cm to remain consistent with previous analysis. Arterial results displayed a gradient of -0.029 relative flow units/cm height, increasing by a factor of 1.53 times from results at 1G (Figure 5.23(a)). Venous results showed a similar increase by a factor of 1.46 times (from 1G) to a value of -0.051 relative flow units/cm height (Figure 5.23(b)). These increases are almost in proportion to the increase in gravity by a factor of 1.8 times. The r^2 correlation values also increased (indicating a greater correlation between flow and gravitationally-dependent height) from values of r^2=0.41 and 0.78 to 0.66 and 0.92 for the arterial and venous models, respectively.

The arterial model results, with an applied gravitational force of 1.8G, were compared with experimental flow measurements from supine pigs collected via the microsphere injection technique with various amounts of gravity (Glenny et al. 2000) (Figure 5.24). The gradient of flow was found to increase from -0.109 to -0.155 relative flow units/cm height when gravity was increased from 1G to 1.8G, this is a factor of only 1.06 times. The model results are found to compare well with the measured data, with large decreases in flow in the upper and lower regions of the lung. The supine pig data shows a larger gradient of both increasing and decreasing flow in the upper and lower portions of the lung, respectively, than the model data. Species and postural differences may contribute to this difference. Hlastala & Glenny (1999) also investigated the effect of gravity on blood flow distribution in prone pigs by measuring flow at 1 (1G), 2 (2G), and 3 (3G) times normal gravity. The measured gradient of flow increased from -0.016 relative flow units/cm height at 1G by a factor of 3.25 (to -0.052 relative flow units/cm) when gravity was increased to 2G. After an increase to 3G the gradient increased by a factor of 1.56 to -0.081 relative flow units/cm height.

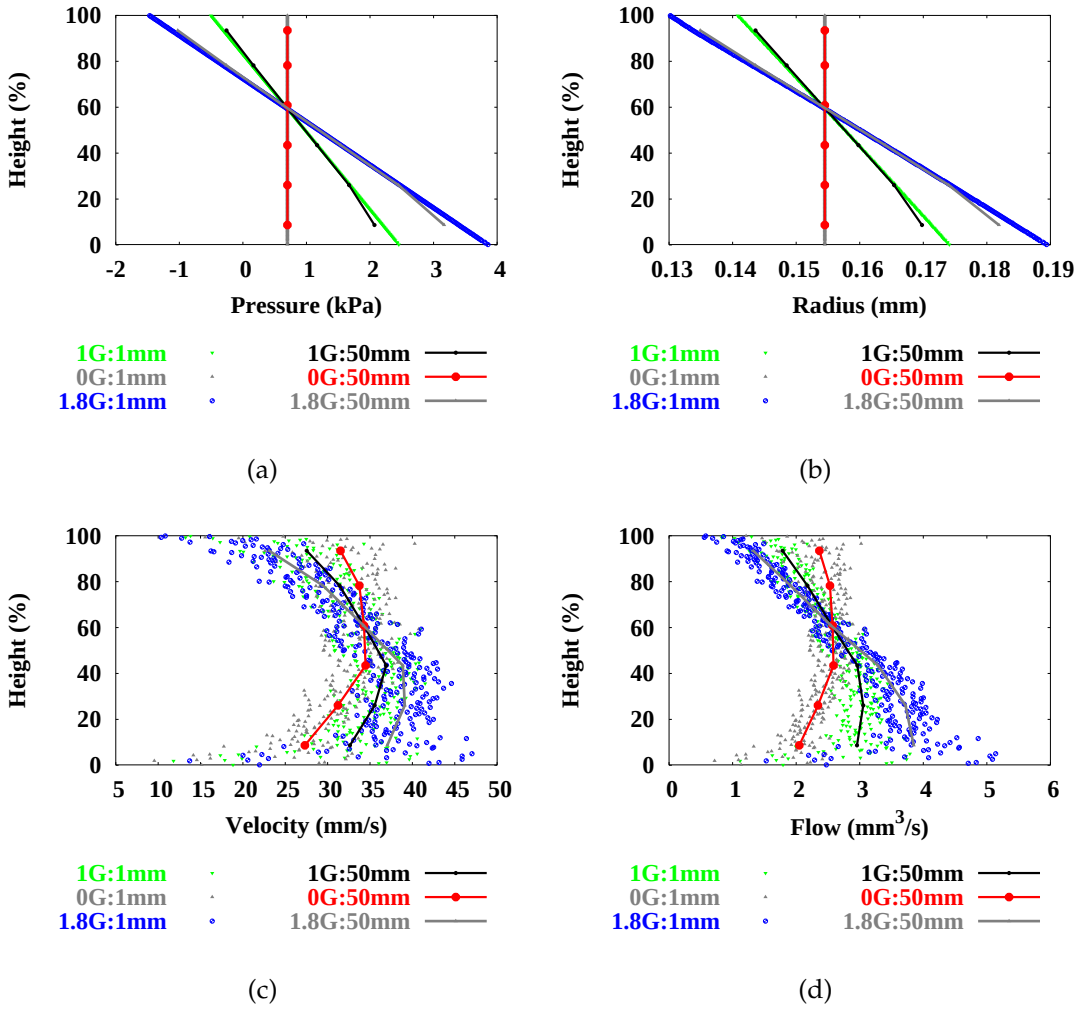

FIGURE 5.22: *Comparison of (a) pressure, (b) radius, (c) velocity and (d) flow solutions with increasing amounts of gravity (0G, 1G, 1.8G) in the anatomically-based venous model averaged within slice thicknesses of 1 and 50* mm.

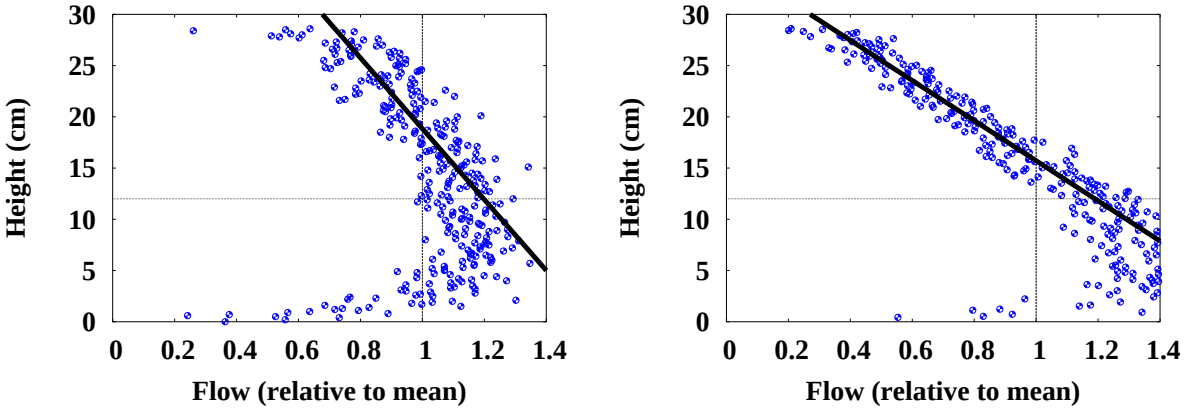

(a) Flow(1.8G)=-0.029xheight+1.54

(b) Flow(1.8G)=-0.051xheight+1.80

FIGURE 5.23: *Flow (relative to mean) with respect to vertical position in the lung, including least squares regression line of flow as a function of gravitationally-dependent height (cm), with increased gravity (1.8G) in (a) the arterial model: flow=-0.029xheight+1.54 (r^2=0.66), (b) venous model: flow=0.051xheight+1.80 (r^2=0.92). Goodness of fit is denoted by r^2. NB: Linear regression only includes data for region of increasing flow from 12-30* cm *height.*

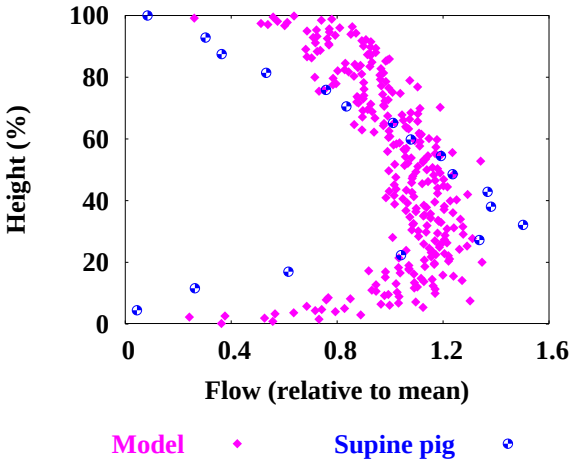

FIGURE 5.24: *Comparison of model results versus flow measurements from supine pigs (Glenny et al. 2000) with increased gravity of 1.8G: flow (relative to mean) plotted with respect to vertical position in the lung.*

5.4.3 Solution at different resolutions

- To investigate the effect that different resolution data may have on the interpretation of flow distribution results.

Model results at all terminal locations were isolated and analysed within various slice thicknesses in order to replicate experimental studies with different resolution sampling methods. Thicker slices represented lower resolution data, similar to early measurements obtained using scintillation detectors, where only a few external measurements of blood flow were obtained. These lower resolution results effectively provide averaged values across a large area of the lung. Higher resolution results were achieved by averaging solutions within smaller slices (the highest resolution data being the set of all terminal nodes) and were thought of as being more indicative of higher resolution studies, such as obtained by Glenny, Polissar & Robertson (1991) using microsphere deposition and counting methods. These higher resolution methods lead to less interpolation and averaging of flow information.

Figure 5.25 illustrates the pressure, radius, velocity, and flow solutions in the arterial model at all terminal locations with respect to lung height in slice thicknesses of 0.2, 1, 5, 10, 30, and 75 mm (displaying different resolutions results extracted from the same initial subset). All of these simulations had a normal applied gravitational force of 1G. Since the pressure is set at all terminal nodes in these simulations the pressure (Figure 5.25(a)) and radius (Figure 5.25(b)) solutions show a linear relationship with respect to gravitationally-dependent height due to the effect of gravitational acceleration in all size slices. The number of points averaged within each of the slices is plotted with respect to vertical height in Figure 5.25(e).

Similar results were obtained with data extracted from the venous model (at 1G) and averaged within various slice thicknesses (Figure 5.26). Averages were again obtained within slices of 0.2, 1, 5, 10, 30, and 75 mm in thickness.

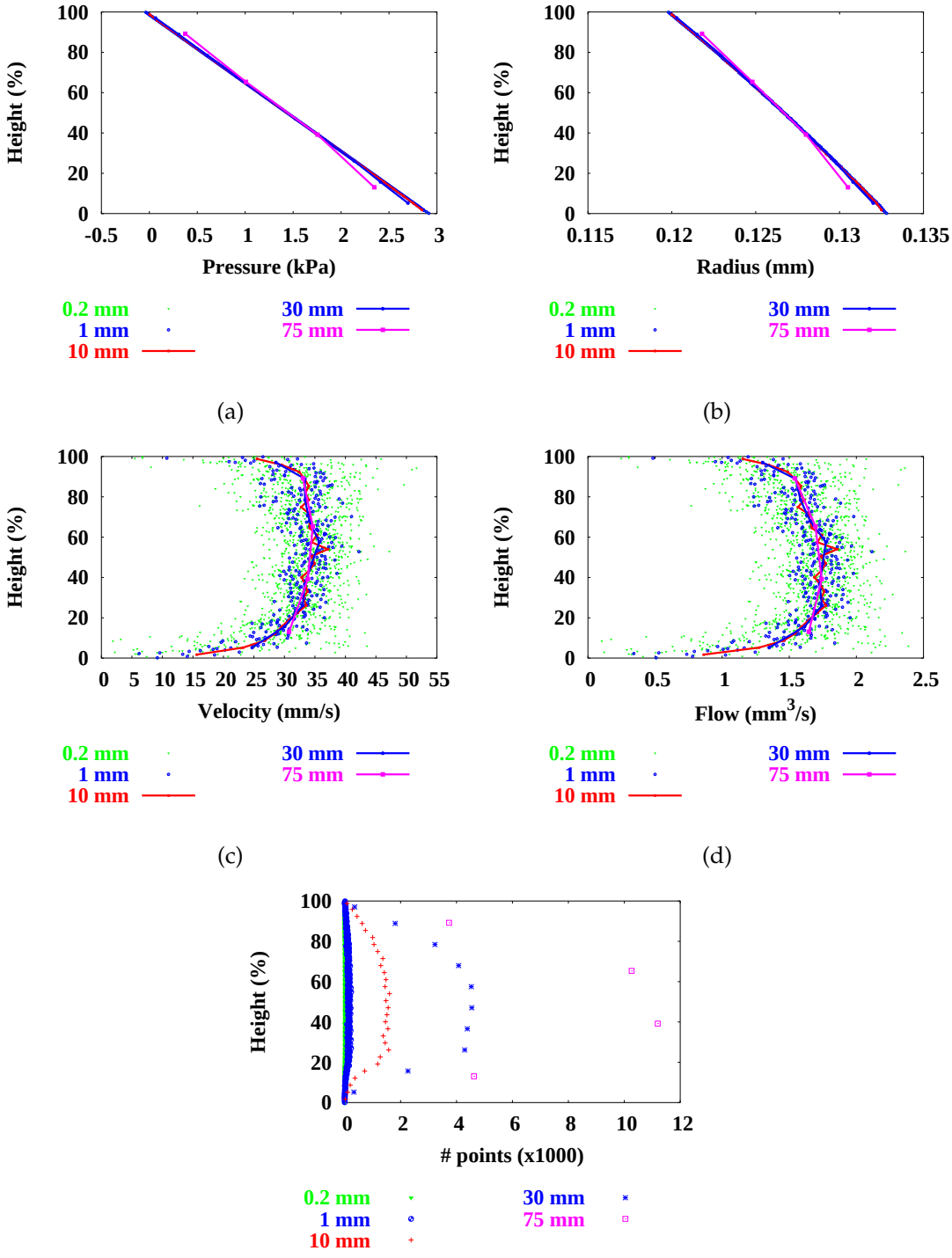

FIGURE 5.25: *Terminal flow solutions in the arterial model averaged within different slice thicknesses: (a) pressure* (kPa)*, (b) radius* (mm)*, (c) velocity* (mm s^{-1})*, (d) flow* (mm^3 s^{-1})*, and (e) number of terminal points per slice, for 0.2, 1, 10, 30, and 75* mm *slices.*

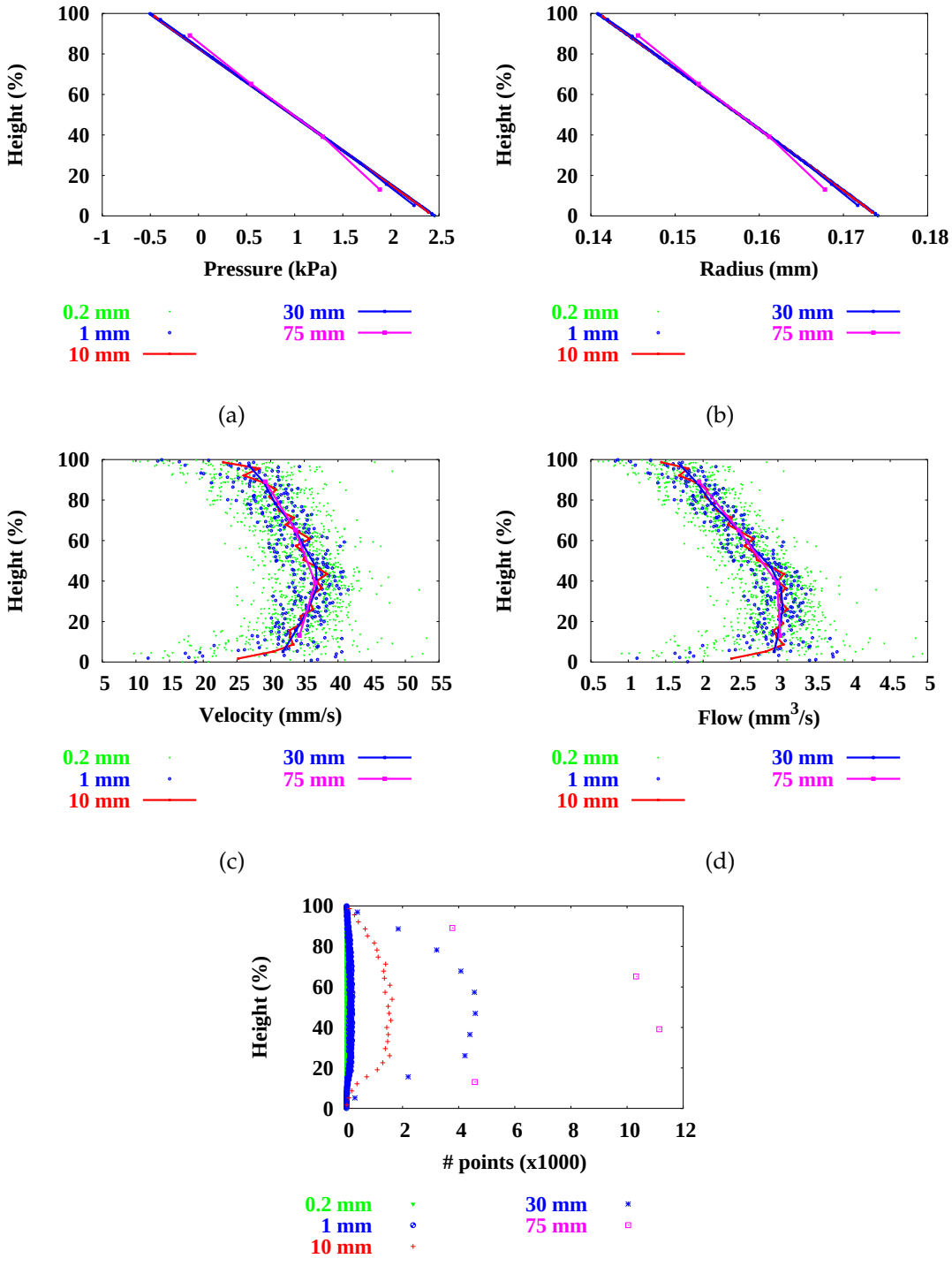

FIGURE 5.26: *Terminal flow solutions in the venous model averaged within different slice thicknesses: (a) pressure* (kPa)*, (b) radius* (mm)*, (c) velocity* (mm s^{-1})*, (d) flow* (mm^3 s^{-1})*, and (e) number of terminal points per slice, for 0.2, 1, 10, 30, and 75* mm *slices.*

5.4.4 Pleural pressure versus blood flow distribution

- To investigate the influence of pleural pressure changes during breathing on blood flow distribution in the human lung;

During the respiratory cycle the pleural pressure induces the pressure driving force required to inspire and exhale air. On inspiration the pleural pressure decreases to approximately -8 $\mathrm{cm\ H_2O}$ (-0.78 kPa) due to the expansion of the chest wall and muscles. On expiration the pleural pressure rises to about -5 $\mathrm{cm\ H_2O}$ (-0.49 kPa) (Guyton & Hall 2000). The influence of the alterations in pleural pressure on blood flow distribution were investigated using the arterial flow model. A simulation was also carried out to investigate the effect of a forced expiration on blood flow distribution, where pleural pressures become positive. Comparison of flow results (at 1G) with applied pleural pressures of -8, -5, 0, and +20 cm water (-0.78, -0.49, 0, 1.96 kPa) are presented in this section.

Terminal pressure, radius, velocity, and flow solutions are plotted with respect to vertical height in the arterial model averaged within slices of 1 and 50 mm in Figure 5.27 with the varying amounts of applied pleural pressure. The negative pleural pressure force distends the pulmonary blood vessels, and therefore a more negative pleural pressure results in an increased radius of the vessels leading to increased velocities and a greater increase in flow rates. The reverse occurs when a more positive pleural pressure is applied, as is demonstrated by the large shift in results with an increased pleural pressure to +20 $\mathrm{cm\ H_2O}$.

These results demonstrated that pleural pressure had a significant role in the overall flow rate values, but the distributions of flow remained fairly constant over the various pleural pressure values. During inspiration, as pleural pressure becomes more negative, the extra-alveolar vessels become more distended and therefore their resistance to flow decreases. However, as the lung expands and with it the alveolar spaces, the alveolar-capillaries become more compressed and therefore offer a higher resistance to flow. A flow model of the complete pulmonary circuit, when the models are coupled, will offer a more realistic representation of blood flow at different lung volumes.

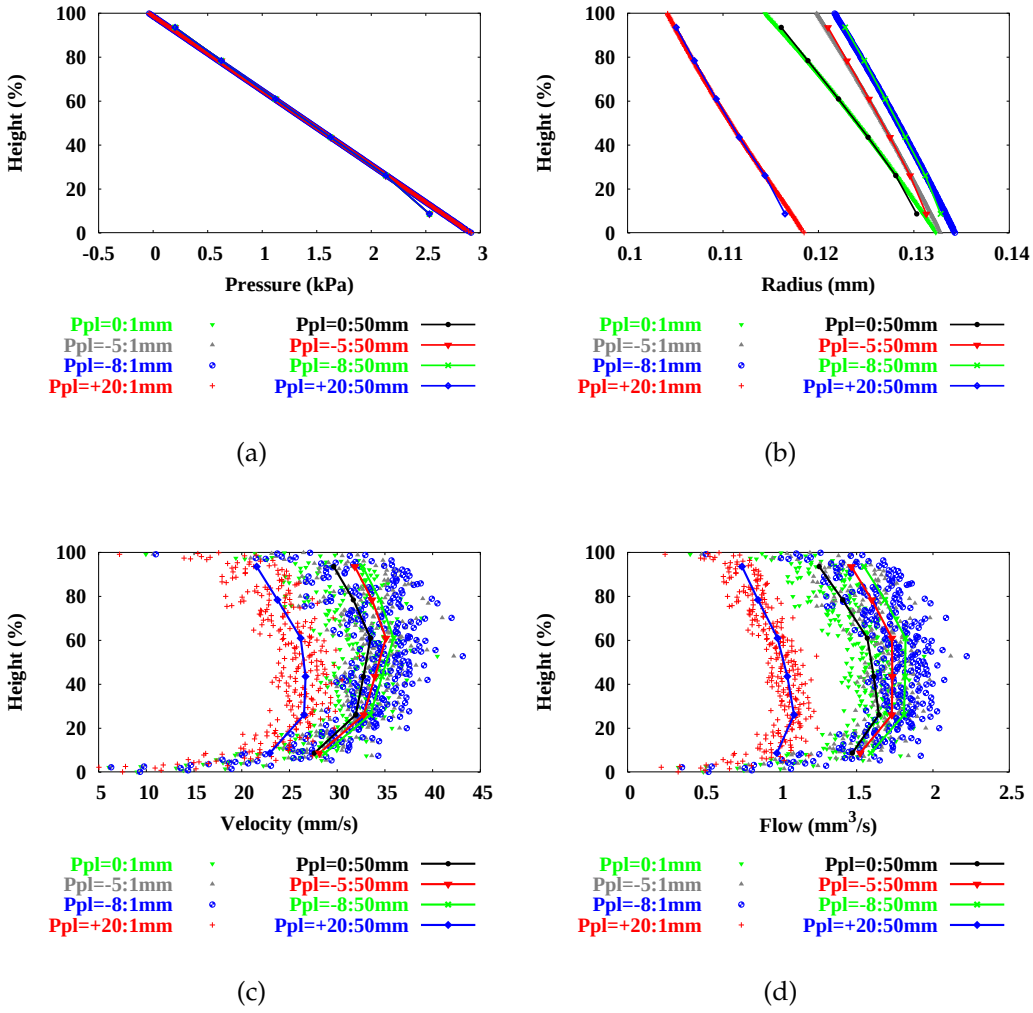

FIGURE 5.27: *Terminal flow solutions in the upright arterial model with varying amounts of pleural pressure (P_{pl}=-8, -5, 0, +20* $\mathrm{cm\ H_2O}$*). Results are averaged within slice thicknesses of 1 and 50* mm*: (a) pressure* (kPa)*, (b) radius* (mm)*, (c) velocity* ($\mathrm{mm\ s^{-1}}$)*, and (d) flow* ($\mathrm{mm^3\ s^{-1}}$)*.*

5.4.5 Effect of body posture on blood flow distribution

- To investigate the effect of posture on blood flow distribution;

Experimental studies have demonstrated a persistent blood flow gradient with respect to position in the lung, somewhat independent of body posture (Glenny et al. 1999). A small effect (flow reversal) is displayed on inversion of postures, but not a complete reversal of the flow gradient, this is another factor pointing towards a less significant role of gravity on the distribution of blood flow. The arterial and venous models were used to investigate the effect of variation of posture on the distribution of blood flow. Comparisons were made between flow results obtained in the upright, inverted, prone, and supine postures. All parameters and pressure boundary conditions (arterial: inlet pressure=2 Pa, outlet pressure=1.25 kPa, venous: inlet pressure=0.7 kPa, outlet pressure=0.2 kPa) used were the same as in all previous simulations.

Terminal solutions were extracted from the models and averaged within 1 and 50 mm slices along the craniocaudal (top-bottom) axis and compared for all postures (Figures 5.28 and 5.30 for the arteries and veins, respectively). Solution in the supine and prone postures were also compared by averaging values within 1 and 30 mm slices across the dorsoventral axis (Figures 5.29 and 5.31 for the arterial and venous trees, respectively).

Inversion of posture showed a clear effect on the gradient of pressure (Figures 5.28(a), 5.30(a)), and therefore radius (Figures 5.28(b), 5.30(b)), at all terminal vessels. Variation in posture had a less significant effect on the distribution of flow (Figures 5.28(d), 5.30(d)) and a minor effect on the gradient of velocity (Figures 5.28(c), 5.30(c)) with respect to height in the craniocaudal direction. The largest change in flow gradient was demonstrated on inversion of the posture from upright to inverted. Craniocaudal flow gradients in the supine versus prone postures do not show a significant change in gradient, but flow in the prone posture is consistently lower than flow in the supine position.

The difference between flows in the supine and prone postures is illustrated more clearly in Figures 5.29 and 5.31 where solutions are plotted with respect to the gravitationally-dependent height in the dorsoventral direction, where 100% height corresponds to the dorsal surface and 0% height to the ventral surface. The reference height with respect to gravity is at the inlet of main pulmonary artery or veins into the heart. The pulmonary trunk is positioned closer to the ventral surface (at a height of 13.9%, as is demonstrated by the intersection of the pressure values in Figure 5.29(a)),

the arterial model shows higher overall pressures when in the supine position due to an increased hydrostatic pressure head due to gravity. This results in a higher overall flow in the supine posture compared to in the prone position. Flow in the ventral region remains relatively unchanged on inversion from the prone to supine posture, while flow in the dorsal region (furthest from the pulmonary trunk) is most effected. This demonstrates a large influence of the positioning of the large pulmonary vessels on flow distribution in the remaining vasculature.

Results in the venous network displayed similar trends to those in the arterial model. Inversion from the prone to supine position resulted in a larger change in flow gradient than was displayed in the arterial model (Figure 5.31(d)). The pressure gradients in the two postures (Figure 5.31(a)) are almost exactly opposite (due to the more central positioning of the main pulmonary veins at a height of 46.8%). All results demonstrate a decrease in velocity and flow in the most peripheral regions (top and bottom) of the lung regardless of posture.

Transit time details for these simulations are displayed in Section 5.4.7, Table 5.1.

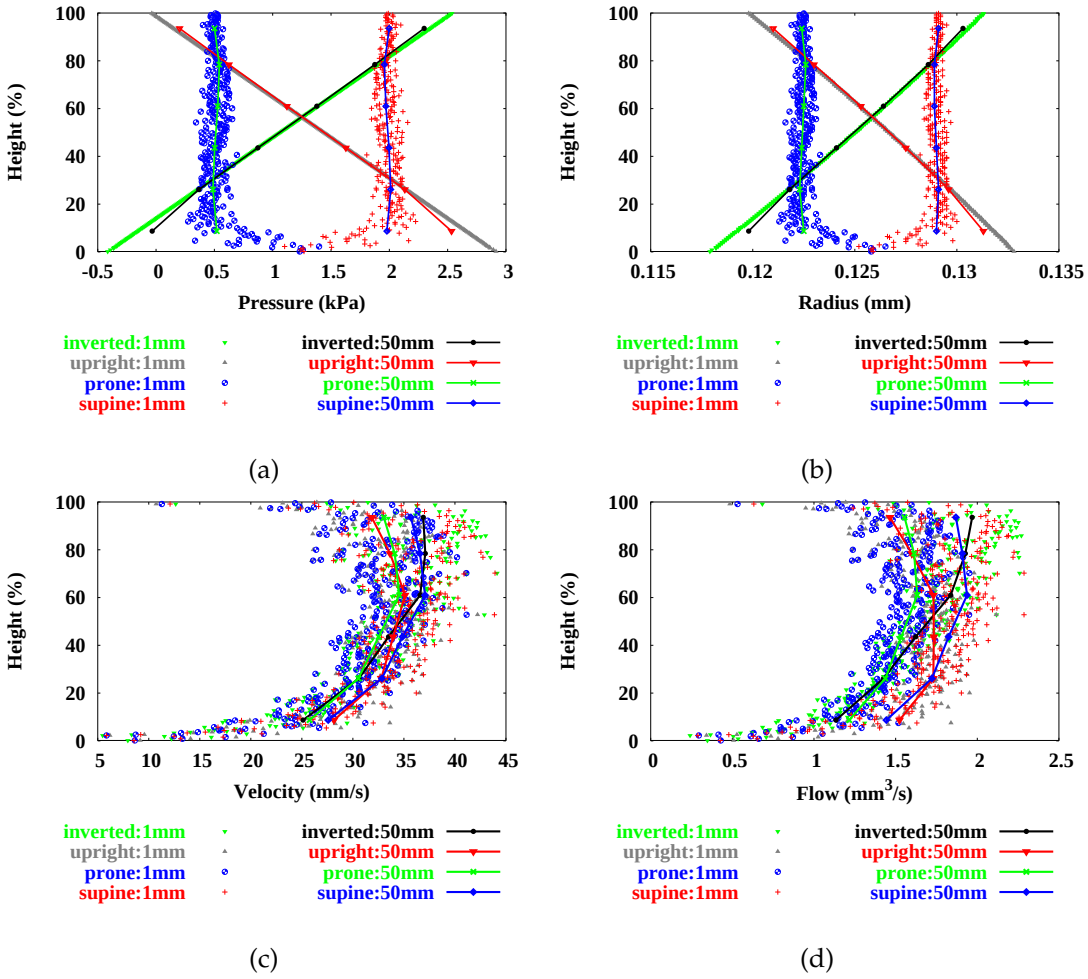

FIGURE 5.28: *Comparison of flow solutions in the arterial model in different postures: - upright, inverted, supine, and prone, averaged within slice thicknesses of 1 and 50* mm*: (a) pressure* (kPa)*, (b) radius* (mm)*, (c) velocity* ($\mathrm{mm\ s^{-1}}$)*, and (d) flow* ($\mathrm{mm^3\ s^{-1}}$)*.*

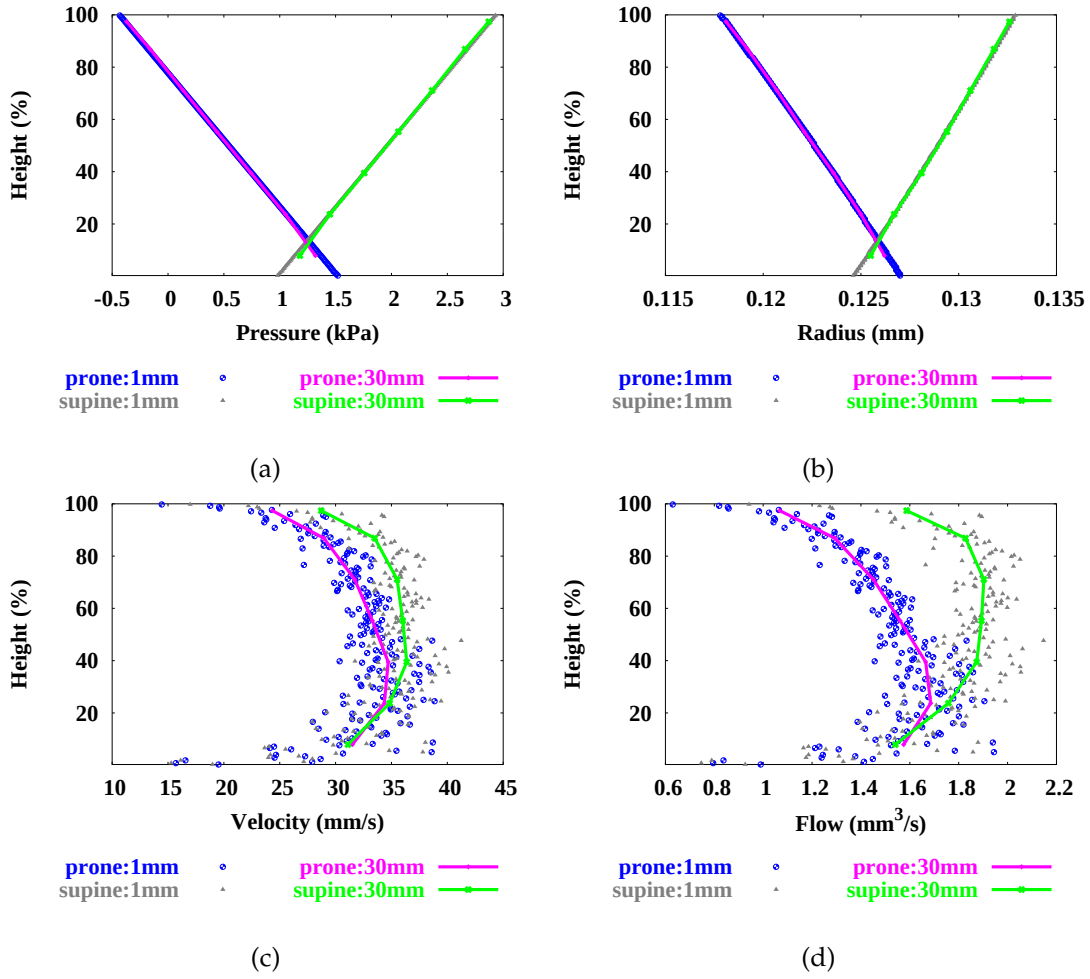

FIGURE 5.29: *Comparison of flow solutions in the arterial model in the prone versus supine positions with respect to the gravitationally-dependent height (dorsoventral axis, where 0% corresponds to the ventral surface). Solutions averaged within slice thicknesses of 1 and 30* mm*: (a) pressure* (kPa)*, (b) radius* (mm)*, (c) velocity* ($\mathrm{mm\ s^{-1}}$)*, and (d) flow* ($\mathrm{mm^3\ s^{-1}}$)*.*

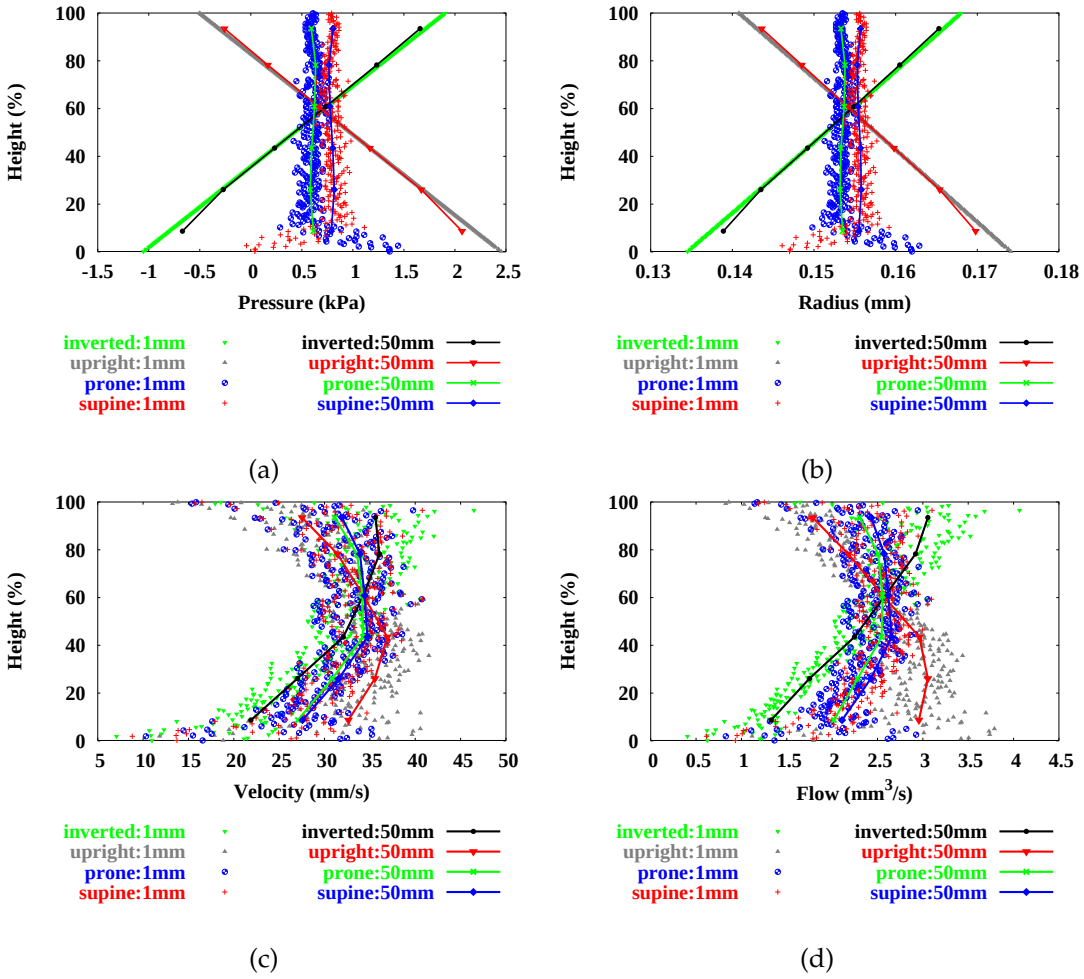

FIGURE 5.30: *Comparison of flow solutions in the venous model in different postures - upright, inverted, supine, and prone, in slice thicknesses of 1 and 50* mm*: (a) pressure* (kPa)*, (b) radius* (mm)*, (c) velocity* (mm s^{-1})*, and (d) flow* (mm^3 s^{-1})*.*

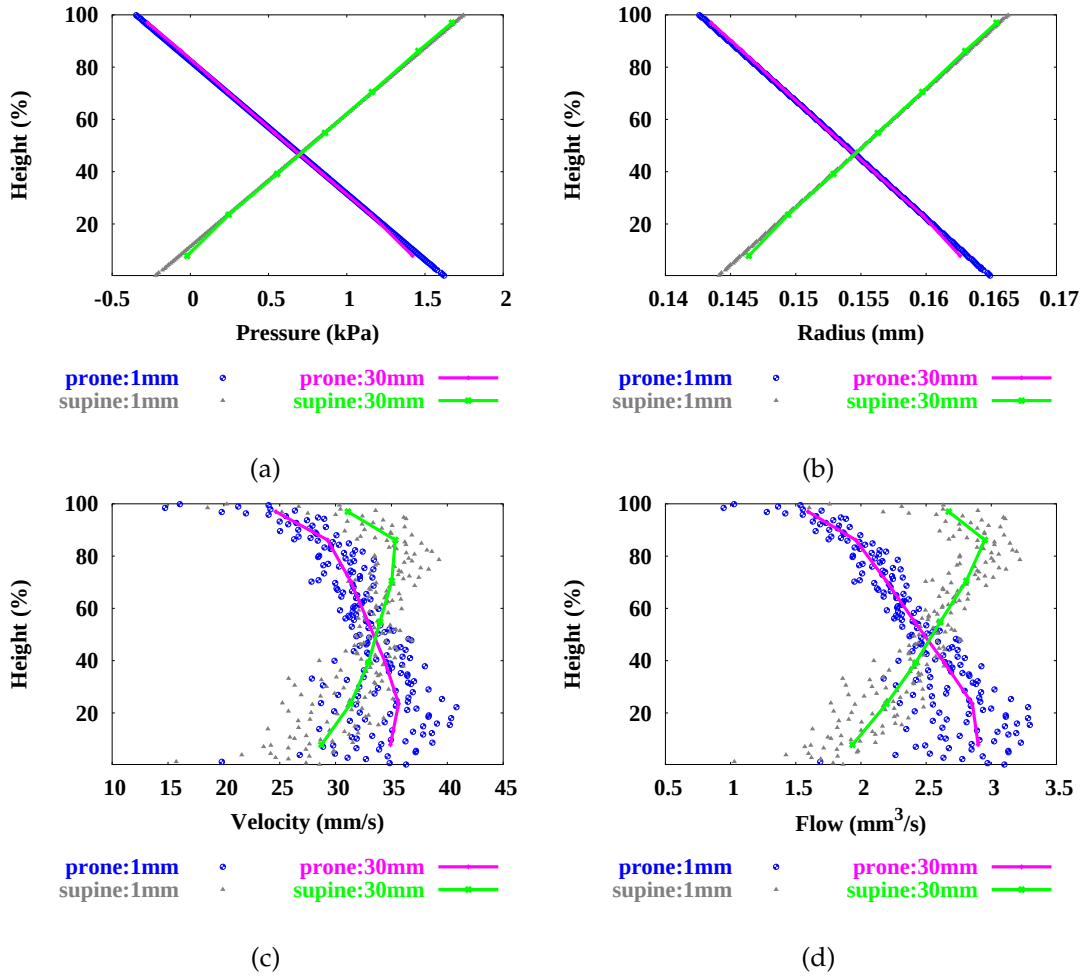

FIGURE 5.31: *Comparison of flow solutions in the venous model in the prone versus supine positions with respect to the gravitationally-dependent height (dorsoventral axis, where 0% corresponds to the ventral surface). Solutions averaged within slice thicknesses of 1 and 30* mm*: (a) pressure* (kPa)*, (b) radius* (mm)*, (c) velocity* ($\mathrm{mm\ s^{-1}}$)*, and (d) flow* ($\mathrm{mm^3\ s^{-1}}$)*.*

5.4.6 Effect of vessel distensibility

The hydrostatic pressure gradient in the lung causes distension of gravitationally-dependent vessels which influences the distribution of blood flow. The finite compliance of the pulmonary vascular system means that gravity can only have a limited effect (Glenny et al. 2000). The effect of vessel distensibility on the distribution of pulmonary blood flow was investigated by conducting simulations with various values of G_0 and β, parameters in the pressure-radius relationship (Equation 5.4). All simulations in the previous sections use G_0=5 kPa and β=3.2. Additional simulations were carried out, in the arterial tree only, with the following vessel elasticity constants: G_0=1 kPa, β=3, G_0=3 kPa, β=3, and G_0=7 kPa, β=3.

Terminal solution values were extracted from the arterial model and averaged within 1 mm slices (Figure 5.32). These results demonstrate that the vessel elasticity has a relatively large influence on the distribution of flow. As the vessels become more distensible the same applied pressure (Figure 5.32(a)) results in vessels with increasing radius values (Figure 5.32(b)). Larger vessel cross-section results in increased velocities (Figure 5.32(c)) and a compounded larger increase in flow (resulting from both the increase in velocity and cross-sectional area, Figure 5.32(d)). When the vessels were more distensible (G_0=1 kPa, β=3) gravity had a much larger influence on blood flow, creating a steeper gradient of increasing flow from the top to the bottom of the lung. Solutions with G_0=3 kPa β=3, G_0=5 kPa β=3.2, and G_0=7 kPa β=3 displayed a relatively small variation in terminal velocity and flow values.

The simulations in this study use a value of β=3.2, this value was estimated due to lack of available experimentally measured values. As more detailed elasticity measures become available these can be easily incorporated in the model to produce more realistic results.

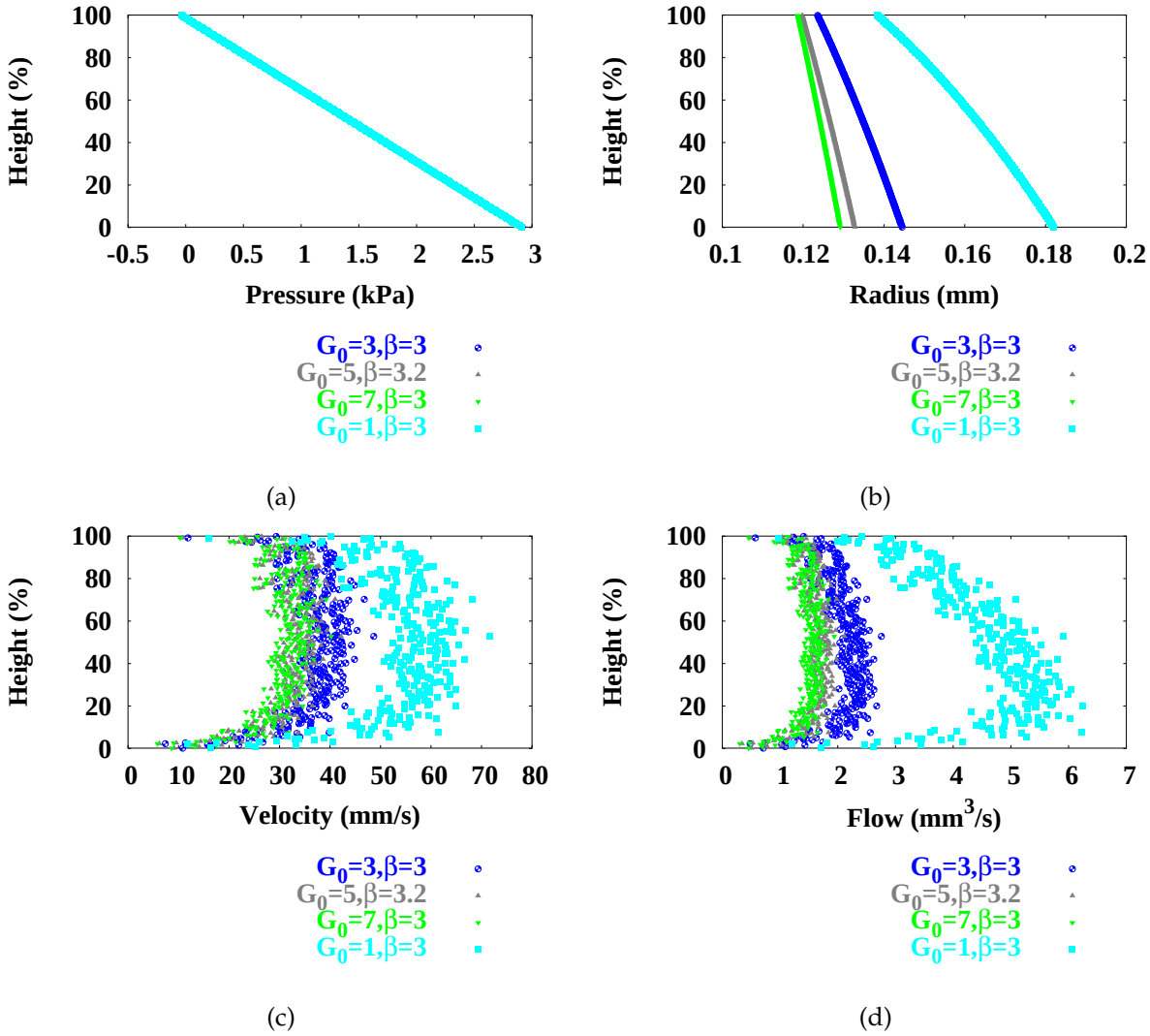

FIGURE 5.32: *Comparison of flow solutions in the arterial model with different vessel distensibilities averaged within 1* mm *slices: (a) pressure (*kPa*), (b) radius (*mm*), (c) velocity (*$\mathrm{mm\ s^{-1}}$*), and (d) flow (*$\mathrm{mm^3\ s^{-1}}$*). Values of G_0 and β used are displayed in the figure key.*

5.4.7 Network transit times

- To evaluate transit times through the pulmonary vasculature, for comparison of model results with experimental data and to increase understanding of the factors governing blood flow distribution;

After calculation of the velocity distribution through the arterial and venous networks, transit time information of blood through each pathway can be calculated. The transit times are simply calculated by following a flow pathway from the inlet vessel until an outlet vessel is reached. Due to the limited number of pathways (as opposed to the large number of possible capillary pathways) information from all arterial and venous pathways was collected. Measurements obtained include the time taken to traverse each pathway, the distribution of path lengths (from inlet to outlet), and the number of elements in each pathway.

Transit time results are presented for the arterial (Figure 5.33) and venous (Figure 5.34) models under normal gravity (1G) and pleural pressure (0.49 kPa) conditions in an upright posture, an attempt is made to find a correlation between the various model results. As has been displayed in previous sections, a linear relationship is displayed between pressure at terminal locations and gravitationally-dependent height, due to gravity (Figures 5.33(a) and 5.34(a)).

The total number of flow pathways through both the arterial and venous models is 29,818, which is the number of terminal vessels. The average path length through the arterial network was 260.5 mm, which consisted of an average of 35.8 vessels. Through the venous tree the average path length was 179.5 mm consisting of an average of 21.6 vessels.

Linear regression was used to generate lines of best fit through the data points (Figures 5.33(b)-(e) and 5.34(b)-(e)). These results illustrate that as the path length (and number of vessels in a path) increases the pathway transit time becomes longer (Figures 5.33(b,c) and 5.34(b,c), respectively). Relatively weak correlations were demonstrated between the terminal velocity (Figures 5.33(d) and 5.34(d)) and flow (Figures 5.33(e) and 5.34(e)) and path length, with r^2 correlation coefficients of 0.031 and 0.018 for the arterial tree, respectively, and 0.053 and 0.040 for the venous model, respectively.

Transit times in the arterial model ranged from 1.46 s to as long as 15 s, and from 1 to 8 s in the venous model. The distribution of transit times with respect to the percentage of pathways is displayed, using 0.1 s bin intervals, in Figures 5.33(f) and 5.34(f) for the arterial and venous trees, respectively.

To produce results comparable to flow solutions presented in previous sections,

transit time data was averaged within slices of 1 and 50 mm in thickness with respect to gravitationally-dependent height. Averaging solutions within slices provides a clearer relationship between transit time information and vertical height. Both the arterial and venous solutions display longer transit times in the upper and lower regions of the lung (Figures 5.35(a) and (b)). This corresponds to an increase in the path length, and therefore number of vessels in a path, in the apical and basal regions, furthest from the inlet or outlet vessels (Figure 5.35).

Averaged transit times from all pathways were calculated from each of the simulations conducted in this chapter, these results are displayed in Table 5.1. The results show that higher levels of gravity lead to marginally faster average transit times through both the arterial and venous networks. Transit times through the arterial network were, on average, longer than travel time through the venous network. Variation of the vessel elasticity parameters (G_0 and β) had a relatively large influence on average transit times through the arterial tree, showing a decreasing average transit time as the vessels became more distensible.

Conditions	**Arterial transit time (s)**	**Venous transit time (s)**
0G (gravity = 0 $\mathrm{m\ s^{-2}}$)	4.06	3.37
1G (gravity=9.81 $\mathrm{m\ s^{-2}}$)	4.03	3.28
1.8G (gravity = 17.66 $\mathrm{m\ s^{-2}}$)	4.02	3.26
Pleural pressure = 0 $\mathrm{cm\ H_2O}$	4.20	3.63
Pleural pressure = -8 $\mathrm{cm\ H_2O}$	3.93	3.10
Pleural pressure = 20 $\mathrm{cm\ H_2O}$	5.36	-
Supine	3.87	3.34
Prone	4.28	3.43
Inverted	4.10	3.52
G_0=7,β=1	4.19	-
G_0=3,β=1	3.57	-
G_0=1,β=1	2.53	-
Sheep 0G	0.54	-
Sheep 1G supine	0.57	-
Sheep 1G prone	0.50	-

TABLE 5.1: *Average transit times (from all pathways) through the arterial and venous networks under the various conditions presented in this chapter.*

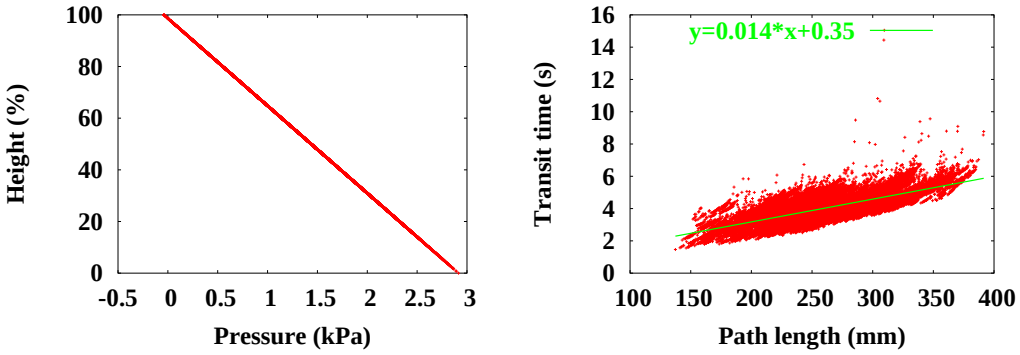

(a)

(b) r^2=0.55

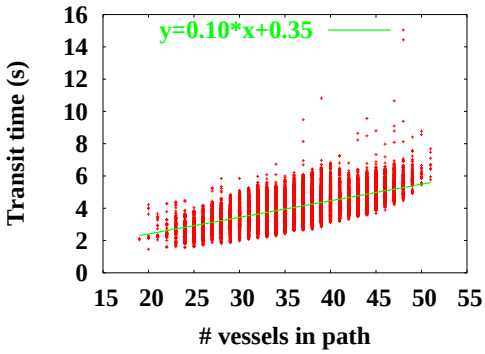

(c) r^2=0.44

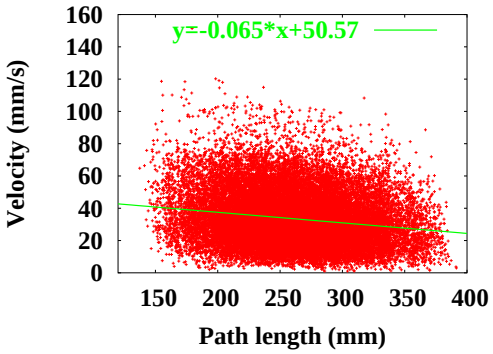

(d) r^2=0.031

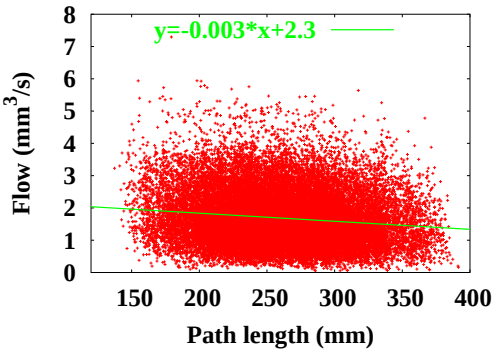

(e) r^2=0.018

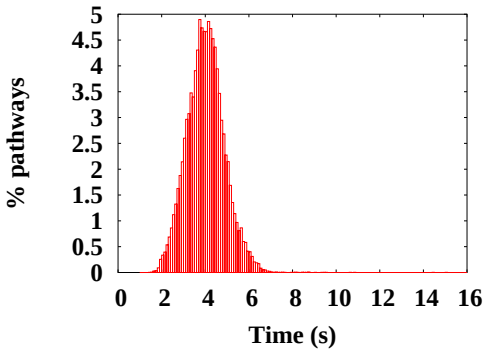

(f)

FIGURE 5.33: *Transit time results through the arterial model under normal gravity (1G) and pleural pressure (-0.49* kPa*) conditions: (a) pressure versus vertical height; (b) path length* (mm) *versus transit time* (s)*; (c) number of vessels per path versus transit time; path length versus terminal node (d) velocity* ($\mathrm{mm\ s^{-1}}$) *and (e) flow* ($\mathrm{mm^3\ s^{-1}}$)*; (f) transit time with respect to the percentage of pathways.*

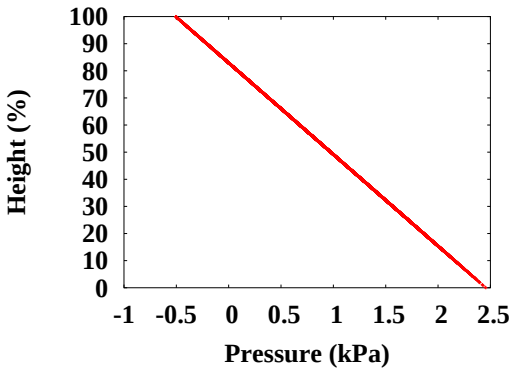

(a)

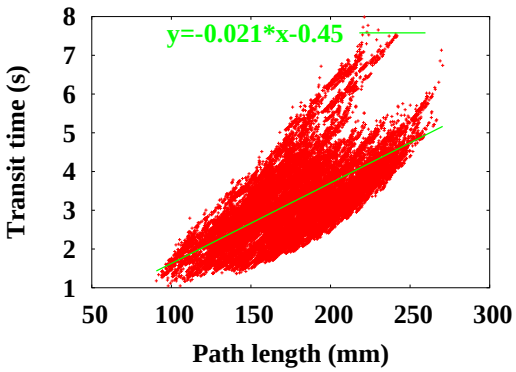

(b) r^2=0.43

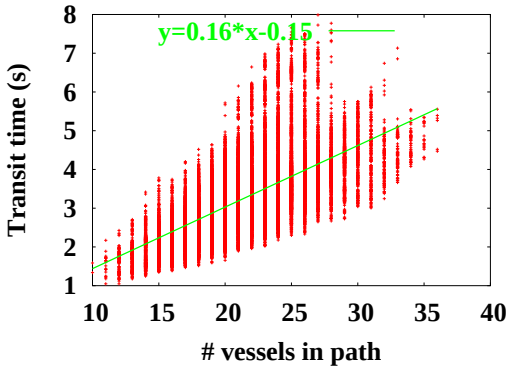

(c) r^2=0.42

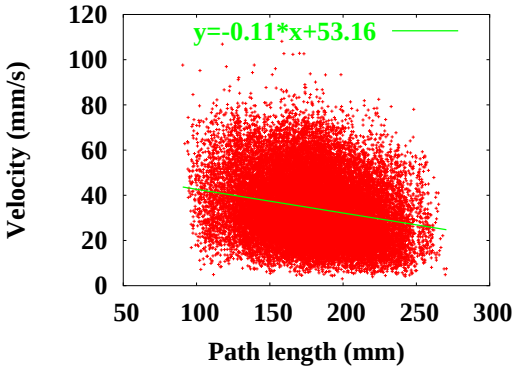

(d) r^2=0.053

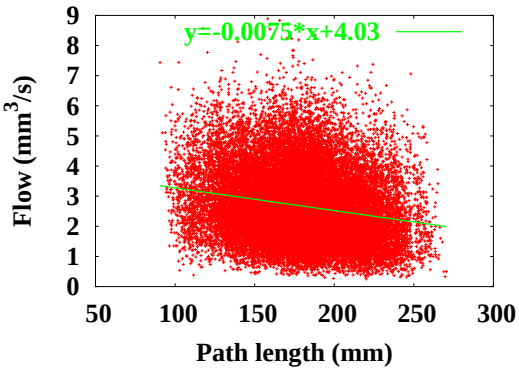

(e) r^2=0.040

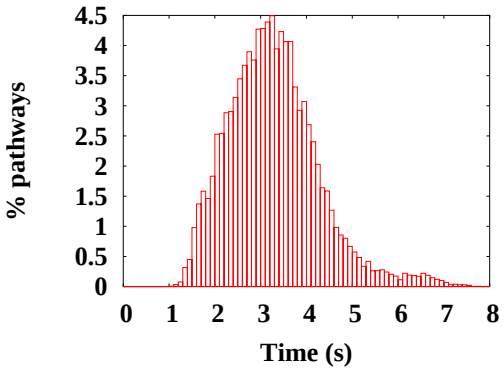

(f)

FIGURE 5.34: *Transit time results through the venous model under normal gravity (1G) and pleural pressure (-0.49* kPa*) conditions: (a) pressure versus vertical height; (b) path length* (mm) *versus transit time* (s)*; (c) number of vessels per path versus transit time; path length versus terminal node (d) velocity* (mm s^{-1}) *and (e) flow* (mm^3 s^{-1})*; (f) transit time with respect to the percentage of pathways.*

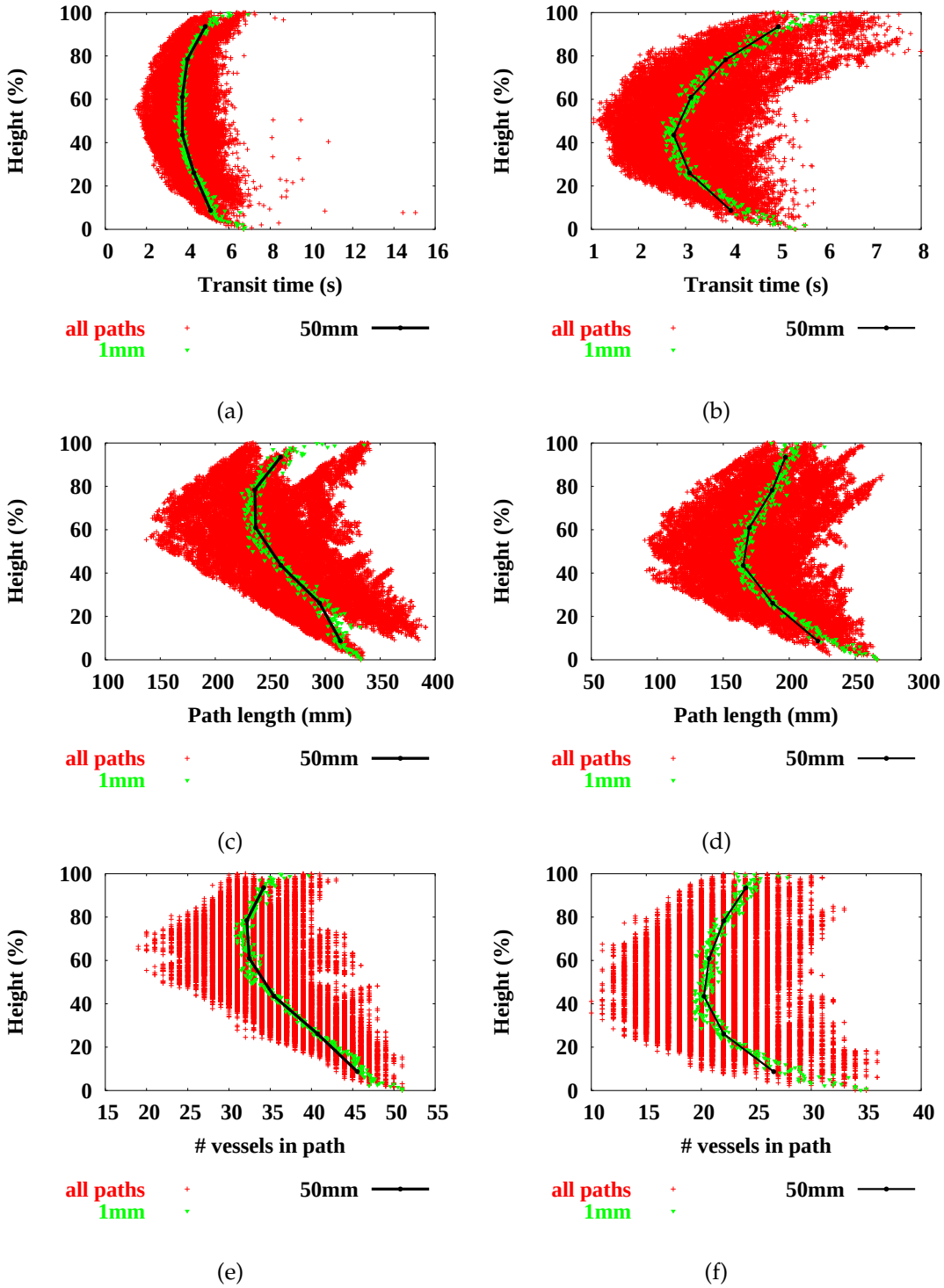

FIGURE 5.35: *Transit time results with respect to vertical position in the lung for the arterial and venous models - all points plus averages within 1 and 50* mm *slices. Arterial results: (a) transit time* (s)*, (c) path length* (mm)*, (e) number of elements per path, venous results: (b) transit time* (s)*, (d) path length* (mm)*, and (f) number of elements per path with respect to vertical position in the lung.*

5.4.8 Pulsatile flow solutions

- To compare the pulsatile solutions with steady-state results;

All results presented so far have been steady-state solutions, this section presents pulsatile flow results in the arterial tree only over a single cardiac cycle. Pulsatile pressure boundary conditions were applied at the pulmonary trunk inlet (Figure 5.37 (Burton 1965)) and all outlet pressures remained fixed at a pressure of 1.25 kPa. The solutions were obtained by first holding the pressure differential over the network constant until a steady-state solution was reached, then applying the pulsatile pressure boundary conditions.

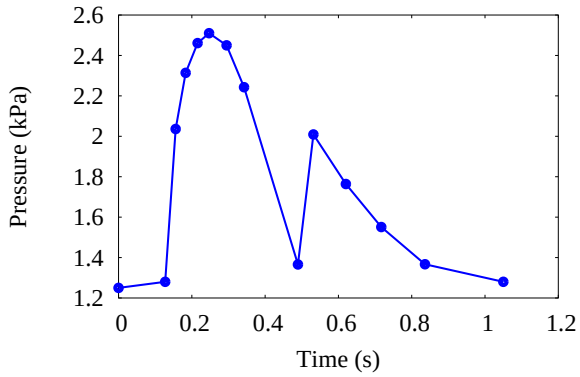

FIGURE 5.36: *Pulsatile pressure boundary conditions applied at the pulmonary trunk inlet. These values were derived from experimental data from (Burton 1965). All outlet pressures remained fixed at a pressure value of 1.25* kPa.

Images of the pressure solution in the arterial model over time are displayed in Figure 5.37. The spectrum used to represent the solution is included at the top of the figure. Over the pulsatile cycle, as pressure is increased at the pulmonary trunk, the pressure wave propagates through the tree and results in regions of high pressure in the most gravitationally-dependent regions of the lung. The corresponding velocity solutions over time are illustrated in Figure 5.38. Two spectrums are used to illustrate the wide range of velocities over the cardiac cycle, these are included at the top of the figure. As the pressure at the pulmonary trunk decreases velocities in the large vessels become negative, indicating reversal of flow. Only a small amount of flow reversal will occur in reality due to valve restrictions at the heart, but these solutions illustrate the potential of the pulsatile solution. Eventual coupling of the arterial and venous trees to the heart will result in a full pulsatile model. The highest velocities in the arterial tree occur at t=0.3 s when the pressure reaches a peak value of 2.5 kPa.

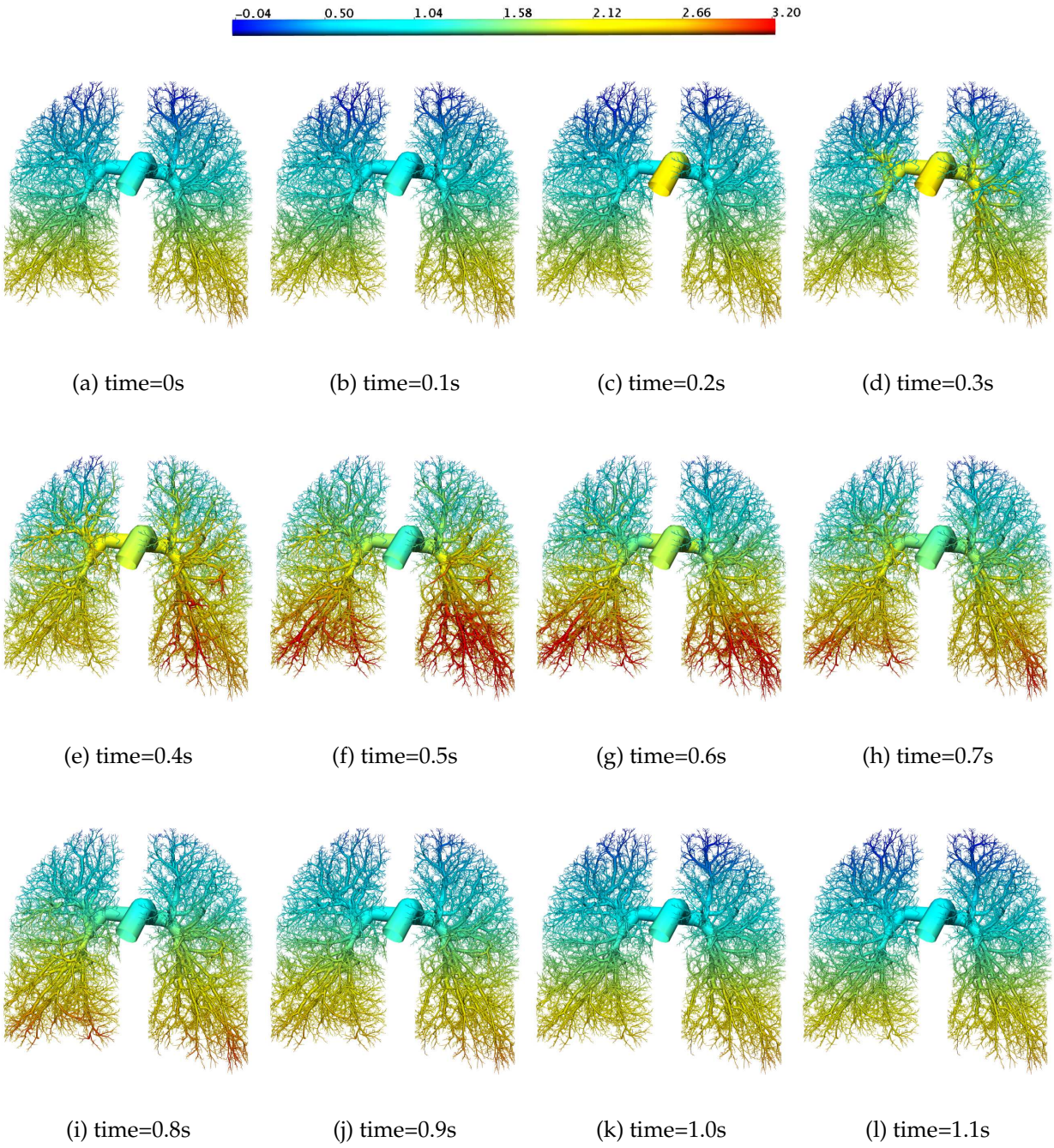

(a) time=0s (b) time=0.1s (c) time=0.2s (d) time=0.3s

(e) time=0.4s (f) time=0.5s (g) time=0.6s (h) time=0.7s

(i) time=0.8s (j) time=0.9s (k) time=1.0s (l) time=1.1s

FIGURE 5.37: *Series of images displaying the pulsatile pressure solution (*kPa*) over time in the arterial model. The spectrum used to illustrate the solution is included at the top of the figure.*

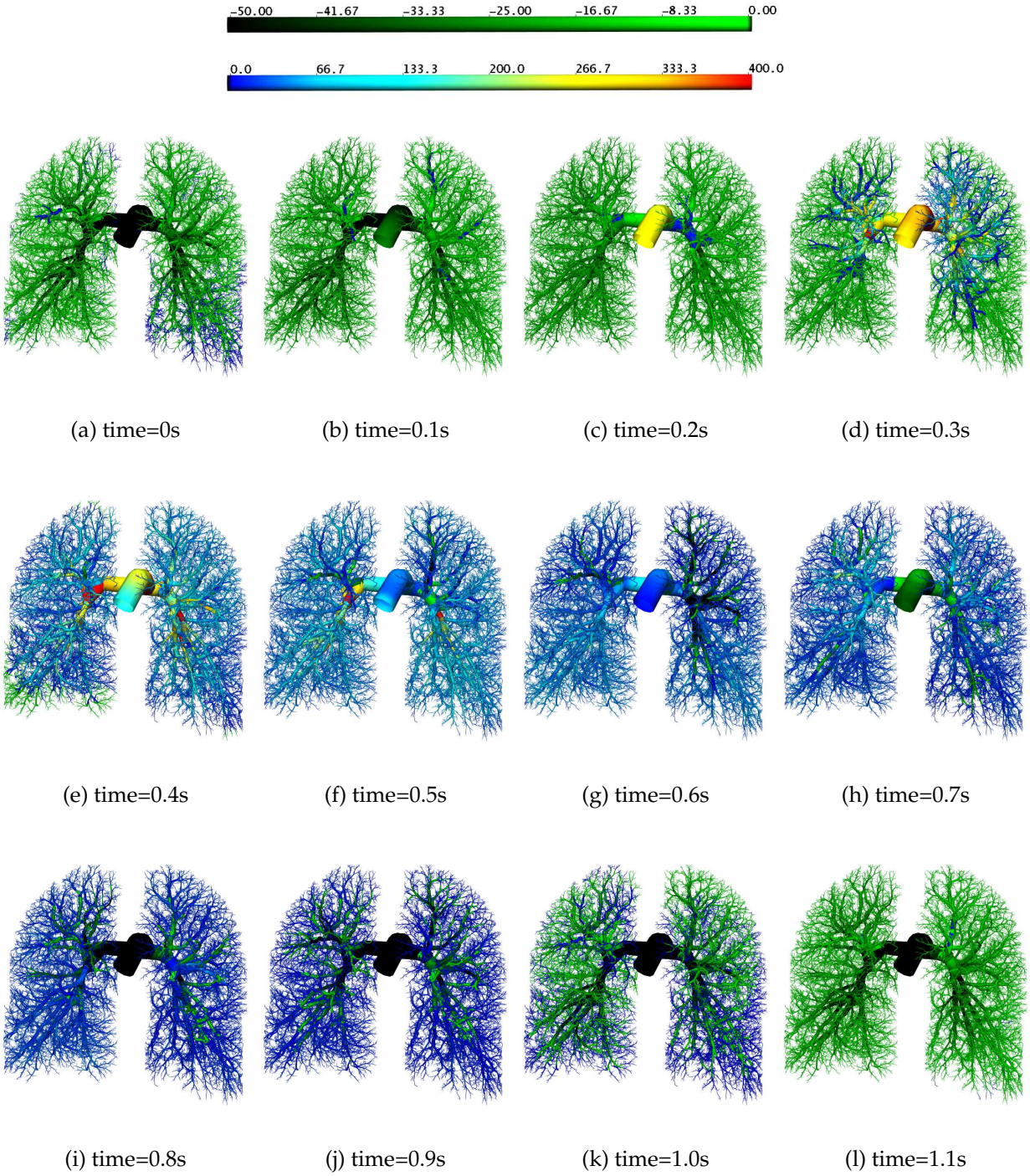

(a) time=0s (b) time=0.1s (c) time=0.2s (d) time=0.3s

(e) time=0.4s (f) time=0.5s (g) time=0.6s (h) time=0.7s

(i) time=0.8s (j) time=0.9s (k) time=1.0s (l) time=1.1s

FIGURE 5.38: *Series of images displaying the velocity solution* ($\mathrm{mm\ s^{-1}}$) *over time in the arterial model with pulsatile pressure boundary conditions prescribed. The two spectrums used to illustrate the solution is included at the top of the figure.*

5.4.9 Comparison of model results with functional imaging

- To compare model results with results obtained from functional imaging studies;

The combination of medical imaging and computational modelling has the potential to increase the understanding of structure-function relationships in the lung, in health and disease. Computational modelling and functional imaging can be used together, both as a method of verifying the other. The computational model developed in this study can be validated by comparison of flow results with data extracted from functional imaging of the human lung.

MDCT (multi-detector row x-ray computed tomography) imaging can be used to obtain functional as well as structural measures in the lung. Blood flow information is acquired by injecting a bolus of contrast agent and extracting information via the time-intensity curves of the contrast material. Denney, Beck, Shikata, McLennan & Hoffman (2004) carried out functional imaging studies using human and sheep lungs to investigate the distribution of blood flow with respect to gravity. Figure 5.39 displays an example of blood flow data extracted via imaging of a slice through a sheep and human lung. The colour spectrum represents blood flow normalised to tissue content (ml/min/g). These functional imaging studies demonstrated that gravity did not significantly contribute to blood flow distribution in the supine human lung. Results showed that gravity contributed to less than 5% of flow heterogeneity in the human lung, and to about 20% in the sheep lung.

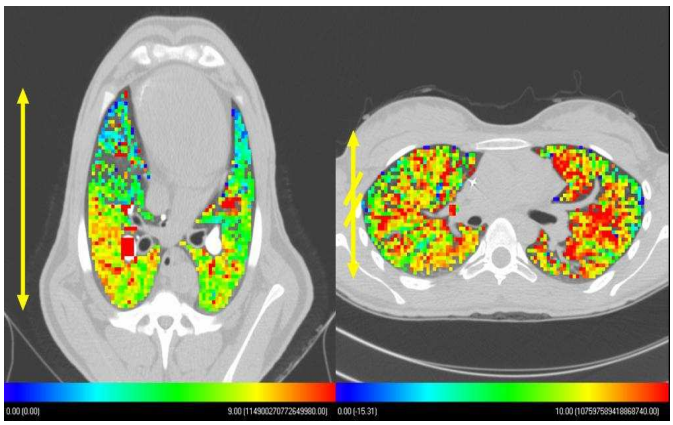

FIGURE 5.39: *Blood flow data extracted from MDCT functional imaging of sheep and human lungs. Colour spectrum represents the blood flow normalised to tissue content (ml/min/g). Picture from (Denney et al. 2004).*

MDCT image data, filtered to remove airways and large blood vessels, was received from the Department of Physiological Imaging at the University of Iowa. Any regions

of interest (ROIs) with an air content of greater than 90% and a blood content of less than 2% were considered to be airways and were removed, anything with a blood content of greater than 50% and an air content of less than 40% were considered to be large blood vessels and were also removed. It is uncertain as to the exact size of the blood vessels remaining after this filtering process, but the vessels are estimated to be below about 250 μm in diameter, with the possibility of some larger vessels being present (personal communication, 2005). To minimise lung movement during scanning, these images were taken between the T and P wave of the cardiac cycle during which time the ventricles are relaxing and refilling and the heart is moving the least. The region of lung tissue imaged is just below the carina to ensure an adequate image of the pulmonary vessels and an good lung sample. The area is also slightly below the heart (and superior vena cava) to minimise artifacts from the contrast bolus and catheter. Raw blood flow information (ml/min/ml) is displayed for two different normal human male subjects in Figures 5.40(a) and (b). This information includes both arterial and venous flow.

For comparison of model results with this image data a slice, in roughly the same location, was taken through the model arterial and venous vessels. Flow values ($\mathrm{mm}^3\ \mathrm{s}^{-1}$) were scaled to units of ml/min/ml for comparison. The volume unit in the model lung was assumed to be 7.05 L divided by the number of terminal accompanying arterial and venous vessels (=7.05 L/29,818). Only terminal nodal flow solutions were included in this analysis.

The range of flow solutions in the model results are slightly lower than the MDCT extracted data. The MDCT raw flow data is illustrated by applying two different flow spectrum ranges. The first spectrum (Figure 5.40(a)) includes the entire flow range (0-17.75 ml/min/ml). The large flow range means it is difficult to visualise changes in flow in the smaller vessels. Figure 5.40(b) illustrates the MDCT flow data with a narrower flow spectrum range (0-4 ml/min/ml), removing the higher flow values (now shown in black) which appear to be from larger vessels. Due to the uncertainty of the range of size of the vessels being measured by MDCT, a possible application of this flow model could be in helping to predict the size of vessels present by comparing flow rate solutions.

5.4.10 Comparison of flow in the human versus sheep lung

- To compare human arterial flow results with flow results obtained in a model of the sheep arterial tree;

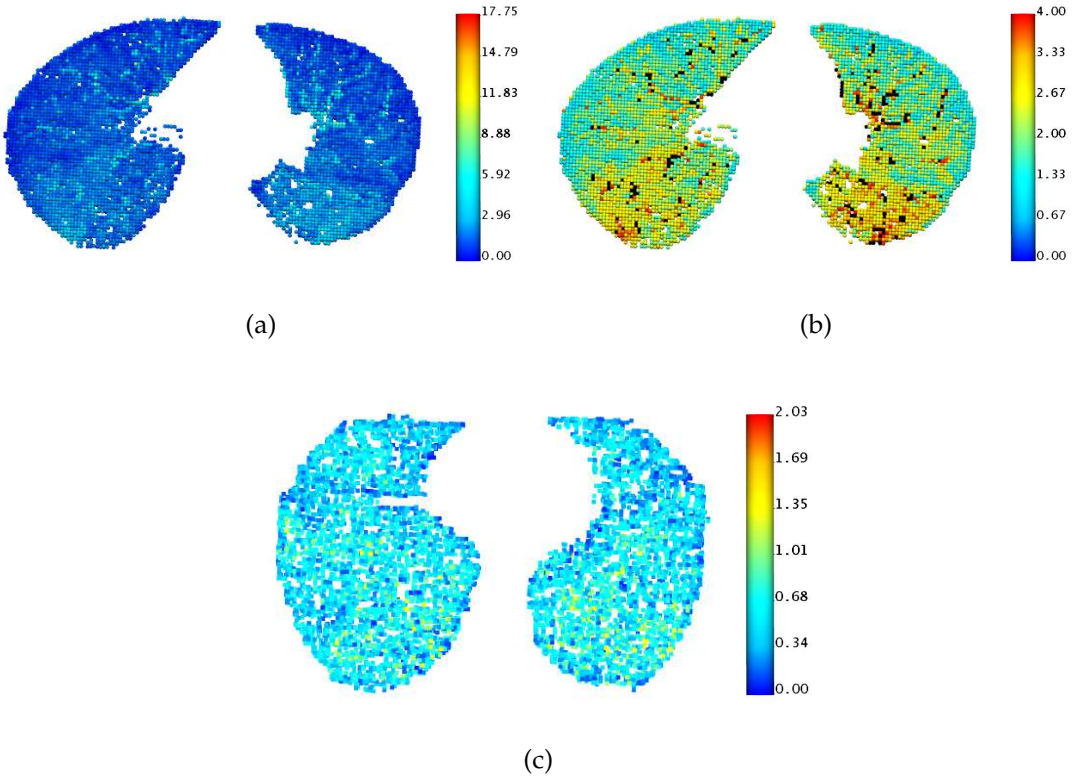

FIGURE 5.40: *Comparison of model results with flow information extracted from MDCT imaging. MDCT functional blood flow data, courtesy of the Physiological Imaging Department at the University of Iowa: (a) and (b) display raw blood flow (ml/min/ml) information within a normal male subject using two different solution scales, (c) display raw blood flow results (ml/min/ml) through a slice of the model - including terminal arterial and venous vessels*

The Navier-Stokes flow solution procedure was implemented within a finite element model of the sheep (ovine) arterial tree. The mesh used for this simulation is the same conducting airway model developed by Tawhai et al. (2004). Geometry and diameters of large airway branches down to a maximum of 23 generations were obtained from MDCT images (Figure 5.41(b)). The VFB algorithm was then used from these end points to generate the remaining branches undetectable via imaging into the lung volume also defined from MDCT (Figure 5.41(a)). This flow investigation assumes that the sheep arterial tree closely follows the bronchial tree, and therefore as a preliminary study blood flow results were obtained in the conducting airway geometry as an approximation to the arterial vessels. All branches have equivalent unstrained radius values as the conducting airway model, except the pulmonary trunk and next two generations of branches. The human pulmonary arterial trunk is larger in

diameter than the trachea, but smaller vessels have approximately the same diameters as their accompanying airways. This fact was applied to the sheep conducting airway model to create the radius distribution for the sheep arterial tree used in these blood flow simulations.

In contrast to the human conducting trees, the ovine branching structure is more monopodial in nature, leading to more asymmetric trees. Monopodial branching tends to produce minor child branches (with a large branching angle) stemming from a larger major child branch (with a small branch angle). This monopodial branching structure is visible in the finite element model of the sheep conducting airway structure displayed in Figure 5.41.

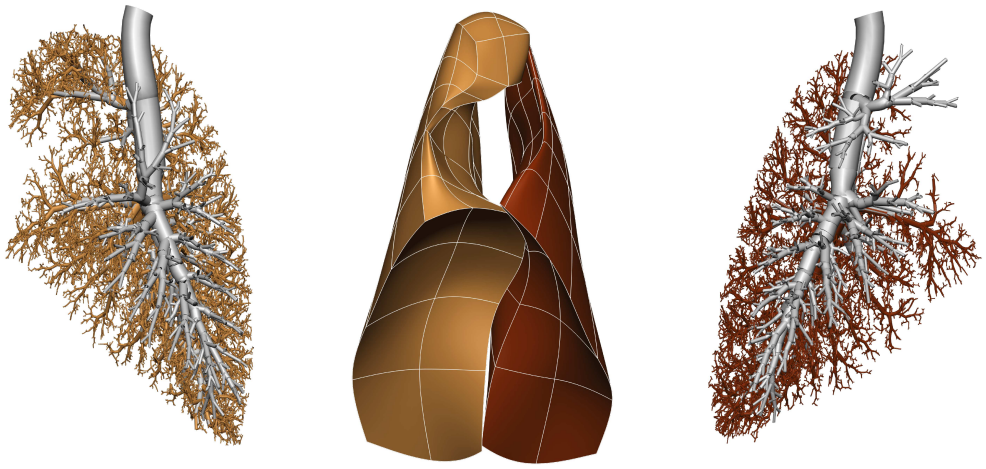

(a) (b) (c)

FIGURE 5.41: *Finite element model of the sheep lung and conducting airways (used to represent the sheep arterial tree). (a) Left side view of the MDCT-derived vessels (gray) plus branches generated into the lung volume using the VFB algorithm (brown) from the MDCT vessel end points. (b) Lung surface model, and (c) right hand view of the branches in the sheep lung. This geometry was used to obtain an arterial flow solution within the sheep lung.*

Steady-state flow solutions in the sheep arterial model without gravity (OG) and with gravity (1G) in the prone and supine postures were obtained (Figure 5.42). The sheep vessel elasticity was assumed to be the same as for the human arterial tree (G_0=5 kPa, β=3.2) due to lack of available data. Pressure boundary conditions (also the same as for human arterial simulations) were 2 kPa and 1.25 kPa at the inlet and outlet vessels, respectively.

As in the human blood flow results, all terminal solution data was extracted from the sheep model and flow information was averaged within slices of 1 and 30 mm in thickness. Inversion of the posture from the supine to the prone position resulted in a similar inversion of the pressure (Figure 5.43(a)), and therefore radius (Figure 5.43(b)), gradients at all terminal nodal locations with respect to height along the ventral to dorsal axis. Intersection of the pressure values for the different simulations indicates the relative positioning of the inlet arterial vessel (at a height of about 77%) with respect to gravity (that is, the inlet vessel defines the reference height for the applied gravitational force). The gradient of velocity and flow remains relatively consistent in the different postures with gravity and without gravity. A lower overall velocity (Figure 5.43(c)) and flow (Figure 5.43(d)) occurs in the supine posture, with the highest flows occurring in the prone position.

Comparison is made between results obtained in the sheep and human models in the supine posture (Figure 5.44). Terminal solution values averaged within 1 and 30 mm slices are plotted with respect to normalised gravitationally-dependent height (%). Due to relatively large differences in the terminal radius values of the sheep and human models (Figure 5.44(b)), there were large differences in the terminal velocity and flow values, and therefore velocity and flow solutions displayed are values relative to mean values. The sheep model displays larger velocity and flow gradients than the human model, which is purely a result of the different vascular geometry of the sheep arterial tree.

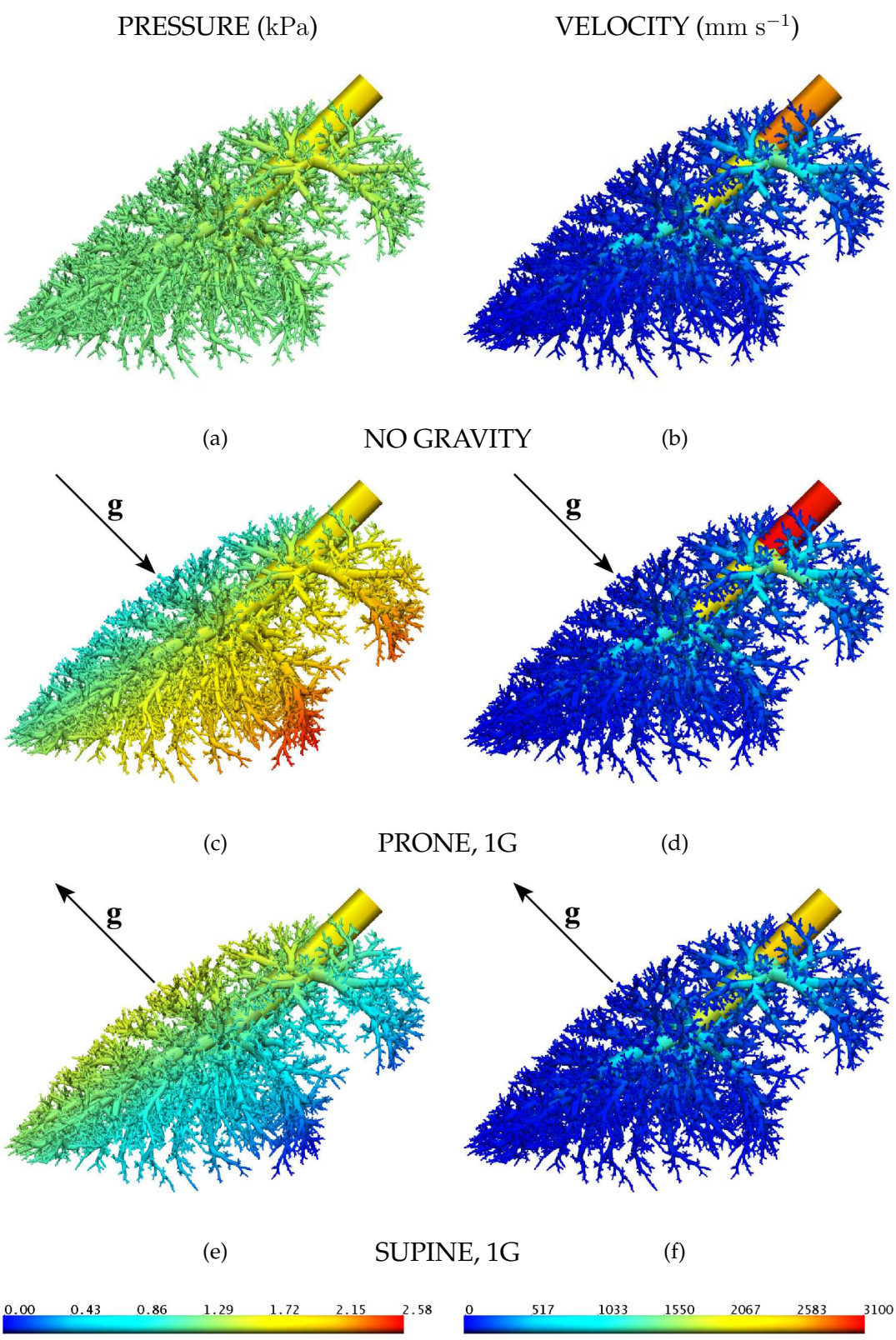

FIGURE 5.42: *Flow results in the sheep arterial model: (a) pressure and (b) velocity solutions without gravity; (c) pressure and (d) velocity results in the prone posture, and (e) pressure and (f) velocity solutions in the supine posture. Arrows indicate the direction of gravity. Pressure solutions have units* kPa*, and velocity solutions are in units of* mm s^{-1}*, spectrums used to illustrate solution are displayed at bottom of figure.*

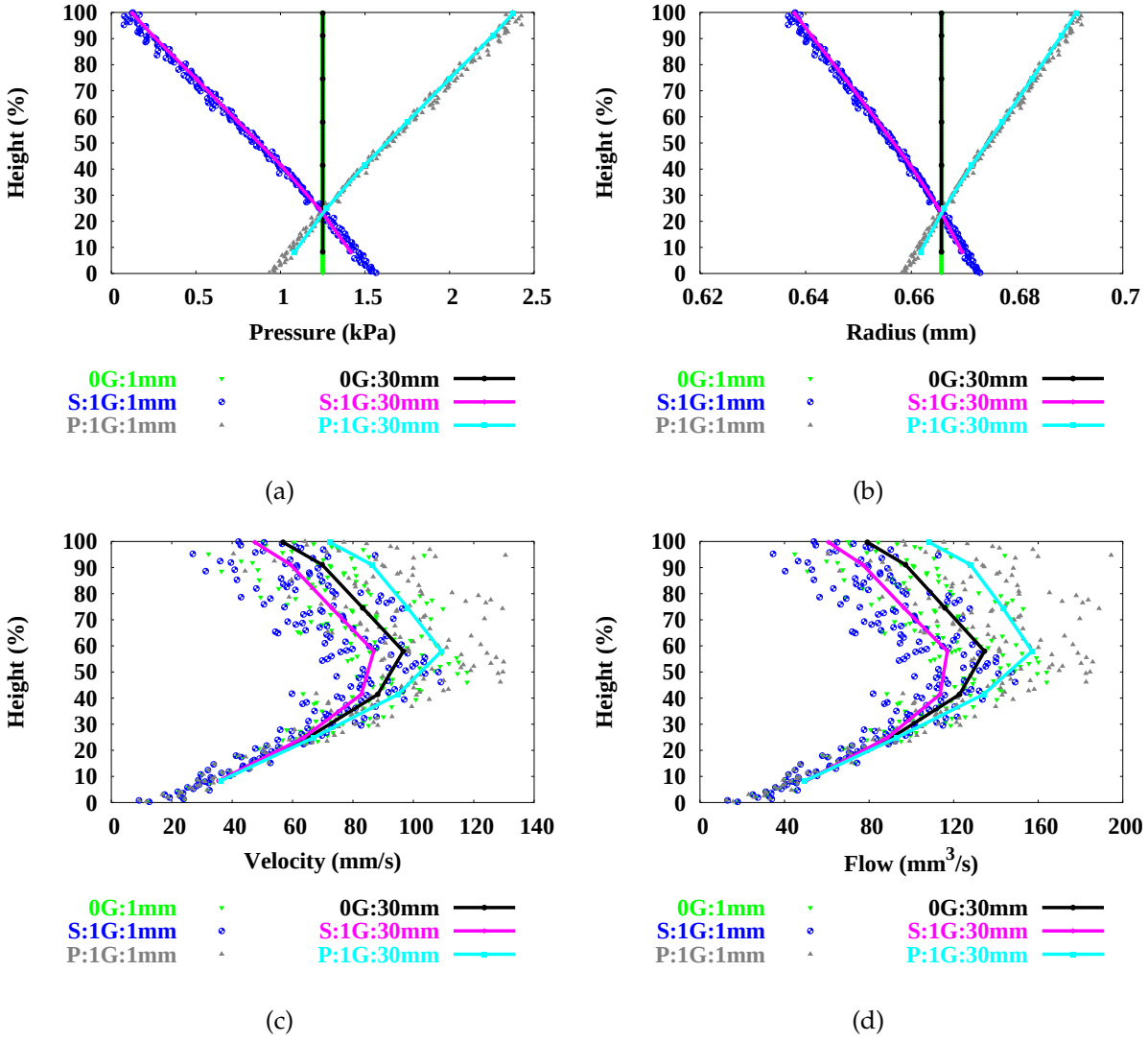

FIGURE 5.43: *Comparison of flow solutions in the sheep arterial model without gravity (0G) and with gravity (1G) in the prone (P) and supine (S) postures. Results plotted with respect to gravitationally-dependent height in the ventral (0%) to dorsal (100%) direction. Results averaged within slice thicknesses of 1 and 30* mm*: (a) pressure* (kPa)*, (b) radius* (mm)*, (c) velocity* (mm s^{-1})*, and (d) flow* (mm^3 s^{-1})*.*

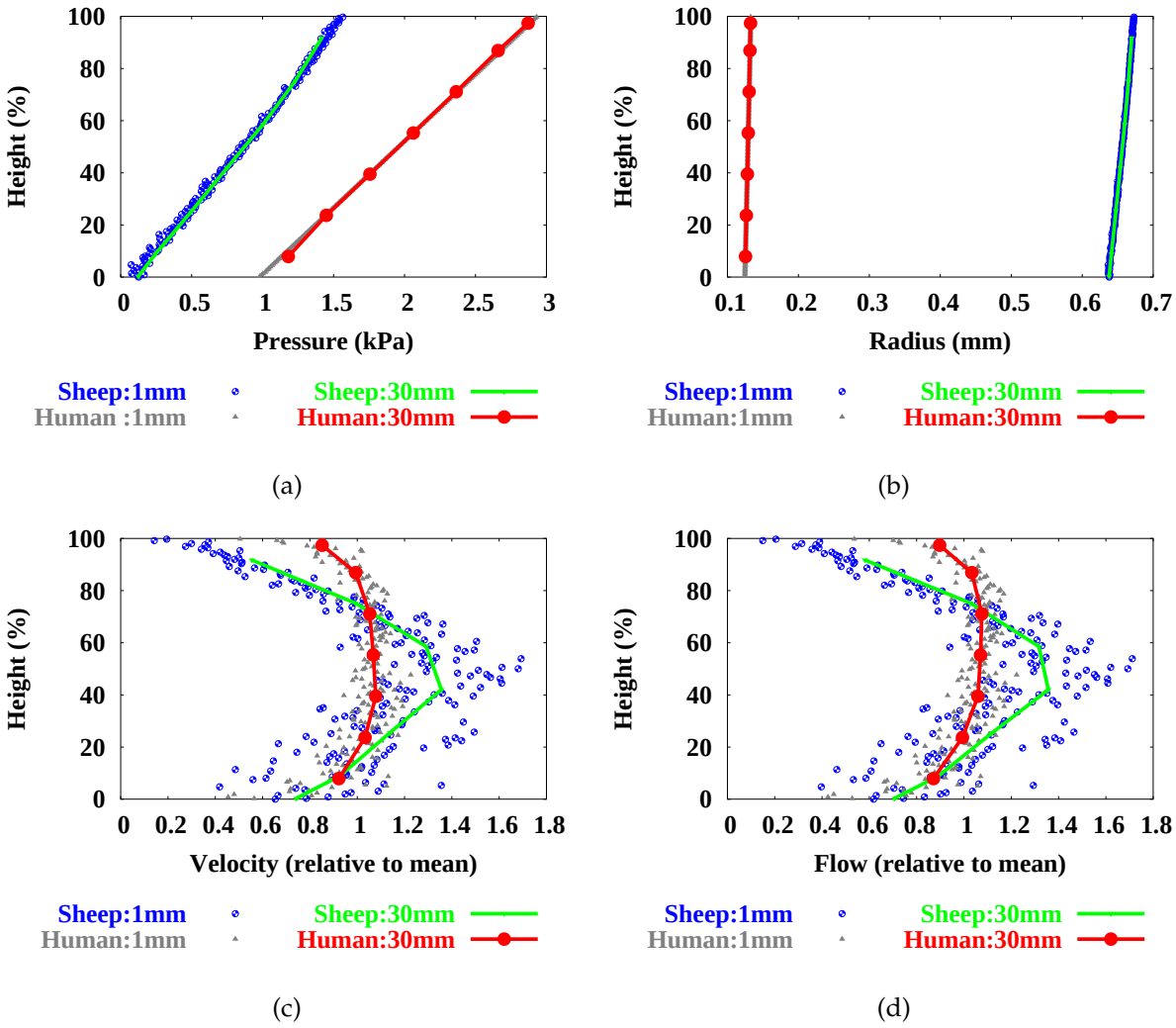

FIGURE 5.44: *Comparison of flow solutions in the sheep versus human arterial model in the supine posture with gravity. Results plotted with respect to gravitationally-dependent height in the dorsal (0%) to ventral (100%) direction. Results averaged within slice thicknesses of 1 and 30* mm*: (a) pressure (*kPa*), (b) radius (*mm*), (c) velocity (relative to mean), and (d) flow (relative to mean).*

Comparison is made between terminal flow data (averaged within 1 mm slices) and experimentally measured values of flow in the supine pig lung (Glenny et al. 2000). This is the same data used to compare against human model results (Figure 5.17). Flow (relative to the mean) is plotted with respect to gravitationally-dependent height (%) in Figure 5.45. The experimentally measured flow data compares well with data from the sheep model. Human flow results did not display as much of a decrease in flow in the upper and lower regions of the lung, this was hypothesised to be due to species differences. The results in the sheep model confirm this hypothesis. A large decrease in flow is displayed in the upper and lower (gravitationally-dependent) regions of the sheep lung, with a large peak flow in the mid region of the lung. These differences in flow are due to the geometry of the arterial tree only.

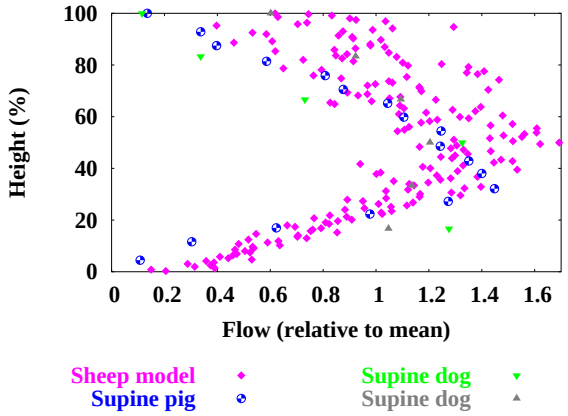

FIGURE 5.45: *Comparison of flow solutions (relative to mean) in the supine sheep model compared with experimental measurements in the supine pig lung (Glenny et al. 2000) and in supine dog lungs (Hogg et al. 1985) plotted with respect to gravitationally-dependent height in the dorsal (0%) to ventral (100%) direction.*

5.5 Discussion

As imaging and image processing techniques improve it will be possible to derive an increasing amount of both structural and functional information from imaging modalities such as CT and MRI (magnetic resonance imaging). The increasing spatial and temporal resolution of imaging is providing an increasing standard of pulmonary perfusion data (Won et al. 2003, Levin & Hatabu 2004). The coupling of imaging and computational modelling techniques will provide an even more powerful tool in the evaluation of structure-function relationships in the lung. This amalgamation

offers potential applications in tracking structural changes via imaging (remodelling, vasoconstriction), and investigating the consequences on global, and regional, lung function via modelling. The use of high resolution imaging data also provides greater scope for establishing normative ranges of variation in geometry and vessel caliber in different orientations or at different blood pressures which is the goal of the Lung Atlas (Li et al. 2003). A normal range of pulmonary perfusion may also be established and used to recognise deviations from normality to help in the early detection of pulmonary diseases, such as emphysema.

Computational modelling tools may be used in conjunction with imaging modalities, each method acting as a means to verify the other. For example, functional imaging data may be used for comparison with flow model results in larger vessels, thereby validating model results (Section 5.4.9). Modelling may then be used to investigate flow in smaller vessels, immeasurable via imaging, or to investigate different conditions, such as the upright posture which is difficult to obtain via imaging. The model may also be used to help interpret results from functional imaging studies, if the quantities being measured are uncertain. Computational models may also be used to obtain quick predictions of the functional consequences of certain changes in vascular geometry, for example the effect of pulmonary vasoconstriction, pulmonary embolism, or pulmonary hypertension, for individual subjects.

Studies into the origin of pulmonary blood flow heterogeneity have highlighted the prominent functional significance of the asymmetric branching structure of the pulmonary vasculature, suggesting that gravitational factors are a minor determinant of flow distribution (Glenny et al. 1999). Previous studies have highlighted the intimate relationship between structure and function in the pulmonary circulatory system through both computational (Parker et al. 1997, Krenz et al. 1992, Dawson et al. 1999) and experimental investigations (Glenny, Polissar & Robertson 1991, Glenny et al. 1999). The current study has simulated blood flow through the human pulmonary arterial and venous trees by solution of the Navier-Stokes flow equations, representing Newtonian fluid flow.

The pulmonary flow model developed in this study builds on an existing model of flow through the coronary blood vessels (Hunter 1972, Smith et al. 2002). The numerical techniques and methodology used are identical to this study, with the exception of the inclusion of a gravitational term. Gravitational factors are more significant in pulmonary flow evaluation due to the relatively large height differential of the organ (≈ 30 cm).

Creation of the finite element arterial and venous models included derivation of the

largest blood vessels and lobar definitions from multi-detector row x-ray computed tomography (MDCT) scans from the Lung Atlas (Li et al. 2003). This technique enables a more accurate description of vessel geometry and allows patient- and species-specific models to be generated. A volume-filling branching (VFB) algorithm (Tawhai et al. 2000) defines the geometry of the smaller accompanying arterial and venous vessels unidentifiable via imaging, producing vascular trees governed by the lobar geometries and the positions of the initial MDCT derived vessels, thereby producing a more realistic, integrated model (Chapter 4) than previous models of the pulmonary vascular trees.

Even in the absence of gravity, flow through the anatomically-based arterial model (and the anatomically-based venous model) showed a large amount of heterogeneity due to the asymmetric branching structure and diameter distribution leading to non-uniform flow pathways. In contrast, flow results within the symmetric arterial model, without gravity, demonstrated homogeneous flow rates at all terminal locations; this was the expected result due to the equivalent geometry of all flow pathways. These results indicate that the vascular branching structure plays a large role in pulmonary flow heterogeneity. With the addition of gravity, both models display a pressure gradient increasing from the top to the bottom of the lung due to hydrostatic forces, resulting in an increase in flow from apical to basal regions. The symmetric model flow results are uniform at any given gravitationally-dependent height, while the anatomically-based model displays heterogeneous flow results within isogravitational regions. The anatomically-based models display a decrease in flow in the most dependent (basal) regions of the lung (due to increased path lengths, described below), the symmetric tree does not demonstrate this decreased flow. Again, the symmetric tree precludes path differences and therefore continues to have an increasing flow through the entire height of the lung from apical to basal regions.

Flow solutions with and without gravity in the anatomically-based arterial model were compared to assess the contribution of gravity to blood flow distribution in the upright lung (Section 5.4.2.2). The gradient of flow with respect to vertical position (as determined by linear regression, Figure 5.16) increased from -0.006 to -0.019 relative flow units/cm with the inclusion of gravity. These results reveal the persistence of a flow gradient even in the absence of gravitational factors. This is in agreement with experimental results in the upright baboon lung, where Glenny et al. (1999) observed an average flow gradient of -0.088 and -0.020 relative flow units/cm with and without gravity, respectively. The linear regression fitting only uses flow data in the upper regions of the lung, where flow is increasing, as was done by Glenny et al. (1999). The

region of decreasing flow in the most dependent regions of the lung is obviously not a result of gravitational forces and therefore should not be incorporated into the gravity-flow relationship.

Similar analysis was conducted comparing flow solutions in the upright venous model with and without gravity (Section 5.4.2.3). Linear regression analysis (Figure 5.20) revealed flow gradients with respect to gravitationally-dependent height of -0.011 and -0.035 relative flow units/cm with and without gravity, respectively. This analysis also only includes data between the heights of 12 and 30 cm as used for the arterial tree. The flow gradients in the venous model are greater than in the arterial model, most probably because of the different distensibility of the vessels, namely the β values of 3.2 and 1.2 applied to the arterial and venous trees, respectively. The effect of various vessel distensibilities has been demonstrated in the arterial model (Figure 5.32), and was shown to have a significant effect on flow solutions (discussed further below).

Figures 5.15 and 5.19 display terminal flow results with respect to vertical position in the lung in the upright arterial and venous models, respectively. These results demonstrate decreasing flow in both the upper and lower regions of the lung. This can (at least partially) be explained by the differences in flow path lengths (from inlet to outlet), as illustrated in Figure 5.35, where paths with the longest lengths (upper and lower regions) have corresponding lower flow rates and longer transit times. The longer path lengths lead to higher resistances to flow meaning that these paths convey smaller amounts of flow. These results again indicate the large influence of the vascular branching structure on blood flow distribution, and also demonstrate that the positioning of the pulmonary trunk feeding into the pulmonary circuit, and the central veins draining back into the heart, is vital in determining the distribution of flow in the lung.

Early studies of perfusion distribution in the human lung used low resolution imaging techniques, such as external scintillation x-ray counters (West et al. 1964) providing flow information averaged over large regions of the lung. Advances in experimental technologies (Glenny, Polissar & Robertson 1991) have provided higher-resolution data with which a clearer idea of regional flow distribution can be obtained. Such studies have indicated that gravity is not the main determinant of pulmonary blood flow heterogeneity. Model results at terminal locations are averaged within 1 and 50 mm slice thicknesses (and also within other various slice thicknesses, Section 5.4.3) in order to mimic these different experimental resolutions and to illustrate the effect of different resolution data on the interpretation of flow results. Microsphere injection techniques (Glenny, Polissar & Robertson 1991) yield high spatial resolution flow data,

as in the 1 mm (averaged) model results. These results demonstrate a large amount of heterogeneity in flow values within isogravitational regions, revealing a less significant contribution of gravity on flow distribution. Model results averaged within 50 mm slices, mimicking lower spatial resolution data, show a clearer gradient due to gravity, suggesting how gravitational dominance was interpreted from earlier investigations. Lower resolution measures cannot detect heterogeneity in isogravitational regions, because only averaged flow information is extracted.

Results averaged within 50 mm slices display the four typical zones of flow (as demonstrated in Figure 1.9), with increasing flow in the upper regions of the lung (categorised as zones 1-3) and a region of decreasing flow (zone 4) present in the lower (basal) region of the models. Zone 4 flow has been suggested to occur as a result of increased resistance in the extra-alveolar vessels, due to the smaller amount of distension in the most gravitationally-dependent region of the lung (West 1999). While the arterial and venous flow models incorporate pleural pressure effects, this region of decreased flow persists even in the absence of external pleural pressure forces (Figure 5.27). Model results suggest that the increased path lengths, and therefore resistance to flow, in these regions furthest from the heart result in the decreased flow in the basal region of the lung. This region of decreased flow remains in all conditions, for example in all postures and in the absence of gravity and pleural pressure.

West's zonal model, in which gravity is named the main determinant of regional vascular perfusion, leads to a number of predictions with respect to blood flow distribution. For example, this model implies that flow within isogravitational planes (equal height and hydrostatic pressure) is uniform, reversal of posture should result in reversal of the flow gradient, heterogeneity should only occur in line with gravity, increased pressure, for example during exercise, should result in more uniform flow throughout the lung. Another major prediction of this zonal model is that in the absence of gravity blood flow distribution should become uniform. Experimental procedures have disproved a lot of these hypotheses with the advent of higher resolution flow data and microgravity experiments (Glenny et al. 1999). Model results clearly display a large amount of heterogeneity within isogravitational regions, and the persistence of a flow gradient in the absence of gravity, indicating that factors other than hydrostatic pressures affect blood flow distribution.

As well as altering the direction of gravity, changes in posture also result in changes of the chest wall, diaphragm, and heart positions, and local parenchymal stresses (Hlastala & Glenny 1999). The current model neglects any of these factors, and looks purely at the behaviour in the isolated vascular system. Flow results in various postures

(prone, supine, upright, and inverted, Figures 5.28-5.31) displayed a persistence of the trend of flow in all positions, namely an increasing flow from the apical to basal regions and a decreasing flow in the most basal regions of the lung. These results suggest that the vascular geometry largely determines the distribution of flow.

Other experimental studies of perfusion heterogeneity in different postures have agreed that factors other than gravity are largely responsible for flow distribution. Musch et al. (2002) used PET (positron emission tomography) imaging to assess the distribution of ventilation ($\dot{V}$) and perfusion ($\dot{Q}$) in prone versus supine humans. This study demonstrated that both $\dot{V}$ and $\dot{Q}$ gradients (favouring dependent lung regions) were maintained in both postures. They also found that flow heterogeneity, as measured by the coefficient of variation squared (CV^2=$(SD/mean)^2$), was unaffected by posture. Jones et al. (2001) produced similar results through electron beam computed tomography (EBCT) scans on healthy humans, also comparing perfusion distribution in the prone versus supine positions. Gravity was estimated to produce 22-34% of perfusion heterogeneity in the supine posture and 27-41% when subjects were prone.

The current study develops a pulmonary flow model of greater detail both structural and functional - than previous models. The asymmetric structure of nearly 60,000 vessels each for the arterial and venous systems are included as opposed to previous symmetric (Parker et al. 1997), fractal type (Glenny & Robertson 1991, Krenz et al. 1992), or lumped parameter type (Huang et al. 1998) models. Previous models implementing Poiseuille type flow solutions (Dawson et al. 1999) within vascular networks, imply that pulsatile (or time-dependent) flow cannot be investigated, unlike in the current model. Li & Cheng (1993) produced a nonlinear fluid model of flow through the pulmonary circulation also using a Lax-Wendroff finite difference method to solve fluid continuity, momentum, and wall equations. Their model solved flow through the entire pulmonary circuit, but only implemented the solution within a simple 2D network model consisting of a total of 18 generations. The use of a more detailed, subject-specific model has great potential for evaluating structure-function relationships in individuals in health and disease.

This flow model obtains results within isolated pulmonary arterial and venous trees, free from external factors such as airway pressures, and forces exerted by the heart and chest wall. Therefore this model best mimics pulmonary blood flow at residual volume (RV) when the lung is in a relaxed state. Experimental measurements have demonstrated that the effect of gravity on blood flow varies with lung volume, with the largest effect displayed at total lung capacity (TLC) and the smallest effect at RV

(Hughes et al. 1968). This may be a contributing factor to the small effect displayed by the inclusion of gravity into the flow model.

The simulations in this study assume a constant vessel compliance throughout the arterial and venous networks. Numerous studies have been conducted to determine pulmonary blood vessel elasticity (the restorative force) and distensibility (the actual change in vessel volume with pressure) using various different techniques. Collation of pulmonary elasticity measurements by Krenz & Dawson (2003) illustrated that even though the pulmonary arterial wall structure varies considerably from the main pulmonary artery to the precapillary terminal arteries, the distensibility is essentially constant and independent of vessel diameter and vessel wall composition. The same was found for venous vessels. Figure 5.32 demonstrates the significant effect of vessel distensibility on flow distribution. The lower values of G_0 (=1 kPa) and β (=3) display a much larger effect of gravity on blood flow distribution. In reality the tethering of the pulmonary fibre network probably results in less distensible vessels. As more detailed elasticity information becomes available this can easily be incorporated into the flow model to more closely mimic the *in vivo* situation.

The application of constant vessel distensibility may have consequences in investigating the effects of vascular remodelling. Vascular regions of consistently high flow may incur structural changes, mainly a thickening of the vessel wall by increased muscle resulting in increased rigidity (Riley 1991). In this case a non-uniform distribution of vascular compliance could be applied to vessels in the model. An increased understanding of the structural changes occurring in the blood vessels would be required to do this.

Transit times through the arterial and venous models during the various simulation conditions are presented in Table 5.1 (Section 5.4.7). Dawson, Capen, Latham, Hanson, Hofmeister, Bronikowski, Rickaby & Wagner Jr (1987) measured the time taken for a bolus of dye to travel from the main pulmonary artery to a subpleural pulmonary arteriole in anesthetised dogs placed in the left lateral decubitus position using fluorescence microscopy. They found a mean transit time of 1.94 s (standard deviation of 1.23 s and a relative dispersion (standard deviation/mean) of 64%). This average transit time value is significantly shorter than the value of 4.03 s calculated in the human arterial model. This may be due to species differences, namely in the geometry of the respective arterial trees, or differences in pressure conditions within the system. This study also measures the transit time to a subpleural arteriole location, which may not be representative of the whole arterial system in the lung. The sheep transit times are significantly shorter than these values, possibly due to similar reasons described above.

The pressure boundary conditions applied to the sheep arterial model were the same used in the human model and may not be representative of pressures in the sheep lung.

MacNee et al. (1989) measured mean transit times of 5.1 $\pm$ 0.5 s and 4.1 $\pm$ 0.6 s of RBCs through the entire human pulmonary circuit in the upper and lower gravitationally-dependent regions of the human lung (in the lateral decubitus position), respectively. Hogg et al. (1985) measured regional differences in RBC transit in supine dogs, finding an average time of 2.86 $\pm$ 0.31 s with transit times ranging from 0.41 to longer than 20 s. These studies have been previously discussed in Chapter 3, Section 3.3.8, and scaled values were used to compare with capillary transit times. Both of these studies measure RBC transit rather than whole blood transit. The transit results in this study refer to transit of whole blood, not just RBCs. RBCs are known to traverse more quickly through the pulmonary system than whole blood in vessels with diameters less than around 500 $\mu\mathrm{m}$, which may have influenced the measured results. The much longer transit times predicted by the model will also be influenced by the steady-state system solution obtained at a single set of boundary pressures instead of integrating the solutions over a pulsatile pressure cycle. That is, the pressure boundary conditions were assumed to represent the mean flow state and therefore the results were used directly to calculate the transit time. The large pressures during systole may reduce the model transit times closer to experimental values.

Peak flows predicted for the venous model were larger than for the arterial model. This is likely to be due to inaccurate estimation of peripheral pressures used as boundary conditions in the model. Currently the arterial and venous systems are completely independent from each other. After coupling of the two models via a microcirculatory unit the system will be interdependent and conservation of mass will apply across the entire pulmonary flow circuit.

While microsphere experimental techniques can yield high spatial resolution flow data in animals, this is a destructive procedure and therefore not applicable to human studies. Therefore this model, in conjunction with functional imaging, will be useful in predicting blood flow distribution in humans in health and disease. Preliminary model validation using functional MDCT imaging data displayed a general agreement in the range of flow values (Section 5.4.9).

Comparison of arterial model flow results were made with experimentally measured flow in upright baboons (Glenny et al. 1999) and supine pigs (Glenny et al. 2000) (Figures 5.17 and 5.24), as a means of validating the model. The pattern of flow and flow values (relative to the mean flow) obtained with this model were similar to these measurements. Future work will include further comparisons with

flow measurements, from both imaging studies and experimental measures.

While the geometric arterial and venous models developed in Chapter 4 include supernumerary vessels, these were not incorporated in the flow solution procedure. The vast number of supernumerary vessels means that it is very difficult (in terms of computational capability) to obtain a solution through the full network. More realistic solutions will also only be obtained through these vessels when the full circuit is modelled through coupling of the arterial and venous models via the microcirculatory flow model. The presence of a muscular sphincter at the inlet to supernumerary vessels has been noted in bovine lungs (Shaw et al. 1999) (thought to act as a means of controlling flow through these vessels) and would have to be accounted for in the model. Addition of the supernumerary vessels would most likely not alter flow results significantly. The nature of supernumerary vessels with their 90^0 branch angle and small diameters would mean that these vessels do not receive much flow. It is believed that these vessels act as a reserve capacity for times of increased flow (Shaw et al. 1999).

Preliminary pulsatile solutions in the arterial tree are presented in Section 5.4.8. Pulsatile pressure is applied only at the pulmonary trunk, and constant pressure is maintained at all terminal locations. More realistic pulsatile solutions will be obtained when the arterial and venous systems are coupled via the microcirculatory model. Pulsatile velocity results demonstrate negative velocities in the larger arterial vessels during the decrease in pressure (typical of the R-S portion of the QRS pulsatile complex). These solutions do not represent physiological behaviour. Reversal of flow cannot occur in the pulmonary circuit due to the heart valve restrictions. These pulsatile solutions do, however, illustrate the potential of the model in simulating pulsatile flow.

Flow distribution in the supine sheep arterial model was significantly different than in the supine human arterial tree (Figure 5.44). Much steeper velocity and flow gradients were demonstrated in the sheep lung, with largely reduced flows in the apical and basal regions of the lung. All simulation parameters in the sheep model (for example, elasticity values, inlet and outlet pressure boundary conditions) were consistent with human simulation parameters. This implies that the differences in flow are a direct result of the arterial tree geometries. These results have implications for comparisons between human and sheep flow phenomena. For example, destructive experimental procedures (such as microsphere injection flow measurements) are only applicable to animal studies. Therefore the ability to interpret flow results obtained in animals under different conditions and predict flow behaviour in human lungs is an important step, with which this model may provide some help. The sheep model results compare more closely to the experimentally measured flow values in the supine

pig and dog lungs (Figure 5.45) than the human model results (Figures 5.17 and 5.24).

The major assumptions in the Navier-Stokes flow model are the pressure-radius relationship (Equation 5.4), the assumed radial velocity profile, and the pressure loss calculation at bifurcation points. These simplifications enable the Navier-Stokes equations to be solved efficiently in the large arterial and venous networks. As computational power increases these additional factors may be able to be incorporated into the solution procedure to allow a full 3D solution to be obtained. At this stage it is believed that the simplified 1D solutions adequately represent pulmonary blood flow distribution.

One of the major limitations in the model as it stands is that the arterial and venous trees are independent of each other, they are not coupled. When the arterial and venous flow models are coupled via a lumped parameter model representing microcirculatory blood flow, more realistic results will be obtained. This is a definite focus for future work, refer Section 6.

5.6 Conclusions

The anatomically-based models of blood flow through the human pulmonary arterial and venous trees developed in this study have demonstrated the large effect of asymmetric vascular branching structure on blood flow heterogeneity, and show that while gravity has an effect on blood flow distribution, it is not necessarily the dominant factor. Results reveal that while the flow gradient due to gravity is clearly present in lower resolution data, a trend is less obvious in higher resolution data. The models display an area of increasing flow from the apical to the basal regions of the lung, with a decrease in flow in the most basal regions. This trend persists in the absence of gravity, pleural pressure, and in various postures, also implying that gravity is not the main determinant of flow. This work agrees with high-resolution experimental studies of blood flow distribution in animals (Glenny, Polissar & Robertson 1991).

The potential for simulating pulsatile flow solutions within the arterial tree has been demonstrated. More realistic results will be obtained when a complete model of the arterial-capillary-venous flow circuit is developed, and cardiac restrictions are accounted for.

Flow results were also obtained within a sheep arterial model and were found to compare well with experimental data from supine pigs and dogs.

A summary of this work can be found in (Burrowes, Tawhai & Hunter 2005*b*).

Chapter 6

Summary

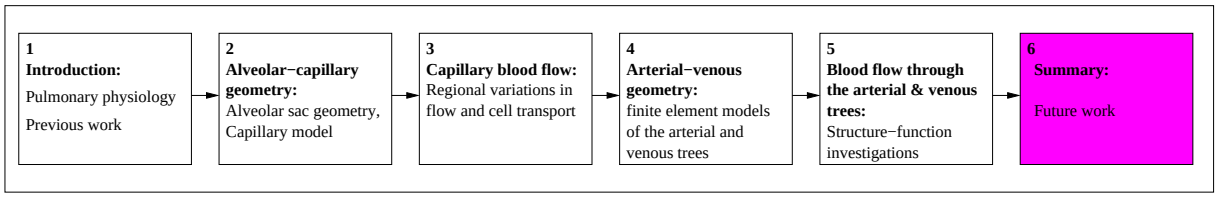

The ultimate goal of this research was to create an anatomically-based model of flow through the pulmonary circulation of a healthy human lung.

Beginning at the microcirculatory level, a 3D Voronoi meshing technique was used to generate an alveolar model into a unit cube of tissue. A single alveolar sac was extracted from this volume-filling model over which to create a capillary network. A 2D Voronoi meshing procedure was used to create a capillary model continuous with the alveolar units. This Voronoi mesh was created on the surface of a unit sphere and projected onto the alveolar surfaces. Only a single capillary mesh was generated between adjacent alveoli, rendering this meshing technique applicable to producing capillary networks continuous with larger units of alveolar tissue.

Poiseuille type flow equations, incorporating a hematocrit-dependent viscosity term, were solved within the 1D capillary segments. A dimensional model was incorporated into the flow procedure which accounts for alveolar, pleural, and capillary blood pressures. This model was used to investigate regional variations in flow and cellular transit phenomena. Gravity-dependent pressure boundary conditions were applied at the inlet arterioles and outlet venules over the height of a 30 cm lung. Flow, diameter, and RBC distributions were calculated, and RBC and WBC transit times from arteriole to venule were determined. Model results displayed physiologically consistent trends of an increasing flow from apical to basal regions of

the lung, with a small region of decreasing flow in the most gravitationally-dependent regions, due to the increase in pleural pressure. Cellular transit times demonstrated an increased average transit time and more homogeneous transit time distributions as flow increased down the lung. WBC cells were found to become trapped more frequently in the upper regions of the lung where the capillaries were, on average, less distended. Model results of RBC transit times and flow (relative to mean) were found to compare well with experimentally measured data.

Finite element models of the conducting arterial and venous trees were created using a combination of data extracted from MDCT, a volume-filling branching algorithm, and an empirically-based supernumerary algorithm. This procedure generated volume-filling vascular trees down to the level of their respiratory bronchiole (Strahler orders 11 and 9 for the arterial and venous trees, respectively) consisting of approximately 60,000 vessels each.

By assuming a radial velocity profile, a reduced form of the Navier-Stokes equations was solved within the arterial and venous geometries. A finite difference two step Lax-Wendroff numerical scheme was implemented to solve the equations. Comparison of flow solutions in a symmetric arterial model with solutions in the anatomically-based model revealed the significant effect of vascular branching structure on blood flow heterogeneity in the lung. In the absence of gravity, the symmetric model displayed homogeneous solutions at all terminal locations while the anatomically-based model displayed a large amount of flow heterogeneity. A gradient of increasing flow from the apical to basal regions, with a decrease in flow in the most basal regions of the model, was present even in the absence of gravity and within various postures (prone, supine, upright, and inverted).

Transit times through the arterial model were significantly longer than experimentally-measured values, but this may be due to the pressure boundary conditions applied, or other specified model parameters, such as vessel distensibility, but the most likely factor is the steady-state nature of the solution, whereby we are assuming that by prescribing mean arterial and venous boundary condition pressures we are replicating mean flow values. Comparison of model results with functional imaging displayed a better correlation with raw blood flow data being within a similar range. For each of the human, arterial, and sheep models the values predicted for flow are likely to become more accurate with model improvements, but at this stage of model development the trends in flow distribution are clear regardless of the total flow prediction.

Pulsatile solutions were obtained within the arterial model, by specifying pulsatile

pressure boundary conditions at the pulmonary trunk. This displays the potential of the model, but more realistic pulsatile solutions will be obtained after coupling the arterial-capillary-venous flow circuits and incorporating restrictions placed by the heart.

Flow solutions were obtained within a model of the sheep arterial tree. Flow distributions within this model were found to compare more closely to measured data from pigs and dogs. Comparison between human and sheep flow solutions demonstrated the large effect of the vascular structure on blood flow distribution in the lung.

This work has developed three flow models - arterial, capillary, and venous - currently independent from each other. In reality these three networks are intimately linked and form an interdependent system. The microcirculatory model is a more detailed version of the sheet-flow model and is governed by gravity-dependent pressure boundary conditions and therefore West's zonal flow theory applies. The typical zones of flow are present (excluding zone 1 where there is no flow). The capillary model simulates isolated flow within the alveolar sac capillary unit and does not account for upstream/downstream flow differences from the arterial/venous vessels. The large vessel flow models are independent of capillary flow and therefore do not incorporate resistance differences arising from the different capillary flow zones. However, the typical zones of flow are visible in the isolated arterial and venous flow models. On coupling of the three systems to form the complete pulmonary flow circuit the influence of gravity may become more pronounced. Formation of the complete pulmonary flow circuit will be the first stage of future work (see Section 6.1). By incorporating the influence of tissue density and soft-tissue mechanics on blood flow an even more accurate flow model will be obtained.

6.1 Future work

This work is ongoing, the major future developments will include the following:

- Coupling of the arterial-capillary-venous flow models to create a full flow circuit to and from the heart. This will include the development of a lumped parameter model of microcirculatory flow (based on the more detailed capillary model).

- Obtain flow solutions in the full pulmonary model including supernumerary vessels. As computational power increases, and after the model is coupled to

form a full flow circuit, the supernumerary vessels can be included into the flow solution procedure.

- Incorporating gas exchange into the flow model. Gas exchange is proportional to the RBC concentration and flow rate of the cells. Including a model of gas exchange will allow the prediction of global gas exchange measures, which are more easily validated through experimentally measured values.

- Using the model to investigate the effect of positive pressure ventilation on pulmonary blood flow. Both the capillary and larger vessel flow models incorporate the effects of pleural pressure. The capillary model also includes alveolar pressure. Therefore the flow will be affected by the onset of positive pressure ventilation, and the model can be used to investigate the effect of this on pulmonary blood flow.

- Coupling of the pulmonary blood flow solution with soft-tissue mechanics deformation solutions. This will involve an iterative procedure where the mechanics and blood flow solutions are co-dependent.

- Application of the model to disease processes. One of the earliest detectable signs of emphysema is alteration in microcirculatory blood flow. This model offers potential in the prediction of normal flow results, to help recognise deviations from normality.

Appendix A

CMISS command files

The computational simulations included in this study were conducted using a software package called CMISS (Continuum Mechanics, Image analysis, Signal processing and System Identification). This is a mathematical modelling tool developed at the Bioengineering Institute, The University of Auckland which allows the application of finite element, boundary element, and collocation techniques to a variety of complex bioengineering problems. Command files (.com) are required for each specific problem and example command files are included in this appendix. Input files (.ip files) are also required to input certain parameters required for each problem. Examples of all the simulations included in this thesis can be found at http://cmiss.bioeng.auckland.ac.nz/development/examples/9/98/.

NB/ All commands begin with 'fem' (finite element method). The text after '#' are comments describing the command.

A.1 Creating the alveolar model

This command file generates the alveolar model into a unit cube using a 3D Voronoi meshing technique (described in Chapter 2).

```
fem de param;r;alveoli ;                          #defines array parameters
fem de coor 3,1;                                  #defines coordinates
fem de reg;r;three;                               #defines 3 regions
fem de base;r;alveoli ;                           #defines linear 1D, 2D, 3D and simplex 2D, 3D bases
fem de node;r;cube_host reg 1;                    #defines 3D unit cube host
fem de elem;r;cube_host reg 1;
fem export node;cube as cube reg 1;               #exports cube host for viewing
fem export elem;cube as cube reg 1;
fem de node;c delaunay reg 1 target 2 div 4 rad 0.01 internal ;   #creates delaunay seed points within host region 1 in target region 2, using
                                                  #4 divisions of cube volume, radius of 0.01 for internal boundary and
                                                  #boundary nodes and defines regularly spaced internal seed points
```

```
fem de mesh;c delaunay basis 4 B boundary IB internal_boundary IN_nodes internal reg 2; #specifies boundary, internal boundary, and internal node groups in region 2
fem update delaunay reg 2;                                                              #updates the Delaunay element arrays etc

fem de mesh;c voronoi basis 3 B boundary IB internal_boundary IN_nodes internal convert reg 2 target 3 gen 3;
                                                                                        #calculates the Voronoi mesh based on the defined Delaunay nodes in region
                                                                                        #2 converts the Voronoi cells to nodes and 1D elements into target
                                                                                        #region 3 gen 3 specifies 3 generations ( bifurcations ) of alveolar ducts
fem export node;cell as cell reg 3;                                                     #exports Voronoi nodes
fem export elem;alveoli as alveoli elem alveoli reg 3;                                  #exports Voronoi alveolar elements
fem export elem;duct as duct elem duct reg 3;                                           #exports Voronoi alveolar duct elements
fem quit;
```

A.2 Generating the capillary model over the alveolar surface geometry

This command file creates a 2D Voronoi mesh over the surface of a unit sphere. The Voronoi capillary mesh is then projected onto the alveolar model surfaces. Adjacent alveoli have only a single capillary layer between them (described in Chapter 2).

```
fem de param;r;capillary ;                                                              #defines parameters
fem de coor 3,1;                                                                        #defines co−ordinates
fem de regi; r ; four ;                                                                 #defines 4 regions
fem de base;r; capillary ;                                                              #defines 2D and 3D linear bases
fem de node;r; alveoli ;                                                                #reads in alveolar mesh nodes
fem de elem;r; alveoli ;                                                                #and elements
fem export node;alveoli as alveoli ;                                                    #exports alveolar mesh
fem export elem;alveoli as alveoli ;

fem group elem 100..107,642..687 as alveolus1;
fem group elem 151..158,642..648,688..727 as alveolus2;                                 #grouping alveolar elements so can project capillary
fem group elem 195..202,688..694,728..767 as alveolus3;                                 #mesh over surface
fem group elem 238..245,728..734,768..807 as alveolus4;
fem group elem 284..291,649..655,768..774,808..841 as alveolus5;

fem export elem;1 as 1 elem alveolus1;
fem export elem;2 as 2 elem alveolus2;
fem export elem;3 as 3 elem alveolus3;                                                  #exports each alveolar element group for viewing
fem export elem;4 as 4 elem alveolus4;
fem export elem;5 as 5 elem alveolus5;

fem de mesh;r;capillary reg 2;                                                          #creates the Delaunay, then Voronoi mesh on unit sphere, then
                                                                                        #projects nodes and elements onto alveolar surfaces

fem export node;capillary as cap reg 2;                                                 #exports Voronoi capillary mesh
fem export elem;capillary as cap reg 2;

fem export node;centre as centre reg 3;                                                 #exports nodes on sphere

fem export node;delaunay as delaun reg 4;                                               #exports Delaunay nodes
fem export elem;delaunay as delaun reg 4;                                               #exports Delaunay elements
fem quit;
```

A.3 Solving for flow through the capillary network

This command file creates the capillary mesh, then solves Poiseuille type flow equations within the capillary network. An iterative solution procedure is implemented which accounts for the nonlinear effect of RBCs and capillary diameters on the flow solution (described in Chapter 3).

```
fem de param;r;capillary ;                                  #defines parameters
fem de coor 3,1;                                            #defines coordinates
fem de regi;r;four ;                                        #creates 4 regions
fem de base;r;capillary ;                                   #defines a 1D linear basis function

fem de node;r;cells ;                                       #reads in alveolar finite element nodes
fem de elem;r;cells ;                                       #reads in alveolar finite elements

fem group elem 100..107,642..687 as alveolus1;              #groups alveolar elements

fem de mesh;r;capillary reg 2;                              #creates the 2D Voronoi capillary mesh

fem define equation;r;capillary reg 2;                      #defines the equations to be solved
fem define material;r;capillary reg 2;                      #defines material parameters to be used
#fem define time;r;capillary reg 2;                         #defines time-dependent pressure boundary conditions, if used
fem define initial ;r;capillary reg 2;                      #defines initial conditions
fem define solve;r;capillary reg 2;                         #defines solve parameters to use

#Below is for time dependent pressure boundary conditions:
 $time_initial =0.00;
 $time_final=1;
$time_step=0.1;
$write_out_period=0.1;

fem export nodes;$time_initial as capillary reg 2;
fem export elem;$time_initial as capillary reg 2;
fem export properties; initial as initial reg 2 index 17,11,5;

for ($time=$time_initial ;$time<$time_final;$time=$time+$write_out_period)
{
fem solve restart to $time+$write_out_period reg 2 delta_t $time_step;
fem export properties;$time+$write_out_period as solution reg 2 index 17,11,5;
}

#Below for single time solution (constant boundary condition)
fem solve from 0 to 1 delta_t 0.5 reg 2;                    #solves system of equations

fem export node;capillary as capillary reg 2;               #exports the nodes for viewing
fem export elem;capillary as capillary reg 2;               #exports the elements for viewing
fem export node;solution as solution reg 2 field pressure;  #exports pressure solutions as nodes
fem export properties;solution as solution reg 2 index 17,11,5;  #exports solution properties within elements
                                                            #properties: 17=blood flow 11=vessel hematocrit 5=hydraulic diameter
fem quit;
```

A.4 Generating the arterial and venous geometries

This command file generates the remaining accompanying blood vessels, unidentifiable via imaging, from the MDCT (multi-detector row x-ray computed tomography) vessel endpoints into the lobar volumes using a volume-filling branching

algorithm (described in Chapter 4).

```
$basis_artery=4;                                                    #basis function for generated arteries (1D linear)
$stem=1;                                                            #element number of stem branch
 $length_limit =1.4;                                                #minimum length of a generated branch, to stop further path generation
$branching_fraction=0.4;                                            #branching fraction: distance to centre of mass
$target_region=1;                                                   # arterial region, where generated arteries will be stored
@lobe=('ruml', ' rll ' , ' lul ' , ' lll ' );                       #lobe names in a list : note that rul and rml are not split

fem de param;r;grow_big;
fem de coor 3,1;
fem de base;r;grow;

fem de node;r;grow_ordered2 reg $target_region;
fem de elem;r;grow_ordered2 reg $target_region;

#CALL GROW_LOBES.COM TO GENERATE VESSELS USING VFB ALGORITHM
read com;grow_lobes;

fem de mesh;c lung field only_radius reg $target_region;            #defines radius field
fem evaluate order reg $target_region;                              #determines the generation, Horsfield, and Strahler order numbers
fem update mesh geometry radius_field 1 element 1 constant 15       #defines a radius of 15 mm for the pulmonary trunk
fem update mesh geometry radius_field 1 rd_strahler ratio_diameter 1.5997;   #defines a Strahler branching ratio of 1.5997 to define radius values

fem export node;arteries as arteries reg $target_region;            #exports nodes for viewing
fem export elem;arteries as arteries reg $target_region;            #exports elements for viewing

#Regrouping elements and exporting the nodes and elements of each individual lobe for viewing:

#RUML
fem group elements all parent 9 reg $target_region;
fem group elements all parent 19 reg $target_region;
fem group elements all parent 37 reg $target_region;
fem export elem;ruml1 as ruml1 elem parent9 reg $target_region;
fem export elem;ruml2 as ruml2 elem parent19 reg $target_region;
fem export elem;ruml3 as ruml3 elem parent37 reg $target_region;

#RLL
fem group elem all parent 36 reg $target_region;
fem export elem; rll as rll elem parent36 reg $target_region;

#LUL
fem group elem all parent 6 reg $target_region;
fem group elem all parent 15 reg $target_region;
fem group elem all parent 29 reg $target_region;
fem export elem;lul1 as lul1 elem parent6 reg $target_region;
fem export elem;lul2 as lul2 elem parent15 reg $target_region;
fem export elem;lul3 as lul3 elem parent29 reg $target_region;

#LLL
fem group elem all parent 28 reg $target_region;
fem export elem; lll as lll elem parent28 reg $target_region;

fem list mesh;arteries_grow_CT reg $target_region;  # lists arterial mesh parameters, such as Strahler–based branching, length, and diameter ratios
fem quit;
```

This command file is called from the previous file. This uses the VFB (volume-filling branching) algorithm to 'grow' the arterial branches into individual lobes.

```
#GROUP TERMINAL NODES FOR EACH LOBE:
fem group elements all parent 9 reg $target_region;                 #group all MDCT–derived elements in RUML (right upper and middle lobes)
fem group elements all parent 19 reg $target_region;
fem group elements all parent 37 reg $target_region;
fem group elem parent9,parent19,parent37 by terminal as terminal_ruml reg $target_region;      #group all terminal elements in RUML
```

```
fem group elem all parent 36 reg $target_region;                                   #group all MDCT−derived elements in RLL (right lower lobe)
fem group elem parent36 by terminal as terminal_rll reg $target_region;            #group all terminal elements in RLL

fem group elem all parent 6 reg $target_region;                                    #group all MDCT−derived elements in LUL (left upper lobe)
fem group elem all parent 15 reg $target_region;
fem group elem all parent 29 reg $target_region;
fem group elem parent6,parent15,parent29 by terminal as terminal_lul reg $target_region;   #group all terminal elements in LUL

fem group elem all parent 28 reg $target_region;                                   #group all MDCT−derived elements in LLL (left lower lobe)
fem group elem parent28 by terminal as terminal_lll reg $target_region;            #group all terminal elements in LLL

$N=0;                                                                              #generate vessels using VFB algorithm
foreach $lobe(@lobe)
{
    fem de data;r;$lobe[$N]_data reg $target_region;                               #read in data points
    fem de mesh;c bifur elem terminal_$lobe[$N] reg $target_region target_region $target_region
    basis $basis_artery stem $stem point data length $length_limit fraction_branching $branching_fraction;
    $N=$N+1;
}
```

A.5 Creating the supernumerary vessel geometry

This command file generates the supernumerary vessels in the left lower lobe (LLL) only. The nodes and elements of the accompanying blood vessels are read in, Strahler order numbers are determined and diameter values are allocated (based on a Strahler diameter ratio). Supernumerary vessels are then generated to 'grow' towards the closest data point (representing an acinar unit) (described in Chapter 4).

```
fem de param;r;super;                                                              #define parameters
fem de coor 3,1;                                                                   #define coordinates
fem de base;r;super;                                                               #define 1D basis function

fem de data;r; lll_data ;                                                          #reads in, then exports the data points for the left lower lobe (LLL)
fem export data;artery_data as artery_data;

fem de node;r; initial_arteries ;                                                  #reads in the nodes and elements of a portion of the arterial mesh in the LLL
fem de elem;r; initial_arteries ;

fem de mesh;c lung field only_radius_field ;                                       #sets up field framework for radius field only

fem evaluate order;                                                                #evaluates the generations and orders of the vessels


fem update mesh geometry radius_field 1 element 1 constant 3.650;                  #this inputs a constant value of 3.650 for the radius of the first element

fem update mesh geometry radius_field 1 rd_strahler ratio_diameter 1.5997;         #defines the radius of each of the vessels, using a strahler diameter ratio of 1.5997

fem de mesh;c lung add_super d_ratio 0.3 sv_freq 1.05 arteries diameter diam_ratio 1.5997 d_max_order 30;
                                                                                   #adds the supernumerary vessels to the existing arterial mesh d_ratio:defines
                                                                                   #the diameter ratio of the supernumerary vessel to the stem vessel
                                                                                   #sv_freq=the supernumerary frequency from each stem vessel diam_ratio=the
                                                                                   #Strahler based diameter ratio −> used to define diameter of each vessel
                                                                                   #d_max_order=the diameter of the maximum order vessel (i.e. Strahler order 17)

fem export node; lll_arteries as lll_arteries ;                                    #exports the arterial mesh nodes and elements
fem export elem; lll_arteries as lll_arteries ;

fem export elem;stem as stem elem stem;                                            #exports the stem element group (containing all stem vessels before
                                                                                   #supernumerary addition)
```

```
fem export elem;supernumeraries as supernumerary elem supernumerary;   #an element group containing all the supernumerary elements (called supernumerary)
                                                                        #gets created in the code, this is exported for viewing
fem quit;
```

A.6 Solving the Navier-Stokes flow equations through the arterial and venous models

This command file implements the finite difference grid-based, two step Lax-Wendroff scheme for solution of the Navier-Stokes flow equations (described in Chapter 5). This file creates a symmetric mesh and solves for pressure, radius, and velocity within this network.

```
fem define param;r;flow;                                                #defines parameters
fem define coord;r;flow;                                                #defines coordinates
fem define base;r;flow;                                                 #defines a 1D linear basis function
fem de node;r;trunk as parent;                                          #reads in vascular nodes
fem de elem;r;trunk as parent;                                          #reads in elements

fem evaluate order;                                                     #evaluate ordering of parent vessels before creating symmetric mesh
fem de mesh;c lung symmetric num_generation 4 branch_angle 40 elem parent;
                                                                        #creates 4 symmetric branch generations from the initial starting elements with a branch
                                                                        #angle of 40 degrees
fem define mesh;c lung field only_radius;                               #sets up radius field only

fem evaluate order;                                                     #calculates the generation and order number of the mesh
fem update mesh geometry radius_field 1 element 1 constant 12;          #defines inlet arterial radius of 12 mm
fem update mesh geometry radius_field 1 Rd_strahler ratio_diameter 1.5997; #defines remaining branch radius values using Strahler diameter ratio of 1.5997
fem de elem;w;test;
fem de elem;r;test;                                                     #sets up NLL — element length array

fem define;add field;d;arteries;                                        #adds two more fields to store the pressure and velocity fields , adds 0 as default value
fem define element;d;arteries field;                                    #defines element field parameters
fem define grid;r;flow coronary;                                        #defines grid points with coronary option to discretise the spatial computational domain
fem update grid geometry;                                               #updates all grid arrays
fem define equation;r;flow;                                             #defines equations options to use
fem define material;r;flow;                                             #reads in physical & mechanical properties
fem update material field material 4 no_field 1;
fem define time;r;step;
fem define initial;r;flow;                                              #defines initial conditions
fem define solve;r;flow;                                                #defines solution parameters

 $time_initial =0.00;                                                   #sets the initial time
 $time_final =1.5;                                                      #sets the final time
$time_step=0.001;                                                       #sets the time step time
$write_out_period=0.1;                                                  #sets the results write out period

fem export points; $time_initial grid as vessel offset 0;
fem export grid;vessel as vessel offset_node 0 elastic_tube;

# Results output loop
for ($time= $time_initial ;$time<$time_final;$time=$time+$write_out_period)
{
fem solve restart to $write_out_period delta_t $time_step;              #solves the equations
fem export points;$time+$write_out_period grid as vessel offset 0
}
fem quit;
```

Appendix B

Movies

A CD-ROM is included with this thesis and contains a series of movies illustrating, in three-dimensions, some of the modelling procedures detailed in this thesis. The following movies are included on the CD-ROM:

1. **Alveolar geometry (alveolar_geometry.mpg):**
   This movie demonstrates the 3D Voronoi meshing technique within a unit cube. Certain Voronoi 'cells' are then allocated as duct cells (shown in blue). All adjacent Voronoi cells are then considered to be alveoli (shown in gray). A single alveolar sac, consisting of 19 alveoli (shown in pink), is isolated for analysis and creation of the capillary model.

2. **Capillary geometry (capillary_geometry.mpg):**
   This movie displays the method used to create the capillary geometry. A 2D Voronoi meshing technique is applied on the surface of a unit sphere. Uniformly distributed points are first created on the unit sphere. The Delaunay triangulation is then formed and the Voronoi mesh is created. This mesh is then projected down onto the alveolar surface of a single alveoli. The entire alveolar sac capillary mesh is also displayed.

3. **Capillary blood flow (capillary_flow.mpg):**
   This movie initiates at the parenchymal (alveolar model) level and zooms out to display the alveolar sac capillary model. A pulsatile pressure solution within the capillary model is then displayed in the movie. The flow rate solution is displayed ($\mathrm{mm}^3\ \mathrm{s}^{-1}$) and ranges from 8.9301e-08 (red) to 0 (dark blue). This solution is obtained by imposing a time-dependent pressure boundary condition at the arteriole inlet vessels.

4. **Lobar geometry fitting (lobes.mpg):**
   This movie demonstrates the fitting of the lobar models to MDCT (multi-detector row x-ray computed tomography) data. MDCT slices are stacked to produce rendered iso-surfaces of the lung surface. The scan data is of high enough resolution to detect the fissures and enable a description of the geometry of each of the five separate lobes. Data points are generated on the iso-surfaces. A geometry fitting procedure is then used to fit initially linear elements to the data points. This movie was created by Dr Merryn Tawhai.

5. **Vascular geometry (vessels_grow.mpg):**
   This movie demonstrates the volume-filling branching (VFB) algorithm used to generate the remaining arterial and venous vessels unidentifiable from the MDCT image data. The algorithm begins from the terminal locations of the vessels identified from MDCT and creates a volume-filling branching structure into the lobar volumes.

6. **Pulsatile pressure solution (pulsatile_pressure.mpg):**
   This movie displays the pulsatile pressure solution through the arterial network. A pulsatile pressure boundary condition is applied at the pulmonary trunk inlet (as defined in Section 5.4.8) and all terminal arterial pressures are constant over time. The solution spectrum ranges from -0.04 to 3.2 kPa.

7. **Pulsatile velocity solution (pulsatile_velocity.mpg):**
   This movie illustrates the pulsatile velocity solution through the arterial network. The solution spectrum ranges from -50 to 400 $\mathrm{mm\ s^{-1}}$.

Bibliography

Bennett, S. H., Goetzman, B. W., Milstein, J. M. & Pannu, J. S. (1996), 'Role of arterial design on pulse wave reflection in a fractal pulmonary network', *J Appl Physiol*.

Bourke, S. J. & Brewis, R. A. L. (1998), *Lecture Notes on Respiratory Medicine*, 5th edn, Blackwell Science.

Bradley, C. P., Pullan, A. J. & Hunter, P. J. (1997), 'Geometric modelling of the human torso using cubic hermite elements', *Ann. Biomed. Eng*.

Burrowes, K. S., Tawhai, M. H. & Hunter, P. J. (2004), 'Modeling rbc and neutrophil distribution through an anatomically based pulmonary capillary network', *Ann Biomed Eng*.

Burrowes, K. S., Tawhai, M. H. & Hunter, P. J. (2005*a*), 'Anatomically based finite element models of the human pulmonary arterial and venous trees including supernumerary vessels', *J Appl Physiol*.

Burrowes, K. S., Tawhai, M. H. & Hunter, P. J. (2005*b*), Evaluation of arterial blood flow heterogeneity in an image-based computational model.

Burton, A. C. (1965), *Physiology and Biophysics of the Circulation, An introductory text*, Year Book Medical Publishers, Inc.

Chang, H. K. & Paiva, M. (1989), *Respiratory Physiology - An Analytical Approach*, Vol. 40, 1st edn, Marcel Dekker, New York.

Clough, A. V., Haworth, S. T., Hanger, C. C., Wang, J., Roerig, D. L., Linehan, J. H. & Dawson, C. A. (1998), 'Transit time dispersion in the pulmonary arterial tree', *J Appl Physiol* **85**(2), 565–574.

Collins, R. & Maccario, J. A. (1979), 'Blood flow in the lung', *Journal of Biomechanics* **12**, 373–395.

Dawant, B., Levin, M. & Popel, A. S. (1986), 'Effect of dispersion of vessel diameters and lengths in stochastic networks - i modelling the microcirculatory flow', *Microvascular Research* **31**, 203–222.

Dawson, C. A., Capen, R. L., Latham, L. P., Hanson, W. L., Hofmeister, S. E., Bronikowski, T. A., Rickaby, D. A. & Wagner Jr, W. W. (1987), 'Pulmonary arterial transit times', *J Appl Physiol*.

Dawson, C. A., Krenz, G. S., Karau, K. L., Haworth, S. T., Hanger, C. C. & Linehan, J. H. (1999), 'Structure-function relationships in the pulmonary arterial tree', *J Appl Physiol* **86**(2), 569–583.

Dawson, C. D., Krenz, G. S. & Linehan, J. H. (1998), *Complexity in Structure and Function of the Lung*, Marcel Dekker, Inc, chapter Complexity and structure-function relationships in the pulmonary arterial tree.

deMello, D. & Reid, L. M. (1991), *The Lung: Scientific Foundations*, Raven Press Ltd, chapter 4.2.5 Arteries and Veins.

Denney, B. W., Beck, K. C., Shikata, H., McLennan, G. & Hoffman, E. A. (2004), Regional pulmonary blood flow in awake supine human subjects by multi-detector ct, *in* 'ATS conference proceedings', American Thoracic Society (ATS).

Denny, E. & Schroter, R. C. (1995), 'The mechanical behaviour of a mammalian lung alveolar duct model', *Journal of Biomechanical Engineering*.

Denny, E. & Schroter, R. C. (1996), 'A mathematical model for the morphology of the pulmonary acinus', *Journal of Biomechanical Engineering*.

Dhadwal, A., Wiggs, B., Doerschuk, C. & Kamm, R. (1997), 'Effects of anatomic variability on blood flow and pressure gradients in the pulmonary circulation', *J Appl Physiol* **83**(5), 1711–1720.

Doerschuk, C. M. (1999), 'Neutrophil rheology and transit through capillaries and sinusoids', *Am J Respir Crit Care Med* **159**(6), 1693–5.

Doerschuk, C. M., Beyes, N., Coxson, H. O., Wiggs, B. & Hogg, J. C. (1993), 'Comparison of neutrophil and capillary diameters and their relation to neutrophil sequestration in the lung', *J Appl Physiol* **74**, 3040–3045.

Doerschuk, C. M., Coxson, H. O. & Hogg, J. C. (1989), 'The site of neutrophil (pmn) accumulation within the pulmonary capillary bed after infusion of zymosan-activated plasma (zap) (abstract)', *Am Rev Respir Dis* **139**, A302.

Drost, E. M., Kassabian, G., Meiselman, H. J., Gelmont, D. & Fisher, T. C. (1999), 'Increased rigidity and priming of polymorphonuclear leukocytes in sepsis', *Am J Respir Care Med* **159**, 1696–1702.

Elliot, F. M. & Reid, L. (1965), 'Some new facts about the pulmonary artery and its branching pattern', *Clinical Radiology*.

Fahraeus, R. (1929), 'The suspension stability of blood', *Physiol. Rev.* **9**(2), 241–274.

Fahraeus, R. & Lindqvist, T. (1931), 'The viscosity of the blood in narrow capillary tubes', *J Appl Physiol* **96**, 562–568.

Fenton, B. M., Wilson, D. W. & Cokelet, G. R. (1985), 'Analysis of the effects of measured white blood cell entrance times on hemodynamics in a computer model of a microvascular bed', *Pflugers Arch* **403**, 396–401.

Fernandez, J., Mithraratne, P., Thrupp, S., Tawhai, M. H. & Hunter, P. J. (2004), 'Anatomically based geometric modelling of the musculo-skeletal system and other organs', *Biomechan Model Mechanobiol* pp. 139–155.

Fung, Y. C. (1988), 'A model of the lung structure and its validation', *J Appl Physiol*.

Fung, Y. C. (1990), *Biomechanics (Motion, Flow, Stress and Growth)*, 1st edn, Springer-Verlag, USA.

Fung, Y. C. & Sobin, S. S. (1969), 'Theory of sheet flow in lung alveoli', *J Appl Physiol* **26**, 472–488.

Fung, Y. C. & Sobin, S. S. (1972*a*), 'Elasticity of the pulmonary alveolar sheet', *Circulation Research* **30**, 451–469.

Fung, Y. C. & Sobin, S. S. (1972*b*), 'Pulmonary alveolar blood flow', *Circulation Research* **30**, 470–490.

Fung, Y. C. & Sobin, S. S. (1977), *Bioengineering Aspects of the Lung*, Marcel Dekker, Inc, chapter Pulmonary Alveolar Blood Flow.

Gebb, S. A., Graham, J. A., Hanger, C. C., Godbey, P. S., Capen, R. L., Doerschuk, C. M. & Wagner Jr, W. W. (1995), 'Sites of leukocyte sequestration in the pulmonary microcirculation', *J Appl Physiol* **79**(2), 493–497.

Glazier, J. B., Hughes, J. M. B., Maloney, J. E. & West, J. B. (1967), 'Vertical gradient of alveolar size in lungs of dogs frozen intact', *J Appl Physiol* **23**, 694–705.

Glenny, R. W. & Robertson, H. T. (1991), 'Fractal modeling of pulmonary blood flow heterogeneity', *J Appl Physiol*.

Glenny, R. W. & Robertson, H. T. (1998), *Complexity in Structure and Function of the Lung*, Marcel Dekker, chapter A changing perspective on blood flow distribution.

Glenny, R. W., Bernard, S., Robertson, H. T. & Hlastala, M. P. (1999), 'Gravity is an important but secondary determinant of regional pulmonary blood flow in upright primates', *J Appl Physiol* **86**(2), 623–632.

Glenny, R. W., Lamm, W. J. E., Albert, R. K. & Robertson, H. T. (1991), 'Gravity is a minor determinant of pulmonary blood flow distribution', *J Appl Physiol* **72**, 620–629.

Glenny, R. W., Lamm, W. J. E., Bernard, S. L., An, D., Chornuk, M., Pool, S. L., Wagner Jr, W. W., Hlastala, M. P. & Robertson, H. T. (2000), 'Physiology of a microgravity environment, selected contribution: redistribution of pulmonary perfusion during weightlessness and increased gravity.', *J Appl Physiol* **89**, 1239–1248.

Glenny, R. W., Polissar, L. & Robertson, H. T. (1991), 'Relative contribution of gravity to pulmonary perfusion heterogeneity', *Journal of Applied Physiology* **71**, 2449–2452.

Godbey, P. S., Graham, J. A., Presson Jr, R. G., Wagner Jr, W. W. & Lloyd Jr, T. C. (1995), 'Effect of capillary pressure and lung distension on capillary recruitment', *J Appl Physiol* **79**(4), 1142–1147.

Gray (1995), *Grays Anatomy*, 38th edn, Churchill Livingstone, USA.

Guntheroth, W. G., Luchtel, D. L. & Kawabori, I. (1982), 'Pulmonary microcirculation-tubules rather than sheet and post', *J Appl Physiol* **53**, 510–515.

Guyton, A. C. & Hall, J. E. (2000), *Textbook of Medical Physiology*, 10th edn, W.B. Saunders Company, USA.

Haefeli-Bleuer, B. & Weibel, E. R. (1988), 'Morphometry of the human pulmonary acinus', *The Anatomical Record* **220**, 401–414.

Hakim, T. S., Lisbona, R. & Dean, G. W. (1987), 'Gravity-independent inequality of pulmonary blood flow in humans', *J Appl Physiol* pp. 1114–1121.

Hanger, C. C., Presson Jr, R. G., Okada, O., Janke, S. J., Watkins, J. J., Wagner Jr, W. W. & Capen, R. L. (1997), 'Computer determination of perfusion patterns in pulmonary capillary networks', *J Appl Physiol* **82**(4), 1283–1289.

Hanger, C. C., Wagner Jr, W. W., Janke, S. J., Lloyd Jr, T. C. & Capen, R. L. (1993), 'Computer simulation of neutrophil transit through the pulmonary capillary bed', *J Appl Physiol* **74**(4), 1647–1652.

Hansen, J. E. & Ampaya, E. P. (1975), 'Human air spaces, sizes, areas, and volumes', *J Appl Physiol* **38**(6), 990–995.

Harris, P. & Heath, D. (1977), *The Human Pulmonary Circulation*, 2nd edn, Churchill Livingstone, USA.

Harris, P. & Heath, D. (1986), *The Human Pulmonary Circulation: It's Form and Function in Health and Disease*, 3rd edn, Churchill Livingstone, USA.

Hill, E. P., Power, G. G. & Longo, L. D. (1973), 'Mathematical simulation of pulmonary o2 and co2 exchange', *American Journal of Physiology* **224**(4), 904–917.

Hislop, A. & Reid, L. (1978), 'Normal structure and dimensions of the pulmonary arteries in the rat', *J Anat*.

Hlastala, M. P. (1972), 'A model of fluctuating alveolar gas exchange during the respiratory cycle', *Respiration Physiology* **15**, 214–232.

Hlastala, M. P. & Berger, A. J. (2001), *Physiology of Respiration*, Oxford University Press.

Hlastala, M. P. & Glenny, R. W. (1999), 'Vascular structure determines pulmonary blood flow distribution', *News Physiol Sci*.

Hlastala, M. P. & Robertson, H. T. (1998), *Complexity in Structure and Function of the Lung*, Vol. 121 of *Lung Biology in Health and Disease*, Marcel Dekker, Inc, USA.

Hogg, J. C. (1987), 'Neutrophil kinetics and lung injury', *Physiol Rev* **67**, 1249–1295.

Hogg, J. C. (1991), Neurophil kinetics in the pulmonary circulation, *in* S. I. Said, ed., 'The pulmonary circulation and acute lung injury', 2nd edn, Futura, NY.

Hogg, J. C. & Doerschuk, C. M. (1995), 'Leukocyte traffic in the lung', *Annu Rev Physiol* **57**, 97–114.

Hogg, J. C., Coxson, H. O., Brumwell, M., Beyers, N., Doerschuk, C. M., MacNee, W. & Wiggs, B. R. (1994), 'Erythrocyte and polymorphonuclear cell transit time and concentration in human pulmonary capillaries', *J Appl Physiol* **77**(4), 1795–1800.

Hogg, J. C., Martin, B. A., Lee, S. & McLean, T. (1985), 'Regional differences in erythrocyte transit in normal lungs', *J Appl Physiol* **59**(4), 1266–1271.

Hogg, J. C., McLean, T., Martin, B. A. & Wiggs, B. (1988), 'Erythrocyte transit and neutrophil concentration in the dog lung', *J Appl Physiol* **65**(3), 1217–1225.

Hoppin, F. G. & Hildebrandt, J. (1977), *Bioengineering Aspects of the Lung*, Vol. 3 of *Lung Biology in Health and Disease*, Marcel Dekker, Inc, chapter Mechanical Properties of the Lung.

Horsfield, K. (1978), 'Morphometry of the small pulmonary arteries in man.', *Circulation Research* **42**, 593–537.

Horsfield, K. (1985), *Anatomical factors influencing gas mixing and distribution*, Marcel Dekker, chapter Gas Mixing and Distribution in the Lung.

Horsfield, K. & Cumming, G. (1967), 'Angles of branching and diameters of branches in the human bronchial tree', *Bull Math Biophys*.

Horsfield, K. & Cumming, G. (1968), 'Morphology of the bronchial tree in man', *J Appl Physiol* **24**, 373–383.

Horsfield, K. & Gordon, W. I. (1981), 'Morphometry of pulmonary veins in man', *Lung* **159**, 211–218.

Horsfield, K. & Woldenberg, M. J. (1989), 'Diameters and cross-sectional areas of branches in the human pulmonary arterial tree.', *The Anatomical Record* **223**, 245–251.

Horton, R. E. (1945), 'Erosional development of streams and their drainage basins; hydrophysical approach to quantitative morphology', *Bull. Geol. Soc. Am* **56**, 275–370.

Huang, W., Tian, Y., Gao, J. & Yen, R. T. (1998), 'Comparison of theory and experiment in pulsatile flow in cat lung', *Annals of Biomedical Engineering* **26**, 812–880.

Huang, W., Yen, R. T., McLaurine, M. & Bledsoe, G. (1996), 'Morphometry of the human pulmonary vasculature', *J Appl Physiol* **81**(5), 2123–2133.

Huang, Y., Doerschuk, C. & Kamm, R. (2001), 'Computational modeling of rbc and neutrophil transit through the pulmonary capillaries', *J Appl Physiol* **90**, 545–564.

Hughes, J. M. B., Glazier, J. B., Maloney, J. E. & West, J. B. (1968), 'Effect of lung volume on the distribution of pulmonary blood flow in man', *Respiration Physiology*.

Hunter, P. J. (1972), Numerical solution of arterial blood flow, Master's thesis, University of Auckland.

Jiang, Z. L., Kassab, G. S. & Fung, Y. C. (1994), 'Diameter-defined strahler system and connectivity matrix of the pulmonary arterial tree', *J Appl Physiol* **76**(2), 882–892.

Jones, A. T., Hansell, D. M. & Evans, T. W. (2001), 'Pulmonary perfusion in supine and prone positions: an electron beam study', *J Appl Physiol* **90**, 1342–1348.

Karau, K. L., Lothen, R. C., Dhyani, A., Haworth, S. T., Hanger, C. C., Roerig, D. L., Johnson, R. H. & Dawson, C. A. (2001), 'Pulmonary arterial morphometry from microfocal x-ray computed tomography', *Am J Physiol Heart Circ Physiol*.

Kassab, G. S., Rider, C. A., Tang, N. J. & Fung, Y. C. (1993), 'Morphometry of pig coronary arterial trees', *Am J Physiol Heart Circ Physiol*.

Kiani, M. F. & Hudetz, A. G. (1991), 'A semi-empirical model of apparent blood viscosity as a function of vessel diameter and discharge hematocrit', *Biorheology*.

Kitaoka, H., Tamura, S. & Takaki, R. (2000), 'A three-dimensional model of the human pulmonary acinus', *J Appl Physiol* **88**, 2260–2268.

Klitzman, B. & Johnson, P. C. (1982), 'Capillary network geometry and red cell distribution in hamster cremaster muscle', *American Journal of Physiology* **242**, H211–H219.

Krenz, G. S. & Dawson, C. A. (2003), 'Flow and pressure distributions in vascular networks consisting of distensible vessels', *Am J Physiol Heart Circ Physiol*.

Krenz, G. S., Linehan, J. H. & Dawson, C. A. (1992), 'A fractal continuum model of the pulmonary arterial tree', *J Appl Physiol*.

Lamm, W. J. E. & Albert, R. K. (2000), 'Effect of zonal conditions and posture on pulmonary blood flow distribution to subpleural and interior lung', *J Appl Physiol*.

Lamm, W. J. E., Kirk, K. R., Hanson, W. L., Wagner Jr, W. W. & Albert, R. K. (1991), 'Flow through zone 1 lungs utilizes alveolar corner vessels', *J Appl Physiol*.

Levin, D. L. & Hatabu, H. (2004), 'Mr evaluation of pulmonary blood flow', *J Thorac Imaging* **19**(4), 241–249.

Levin, D. L., Chen, Q. & Zhuang, M. (2001), 'Evaluation of regional pulmonary perfusion using ultrafast magnetic resonance imaging', *Magnetic Resonance in Medicine* **46**, 166–171.

Levin, M., Dawant, B. & Popel, A. S. (1986), 'Effect of dispersion of vessel diameters and lengths in stochastic networks - ii modelling of microvascular hematocrit distribution', *Microvascular Research* **31**, 223–234.

Levitzky, M. G. (1990), *Pulmonary Physiology*, 5th edn, McGraw-Hill, USA.

Li, B., Christensen, G. E., Hoffman, E. A., McLennan, G. & Reinhardt, J. M. (2003), 'Establishing a normative atlas of the human lung: Intersubject warping and registration of volumetric ct images', *Acad Radiol*.

Li, C. W. & Cheng, H. D. (1993), 'A nonlinear fluid model for pulmonary blood circulation', *J Biomechanics*.

Lien, D. C., Wagner Jr, W. W., Capen, R. L., Haslett, C., Hanson, W. L., Hofmeister, S. E., Henson, P. M. & Worthen, G. S. (1987), 'Physiological neutrophil sequestration in the lung: visual evidence for localization in capillaries', *J Appl Physiol* **62**, 1236–1243.

Liu, Y. H., Hoffman, E. A. & Ritman, E. L. (1987), 'Measurement of three-dimensional anatomy and function of pulmonary arteries with high-speed x-ray computed tomography', *Investigative Radiology*.

MacNee, W., Martin, B. A., Wiggs, B. R., Belzberg, A. S. & Hogg, J. C. (1989), 'Regional pulmonary transit times in humans', *J Appl Physiol* **66**(2), 844–850.

Maina, J. N. & van Gils, P. (2001), 'Morphometric characterization of the airway and vascular systems of the lung of the domestic pig, sus scrofa: comparison of the airway, arterial and venous system', *Comparative Biochemistry and Physiology Part A* **130**, 781–798.

Mercer, R. R., Laco, J. M. & Crapo, J. D. (1987), 'Three-dimensional reconstruction of alveoli in the rat lung for pressure-volume relations', *J Appl Physiol* **62**, 1480–1487.

Musch, G., Layfield, J. D. H., Harris, R. S., Melo, M. F. V., Winkler, T., Callahan, R. J., Fischman, A. J. & Venegas, J. G. (2002), 'Topographical distribution of pulmonary perfusion and ventilation, assessed by pet in supine and prone humans', *J Appl Physiol* **93**, 1841–1851.

Needham, D. & Hochmuth, R. M. (1990), 'Rapid flow of passive neutrophils into a 4 micrometer pipet and measurement of cytoplasmic viscosity', *Journal of Biomechanical Engineering* **112**, 269–276.

Okabe, A., Boots, B. & Sugihara, K. (1992), *Spatial Tessellations: concepts and applications of Voronoi diagrams*, John Wiley and Sons, England.

Okada, O., Presson Jr, R. G., Godbey, P. S., Capen, R. L. & Wagner Jr, W. W. (1994), 'Temporal capillary perfusion patterns in single alveolar walls of intact dogs', *J Appl Physiol* **76**, 380–386.

Palagyi, K., Sorantin, E., Balogh, E., Kuba, A., Halmai, C., Erdohelyi, B. & Hausegger, K. (2001), A sequential 3d thinning algorithm and its medical applications, *in* '17th Int Conf Information Processing in Medical Imaging, IMPI'.

Parker, J. C., Cave, C. B., Ardell, J. L., Hamm, C. R. & Williams, S. G. (1997), 'Vascular tree structure affects lung blood flow heterogeneity simulated in three dimensions', *J Appl Physiol* **93**(4), 1370–1382.

Permutt, S., Bromberger-Barnes, B. & Bane, H. N. (1962), 'Alveolar pressure, pulmonary venous pressure, and the vascular waterfall', *Med Thorac* **19**, 239–260.

Presson Jr, R. G., Hanger, C. C., Godbey, P. S., Graham, J. A., Lloyd, T. C. & Wagner Jr, W. W. (1994), 'Effect of increasing flow on distribution of pulmonary capillary transit times', *J Appl Physiol* **76**(4), 1701–1711.

Presson Jr, R. G., Todoran, T. M., Witt, B. J. D., McMurtry, I. F. & Wagner Jr, W. W. (1997), 'Capillary recruitment and transit time in the rat lung', *J Appl Physiol* **83**(2), 543–549.

Presson, R. G., Graham, J. A., Hanger, C. C., Godbey, P. S., Gebb, S. A., Sidner, R. A., Glenny, R. W. & Wiltz, W. (1995), 'Distribution of pulmonary capillary red blood cell transit times', *J Appl Physiol* **79**(2), 382–388.

Pries, A. R. & Secomb, T. W. (2000), 'Microcirculatory network structures and models', *Annals of Biomedical Engineering* **28**, 916–921.

Pries, A. R., Secomb, T. W. & Gaehtgens, P. (1996), 'Biophysical aspects of blood flow in the microvasculature', *Cardiovascular Research* **32**, 654–667.

Pries, A. R., Secomb, T. W., Gaehtgens, P. & Gross, J. F. (1990), 'Blood flow in microvascular networks - experiments and simulation', *Circulation Research* **67**, 826–834.

Pries, A. R., Secomb, T. W., Geβner, T., Sperandio, M. B., Gross, J. F. & Gaehtgens, P. (1994), 'Resistance to blood flow in microvessels in vivo', *Circulation Research*.

Prisk, G. K., Paiva, M. & West, J. B., eds (2001), *Gravity and the Lung - Lessons from microgravity*, Vol. 160 of *Lung Biology in Health and Disease*, Marcel Dekker, Inc.

Riley, D. J. (1991), *The Lung: Scientific Foundations*, Raven Press Ltd, chapter 5.2.7 Vascular Remodeling.

Sauret, V., Halson, P. M., Brown, I. W., Fleming, J. S. & Bailey, A. G. (2000), 'Study of the three-dimensional geometry of the central conducting airways in man using computed tomographic (ct) images', *J Anat*.

Scharf, S. M., Pinsky, M. R. & Magder, S., eds (2001), *Respiratory-Circulatory Interactions in Health and Disease*, 1st edn, Marcel Dekker, Inc., USA.

Schmid-Schoenbein, G. W., Skalak, R., Usami, S. & Chien, S. (1980), 'Cell distribution in capillary networks', *Microvascular Research*.

Secomb, T. W. (1995), Mechanics of blood flow in the microcirculation, *in* 'Biological Fluid Dynamics', Vol. 49, pp. 305–321.

Shaw, A. M., Bunton, D. C., Fisher, A., McGrath, J. C., Montgomery, I., Daly, C. & MacDonald, A. (1999), 'V-shaped cushion at the origin of bovine pulmonary supernumerary arteries: structure and putative function', *J Appl Physiol*.

Shikata, H., Sonka, M. & Hoffman, E. A. (2004), Fully automated pulmonary vascular tree segmentation using human and sheet 3d ct data, *in* 'ATS conference proceedings', ATS.

Skalak, R. & Chien, S. (1987), *Handbook of Bioengineering*, 1st edn, McGraw-Hill, Inc, USA.

Smith, N. (1999), Coronary Flow Mechanics- An anatomically based mathematical model of coronary blood flow coupled to cardiac contraction., PhD thesis, University of Auckland.

Smith, N. P., Pullan, A. J. & Hunter, P. J. (2002), 'An anatomically based model of transient coronary blood flow in the heart', *Siam J Appl Math* **62**(3), 990–1018.

Sobin, S. S., Tremer, H. M. & Fung, Y. C. (1970), 'Morphometric basis of the sheet-flow concept of the pulmonary alveolar microcirculation in the cat', *Circulation Research* **26**, 397–414.

Staub, N. C. & Shultz, E. L. (1968), 'Pulmonary capillary length in dog, cat and rabbit', *Respiration Physiology* **5**, 371–378.

Strahler, A. N. (1953), 'Revision of horton's quantitative factors in erosional terrain', *Trans. Am. Geophys. Union* **34**, 345.

Strang, G. (1986), *Introduction to Applied Mathematics*, Wellesley-Cambridge Press, chapter 7, Network Flows and Combinatorics.

Swenson, E. R., Domino, K. B. & Hlastala, M. P. (1998), *Complexity in Structure and Function of the Lung*, Marcel Dekker, chapter Physiological effects of oxygen and carbon dioxide on $\dot{V}_A/Q$ heterogeneity, pp. 511–548.

Takamasa, O. & Nitta, S. (1993), 'Computer simulation of geometry and hemodynamics of canine pulmonary arteries', *Annals of Biomedical Engineering*.

Tawhai, M. H. & Burrowes, K. S. (2003), 'Developing integrative computational models of pulmonary structure', *The Anatomical Record (Part B: New Anat)* **275B**, 207–218.

Tawhai, M. H., Hunter, P. J., Tschirren, J., Reinhardt, J., McLennan, G. & Hoffman, E. A. (2004), 'Ct-based geometry analysis and finite element models of the human and ovine bronchial tree', *J Appl Physiol*.

Tawhai, M. H., Pullan, A. J. & Hunter, P. J. (2000), 'Generation of an anatomically based model of the conducting airways', *Annals of Biomedical Engineering*.

Terashima, T., Klut, M. E., English, D., Hards, J., Hogg, J. C. & van Eeden, S. F. (1999), 'Cigarette smoking causes sequestration of polymorphonuclear leukocytes released from the bone marrow in lung microvessels', *Am J Respir Cell Mol Biol* **20**, 171–177.

Wagner Jr, W. W., Latham, L. P., Hanson, W. L., Hofmeister, S. E. & Capen, R. L. (1986), 'Vertical gradient of pulmonary capillary transit times', *J Appl Physiol* **61**(4), 1270–1274.

Wagner Jr, W. W., Todoran, T. M., Tanabe, N., Wagner, T. M., Tanner, J. A., Glenny, R. W. & Presson Jr, R. G. (1999), 'Pulmonary capillary perfusion: intra-alveolar fractal patterns and interalveolar independence', *J Appl Physiol* **86**(3), 825–831.

Weibel, E. R. (1963), *Morphometry of the Human Lung*, 1st edn, Springer-Verlag, Berlin.

Weibel, E. R. (1984), *The Pathway for Oxygen - Structure and Function of the Mammalian Respiratory System*, 1st edn, Harvard University Press, USA.

West, J. B. (1979), *Respiratory Physiology - the essentials*, 2nd edn, Williams and Wilkins, USA.

West, J. B. (1992), 'Gravity and pulmonary blood flow distribution', *J Appl Physiol* **73**, 2201–2202.

West, J. B. (1995), *Respiratory Physiology - The Essentials*, 5th edn, Williams and Wilkins, USA.

West, J. B. (1999), 'How it really happened - distribution of pulmonary blood flow', *Am J Respir Crit Care Med* **160**, 1802–1803.

West, J. B. (2000), *Respiratory Physiology: The Essentials*, Lippincott Williams and Wilkins.

West, J. B., Dollery, C. T. & Naimark, A. (1964), 'Distribution of blood flow in isolated lung; relation to vascular and alveolar pressures', *J Appl Physiol* **19**, 713–724.

West, J. B., ed. (1977), *Regional Differences in the Lung*, Academic Press.

West, J. B., Glenny, R. W., Hlastala, M. P. & Robertson, H. T. (2002), 'letters to the editor: Importance of gravity in determining the distribution of pulmonary blood flow', *J Appl Physiol* **93**, 1888–1891.

Wiggs, B. R., English, D., Quinlan, W. M., Doyle, N. A., Hogg, J. C. & Doerschuk, C. M. (1994), 'Contributions of capillary pathway size and neutrophil deformability to neutrophil transit through rabbit lung', *J Appl Physiol* **77**(1), 463–470.

Won, C., Chon, D., Tajik, J., Tran, B. Q., Robinswood, G. B., Beck, K. C. & Hoffman, E. A. (2003), 'Ct-based assessment of regional pulmonary microvascular blood flow parameters', *J Appl Physiol*.

Wood, S. A., Zerhouni, E. A., Horford, J. D., Hoffman, E. A. & Mitzner, W. (1995), 'Measurement of three-dimensional lung tree structures by using computed tomography', *J Appl Physiol*.

Yen, R. T. & Foppiano, L. (1981), 'Elasticity of small pulmonary veins in the cat', *Journal of Biomechanical Engineering*.

Yen, R. T., Fung, Y. C. & Bingham, N. (1980), 'Elasticity of small pulmonary arteries in the cat', *Journal of Biomechanical Engineering*.

Yeung, A. & Evans, E. (1989), 'Cortical shell-liquid core model for passive flow of liquid-like spherical cells into micropipettes', *Biophys J* **56**, 139–149.

Zhuang, F. Y., Fung, Y. C. & Yen, R. T. (1983), 'Analysis of blood flow in cat's lung with detailed anatomical and elasticity data', *J Appl Physiol: Respirat. Exercise Physiol.* **55**(4), 1341–1348.

Zhuang, F. Y., Yen, M. R. T., Fung, Y. C. & Sobin, S. S. (1985), 'How many pulmonary alveoli are supplied by a single arteriole and drained by a single venule?', *Microvascular Research* **29**, 18–31.